Characterization of air pollutant and greenhouse gas emissions from energy use and energy production processes in United States

Submitted in partial fulfillment of the requirements for

the degree of

Doctor of Philosophy

in

Mechanical Engineering

Xiang Li

B.S., Environmental Engineering, Nankai University

Carnegie Mellon University

Pittsburgh, PA

September 2017

Dedicated to my parents:

Ms. Hong Cai, and Mr. Cuilin Li

献给我的父母

蔡红 女士，李翠林 先生

Acknowledgements

I would like to firstly express my sincere gratitude to my advisor, Dr. Albert Presto. This thesis would not have been possible without his guidance. I want to thank Albert for the opportunity to join such vibrant and vigorous research group, and for his genuine support throughout my entire Ph.D. study. I am blessed to have such a wonderful journey by working and learning with such an exceptional scientist, from basic instrumentation and data analysis to writing research proposals and peer-reviewed journal articles. Albert treated me as if I was his equal, and he was more than willing to get his hands dirty when we were building the measurement station in the Fort Pitt Tunnel. He always makes time for his students and always points me to the right directions when I am running out of ideas. His passion for air pollution studies inspired me profoundly to pursue my career as an environmental scientist.

I would also like to thank my co-advisor, Dr. Peter Adams, for his support for my application of NASA Earth and Space Science Fellowship, his help on my GEOS-Chem modeling project, and his advice on pursing an academic career. I cannot resist but also thank Peter for all those excellent courses he taught. Peter is one of the best lecturers I have ever had, and his classes are always so elegantly organized and straight to the point. It was always such an enjoyable experience to sit through one of Peter's classes and it helped shape my way of approaching scientific problems.

I am appreciative of a thesis committee composed of five extraordinary and inspiring scientists. I would like to thank Dr. Shi-Chune Yao, Dr. Allen Robinson, and Dr. Neil Donahue for all of their invaluable comments and suggestions that help improve this work immensely. I would also like to use this opportunity to thank Dr. Spyros Pandis, Dr. Ryan Sullivan, and Dr. Satbir Singh at the Center for Atmospheric Particle Studies (CAPS) for their comments and suggestions along the course of my Ph.D. study.

The collaborative environment of CAPS provided the opportunity for me to work with so many exceptional scientists during the early stage of my academic career. Specifically for my tunnel study, I would like to thank Dr. Andrew May, Dr. Daniel Tkacik, and Dr. Timothy Dallmann, all of whom worked with me during the tunnel measurement campaign. I would also like to thank Dr. Eric Lipsky for his instructions on how to run,

maintain, and calibrate all the instruments in the tunnel. Mr. Jie Lu wrote the computer program to help integrate diesel vehicle emission plumes, and Mr. Peishi (Bob) Gu helped analyze the quartz filters using the lab OC/EC analyzer. Ms. Yutong Guo, Dr. Satbir Singh, and Dr. Wayne Chuang helped me simulate the particle evaporation inside the thermodenuder. I want to use this opportunity to thank them for their help. And I would also like to thank the staff of the Fort Pitt Tunnel for their assistance during our campaign.

I would like to thank everyone that I have worked with during our sampling in the natural gas production fields in Colorado, Utah, and Pennsylvania, Dr. Mark Omara, Dr. R. Subramanian, Ms. Melissa Sullivan, Dr. Naomi Zimmerman, Dr. Aja Ellis, and Ms. Rebecca Cesa. Subu, Mark and Naomi are fantastic at organizing and leading these field campaigns. I learned so much from them in the field, especially how to cope with unexpected situations. I also sought inspirations from Mark's and Naomi's excellent research presentations.

I would like to thank Ms. Marguerite Marks for her help with the GEOS-Chem. I know little about the GEOS-Chem when I first started, and Marguerite was so patient to answer all my questions, which earned me valuable time and energy to dig deeper into the research. I would also like to acknowledge Dr. Melissa Sulprizio and Mr. Joannes Maasakkers from Harvard Uniersity, who programmed and provided the code for me to compare the GEOS-Chem simulations with the GOSAT satellite measurements. They also answered a lot of my questions about GEOS-Chem methane simulation.

I also want to use this opportunity to thank Dr. Yunliang Zhao, Dr. Yi Tan, and Dr. Rawad Saleh for their help with my Ph.D. studies. I want to thank Yunliang for all our research discussions that greatly improved my understanding about aerosol chemistry, aerosol volatility, and vehicle emissions. I want to thank Tan for all the intelligent ideas he shared with me, and also his help with my presentation skills at the beginning of my Ph.D. studies. Both Yunliang and Tan are not just mentors but also best friends to me. They offered me so much assistance and invaluable comradery in my life. I would also like to thank Rawad for the valuable discussions we had about particle size distribution and aerosol volatility, and also for all his advice on pursuing an academic career.

I would like to acknowledge the Steinbrenner Institute at Carnegie Mellon University and the NASA Earth and Space Science Fellowship (15-EARTH15F-181) for funding my Ph.D. studies. And I would also like to thank the National Oceanic and Atmospheric Administration (NOAA, project NA14OAR4310135) and the National Energy Technology Laboratory (NETL, project DE-FE0014055) for funding our VOC and methane measurements in natural gas production fields.

I have made so many good friends in CAPS and in CMU during my Ph.D. years, Ms. Ningxin Wang, Ms. Qing Ye, Dr. Fan Tong, Dr. Penglin Ye, Mr. Peishi (Bob) Gu, Mr. Zhongju (Hugh) Li, Dr. Wayne Chuang, Mr. Rishabh Shah, Mr. Andrew Hix, Mr. Georges Saliba, Dr. Antonios Tasoglou, Dr. Ellis Robinson, Dr. Kyle Gorkowski, Dr. Hassan Beydoun, Dr. Adam Ahern, Dr. Elina Karnezi, Mr. Quanyang Lu, Dr. Yanwei Li, etc. We all share the same passion for air pollution studies. I want to thank all of them for offering me their companionship and support in the past 5 years. Ningxin and Qing have become such good friends of mine. We shared so many happy moments together and were always looking out for each other. I had so many delightful dinner chats with Fan during my Ph.D. years. Apart from being a committed research, Bob is simply just an amazing photographer, and I owe him so many thanks for capturing precious moments of my life. And we share the same passion for beers... There are simply too many invaluable memories that are beyond words.

I would also like to thank all other members in CAPS, and the Mechanical Engineering Department at Carnegie Mellon University. I want to thank everyone that had ever offered me assistance during my Ph.D. studies.

I would like to give a special thanks to my best friend and soulmate, Mr. Yuan Bian. I am so lucky to have him in my life, and make my life full of happiness and sweetness. His companionship supported me through some of the tough times. He always manages to touch the tenderest of my heart.

Finally, I want to express my deepest gratitude to my wonderful families. I am forever grateful to my parents, Mrs. Hong Cai and Mr. Cuilin Li, for their unconditional and endless love and support. They are everything that I can ask for. I certainly would have not come this far without them. I love you!

感谢我的父母，蔡红女士，以及李翠林先生， 感谢他们一直以来对我无条件的爱以及付出。他们给予了我所能够要求的一切。没有我的父母，我断然无法取得今天的成绩。我爱你们！

感谢我的爷爷奶奶，李丰禄先生，以及华金英女士，还有我的姥爷和姥姥，蔡开惠先生，以及李成玉女士，感谢你们一直以来对我的爱和牵挂。在我写作我的博士论文期间，我亲爱的姥姥，李成玉女士，不幸因肺癌于 2017 年 2 月 20 日病逝，使我陷入巨大的悲痛之中。空气污染被认为是肺癌的诱因之一。我衷心希望我的工作可以帮助更多的家庭免于承受同样的痛苦。愿我美丽慈爱的姥姥在天堂安息！

Abstract

Air pollutants and greenhouse gases are two groups of important trace components in the earth's atmosphere that can affect local air quality, be detrimental to the human health and ecosystem, and cause climate change. Human activities, especially the energy use and energy production processes, are responsible for a significant share of air pollutants and greenhouse gases in the atmosphere.

In this work, I specifically focused on characterizing air pollutants and greenhouse gas emissions from the on-road gasoline and diesel vehicles, which is an important energy use process that largely contributes to the urban air pollutions, and from the natural gas production systems, which is a major energy production process that has increased dramatically in recent years and is expected to have a long-lasting impact in the future. We conducted multi-seasonal measurements in the Fort Pitt Tunnel in Pittsburgh, PA to update the on-road vehicle emission factors, to measure the size distribution of vehicle emitted particulate matter (PM), and to quantify the volatility distributions of the vehicle emitter primary organic aerosol (POA). We also conducted mobile measurements in the Denver-Julesburg Basin, the Uintah Basin, and the Marcellus Shale to quantify facility-level VOC emission from natural gas production facilities, and I constructed a gridded (0.1° × 0.1°) methane emission inventory of natural gas production and distribution over the contiguous US.

I found that the stricter emission standards were effective on regulating NO_x and PM emissions of diesel vehicles and the NO_x, CO and organic carbon (OC) emissions of gasoline vehicles, while the elemental carbon (EC) emissions of gasoline vehicles did not change too much over the past three decades. Vehicle-emitted particles may be largely externally mixed, and a large fraction of vehicle-emitted particles may be purely composed of volatile component. Vehicle-emitted smaller particles (10– 60 nm) are dominantly (over 75%) composed of volatile component. The size-resolved particles and particles emission factors for both gasoline and diesel vehicles are also reported in this work. I also found that the POA volatility distribution measured in the dynamometer studies can be applied to describe gas-particle partitioning of ambient POA emissions. The POA volatility distribution measured in the tunnel does not have significant diurnal

or seasonal variations, which indicate that a single volatility distribution is adequate to describe the gas-particle partitioning of vehicle emitted POA in the urban environment.

The facility-level VOC emission rates measured at gas production facilities in all three gas production fields are highly variable and cross a range of ~2-3 order of magnitudes. It suggests that a single VOC emission profile may not be able to characterize VOC emissions from all natural gas production facilities. My gridded methane emission inventory over the contiguous US show higher methane emissions over major natural gas production fields compared with the Environmental Protection Agency Inventory of US Greenhouse Gas Emission and Sinks (EPA GHGI) and the Emission Database for Global Atmospheric Research, version 4.2 (Edgar v4.2). The total methane emissions of the natural gas production and distribution sector estimated by my inventory are 74% and 20% higher than the Edgar v4.2 and EPA GHGI, respectively. I also run the GEOS-Chem methane simulation with my inventory and EPA GHGI and compare with the GOSAT satellite data, and results show that my inventory can improve the model and satellite comparison, but the improvement is very limited.

The size-resolved emission factors of vehicle emitted particles and POA volatility distribution reported in this work can be applied by the chemical transport models to better quantify the contribution of vehicle emissions to the PM in the atmosphere.

Since our measurement of VOC emissions of natural gas production facilities were conducted before EPA started to regulate VOC emissions from the O&NG production facilities in 2016, the facility-level VOC emission rates reported in this work can serve as the basis for future studies to test the effectiveness of the regulatory policies. The spatially resolved methane emission inventory of natural gas production and distribution constructed in this work can be applied to update the current default methane emission inventory of GEOS-Chem, and the updated methane emission inventory can be used as a better a priori emission field for top-down studies that inversely estimate methane emissions from atmospheric methane observation.

Table of Contents

List of Figures

List of Tables

Chapter 1
Introduction

1.1 Air pollutants and greenhouse gases

Air pollutants are trace components of the atmosphere that can affect local air quality, be detrimental to the human health and the ecosystem, and cause other environmental damages. Air pollution currently is a significant environmental issue world-widely. World Health Organization (WHO) estimated that in 2012, about 7 million people died as a result of air pollution exposure, and it is about 1/8 of the total global death [1]. Among all the risk factors that lead to premature death, the urban out door air pollution ranked 8th for the high-income countries [2]. The lifetime and major health and environmental effects of air pollutants studied in this thesis are summarized in Table 1.1. Because air pollution poses a threaten to the public health, since 1963, the US congress has enacted the Clean Air Act and its amendments [3] to authorize US Environmental Protection Agency (EPA) to establish National Ambient Air Quality Standards (NAAQS) [4] to regulate the emissions of the hazards air pollutants. The current NAAQS [4] contains standards for 6 criteria air pollutants, including the carbon monoxide (CO), lead (Pb), nitrogen dioxide (NO_2), tropospheric ozone (O_3), particulate matter (PM), and sulfur dioxide (SO_2). The NO_2 is usually grouped with NO to be the nitrogen oxides (NO_x). Besides these criteria air pollutants, the volatile organic compounds (VOC) are also a group of important air pollutants, and many of them are categorized as hazardous air pollutants by EPA and are regulated by the National Emission Standards for Hazardous Air Pollutants (NESHAP) [5].

Most air pollutants stay in the gas-phase in the atmosphere, except the PM, also known as atmospheric aerosols, are solid or liquid particles in the atmosphere with the size range from 0.001-200 μm. PM_{10} and $PM_{2.5}$, namely the coarse particles and fine particles, are used to refer to atmospheric particles with diameters less than 10 μm and 2.5 μm, respectively. Roughly 50% of fine particle mass is constituted by organic species, i.e. the organic aerosol (OA) or the organic carbon (OC) [6,7]. Black carbon (BC), or the elemental carbon (EC), is referred to as the strong light absorbing and refractory components, i.e., not evaporate under high temperature, of PM. Other components of the PM include

inorganic component such as sulfate, ammonium, nitrate, sodium, chloride, trace metals, and water [8]. $PM_{2.5}$ can cause the visibility degradation [9–11], the increase of mortality [12,13], and the climate change [14]. The atmospheric aerosols can cool the earth's surface by the scattering of solar radiation (direct effect) and interacting with surrounding clouds (indirect effect) [15]; and the BC in the atmosphere aerosols can warm the earth's surface by absorbing the sunlight reducing the surface albedo when depositing onto snow and ice [16].

Greenhouse Gases, including carbon dioxide (CO_2), methane (CH_4), and nitrous oxide (N_2O), are a group to trace gases in the atmosphere that can trap heat in the atmosphere by absorbing thermal infrared radiation emitted by the earth's surface and can potentially cause global warming [14]. The Intergovernmental Panel on Climate Change (IPCC) estimated that the CO_2 and CH_4 are the 1^{st} and 2^{nd} strongest greenhouse gases in the earth's atmosphere. The lifetime of CO_2 and CH_4 are listed in Table 1.1, and they can potentially stay in the atmosphere for 1 to several decades and have a long-lasting impact on the climate [14].

The burden of the air pollutants and greenhouse gases in the atmosphere depends on the rate that they enters the atmosphere, mainly through primary emissions and chemical reactions, and the rate that they are removed from the atmosphere, mainly through chemical reactions and wet and dry depositions [8]. For CO, NO_x, VOC, CO_2 and CH_4, they enter the atmosphere predominantly through the primary emissions. Therefore, it is important to understand the emission sources of these pollutants in order to better quantify their burden in the atmosphere. The tropospheric ozone (O_3) is formed primarily through a series of chemical reactions in the atmosphere that involves the NO_x and VOC. Part of the PM in the atmosphere are contributed by primary emissions, while a significant portion (>50%) of the organics in PM, referred to as the secondary organic aerosols (SOA), are formed through the oxidation of VOC in the atmosphere [6]. Although O_3 and a large fraction of PM are not directly emitted by the primary emission sources to the atmosphere, their concentrations in the atmosphere strongly depends on their precursors like NO_x and VOC, which are primarily coming from the primary emissions. Therefore, it is also important to understand

the primary emission sources in order to better estimate the burden of secondary pollutants, such as O_3 and SOA, in the atmosphere.

1.2 Air pollutants and greenhouse gases emissions and the energy use and production

The major sources and sinks of the air pollutants and greenhouse gases studied in this thesis are listed in Table 1.1. Emission sources of the air pollutants and greenhouse gases can be categorized into anthropogenic sources and natural sources. The anthropogenic emissions sources contributed to a significant portion of air pollutants and greenhouse gases. For example, ~65% of the NO_x emissions [17], ~55-70% of the CH_4 emissions [8], and ~30% of the VOC emissions [18] are contributed by the anthropogenic emission sources. Especially in urban area, the air pollution is primarily caused by human actives. Recent studies also showed that the anthropogenic emission can influence the formation of biogenic SOA [19–21]. Besides, it is also estimated that the largely increase of major greenhouse gases over the past 250 years are largely due to human activity [14]. Therefore, it is important to understand the anthropogenic emission sources in order to control the concentrations of air pollutants and greenhouse gases in the atmosphere.

The anthropogenic emission sources of air pollutants and greenhouse gases summarized in Table 1.1 are mostly related to the energy use and energy production processes. The global energy consumption, especially the fossil fuel combustion, has increased dramatically since the industrial revolution [22], and the CO_2 and CH_4 concentrations in the atmosphere also increased from ~280 ppm and ~700 ppb in the pre-industrial time to ~400 ppm and ~1840 ppb in recent years, respectively [8].

The energy use processes that emit air pollutants and greenhouse gases to the atmosphere include stationary emission sources, such as industrial manufacturing, commercial energy consumption, residential energy consumption, production of electrical power, etc., and mobile emission sources, such as the

on-road gasoline and diesel vehicles, railways, aircraft, etc. Among all these energy use processes, on-road gasoline and diesel vehicles are a major source of air pollution in the urban area. The transportation sector accounts for a significant portion (28%) of the total energy consumption in US [23]; and on-road gasoline and diesel vehicles account for 85% of the total mobile source fuel consumption in US [24]. It is estimated that in 2015, there are over 263 million on-road gasoline and diesel vehicles in US, and the volume of on-road vehicles kept increasing at a rate of ~1% per year in recent years[25]. Therefore, although the EPA kept regulating the on-road vehicle emissions since 1970s [26], they still remain to be an important source of air pollutants and are expected to have a long-lasting impact.

The types of energy that produced in US include fossil fuels (petroleum, natural gas, and coal), nuclear electric power, and renewable energy (Hydro-electric power, wind and solar energy, etc.) [27]. Since 2010, the U.S. natural gas production has increased dramatically because of rapid advancement in horizontal drilling and hydraulic fracturing techniques and subsequent development of unconventional resources such as shale gas, the tight gas and oil, and the coalbed methane production [28]. Natural gas currently contributes to ~29% of the total U.S. energy consumption [27], and U.S. is expected to become a net exporter of natural gas in 2017 [29]. It is projected that natural gas production and consumption in the U.S. will increase for the next two decades [28]. The dramatic increase of unconventional O&NG production has raised concerns on the increase of emissions of greenhouse gases, primarily CH_4 [30–34], and Volatile Organic Compounds (VOC) [35–38], which are detrimental to local air quality [39–44] and public health [45–47].

Therefore, in this work, I specifically focused on characterizing air pollutants and greenhouse gas emissions from the on-road gasoline and diesel vehicles, which is an important energy use sector that largely contributes to the urban air pollutions, and from the natural gas and oil production, which is an energy production sector that has increased dramatically in recent years in US and is expected to have a long-lasting impact in the future.

1.3 Air pollutant emission from on-road gasoline and diesel vehicles

1.3.1 Measurement of vehicle emission factors

On-road gasoline and diesel vehicles are a major source of air pollutants in the urban atmosphere [24,48]. Approximately 86% of CO emissions, 45% of Volatile Organic Compound (VOC) emissions, 60% of NO_x emissions, and 10% of primary $PM_{2.5}$ emissions are contributed by mobile source [48]; and the on-road gasoline and diesel vehicles account for 85% of the total mobile source fuel consumption [24]. The on-road gasoline and diesel vehicles are also a large contributor of SOA in the atmosphere [49]. It is estimated that in US, the on-road gasoline and diesel vehicles produce 2.9 ± 1.6 Tg SOA per year [50].

Numerous studies have been conducted to measure vehicle emissions, including dynamometer studies [51–53], on-road and near-road measurements [54–57], vehicle chase studies[58–60], and tunnel studies [61–70]. Dynamometer studies, in which the vehicle exhaust is sampled under a prescribed driving cycle [71], offer a controlled sampling condition, though questions remain whether dynamometer tests are representative of real-world driving conditions. In addition, the vehicle population sampled in a typical dynamometer campaign is tiny compared with the real-world traffic volume. For on-road, near-road, and vehicle chase studies, the vehicle exhaust are sampled under real-world driving conditions, but it is still hard to sample a large enough fleet to be representative for the entire vehicle population, and these studies have to deal with the dilution of emissions with the background air.

Tunnel studies offer real-world driving conditions and a large-volume traffic fleet. The relatively closed environment of the tunnel makes an enhancement of pollutants emitted from vehicles and reduces the background dilution problems that face on-road and near-road studies. Thus, tunnel studies are a good method to quantify vehicle emissions under real-world situations. The major challenge of the tunnel studies is to separate the gasoline and diesel vehicle emission from a mixed fleet [67]. Also, since vehicles are usually driving under a constant high

speed in the tunnel, the vehicle emissions measured in the tunnel can only represent vehicle emissions under high-speed driving conditions, and previous studies showed that the vehicle emissions during the cold-start are significantly higher than it driving under high-speed [72].

Tunnel studies have been conducted in many places around the US [61–70] and the world [73–79] to quantify the emissions from vehicles in the past. Two main reasons make it necessary for us to quantify the vehicular emissions in the tunnel again under current conditions. First, the U.S. Environmental Protection Agency (EPA) frequently implements new vehicle emissions standards. For example, new PM and NO_x emission standards were introduced for diesel engines in 2007 and 2010, respectively. New, stricter emission standards compel vehicle manufacturers to improve the combustion technology and to use exhaust treatment technology, such as diesel particle filters (DPF) [80] and selective catalytic reduction (SCR) [81] to reduce vehicle-emitted pollutants. Measurements are needed to quantify the effectiveness of these policies on vehicle emission reduction. Second, the fleet age and the fleet composition are changing over time. May et al. [52] measured gasoline vehicles in different age groups, which are classified based on the EPA Tire-1 and Tire-2 emission standards, and showed that they have different emissions factors of NO_x, CO and PM. Also, gasoline and diesel vehicles have different characteristics on pollutant emissions [52,63,67,68].. Therefore, emissions from on-road vehicles may be changing over the past years. Chemical transport models and exposure models of epidemiological studies requires accurate and up-to-date on-road vehicle emission factors to predict the impact of vehicle emission on air quality, climate, and human health.

1.3.2 Size distribution of vehicle emitted PM

Many previous vehicle studies also specifically focused on the properties of the vehicle emitted PM, which mainly consists of BC and primary organic aerosol (POA) [53,82–84]. Vehicle emitted PM is a major source of PM in the urban

environment [24,48,85], and PM emitted from on-road vehicles can have a significant impact on both climate and human health.

Vehicle PM emitted to the atmosphere could potentially become cloud condensation nuclei (CCN) and impact climate through the aerosol indirect effect.[15] Primary emissions are a major source of uncertainty in quantifying global CCN concentrations.[86,87] Specifically, for the primary emissions from fossil fuel combustion, better constraining the size of the particles is more important than the emission flux for reducing the uncertainty of CCN quantification.[87]

To better quantify the size distribution of vehicle emitted particles can also lead to a better understanding on how vehicle emitted PM can impact the public health, since the on-road gasoline and diesel vehicles are a major source of ultrafine particles[88], namely particles with diameter smaller than 100 nm. Ultrafine particles are able to penetrate and deposit in the human lung and cause respiratory diseases and other health concerns [89–91]. And exposure to ultrafine particles may have health effects distinct from exposure to fine particle mass alone.

Many previous studies measured the size distributions of vehicle emitted particles, including engine tests in the lab[92–94], on-road measurements[93–95], and tunnel measurements[66,96–99]. Since the Environmental Protection Agency (EPA) frequently implements stricter emission standards for on-road vehicles[100], and the application of after-treatment technology, such Diesel Particulate Filter (DPF) and Selective Catalytic Reduction (SCR), can potentially change the size-distribution of vehicle emitted particles[101,102], the size distribution of vehicle emitted particles needs to be monitored over time in order to understand the potential influence of new standards and technology.

1.3.3 Volatility of vehicle emitted POA

Besides the size distribution, another important property of the vehicle emitted PM that has been specifically focused on is the volatility of the vehicle emitted

POA. Traditionally, chemical transport models treated POA as non-volatile, which contributed to a discrepancy between modeled and measured PM mass[103,104]. We know now that a substantial fraction of POA from combustion exhaust is semivolatile [105–114] and actively partitions between the vapor and condensed phases. Accurate accounting of POA mass therefore requires knowledge of both the emission rate of condensable material and the volatility of the emissions.

Numerous studies have investigated gas-particle partitioning of vehicle emitted POA through both field measurements and laboratory studies [84,113–118]. Some earlier studies [84,116,117] indicate the presence of POA partitioning, but do not provide a volatility distribution. Recently, May et al. [113,114] tested 51 gasoline vehicles and 5 diesel vehicles on chassis dynamometers and derived POA volatility distributions. Worton et al. [118] conducted tunnel measurements and derived POA volatility distributions, and concluded that the vehicle emitted POA are dominated by lubricating oil. Both May et al. [113,114] and Worton et al. [118] concluded that volatility distributions of gasoline and diesel vehicles are similar, suggesting that a single volatility distribution can be used to describe the POA gas-particle partitioning of all vehicles.

Kuwayama et al. [115] also observed POA gas-particle partitioning. They used a combination of two volatility distributions, lower volatility fuel-combustion POA and motor oil POA, to describe POA gas-particle partitioning measured in their dynamometer studies. Kuwayama et al. [115] used a large range in the fraction of motor oil POA to total POA (24-86%) to describe the emissions from individual vehicles in their test fleet. Their results suggest that POA gas-particle partitioning cannot be predicted by a single fleetwide volatility distribution. However, since Kuwayama et al. [115] tested only eight cleaner gasoline vehicles, data from a larger fleet may be required to validate this claim.

The measurements presented by both May et al. [113,114] and Kuwayama et al. [115] represent relatively small fleets tested under controlled conditions. Nonetheless, POA emission factors and volatility distributions from May et al.

[113,114] and other small test fleets have been incorporated into chemical transport models [119,120]. To our knowledge, no studies have been published to demonstrate whether these laboratory-derived POA volatility distributions can be applied to describe POA gas-particle partitioning of a larger mixed vehicle fleet operating under real-world driving conditions.

1.4 Greenhouse gas and air pollutant emissions from natural gas production

As discussed in section 1.2, the dramatic increase of unconventional O&NG production in US in recent years has raised concerns on the increase of emissions of greenhouse gases, primarily CH_4 [30–34], and Volatile Organic Compounds (VOC) [35–38], including air toxics like benzene, toluene, ethylbenzene, and xylene, collectively known as BTEX, which are detrimental to local air quality[39–44] and public health[45–47]. Also, natural gas has been considered as a 'bridge fuel' as it emits less carbon dioxide than other fossil fuels during combustion [121,122], and since the global warming potential of CH_4 for a time horizon of 100 years is 25 times as it of CO_2, too much methane leaks from the natural gas system may offset the climate benefit of natural gas [31,123]. Therefore, a better estimation of CH_4 and VOC emissions from natural gas production can also help justify the development of shale gas.

Oil and natural gas (O&NG) producing well pads generally consist of well heads, separation units, tanks, and combustors [124]. The raw natural gas is mainly composed of CH_4 (~70-98%), ethane (1-10%), a mixture of VOC, including alkanes and aromatics; inorganic gases like H_2S and SO_2; and water [125]. Gas from a well that also produces petroleum liquid may contain lower fraction of CH_4 and higher fraction of ethane and VOC. The raw natural gas is extracted from the underground wells and is piped from the wellheads to the separation unit [124]. The separation unit then removes the liquid condensate and the water from the natural gas and oil stream, and the removed liquid condensate and water are stored in storage tanks on site [124]. Liquids in the storage tank will be

removed by trucks or pipelines, and there may also be combustors on site to burn the VOC vapors accumulated in the storage tank [124]. Besides well pads, in natural gas production field, there are also compressor stations in the gathering system that transport natural gas from well pads to the processing plants. During all stages of the natural gas exploration and production, the O&NG facilities may emit CH_4 and VOCs through fugitive emissions, venting, flaring, accidental release, or storage losses [126]. Many previous studies have shown that the CH_4 and VOC emissions from the O&NG production system in U.S. have been underestimated by state and national emission inventories [37,127,128].

1.4.1 VOC emissions from the natural gas production

Many previous studies [35,37,38,129,130] measured the VOC concentrations and quantified the regional VOC emissions associated with O&NG production in some major gas production regions with ground and aircraft measurements. Gilman et al. [35] measured a set of VOCs at the Boulder Atmospheric Observatory (BAO), which is close to the natural gas production region in the Denver-Julesburg Basin. They detected clearly differentiable VOC source signatures of O&NG production. Pétron et al. [37] conducted aircraft measurements in the Denver-Julesburg Basin and estimated methane and VOC emissions from O&NG production, and their estimated benzene emission rate was 7 times larger than the state inventory. Helmig et al. [38] measured the VOCs in Horse Pool near the Uintah Basin. They detected elevated VOC concentrations that could be linked with O&NG production during winter inversion events and estimated that the annual emissions of C2-C7 VOCs from O&NG production in the Uintah Basin was equivalent to annual VOC emissions from ~100 million automobiles. Yuan et al. [129] conducted an aircraft campaign over the Haynesville Shale and Marcellus Shale and used airborne eddy covariance method to quantify the flux of CH_4 and some VOC species. They reported enhancement ratios of CH_4 to benzene and toluene to benzene, which clearly indicates that these VOC species were dominantly emitted from O&NG

production in these shale gas extraction regions. The VOCs emissions estimated by these studies are all top-down estimations of total VOCs emissions from all O&NG production facilities in the entire region; no facility-level VOCs emissions were reported in these studies.

Very few studies [36,131] measured the VOCs emissions at individual O&NG production facilities. Warneke et al. [36] measured VOC concentrations at individual gas production sites in the Uintah Basin with a PTR-MS (proton transfer reaction – mass spectrometry). They reported that dehydrators, condensate tanks, pneumatic devices, and pumps are major VOCs sources of gas production well pads, and they compared VOCs measured at gas wells and oil wells. However, Warneke et al. [36] only reported the VOC-to-CH_4 ratio measured at facilities and did not report VOCs emission rates. Goetz et al. [132] used tracer-release method to quantify methane and VOCs emission rates from individual gas production site in the Marcellus Shale. They visited only 5 sites for VOC measurement, and they did not see enhanced VOCs concentrations at all sites they visited.

It is important to understand the characteristic of facility-level VOCs emissions in order to better control the VOCs emissions from O&NG production facilities. Also, since the Environmental Protection Agency (EPA) started to regulate the CH_4 and VOCs emissions of O&NG production facilities since Aug. 2016, it is necessary to conduct facility-level VOCs emission measurements before and after the regulations to test the effectiveness of the policy. Besides, the facility-level VOCs emission rates could also be used to conduct bottom-up estimation of the VOCs emissions from the entire O&NG production sectors. The comparison of the bottom-up estimation and the top-down estimation can help better constrain the contribution of O&NG production to the total VOCs emissions in major gas production regions.

To quantify VOC emissions from O&NG production facilities is important for detecting the potential high exposure of air toxics for people working on O&NG production sites or living near the O&NG production field. Also, VOC emissions

from O&NG production can affect local air quality since they are precursors of the tropospheric ozone (O_3) [8]. Previous studies [35,38,41] have shown that the high ozone levels in O&NG regions are associated with VOCs emissions from the O&NG production. Schnell et al. [41] reported that in Green River Basin in Wyoming, which is near the Jonah-Pinedale Anticline natural gas field, the wintertime ozone concentrations in the night could reach 140 ppb, which is 2 times as the 8-hour averaged ozone levels of NAAQS. Helmig et al. [38] measured the wintertime VOCs concentrations in the Uintah Basin and found a strong causal link between the accumulation of VOCs emissions from O&NG production and the significant production of surface layer ozone. Measurement conducted by Gilman et al. [35] at BAO near the Denver-Julesburg Basin suggest that ~55% of the VOCs-OH reactivity was contributed by VOCs emissions from O&NG operations, which was a major source of ozone precursors in the region.

1.4.2 Methane emissions from the natural gas production and distribution

Natural gas production and distribution is a major anthropogenic source of methane emissions in US. According to the EPA Inventory of US Greenhouse Gas Emission and Sinks (GHGI) [126], among all these anthropogenic methane emission sources, the natural gas production and distribution contributes to about 23% of the total US anthropogenic methane emission in 2012. The rapid increase of methane production in recent years raised concerns on potential increasing methane emissions over US. The GOSAT (Greenhouse Gases Observing Satellite) measurements from 2010-2014 show that methane concentration was increasing over the contiguous US, which corresponds to more than 30% increase of methane emissions in US over the past decade [133].

There are two most commonly used inventories of methane emissions in US. One is the Emission Database for Global Atmospheric Research, version 4.2 (Edgar v4.2) [134]. The methane emission inventory of Edgar v4.2 is a gridded annually global inventory that has a spatial resolution of 0.1° latitude × 0.1° longitude. Edgar v4.2 has methane emission data from 1970 to 2008, and it is

currently the default anthropogenic methane emission inventory for the GEOS-Chem, a commonly used 3-D global chemical transport model. Another commonly used methane emission inventory is the EPA GHGI [135]. It reports annual methane emissions of major anthropogenic emission sources in US from 1990 to 2016. Recently, Maasakkers et al. [136] spatially distributed the annual total methane emissions of 2012 estimated by EPA GHGI using a range of spatially resolved activity datasets. They built a gridded methane emissions inventory that has a spatial resolution of 0.1° latitude × 0.1° longitude and is consistent with EPA GHGI. Maasakkers et al. [136] also compared spatial patterns of the EPA GHGI and Edgar v4.2 and they found that the Edgar v4.2 has significantly lower methane emission estimations over major gas production fields in the contiguous US, and the total methane emissions from the natural gas production and distribution estimated by the EPA GHGI is about 45% higher than the Edgar v4.2.

In recent years, there has been a lot of field measurements conducted to quantify the methane emissions from natural gas production and distribution in US, including the measurement of methane emissions from natural gas production [128,137,138], gathering and processing [139–141], transmission [142], and distribution systems [143]. Brandt et al. [144] compared the recently measured methane emissions of the natural gas production and distribution sector at a range of scales (device-level to continental-level) with the EPA GHGI and found that the EPA GHGI consistently underestimated the methane emissions from the natural gas production and distribution. The EPA GHGI has already included results from recent ground measurements [142,143] for the estimation of methane emissions from the natural gas transmission and distribution systems. However, for the natural gas production system, which accounts for 64% of the total methane emissions from the natural gas production and distribution sector, the emission factors used by the EPA GHGI are mostly adapted from the 1996 EPA/GRI (Gas Research Institute) studies [145], which may not be able to represent the methane emissions from the natural gas system in recent years. Since 2014, our research team at Carnegie Mellon University conducted

measurements in the Marcellus Shale, the Denver-Julesburg Basin, and the Uintah Basin to quantify the facility-level methane emissions from the natural gas production [137,138]. Goetz et al. [131] and Brantley et al. [146] also conducted field studies in the Marcellus Shale and the Denver-Julesburg Basin, respectively, to measure the facility –level methane emissions from natural gas production. Ground measurements were also conducted in other gas production field, including the Barnett Shale[146–149], the city of Fort Worth [150], and Pinedale [146]. Omara et al. [137] combined results from all these studies and provided a spatial distribution of methane emissions from onshore natural gas production over contiguous US. Lyon et al.[151] and Allen et al. [152] developed spatially resolved methane emission inventories of natural gas production and distribution in the Barnett Shale region. However, no spatially resolved and up-to-date methane emission inventory for the entire natural gas production and distribution sector over the contiguous US exists at this moment.

Recently, Littlefield et al. [153] synthesized the recent ground measurement results and estimated the total methane emissions from the US natural gas system, but they did not provide spatially resolved methane emissions. A spatially resolved methane emission inventory is not only needed by the chemical transport models and climate models to estimate the impact of natural gas production and distribution on the methane concentrations in the atmosphere and the climate. Also, for those top-down studies that use atmospheric methane observations and chemical transport model to inversely estimate methane emissions, they usually need an existing spatially resolved methane emission inventory as the a priori emission field, and the source attributions of the final inversion results fully depend on the source attributions of the a priori emission field [133,136,154,155].

1.5 Thesis overview

In this work, to study air pollutants emitted by on-road gasoline and diesel vehicles, we conducted tunnel measurements to update the vehicle emission

factors, quantify the size distribution of vehicle emitted PM, and explore the volatility of vehicle emitted POA. To study greenhouse gas and air pollutant emissions from natural gas production system, we conducted mobile measurements in the Denver-Julesburg Basin, the Uintah Basin, and the Marcellus Shale to measure the facility-level VOC emissions from natural gas production facilities, and I constructed a methane inventory of natural gas production and distribution over the contiguous US.

In Chapter 2, I summarize the methods used for this study. The information about the tunnel, traffic conditions in the tunnel, and the air quality station are described in this chapter. The setup of the mobile lab, the measurement of VOC and methane concentrations downwind of natural gas production facilities, and the construction of methane emission inventory are also described in Chapter 2.

In Chapter 3, I describe the multi-seasonal vehicle emission factor measurements conducted in the Fort Pitt Tunnel in Pittsburgh, PA. The fleet average emission factors were combined with traffic data to apportion the fuel-based vehicle emission factors of gasoline and diesel vehicles. The data collected in both spring and winter seasons allow us to investigate the potential seasonal influence on vehicle emission factors. In order to study the long-term trend of the vehicle emissions, the emission factors measured in this study are compared with emission factors measured by Grieshop et al. [108] about 10 years ago in the Squirrel Hill Tunnel in Pittsburgh, PA. I also summarize gasoline and diesel emission factors measured in this study and previous tunnel studies in United States in the past three decades and compared them with the change of vehicle emission standards to show the effectiveness of emission standards on regulating vehicle emissions.

In Chapter 4, I report the size distribution measurement of vehicle emitted primary particles conducted in the Fort Pitt Tunnel with a pair of Scanning Mobility Particle Sizers (SMPS). Both number-size distribution and mass-size distribution of vehicle-emitted particles are reported. The particle mass are calculated assuming vehicle emitted particles in the tunnel are fractal rather than

spherical. A thermodenuder (TD) was deployed in the sampling line to periodically remove the volatile particle component with high temperature (250 °C) to determine the size-dependent volatility of vehicle-emitted particle. A size-resolved volatile-to-non-volatile component ratio of vehicle-emitted particles is reported based on the SMPS-TD measurement. Finally, I calculated the size-resolved emission factors of particles emitted by the mixed fleet in the tunnel, apportioned the contribution from both gasoline and diesel vehicles, and compared the apportioned size-resolved gasoline and diesel vehicle emission factors with previous studies.

In Chapter 5, we measured the gas-particle partitioning of POA in the Fort Pitt tunnel with three independent methods: 1) a thermodenuder (TD), 2) quartz filter sets analyzed by thermal-optical OCEC and 3) analysis of quartz filters with thermal desorption gas chromatography mass spectrometry (TD-GC-MS) to determine volatility distributions. And I show in this chapter that POA emitted from a large and real-world driving fleet is semivolatile under a wide range of ambient conditions, the POA volatility distribution derived from the dynamometer studies can be applied to explain gas-particle partitioning of ambient POA, and that gas-particle partitioning of the POA measured in the traffic tunnel does not have large diurnal or seasonal variations.

In Chapter 6, I describe the VOC measurement downwind of individual natural gas production well pads and compressor stations in the Denver-Julesburg Basin, the Uintah Basin, and the Marcellus Shale. VOC concentrations, the background-corrected VOC-to-CH_4 ratios, and facility-level VOC emission rates are reported. I show that the facility-level VOC emission rates measured in all gas production fileds are highly variable, indicating that a single VOCs emission profile may not be able to characterize VOCs emissions from all natural gas production facilities. VOC emissions from different types of facilities, specifically gas wells vs. compressor stations, and unconventional vs. conventional gas wells, are compared. I also test the hypothesis that VOC emission rates of O&NG production facilities in different regions are different.

In Chapter 7, I constructed a gridded methane emission inventory of the natural gas production and distribution over the contiguous US using facility-level methane emissions reported by recent ground measurements in US [128,137,140,142,143]. The annual total methane emissions and the spatial pattern of our constructed inventory are compared with the EPA GHGI and the Edgar v4.2. In order to explore whether my inventory could potentially improve the prediction of methane concentrations in the atmosphere, I modified the GEOS-Chem default methane emission inventory with my inventory and the EPA GHGI, and then run the GEOS-Chem methane simulations with either my inventory or the EPA GHGI. The simulated methane concentrations are compared with the GOSAT measurements to determine whether the simulation with my inventory or the simulation with the EPA GHGI could better represent the actual methane concentrations in the atmosphere.

In Chapter 8, I summarize the major findings of this work, and provide suggestions for future studies.

1.6 Publications resulting out of this thesis

Chapter 5 has already been published as:

Li, X., Dallmann, T. R., May, A. A., Tkacik, D. S., Lambe, A. T., Jayne, J. T., Croteau, P. L., and Presto, A. A., 2016, “Gas-Particle Partitioning of Vehicle Emitted Primary Organic Aerosol Measured in a Traffic Tunnel,” *Environ. Sci. Technol*., **50**(22), pp. 12146–12155.

Chapter 3 is planned to be published as:

Li, X., Lu, J., Dallmann, T. R., May, A. A., and Presto, A. A., 2017, “Long-Term Trend of on-Road Gasoline and Diesel Vehicle Emission Factors Measured in the Traffic Tunnel,” *in prep. for Environ. Sci. Technol.*

Chapter 4 is planned to be published as:

Li, X., Dallmann, T. R., May, A. A., and Presto, A. A., 2017, “Size Distribution of Vehicle Emitted Primary Particles Measured in a Traffic Tunnel,” *in prep. for Aerosol Sci. Technol.*

Chapter 5 is planned to be published as:

Li, X., Omara, M., Zimmerman, N., Ellis, A., Sullivan, M. R., Subramanian, R., Robinson, A. L., and Presto, A. A., 2017, “Volatile Organic Compound Emissions from Natural Gas Facilities in the Denver-Julesburg Basin, the Uintah Basin and the Marcellus Shale,”*in Prep. for Atmospheric Environment*.

Table 1.1 The atmospheric lifetime, emission sources, sinks, health and environmental effect of air pollutants and greenhouse gases studied in this work

Air Pollutants/ Greenhouse Gas	Lifetime in the atmosphere	Major Anthropogenic Emission Sources	Major Natural Emission Sources	Major sink	Health Effect	Other Environmental Effect
CO	30-90 days [8]	Mobile, Fires, Fuel Combustion, Industrial Processes [8]	Biomass burning, oxidation of methane and VOC [8]	Surface deposition and OH reaction [8]	High concentrations of CO can cause death by preventing the transport of oxygen around body	React with other pollutants to form ozone [8]
NO_x ($NO+NO_2$)	~1 day [17]	Fossil fuel combustion, air craft, biomass burning [8]	Soils, NH3 oxidation, Lightning, Stratosphere [8]	Chemical reaction, wet and dry deposition [17]	Visibility impairment; Cause or worsen respiratory diseases by forming PM and ozone [156]	Precursors of tropospheric ozone and PM; Form acid rain; React to form air toxics [156]
PM (aerosols)	A few days - a few weeks [8]	Vehicles, Industry, Construction & Agriculture, fires [8]	Plants (mainly secondary organic aerosol), sea-spray, fires [8]	Chemical reaction, wet and dry deposition [8]	Linked with premature death; Cause heart attack and irregular heart beat; Cause or worsen respiratory diseases [157]	Visibility impairment, climate change; Depleting nutrients in soil, damaging sensitive forests and farm crops, contribute to acid rain [157]

VOC	Fractions of a day to months [158]	Fires, industrial processes, mobile, solvent, fuel combustion, agriculture [18]	Vegetation [18]	Photo-chemical reaction, wet and dry deposition [159]	Long term exposure: damage liver, kidney, and central nervous system; Short term exposure: eye and respiratory tract irritation, headaches, dizziness, visual disorder, etc.; Benzene and formaldehyde are human carcinogens [160]	Hazardous air pollutants Precursors of tropospheric ozone and PM
Tropospheric Ozone (O_3)	~20-30 days [14]	Anthropogenic processes that produces NO_x and VOC, such as vehicle emissions, biomass burning, fossil fuel combustion, industrial processes, etc.	Natural processes that produces NO_x and VOC	Chemical reaction and dry deposition[14]	Cause breathing problems and respiratory diseases; Cause asthma; Damage lungs [161]	Affect growth of some plants that may lead to a loss of species diversity and change to water and nutrient cycles [162]
CO_2	~35 years [8]	Electricity production, transportation, industry, commercial and residential, agriculture, land use and forestry [126]	Ocean-atmosphere exchange, Plant and animal respiration, Soil respiration and decomposition, Volcanic eruptions [14]	Ocean-atmosphere exchange, plant photosynthesis	No direct health effect	Global warming [14]
CH_4	~ 10 years [163]	Natural gas, oil, coal mines, agriculture (rice and manure), waste treatment [126]	Wetlands, termites, ocean, hydrates [14]	Soils, tropospheric OH, stratospheric loss [14]	Relatively non-toxics, but can be an asphyxiate displacing oxygen in the lungs [164]	Global warming [14]

Chapter 2
Methods

2.1 The tunnel measurement station

2.1.1 The Fort Pitt Tunnel

Our tunnel measurement campaign was conducted in the two-lane outbound (westbound) bore of the Fort Pitt Tunnel in interstate 376 in Pittsburgh, PA. The tunnel is 1.1-km long with a 2.5% upward grade to the west. It connects the Pittsburgh downtown to the Pittsburgh International Airport and other suburban areas. The tunnel has a ventilation duct located on top of the ceiling. During our measurements, all instruments were placed in the ventilation duct. The ventilation duct has fans to mechanically ventilate the tunnel; but these fans were never turned on during the measurement period. The tunnel is only mechanically vented by the motion of the vehicles driving through. A sketch of the tunnel measurement station is shown in Figure 2.1.

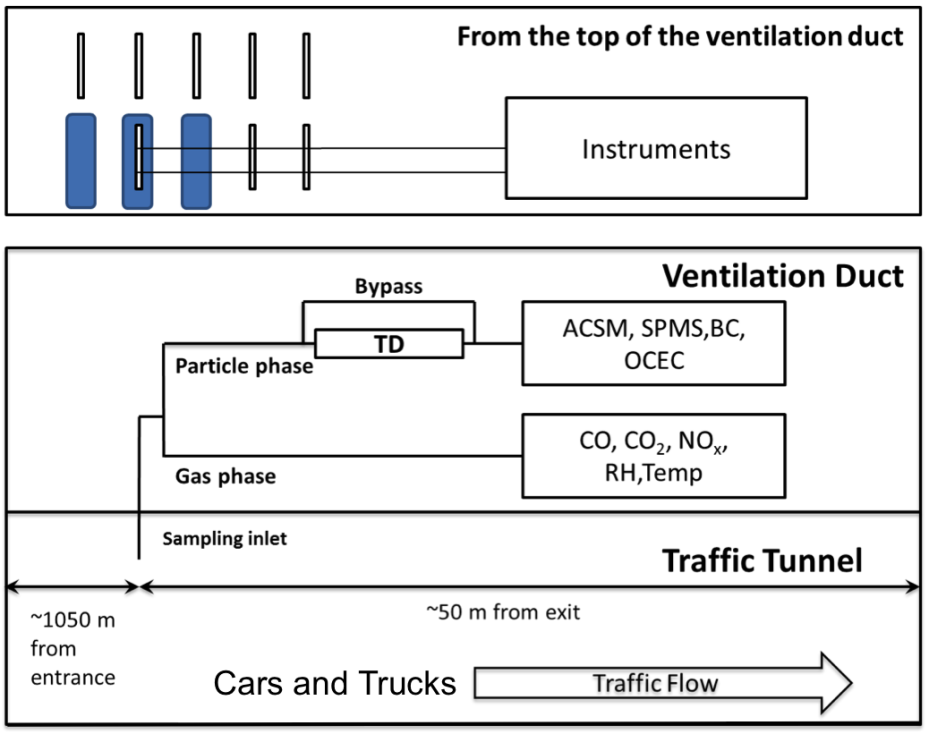

Figure 2.1 Schematic of the tunnel measurement station.

As shown in Figure 2.1, the sampling inlet was inserted through one of the ventilation slits in the tunnel ceiling. The slit where the sampling inlet was located and two adjacent slits were all blocked to prevent potential dilution of the sample. The sampling inlet is about 50 m from the tunnel exit. The spring measurements were conducted in Apr. and May in 2013, together with the work presented in Tkacik et al.[50]. The winter measurements were conducted in Jan. and Feb. in 2014. A one-week measurement was conducted in Apr. 29th – May. 4th, 2014 in order to study the difference of emission factors measured over different lanes, which will be described in detail later.

2.1.2 Traffic conditions in the Fort Pitt Tunnel

The weekday and weekend diurnal pattern of the vehicle speed, the vehicle volume and the number fraction of heavy-duty diesel vehicle (HDDV) in the Fort Pitt Tunnel are presented in Figure 2.2. A Remote Traffic Microwave Sensor (RTMS) operated by the Pennsylvania Department of Transportation (PennDOT) was placed at the tunnel exit to count vehicles and measure the vehicle speed and the vehicle length. The traffic count and speed data obtained from the PennDOT were from 12/03/2012 to 12/14/2012. It was not the exact same time periods with our measurements, but traffic patterns are very similar in typical weekdays or in typical weekends in the tunnel, and the day-to-day variations of the traffic data in each hour are in general smaller than the diurnal variation of the traffic data. Therefore, these data can still well represent the traffic situation during our measurement. Based on the vehicle length, the traffic sensor classified all vehicles into 4 types: automobiles (Class 1); motorcycles (Class 2); pickup trucks, SUVs, and vans (Class 3); and large trucks (Class 4). Almost all vehicles in the first three classes are powered by gasoline engines, and most of the Class 4 vehicles are powered by diesel engines. In practice, the sensor cannot efficiently separate Classes 3 and 4. Therefore, the number fractions of HDDV showed in Figure 2.2(c) are the number fractions of vehicles in Classes 3

and 4, and it represents the upper limit estimations for the fraction of diesel vehicles, primarily medium- and heavy-duty trucks.

The vehicle speed in the Fort Tunnel (Figure 2.2(a)) was relatively constantly around 65 mph during the whole day, expect for the afternoon rush hour (15:00 – 17:00) in weekdays, during which the vehicle speed dropped to about 50 mph and was also more variable compared with other time periods. Since vehicles in the tunnel were always driving under high speed, the emission factors measured in the tunnel only represent the vehicle emissions during the high-speed driving and do not include emissions during the vehicle cold-start or hot-start.

The vehicle volumes (Figure 2.2(b)) in the tunnel had two peaks in weekdays, one in the morning rush hour (6:00 – 8:00), and another one in the afternoon rush hour (15:00 – 18:00). There was no morning rush hour in the weekends; only one traffic volume peak showed up in the afternoon rush hour (15:00 – 18:00) in weekends. The hourly averaged number fraction of HDDV (Figure 2(c)) peaked at nighttime (0:00 – 4:00), in weekdays about 6 – 10 % and in weekends about 4 - 6%. For the rest of the day, the hourly averaged number fraction of HDDV was in general lower than 4%.

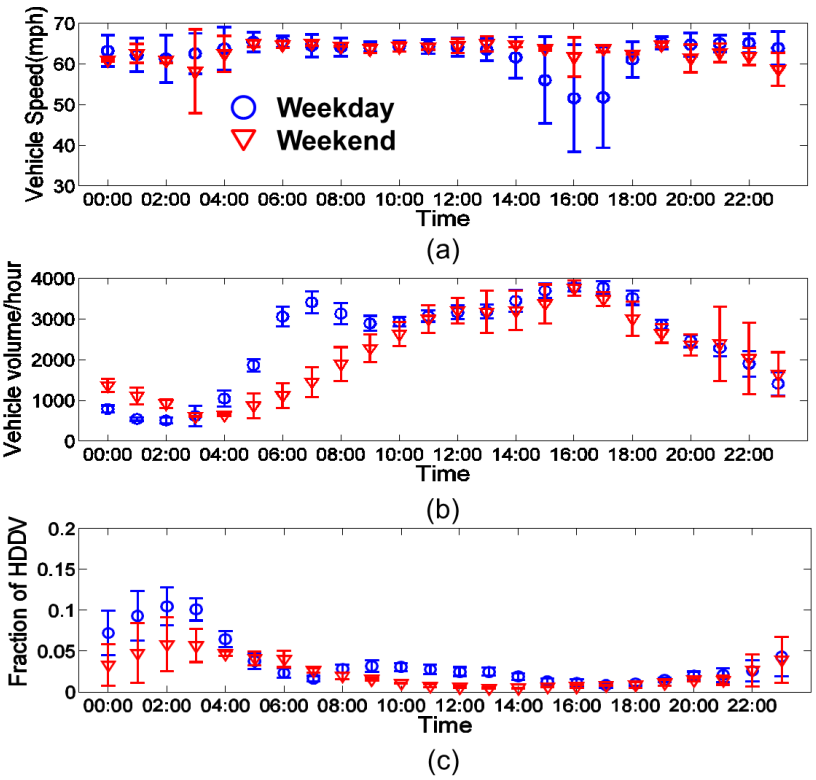

Figure 2.2 Weekday and weekend diurnal pattern of (a) vehicle speed (b) vehicle volume (c) number fraction of heavy duty diesel vehicle (HDDV) in the Fort Pitt Tunnel in Pittsburgh, PA. Bars in the figure represent the standard deviation of the measurement.

We do not exactly know the distribution of the vehicle model years in the Fort Pitt Tunnel during our measurement time period. According to the data from US Bureau of Transportation Statistics [165], in 2013 and 2014, the average age of automobiles and trucks in operation in the United States is about 11.3 – 11.4 years. The actual vehicle fleet age in the Fort Pitt Tunnel might be younger than this national average.

We quantify the presence of diesel vehicles by calculating the diesel fuel fraction ($\%fuel_D$) with the following equation:

$$\%fuel_D = \frac{f_D U_D}{f_D U_D + (1\text{-}f_D) U_G} \qquad (1)$$

The $\%fuel_D$ represents the percentage of fuel consumed by HDDV in the tunnel during a certain measurement time period. Here f_D is the number fraction of diesel vehicles in the tunnel. It is determined based on the traffic counts obtained from the Pennsylvania Department of Transportation at the tunnel exit. U_G and U_D are the fuel economies of gasoline vehicles (25 mile/gallon) and diesel vehicles (6 mile/gallon), calculated based on the total vehicle-mileage data and total fuel consumption data of light duty vehicles and trucks in 2011 from the US Department of Transportation [25].

2.1.3 Air quality measurement station

The instruments deployed in the spring campaign and the winter campaign are summarized in Table 2.1. As shown in Figure 2.1, for both winter campaign and the spring campaign, we have one gas-phase sampling line (0.25" diameter Teflon tubing) for all gas monitors and one particle-phase sampling line (0.325" diameter copper tubing) for all particle instruments. A thermodenuder (TD) was placed in the particle-phase sampling line in order to study the volatility of vehicle emitted particles, but it was never deployed during the emission factor measurements reported in this manuscript.

During the spring campaign, we continuously measured the CO_2, CO, NO_x, particle-phase OC and EC concentrations in the tunnel. A denuder was placed upstream of the OC/EC analyzer to remove gas-phase organics and reduce sampling artifacts [166,167]. The sampling inlet was over the left lane, and the sampling lines were about ~22 m long due to constraints on where instruments could be deployed. An Aerodyne Aerosol Chemical Speciation Monitor (ACSM) was also deployed with the TD to study the volatility of vehicle emitted POA. The Reynolds number of the particle sampling line was less than 2000, indicating the airflow inside was laminar flow. The long length of the particle-phase sampling line may potentially lead to a high particle loss for smaller particles. Smaller

particles are negligible in mass, so any losses should have a minor impact on the measured particle mass concentration.

During the winter campaign, except measuring the CO_2, CO, NO_x, and particle phase OC and EC, we also continuously measured black carbon (BC) and particle bound PAHs (polycyclic aromatic hydrocarbons) concentrations. A nano-SPMS (scanning mobility particle seizer) and a long-SMPS were running at the same time to measure the size distribution of vehicle emitted PM in tunnel. In order to better capture emissions from HDDV, the sampling inlet was placed on top of the right lane, where most trucks drive. All instruments were also moved next to the sampling inlet to minimize the length of the sampling line to reduce losses and to capture exhaust plumes from individual trucks.

Since the sampling inlet were over different lanes during the spring and winter campaigns, we conducted one-week short campaign to characterize the effect of lane-shift on measured emission factors. During the week, only NO_x, CO and CO_2 were continuously measured. We were sampling over right lanes in 04/29 – 04/30, and over right lanes in 05/01 – 05/02, in 2014. All these days are typical weekdays and traffic conditions in the tunnel followed the typical weekday traffic conditions in the tunnel.

Table 2.1 Instruments deployed in the Fort Pitt Tunnel measurement

Species measured	Instrument	Time	Sampling
Temperature and Humidity	Vaisala HMT 330	1 s	-
CO_2	Li-Cor LI-820	1 s	1.0 LPM
NO_x/NO	API 200EU	1 s	1.0 LPM
CO	API T300U	1 s	1.0 LPM
Elemental (EC) and organic carbon (OC)	Sunset Laboratory Semi-Continuous OCEC (Model 4F)	1 h	8.7 LPM
Particle number/volume size distribution	Scanning Mobility Particle Sizer (SMPS, 3081 and 3085)	2 min	2.5 LPM
Black carbon (BC)	Aethalometer (AE-31), Magee Scientific	2 min	2-6 LPM

Particle Bound PAHs	Photoelectric aerosol sensor (PAS), EcoChem, Model 2000	2 s	1 LPM
Non-refractory particle phase organics	Aerodyne Aerosol Chemical Speciation Monitor (ACSM)	1 min	3 LPM

For BC concentrations measured by the Aethalometer, similar with Dallmann et al. [69], in order to minimize the uncertainties caused by the filter-loading artifact [168] for the highly absorbing particles measured in the tunnel, we adjusted the raw BC concentrations using the following equation [169]:

$$BC_{adj} = \frac{BC_{raw}}{1.5 \times [0.73 \times \exp(\frac{-ATN}{100}) + 0.27]} \quad (2)$$

The coefficient in the equation are kept consistent with Dallmann et al.[69] and were derived based on the tunnel measurement results.

During the winter campaign, besides measuring the particle-phase OC and EC with the semi-continuous OC/EC analyzer in the tunnel, we also measured the OC and EC with a two channel sampler: one channel has only one bare-quartz filter (bare-Q), and the other channel has a Teflon filter and a quartz-behind-Teflon filter (QBT). The collected quartz filter sets were analyzed with the Sunset Laboratories OCEC Aerosol Analyzer (Model 3) following the IMPROVE-A protocol [170]. We assume the bare-Q filter captures both particle phase organics and absorbed organic vapors, which is considered the positive artifact. This positive artifact is quantified by the QBT filter, which is assumed to only absorb gas phase organics [167,171]. Therefore, the particle phase OC concentration can be derived from the artifact-corrected bare-Q (bare-Q minus QBT).

We collected in total 18 quartz filter sets, and 13 of them were collected simultaneously with the semi-continuous OC/EC measurements during either midday (12:00 – 14:00) or afternoon rush hour (15:00 – 18:00), and we compared the tunnel and the lab OC/EC measurements in Figure 2.3. The EC measured by the tunnel and lab OC/EC analyzers are highly correlated and have

a ratio close to 1. The OC measured by the tunnel and lab OC/EC analyzer are also highly correlated. However, the OC measured by the semi-continuous OC/EC analyzer in the tunnel are constantly about 70% higher than the particle phase OC measured from the bare-Q and QBT filters, but they are close to the OC measured by the bare-Q filters, which contains both gas phase artifacts and the particle phase OC. It indicates that OC measured by the semi-continuous OC/EC analyzer in the tunnel may contain the gas-phase organic artifact, and the filters inside the organic denuder might be saturated and lose efficiency over time. Therefore, for all the particle-phase OC concentrations measured by the semi-continuous OC/EC analyzer in the tunnel in the winter campaign, we divided them by an averaged factor of 1.7 to avoid potential bias caused by the gas-phase organic artifact. For OC concentrations measured by the semi-continuous OC/EC analyzer the spring campaign, since we did not collect quartz filter sets, there is no reliable particle phase OC data we could use to estimate the gas-phase artifact. Therefore, we did not correct the OC concentrations measured in the tunnel in spring, and they may potentially overestimate the particle phase OC concentrations.

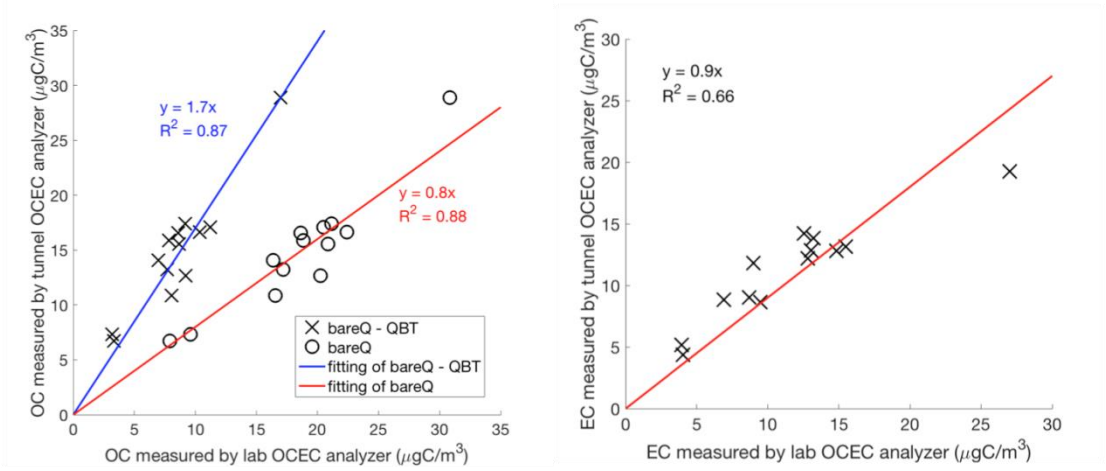

Figure 2.3 Comparison of OC measured by the semi-continuous OC/EC analyzer in the tunnel and the OC measured by the quartz filter sets and OC/EC analyzer in the lab. Solid lines are the linear regression fitting of the data. In figure (a), for circles and red lines, the lab OC/EC data are from the bare-Q filter, which includes both gas and particle phase OC; while for crosses and blue lines, the lab OC/EC data are from the bare-Q minus QBT filters, which only has particle phase OC.

2.1.4 Background pollutant concentrations

The background pollutant concentrations used in this work were the ambient monitoring data from nearby U.S. EPA national air monitoring sites [172]. The NO_x and CO background concentrations were the daily ambient monitoring data from the Carnegie Science Center site (40.4456° latitude, -80.0162° longitude), which is ~900 m away from the Fort Pitt Tunnel. For the particle-phase OC and EC concentrations, we used the ambient monitoring data from the Allegheny County Health Department (ACHD) site (40.4654° latitude, -79.9608° longitude). The data was reported every 3 or 6 days. The ACHD site was ~5 km away from the tunnel, but the OC and EC concentrations measured in the ACHD site can still represent the regional ambient background of the Pittsburgh area.

The background CO_2 concentrations were measured on campus of Carnegie Mellon University with a Li-Cor LI-820 CO_2 monitor at 1 Hz from Apr. 29th, 2014 to May 17th, 2014. Diurnal patterns of weekday and weekend CO_2 ambient concentrations were used to background correct the CO_2 concentrations measured in the tunnel.

The pollutant concentrations measured in the tunnel are in general much larger than the ambient background concentrations. In Figure 2.4 we present the hourly-averaged diurnal ambient-background-to-tunnel-measurement ratio of all pollutants we measured during the spring campaign. The NO_x background concentrations were less than 3% of the tunnel measurement, and the EC background concentrations were around 10% of the tunnel measurement. The background ratios of CO in the late night (2:00 – 4:00 am) were higher, around 30%, while in other time of the day the CO background ratios were around 20%. Compared with other pollutants, the OC and CO_2 measured in the tunnel had a higher background ratio and were influenced more by the ambient background. The OC background ratios were in general around 40%, while in nighttime (18:00 – 23:00) it could reach 60%. The CO_2 background ratios were around 50-60%, while in the late night (0:00 – 3:00) it could reach 75%.

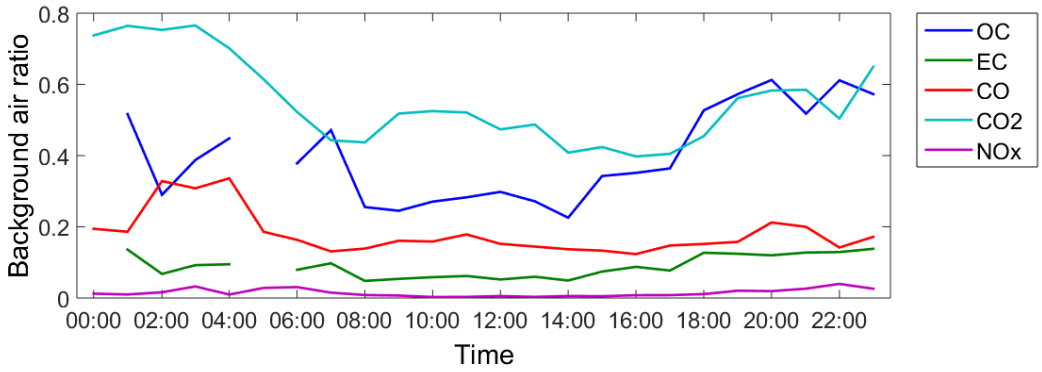

Figure 2.4 Background ratio of pollutants measured in the tunnel in the spring campaign.

2.2 Mobile measurements of VOC emissions from natural gas production facilities

We conducted mobile measurements in the Denver-Julesburg Basin in March – April 2015, in the Uintah Basin in April – May 2015, and in the NEPA in May – June 2016 to quantify the facility-level CH_4 and VOC emissions from individual natural gas production facilities. A detailed description of the set-up of our mobile lab can be found in Roscioli et al. [139]. Specifically related to this work, we have a GC-FID (gas chromatography with flame ionization detection; SRI model 8610C), a Picarro cavity ring-down spectrometer, and a Tunable Infrared Laser Differential Absorption Spectrometer (TILDAS; Aerodyne Research Inc.) placed on the mobile lab to measure the VOC, methane, and ethane concentrations, respectively. The mobile lab was standing still while conducting the VOC measurements with GC-FID. A suite of 15 VOC species ranging from C2 to C12, together with the CH_4 and ethane concentrations, were measured ~50 – 1000 m downwind of individual natural gas production well pads and compressor stations. We conducted GC-FID measurement at 32 well pads and 10 compressor stations and collected in total 47 samples. A detailed site count in each region, locations of the sites, further details about the GC-FID measurement, and the calculation of the VOCs emission rates are discussed in Chapter 6.

A detailed description of the size selection criteria can be found in Omara et al [128]. To briefly summarize here, the selected sites must have a downwind road access within 50 – 1000 m. The terrain near the selected site must be relatively flat, and there must be no other VOC and CH_4 sources near the selected site that could potentially interfere with the VOC and CH_4 measured from the site.

2.3 Construction of the methane emission inventory of natural gas production and distribution

To construct a methane emission inventory of natural gas production and distribution over contiguous US, I estimated the total methane emissions using the emission factors and activities. The emission factors I used to construct the inventory are methane emissions per gas well or methane emissions per facility reported by previous field measurement studies [128,137,140,142,143] and the EPA Greenhouse Gas Reporting Program (GHGRP) [173]. The activity data are number and locations of the natural gas facilities in the Contiguous United states, and the data are obtained from Drillinginfo [174], U.S. Energy Information Administration (EIA) [175], and EPA GHGRP [173]. The known locations of the natural gas facilities allow us to spatially distribute the methane emissions from the natural gas production and distribution processes.

Following the EPA GHGI [126], the methane emissions of the natural gas production and distribution are composed of 4 sectors: the natural gas production, processing, transmission and distribution. Details about the calculation of the methane emissions from each of these sectors are described in Chapter 7.

Chapter 3

Long-term trend of on-road gasoline and diesel vehicle emission factors measured in traffic tunnels

3.1 Introduction

On-road gasoline and diesel vehicles are a major source of air pollutants in the urban atmosphere, including CO, VOC, NO_x and $PM_{2.5}$ [24,48]. These pollutants are important participants in atmospheric chemical reactions and have adverse effects on regional air quality, human health, and climate [8–14,176]. The vehicle emitted PM mainly consists of unburned carbon soot, which is also known as EC or BC, and OA or OC [82].

Gasoline vehicles and diesel vehicles have distinctive emission characteristics because of the difference of the engine technology. Gasoline vehicles are mostly powered by spark-ignition (SI) engines, while diesel vehicles are powered by compression-ignition (CI) engines. The temporarily highly fuel-rich conditions and the high combustion temperature of the CI engine favor the formation of PM and NO_x; while the overall fuel-to-air ratio in SI engine is higher than the CI engine, and there is not enough combustion time to fully convert CO into CO_2 in SI engine [177]. Many lab and on-road studies found that the gasoline vehicle emit higher CO than the diesel vehicles, while uncontrolled diesel vehicles emit much higher NO_x and PM than gasoline vehicles [52,63,67,68].

Compared with other vehicle emission measurement methods, tunnel studies hold the advantage of sampling vehicle exhaust from a large-volume traffic fleet under real-world driving conditions. The relative closed environment of the tunnel makes an enhancement of vehicle-emitted pollutants and reduces the uncertainties caused by the background air dilution. But the challenge inherent to tunnel studies is to separate the gasoline and diesel vehicle emissions from a mix fleet. Many studies have been done to measure vehicle emissions factors in US [61–70]. But the continuously changing emission standards and vehicle technologies, especially the exhaust after-treatment technologies [80,81], make it necessary for us to quantify the vehicular emissions in the tunnel again under current conditions in order to update the vehicle emission factors and test the effectiveness of the policy.

The purpose of this study is to quantify vehicle emissions under real-world driving conditions and current fleet composition. We conducted multi-seasonal measurements in the Fort Pitt Tunnel in Pittsburgh, PA. The fleet average emission factors were combined with traffic data to apportion the fuel-based vehicle emission factors of gasoline and diesel vehicles. The data collected in both spring and winter seasons allow us to investigate the potential seasonal influence on vehicle emission factors. In order to study the long-term trend of the vehicle emissions, the emission factors measured in this study are compared with emission factors measured about 10 years ago in the Squirrel Hill Tunnel in Pittsburgh, PA by Grieshop et al. [108]. I also summarized gasoline and diesel emission factors measured in this study and previous tunnel studies in United States in the past three decades and compared them with the change of vehicle emission standards to show the effectiveness of emission standards on regulating vehicle emissions.

3.2 Methods

3.2.1 Fuel-based emission factors

The Fort Pitt Tunnel, traffic conditions in the tunnel, setup of the tunnel measurement stations, instruments deployed in the measurements, and background concentration measurements are all described in Chapter 2.

Emission factors reported in this work are fuel-based emission factors calculated using the following equation, which assumes a carbon balance between the fuel and the combustion exhaust: [63,178]

$$EF_P = \frac{\Delta P}{(\Delta CO_2 + \Delta CO)} \frac{MW_P}{MW_C} w_c \quad (1)$$

Where EF_p is the emission factor of pollutant P (in g/kg-fuel). ΔP, ΔCO_2 and ΔCO are background corrected concentrations of pollutant (P), CO_2 and CO. MW_p and MW_c are molecular weights of pollutant P and carbon. w_c is the weight fraction of

carbon in the fuel. The w_c of gasoline and diesel are 0.85 and 0.87,[63] respectively; the w_c of each hour of the day in the tunnel were calculated as the weighted averaged w_c based on the $\%fuel_D$. This method assumes that the carbon in the fuel was dominantly transformed into CO_2 and CO during the combustion, and the gas-phase and particle-phase OC and EC are negligible for the carbon balance.

3.2.2 Comparison of the EC and BC measured in the tunnel

In order to test the consistency between instruments, in Figure 3.1, I compared the BC measured by Aethalometer and the EC measured by the OC/EC analyzer in the tunnel. The BC and EC data presented in Figure 6 are not background corrected. BC is usually defined as the carbonaceous particle component that strongly absorbs visible light, while EC is usually operationally defined as refractory components of carbonaceous particles, i.e., the component that is not evaporate under high temperature. Although BC and EC are defined based on different properties, they are both generated from incomplete combustion of carbonaceous fuel and have strong light-absorbing properties [179–181]. Previous studies showed that BC and EC emitted from the same sources are well correlated but can be different in total mass [180,181]. Similar with previous studies, the BC and EC measured in the tunnel in this study are well correlated (R^2 = 0.77), and the BC concentrations measured by Aethalometer in average were about 17% lower than the EC concentrations measured by the OC/EC analyzer.

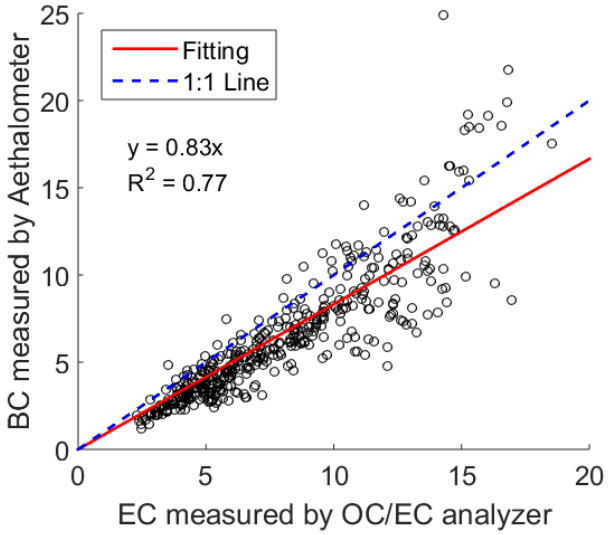

Figure 3.1 Comparison of the BC concentration measured by the Aethalometer and the EC concentration measured by the OC/EC analyzer. All data presented in the figure are not corrected for ambient background.

3.3 Result and discussion

3.3.1 Pollutant concentrations and emission factors

The time series of gaseous and particulate pollutants measured in the tunnel in a typical week (Feb 3rd to Feb 9th, 2014) are presented in Figure 3.2. Since the trend of BC and EC measured in the tunnel are similar, only BC concentrations are presented in Figure 3.2. Except the PAH, all other pollutants presented in Figure 3.2 are background-corrected. All pollutants measured in the tunnel showed strong diurnal patterns, and the diurnal trends of the pollutants measured in the tunnel are good indicators of the traffic conditions in the tunnel. As shown in Figure 3.2(a) and (b), the CO_2 and CO concentrations both showed two peaks during weekdays, one at the morning rush hour (around 8 am), and the other one at the afternoon rush hour (15:00 – 17:00). During weekends, the CO_2 and CO concentrations showed only one peak at the afternoon rush hour, and the CO_2 and CO concentrations measured on the weekends are lower than on weekdays. These CO and CO_2 trends are consistent with the overall traffic patterns, driven by the number of gasoline vehicles, shown in Fig 2.2.

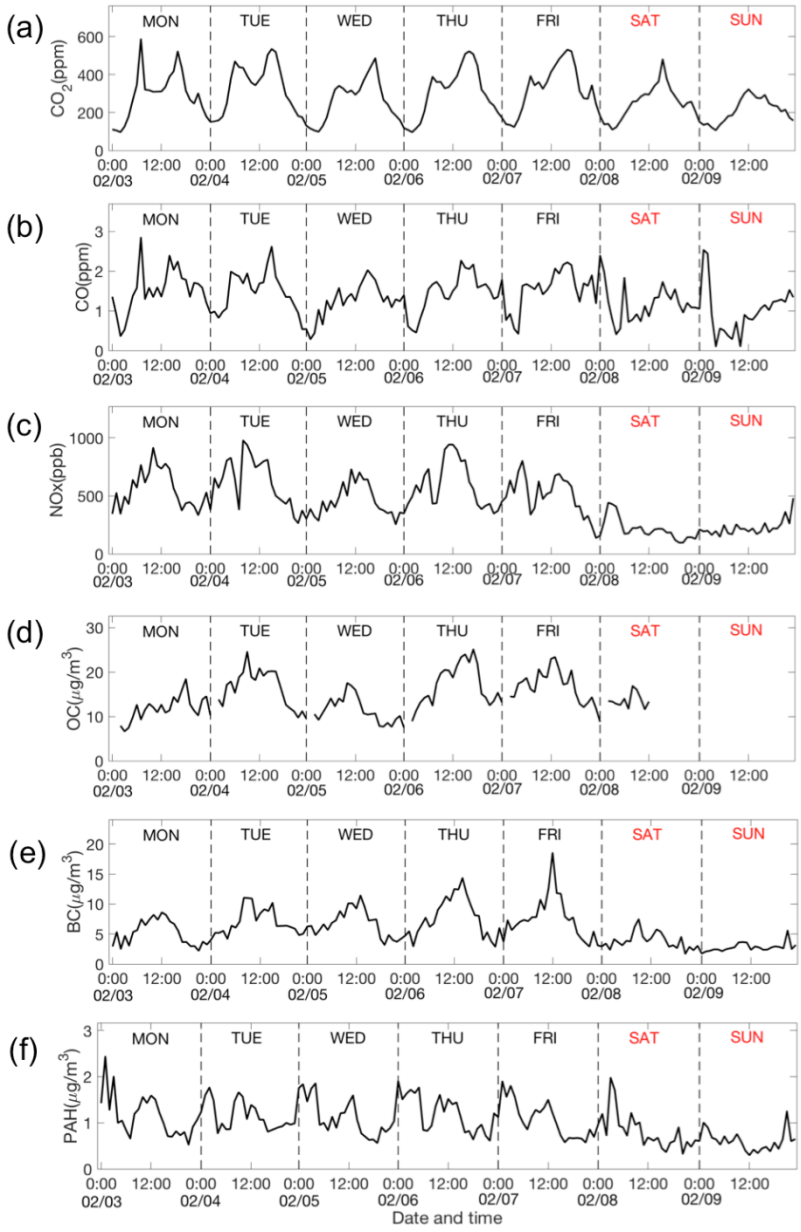

Figure 3.2 One-week time series of (a) CO_2, (b) CO, (c) NO_x, (d) OC, (e) BC, and (f) PAH concentrations measured in the tunnel. All data presented in the figure are 1-h averaged data. Except PAH, all other pollutants are background corrected.

We are uncertain about the reason why CO concentrations showed peak at the Sunday night, and the reason why there was no afternoon rush hour peak for CO might be that the traffic volume in that specific day was low. In general, the diurnal trends of CO_2 and CO concentrations measured in the tunnel are highly

correlated with the diurnal trend of the total traffic volume in the tunnel. The LDV and HDDV emit similar amount of CO_2, while the LDV emit much higher CO compared with the HDDV [52]. Therefore, the CO_2 concentrations measured in the tunnel are good indicators of the total traffic volume in the tunnel, while the CO concentrations measured in the tunnel are good indicators of LDV volume in the tunnel. Since LDV dominates the traffic volume in the tunnel (over 90% by number), the diurnal trend of LDV volume is expected to be similar with the diurnal trend of the total traffic volume.

The time series of NO_x, OC, EC, BC, and PAH concentrations have a different temporal pattern than CO and CO_2. During weekdays, NO_x, OC, EC, and BC showed only one peak at noontime. This seems to be associated with diesel truck activity. Although the number fraction of the HDDV was highest at midnight, since the traffic volume was much higher in the daytime, the peak volume of HDDV in the tunnel was at noontime. Weekend concentrations of NO_x, PAH, and BC were generally lower than weekdays. One exception occurred on Saturday at ~1-2am, when a spike in NOx, PAH, and CO was observed. This spike may be indicative of high diesel truck volumes during that specific time.

The hourly-averaged diurnal patterns of NO_x, OC, EC, and CO emission factors measured in weekdays in the spring campaign are presented in Figure 3.3. The diurnal trends of emission factors measured in the winter campaign were similar with the spring campaign. Unlike the NO_x, OC, and EC concentrations, which followed the trend of the HDDV volume and peaked at noontime, the NO_x, OC, and EC emission factors closely followed the trend of the $\%fuel_D$(Figure 3.3) and had the highest value in during overnight hours (0:00 – 4:00) and dropped by about 65% in the daytime. It is because that the HDDV emit much higher NO_x, OC, and EC than the LDV, and the fraction of HDDV in the tunnel was much higher in the midnight than it in the daytime. The diurnal trends of NO_x, OC, and EC emission factors measured in the Fort Pitt Tunnel in this study are similar with Grieshop et al. [67]. They separated the measured emission factors into three time periods: the early morning (high truck, 0:00 – 6:00), the rush hour (low

speed, 7:00 – 9:00), and the mid-day (high speed, 10:00 – 16:30), and they found that the NO_x, OC, and EC emission factors were much higher in the early morning than other time periods, and the emission factors in the rush hour were slightly lower than the mid-day since the $\%fuel_D$ were lower in the rush hour. Unlike NO_x, OC and EC, the diurnal pattern of the CO emissions factors measured in the tunnel does not follow the trend $\%fuel_D$; the hourly averaged CO emission factor measured in the tunnel are relatively constant during the entire day, and in midnight (0:00 -3:00 am), the CO emission factors were slightly higher and more variable. It may be because that during these hours, the background CO ratio was also higher (Figure 2.4), and the measured CO emission factors were subject more to the influence of the background air.

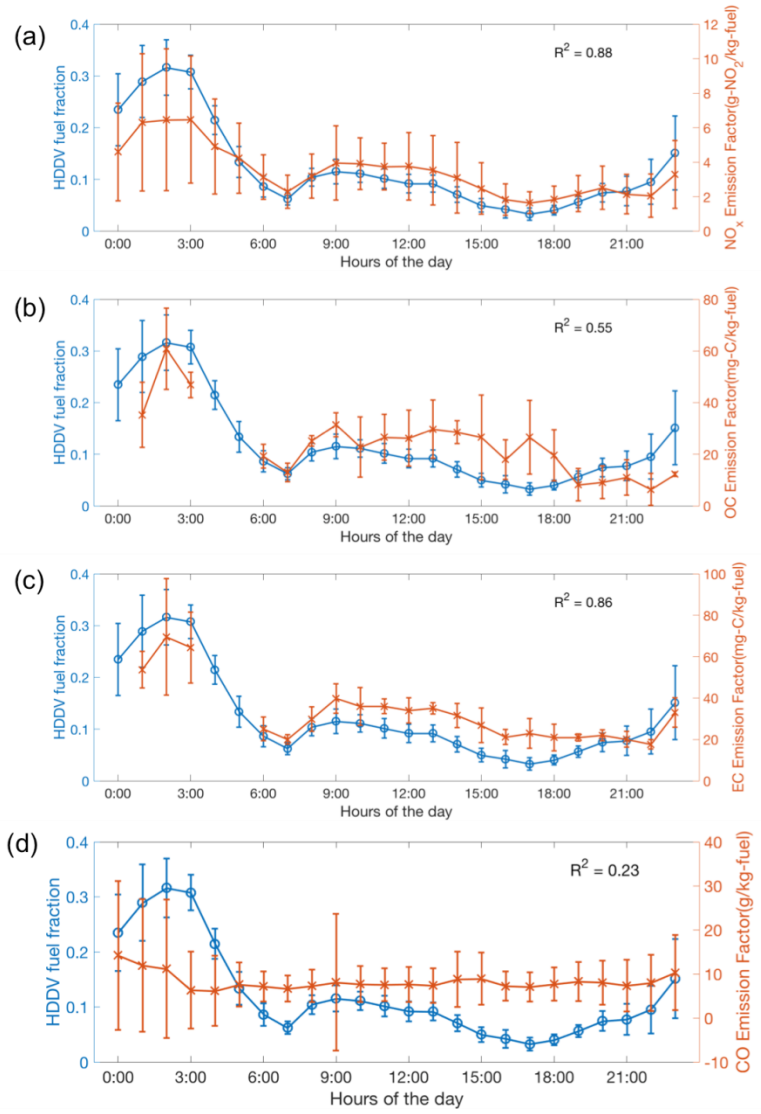

Figure 3.3 The diurnal patterns of the hourly-averaged (a) NO_x, (b) OC, (c) EC, and (d) CO emission factors measured in the tunnel in weekdays in spring and the heavy-duty diesel vehicle (HDDV) fuel fractions. Bars represent the standard deviation of the measurement.

3.3.2 Emission factors of LDV and HDDV

The hourly-averaged emission factors measured in the tunnel are mixed emission factors of gasoline and diesel vehicles. They cannot be directly compared with other tunnel studies since different tunnels may have different traffic volume and vehicle composition ($\%fuel_D$). The strong correlations between

the emission factors and the $\%fuel_D$ measured in the tunnel (Figure 3.3) offer a chance to apportion LDV and HDDV emissions. Following previous studies [67,182,183], I performed a linear regression of emission factors as a function of $\%fuel_D$ to extrapolate the LDV emission factor (when $\%fuel_D$ = 0) and the HDDV emission factor (when $\%fuel_D$ = 1). I performed the linear regression separately for spring measurements and winter measurements, and the data points used for the linear regression are hourly averaged diurnal emission factors and hourly averaged $\%fuel_D$ measured in either weekdays or weekends. The uncertainty of the linear regression was calculated as the simultaneous functional bonds of the linear fitting at a confidence level of 95%. Results of linear regressions are presented in Figure 3.4, and the uncertainty ranges of linear regressions are presented Figure A.1 (seasonal measurements) and Figure A.2 (lane difference measurements).

Because the spring and winter measurements were conducted over left and right lanes, respectively, I firstly characterize the effect of the lane shift on measured emission factors, and result is presented in Figure 3.4 (a). The right-to-left-lane ratios of apportioned NO_x emission factors of LDV and HDDV are listed in Table 3.1. The shift of lanes does not affect the apportioned LDV emission factors, however, for the HDDV, the NO_x emission factors measured over the right lane are 50% higher than it measured over the left lane. Since most diesel trucks stayed on the right lane while passing by the tunnel, I assume that the HDDV emission factor measured over the right lane are more reliable than it measured over the left lane. Therefore, in order to directly compare the emission factors measured in different seasons, for the spring measurements, I corrected the emission factors with the right-to-left-lane ratios to remove the influence of lane shift. I only characterize the lane difference for NO_x Emission factors. For OC and EC emission factors, since they are highly correlated with NO_x emission factors (Figure A.3), I assume their right-to-left-lane ratios are the same as NO_x.

Table 3.1 Ratio of emission factors measured over right and left lanes and ratio of emission factors measured in winter and spring in the tunnel

Species (emission factor units)	Vehicle type	Right/left lane ratio	Winter/spring ratio (corrected for lane difference
NO_x (g-NO_2/kg-fuel)	LDV	1.0 ± 0.5	1.7 ± 1.0
	HDDV	1.5 ± 0.7	1.2 ± 0.6
OC (mg/kg-fuel)	LDV	1.0 ± 0.5	0.8 ± 0.6
	HDDV	1.5 ± 0.7	1.0 ± 0.8
EC (mg/kg-fuel)	LDV	1.0 ± 0.5	1.6 ± 0.9
	HDDV	1.5 ± 0.7	0.8 ± 0.5

NO_x, OC and EC emission factors measured in the tunnel in spring and winter are presented in Figure 3.4 (b) – (d), and for spring measurements, the red solid lines represent the original result, and the dashed red lines represent result corrected for the lane difference. The apportioned LDV and HDDV emission factors are listed in Table 3.2. The winter-to-spring ratio of the LDV and HDDV emission factors are summarized in Table 3.1. For LDV, the NO_x and BC emission factors are ~60-70% higher in the winter, while the OC emission factors are slightly lower (~20%) in the winter. The reason of higher emissions of BC and NO_x of LDV in the winter remains uncertain. For HDDV, the NO_x emission factors in winter are about 20% higher than in spring, and the EC emission factors in winter are about 20% lower. The OC emission factors of HDDV measured in spring and in winter are similar, which is different with Grieshop et al. [67], and they reported that the OC emission factor measured in the tunnel in winter were higher than it measured in summer. As discussed in Chapter 2, The OC concentrations measured in spring in this work could potentially contain gas-phase artifacts and be overestimated; therefore, the seasonal trend of the OC emission factors reported in this work is highly uncertain.

Table 3.2 LDV and HDDV emission factors measured in the Fort Pitt Tunnel

Species (emission factor units)	Vehicle type	Spring regression (corrected for lane difference)	Winter regression	Dynamometer (May et al.[52])	Winter peak Integration
NO_x (g-NO_2/kg-fuel)	LDV	1.2 ± 0.7	2 ± 0.5	2.7 ± 2.4	-
	HDDV	25.7 ± 12.5	29.2 ± 3.2	18.2 ± 12.9 (no SCR) 5.2 ± 4.0 (with SCR)	11.9 ± 15.7
OC (mg/kg-fuel)	LDV	18.5 ± 11.7	14.7 ± 4.8	11.3 ± 11.6	-
	HDDV	164.1 ± 111.5	167.8 ± 36.3	117.0 ± 114.2 (no DPF) 7.6 ± 7.0 (with DPF)	-
EC (mg/kg-fuel)	LDV	15.9 ± 9.1	24.4 ± 5.5	17.2 ± 14.1	-
	HDDV	238.1 ± 122.1	196.8 ± 41.1	182.8 ± 110.0 (no DPF) 0.3 ± 0.5 (with DPF)	-
BC (mg/kg fuel)	LDV	-	19.2 ± 5.2	-	-
	HDDV	-	153.5 ± 37.0	-	-

In order to show the long-term trend of LDV and HDDV emission factors, in Figure 3.4, I compared the emission factors measured in the Fort Pitt Tunnel with the emission factors measured ~10 years prior in the Squirrel Hill Tunnel in Pittsburgh, PA by Grieshop et al. [67] (black dashed lines). Results show that over the past ten years, except for the EC emission factors of LDV, which only decreased by about 8%, the EC emission factors of HDDV and the NO_x and OC emission factors of both LDV and HDDV are all significantly decreased (~50 – 70%). It indicates that the emission regulation policies and the advancement of vehicle and emission control technologies were effective on reducing the on-road vehicle emissions in the past 10 years.

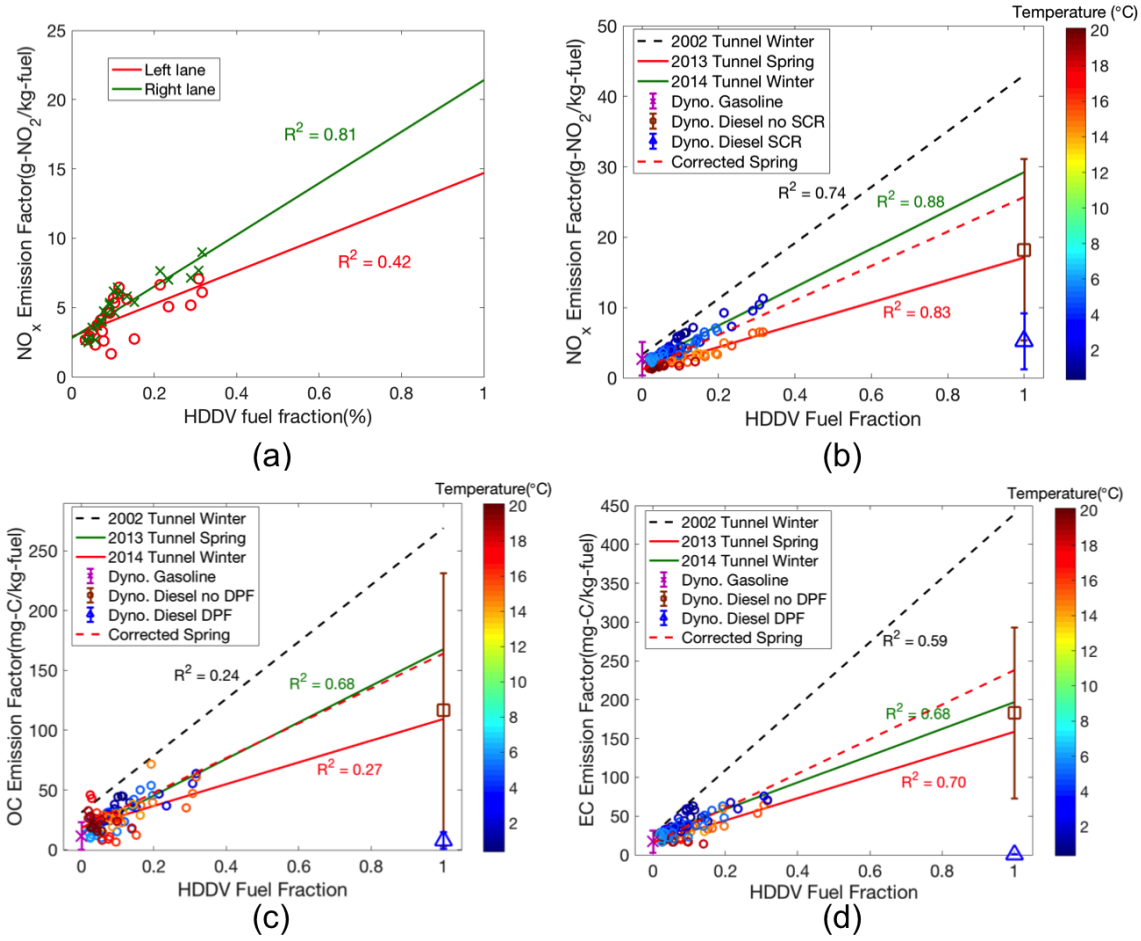

Figure 3.4 (a) Comparison of the NOx emission factors measured over right lane and left lane, and the (b) NO_x, (c) OC, and (d) EC emission factors as a function of the fuel fraction used by HDDV measured in the tunnel. Circles represent measurement data and the color represents the averaged ambient temperature during the measurement. The linear regression lines of spring and winter measurements are shown as red and green lines, respectively. Black dashed lines are linear regression results of Grieshop et al. [67]. Red dashed lines are spring measurements corrected for lane difference. Symbols with error bards represent mean values and standard deviations measured in recent dynamometer studies by May et al. [52].

I also compared the vehicle emission factors measured in the traffic tunnel with the vehicle emission factors measured in a recent dynamometer studies by May et al. [52] in Figure 3.4, and data from May et al. [52] are also summarized in Table 3.2. May et al. [52] classified all tested LDV into three groups based on the vehicle model year: pre-LEV (before 1994), LEV-I (1994-2003), and LEV-II (2004 and later). In order to compare with May et al. [52], I calculated the fractions of

pre-LEV, LEV-I, and LEV-II vehicles in the Allegheny County based on the vehicle inspection records of Allegheny County in 2010 (Table A.1), and then I calculated a weighted-averaged LDV emission factors of dynamometer studies using these fractions and averaged emission factors of different vehicle groups in May et al. [52]. As shown in Figure 3.4 and Table 3.2, for LDV, the averaged NO_x emission factor measured in dynamometer studies are about 35% higher than it measured in the tunnel in winter, while the averaged OC and EC emission factors measured in dynamometer studies are about 23% and 29% lower. All LDV emission factors measured in dynamometer studies are within or very close to the uncertainty range of the tunnel measurements. May et al.[52] tested HDDV that equipped or not equipped exhaust after-treatment devices on the chassis dynamometer, and the averaged emission factors of HDDV with and without after-treatment devices are presented in Figure 3.4 to compare with the tunnel measurements. As shown in the figure, for HDDV that were not equipped with after-treatment devices, the averaged NO_x, OC and EC emission factors measured in the dynamometer studies are 37%, 30% and 7% lower than the tunnel measurements. But the HDDV emission factors measured in dynamometer studies are close to or within the uncertainty range of the tunnel measurements. The deployment of SCR significantly cuts the NO_x emissions of HDDV to a level that is similar with the NO_x emissions of LDV, and the HDDV equipped with DPF emit lower amount of OC than the LDV and emit almost no EC. To summarize, the emission factors of LDV and HDDV measured in dynamometer studies are in general lower than tunnel studies, but still within or close to the uncertainty range of tunnel studies. It suggests that vehicle emission factors measured in dynamometer studies in the lab can be applied to estimate vehicle emissions from larger fleet under real-world driving conditions.

3.3.3 Limitations of the linear regression method

The emission factor data that I used to perform linear regression to estimate the LDV and HDDV emission factors are all hourly-averaged data, and many

pollutants, such as NO_x, CO, CO2, PAH, and BC, were measured at a much higher time resolution (1 s or 2 min) in the tunnel. As mentioned in the method section, during our winter campaign, we shortened the sampling line and the instrument inlets was right next to the sampling inlet at the tunnel slit, therefore, those instruments that sampled at 1 Hz were able to capture the exhaust plumes from individual HDDV, and an example is shown in Figure A.4. To average these 1 Hz data down to hourly-averaged data will lead to the loss of information about individual diesel truck emissions.

The lower time resolution of the measurement data may potentially also lead to an overestimation of median and mode values of the emission factors. As shown in Figure 3.5 (a), I calculated the NO_x emission factors measured in the tunnel in winter at 1 Hz, and then fit the frequency density distribution of the 1-s NO_x emission factors with a lognormal distribution. The same analysis was also performed with 1-s NO_x emission factors measured in spring and hourly-averaged NO_x emission factors measured in both winter and spring. The comparison of the 1-s and 1-h NO_x emission factor distributions is shown in Figure 3.5(b). For both winter and spring measurement, compared with 1-s emission factor distribution, the mode of the 1-h emission factor distribution shift towards larger NO_x emission factors, and the variance of the 1-h emission factors are smaller than 1-s emission factors. To better show the effect of data averaging time on the emission factor estimation, I averaged the 1 Hz NO_x, CO and CO_2 data measured in the winter campaign down to 1-min, 10-min, 30-min, and 1-h data, and then calculated the NO_x emission factors at different time resolutions. The median, mean, mode, and variance of the NO_x emission factors calculated at different time resolutions are compared in Figure A.5 and Table A.2. As the time resolution decreases, both mean and median value of the NO_x emission factors increased, while the mean values are constant. The variance of the NO_x emission factors decreases as the time resolution decreases. The reason that the median and mode value of NO_x emission factors increase while the data time resolution decrease is because of the influence of HDDV emissions. The tunnel traffic was dominated by the LDV, so the most abundant signals of 1-s NO_x

emission factor are the LDV emission factors. When the data was averaged into 1-h, the most abundant signal would be influenced by both LDV and HDDV emissions. Since HDDV emit much higher NO_x than LDV, the most abundant signal of 1-h NO_x emission factors would shift towards higher end.

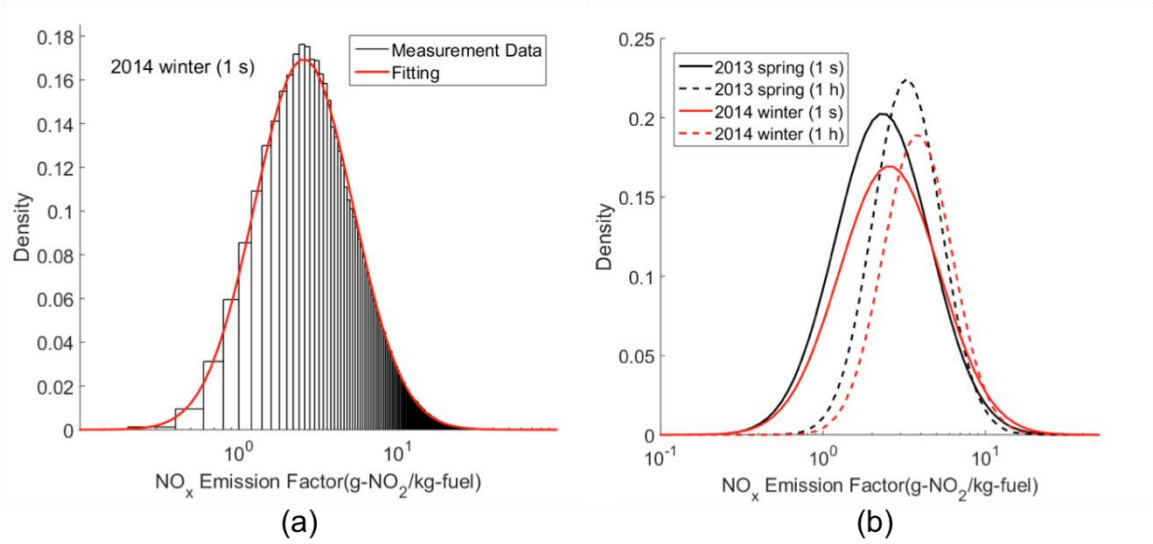

Figure 3.5 (a) The frequency density distribution of 1-s NO_x emission factors measured in the tunnel in winter. Red lines represent the lognormal distribution fitting of the distribution. (b) Comparison of the frequency density distributions of 1-h and 1-s NO_x emission factors measured in the tunnel.

The hourly averaged emission factors are not the only source of uncertainties of the linear regression method presented in the previous section. There are also uncertainties associated with the $\%fuel_D$, since 1) we do not have the real time traffic count, 2) the traffic data from PennDOT were not able to distinguish Medium Duty Vehicle (MDV) and HDDV, 3) I assumed averaged fuel economies for all LDV and HDDV in the tunnel, and 4) the amount of HDDV passing by the right lane and the left lane are different. Therefore, for pollutants measured at 1 Hz (PAH, NO_x and CO), following Dallmann et al. [69], we integrated peaks from exhaust plumes of individual trucks and got better estimations of HDDV emission factors. The peak integration was done by Jie Lu and will be described in an upcoming publication [184]. To briefly summarize here, we analyzed in total 17-hour tunnel measurement data and integrated exhaust plume peaks from ~190 diesel trucks. For all the integrated plume peaks, we checked the traffic video

took in the tunnel and made sure that there was a truck passing by our sampling inlet at that time. Results of the NO_x, PAH, and CO emission factors of HDDV estimated with the peak integration method are listed in Table 3.2 and Table 3.3-2. For emission factors of those pollutants (OC, EC and BC) that we do not have 1-Hz measurement data, and for the LDV emission factors, I took the linear regression results of the winter measurements as our best estimations.

Unlike NO_x and PAH, for which I reported the mean value and standard deviation of all the integrated HDDV plumes as the estimated emission factors, for CO emission factors, I reported the median value and the interquartile range of all integrated HDDV plumes. It is because that the mean value of the CO emission factors (18.9 g/kg-fuel) is significantly biased by high CO emitting trucks and is ~2 times higher than the median value (6.4 g/kg-fuel). The CO emission factors measured in the tunnel are not well correlated with $\%fuel_D$ (Figure 3.3(d)). Therefore, I cannot use the linear regression method to estimate the CO emission factors of LDV. Since the LDV had the highest fraction during the afternoon rush hour (16:00 – 18:00, the averaged $\%fuel_D$ is 3.4%), and the 1-s emission factor data are dominated by signals of LDV, I fitted the 1-s CO emission factor measured during the afternoon rush hour in winter with the lognormal distribution (Figure A.6) and assume that the mean and standard deviation of fitted lognormal distribution is a good estimation of the CO emission factor of LDV. The result is listed in Table 3.3-1.

3.3.4 Long-term trend of LDV and HDDV emission factors

In previous section I compared results from our tunnel measurement with results from Grieshop et al. [67] and concluded that the on-road gasoline and diesel vehicle emission factors significantly dropped in the past ten years. However, this conclusion is based on only two studies, and both our study and Grieshop et al. [67] were conducted in Pittsburgh and may not geographically represent the situation over the entire United States. Therefore, to further confirm the decreasing trend of on-road vehicle emission factors, I summarized emission

factors reported by previous tunnel studies [61–70] in United States since 1990s and compared them with the change of federal vehicle emission standards, and the results are presented in Figure 3.6. All data presented in Figure 3.6 and the cited pervious studies are summarized in Table 3.3-1 (LDV) and Table 3.3-2 (HDDV).

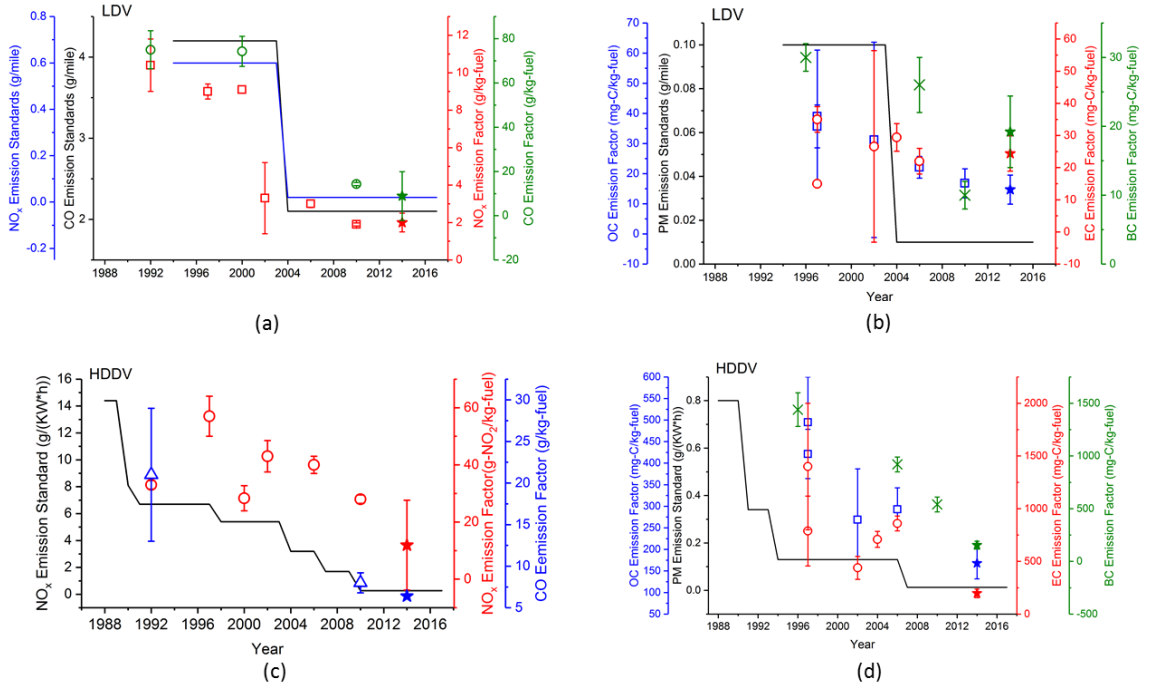

Figure 3.6 Emission factors of (a) gaseous pollutants emitted by LDV, (b) particulate pollutants emitted by LDV, (c) gaseous pollutants emitted by HDDV, and (d) particulate pollutants emitted by HDDV measured in the tunnel in United States since 1990s. The U.S. vehicle emission standards of LDV and HDDV are also presented in the figure as solid lines. Filled stars represent emission factors measured in this study in 2014, and other symbols represent emission factors reported by previous tunnel studies. The data and cited previous studies of emission factors are summarized in Table 3.3-1 (LDV) and Table 3.3-2 (HDDV). For CO emission factor of HDDV in 2014, only the median value of the diesel truck plume integration results in this study is shown in the figure. For EC emission factors of LDV measured in 1997 and reported by Allen et al. [64], the uncertainty range is too large and is not shown in the figure. For emission factors measured in 1992 and reported by Pierson et al. [61], only the uphill measurements conducted in the Fort McHenry Tunnel are shown in the figure.

As shown in Figure 3.6, over the past three decades, except the EC emission factors for gasoline vehicles, both gasoline and diesel vehicle emission factors

kept decreasing as the emission standards became stricter. It indicates that the stricter emission standards were effective on regulating the on-road vehicle emissions in U.S. The U.S. EPA Tier 1 (1994-2003) [185] and Tire 2 (2004 and later) [186] emission standards of LDV are presented in Figure 3.6(a) and (b). As shown in Figure 3.6 (a), the LDV emission standards of CO and NO_x decreased by 50% and 95%, respectively, in 2004. The CO and NO_x emission factors of LDV measured in the tunnel followed the trend of LDV emission standards. They were constantly at a higher value before 2002 and then significantly dropped by about 70-80% since 2002. The CO and NO_x emission factors of LDV measured from 2002 – 2014 are relatively constant. The PM emissions of LDV are presented in Figure 3.6 (b). The PM emission standards of LDV decreased by 90% at 2004. The OC emission factors of LDV measured in the tunnel kept decreasing from 1996 – 2014, however, the EC emission factors of LDV measured in the tunnel did not change too much since 2002, which is similar with the trend seen in dynamometer studies [52]. The BC emission factor of LDV measured before 2010 indicates that the BC emissions of LDV were decreasing overtime. The BC emission factor of LDV measured in this study in 2014 almost doubles the BC emission factor of LDV measured in 2010, but is still about 30% lower than BC emission factors of LDV measured before 2006.

The long-term trend of gas-phase pollutants and PM emitted by HDDV measured in the tunnel are presented in Figure 3.6 (c) and (d), respectively. The U.S. EPA heavy-duty diesel truck emission standards of NO_x and PM are also presented in Figure 3.6 (c) and (d), respectively, and the data of the emission standards were summarized in Ban-Weiss et al. [68]. As shown in Figure 3.6 (c), the CO and NO_x emission factors of HDDV measured in the tunnel in the past years kept decreasing and followed the trend of the NO_x emission standards of HDDV. Similarly, the OC, EC, and BC emission factors of HDDV also kept decreasing in the past years with the PM emission standard of HDDV became stricter (Figure 3.6(d)). The OC and EC emission factors of HDDV slightly increase from 2002-2006, but they are in general ~50% lower than the OC and EC emission factors of HDDV measured in 1996, and the OC and EC emission factors of HDDV

measured in this study in 2014 are ~50% lower than they measured in 2002-2006.

Although both LDV and HDDV emission factors measured in the tunnel were decreasing in the past three decades, they were not decreasing at the same rate. The relative significance of HDDV to the on-road vehicle emissions was also changing overtime. In Table 3.4 I summarized the ratio of HDDV-to-LDV emission factors measured in previous tunnel studies and in this study in United States. The HDDV-to-LDV ratio of NO_x emission factors was almost doubled in 2002-2010 compared with it measured before 2000, but it measured in this study in 2014 dropped down to the same level as it measured before 2000. The HDDV-to-LDV ratio of the OC emission factor was not significantly changed over time, while the HDDV-to-LDV ratios of EC and BC emission factors were in general decreased overtime. The comparison between our study and Grieshop et al. [67] indicates that the NO_x and EC emissions of HDDV were decreased much faster than the LDV in the past ten years, while the OC emissions factors of HDDV were decreased slower than the LDV. Although the relative importance of HDDV to the NO_x and OC emissions is lower, the emission factors of HDDV are still significantly (~5-10 times) higher than the emission factors of LDV.

3.4 Conclusion

In this work, the gaseous and particulate pollutants emitted by on-road gasoline and diesel vehicles under real-world driving conditions are measured in a traffic tunnel. Since the measured fleet average vehicle emission factors are strongly correlated with the $\%fuel_D$ in the tunnel, I performed linear regression of vehicle emission factors as a function of $\%fuel_D$ to apportion the gasoline and diesel vehicle emission factors of NO_x, OC, and EC measured in both spring and winter. After removing the difference caused by the lane shift, I found that the NO_x and EC emission factors of LDV are about 70% and 60% higher in the winter than in the spring, respectively. The OC emission factors of LDV and the NO_x, OC, and

EC emission factors of HDDV are similar in winter and spring (difference within 20%).

There are several sources of uncertainties for the linear regression method. First, it is using the hourly averaged emission factor data. The lower time resolution of the measurement data may lead to a loss of information, such as the emission plumes from individual trucks, and it may potentially lead to an overestimation of vehicle emission factors. Second, there are also uncertainties associated with the $\%fuel_D$ since it was not measured at the same time with the pollutant monitoring, and the number fraction of the HDDV may potentially overestimated by the traffic data. Therefore, for NO_x, PAH and CO, which we measured at 1 Hz in the tunnel, I used the 1 Hz data and integrated peaks of individual truck plumes to estimate emission factors of HDDV.

I compared the emission factors measured in this study with emission factors measured by Greishop et al. [67] ~10 years ago in another traffic tunnel in Pittsburgh and found that the NO_x, OC and EC emission factors of diesel vehicles and the NO_x and OC emission factors of gasoline vehicles significantly dropped (~50 - 70%) over the past 10 years, while the EC emission factors of gasoline vehicles measured in both studies are similar. To further confirm this long-term trend, I summarized emission factors measured in previous tunnel studies in U.S. since 1990s and compared them with the change of vehicle emission standards in U.S. The stricter emission standards were effective on regulating NO_x and PM emissions of diesel vehicles and the NO_x, CO and PM emissions of gasoline vehicles, while the EC emissions of gasoline vehicles did not change too much over the past three decades. By studying the trend of HDDV-to-LDV emission factor ratios measured in the tunnel since 1990s, I found that the relative importance of HDDV on NO_x and EC emissions decreased, but the NO_x, OC and EC emissions of HDDV are still significantly higher (~5-10 times) than the LDV.

The gasoline and diesel vehicle emission factors reported in this study can be used by policy makers to develop policy plans on regulating air pollutant

emissions from on-road vehicles. As the application of new vehicle technology, such as the gasoline direct injection (GDI) engine, may alter the characteristic of vehicle emissions [187,188], and the vehicle emission standard may become stricter, it is necessary to conduct on-road studies to continuously monitoring vehicle emissions in the future in order to test the effectiveness of policies on regulating vehicle emissions, and to provide up-to-date vehicle emission factors.

Table 3.3-1 Emission factors of Light Duty Vehicle (LDV) measured in traffic tunnels in the United States

References	Tunnel	Year of measurement	NO_x (g-NO_2/kg-fuel)	CO (g/kg-fuel)	OC (mg-C/kg-fuel)	EC (mg-C/kg-fuel)	BC (mg/kg-fuel)	$PM_{2.5}$ (mg/kg-fuel)
Pierson et al.[61]	Fort McHenry Tunnel, MD, Downhill	1992	7.5 ± 0.7[a]	63.2 ± 3.2[a]	-	-	-	-
Pierson et al.[61]	Fort McHenry Tunnel, MD, uphill	1992	10.4 ± 1.4[a]	75 ± 8.6[a]	-	-	-	-
Pierson et al.[61]	Tuscarora Mountain Tunnel, PA, level	1992	5 ± 3.6[a]	64.6 ± 6.4[a]	-	-	-	-
Miguel et al.[178]	Caldecott Tunnel, CA	1996	-	-	-	-	30 ± 2	-
Kirchstetter et al.[63]	Caldecott Tunnel, CA	1997	9 ± 0.4[b]	-	35.7 ± 7.1[bc]	35 ± 4[b]	-	110 ± 10[b]
Allen et al.[64]	Caldecott Tunnel, CA	1997	-	-	39.0 ± 22.0[d]	15.0 ± 71.0[d]	-	73.0 ± 51.0[d]
McGaughey et al.[65]	Washburn Tunnel, TX	2000	9.1 ± 14.9[e]	74.3 ± 6.8[e]	-	-	-	-
Gëller et al.[66]	Caldecott Tunnel, CA	2004	-	-	-	29.4 ± 4.3[f]	-	67.1 ± 11.2[f]
Grieshop et al.[67]	Squirrel Hill Tunnel, PA	2002 and 2004	3.3 ± 1.9	-	31.2 ± 32.4	26.6 ± 29.8	-	30.6 ± 43.8
Ban-Weiss et al.[68]	Caldecott Tunnel, CA	2006	3.0 ± 0.2	-	22.1 ± 3.6[g]	22 ± 4	26 ± 4	70 ± 20
Dallmann et al.[70]	Caldecott Tunnel, CA	2010	1.9 ± 0.08[h]	14.3 ± 0.7[h]	16.8 ± 4.8[hi]	-	10 ± 2[h]	38 ± 10[h]
This work	Fort Pitt Tunnel, PA	2013 and 2014	2 ± 0.5[j]	8.9 ± 11.0[k]	14.7 ± 4.8[j]	24.4 ± 5.5[j]	19.2 ± 5.2[j]	-
Difference of this work with Grieshop et al.(%)			-39.4 ± 63.7	-	-52.9 ± 118.5	-8.3 ± 114.3	-	-

a. I assumed one gallon of gasoline weighs 2.80 kg and one gallon of diesel weighs 3.24 kg to convert unit.
b. Data calculated by Ban-Weiss et al.[68] using the revised regression method are reported here.
c. A factor of 1.4 is used to convert Organic Matter (OM) concentration to OC concentration.
d. Data reported here are for $PM_{1.9}$.
e. I assumed the density of gasoline equals to 0.74 kg/L to convert unit.
f. Data reported here are for $PM_{2.5}$.
g. A factor of 1.4 is used to convert OM concentration to OC concentration.
h. Data reported here are adjusted light-duty-vehicle emission factors reported in Dallmann et al.[70].
i. A factor of 1.25 is used to convert Organic Aerosol (OA) concentration to OC concentration.
j. Results from linear regression of winter data are reported here.
k. The result of the rush hour 1-s emission factor distribution fitting is reported here.

Table 3.3-2 Emission factors of Heavy Duty Diesel Vehicle (HDDV) measured in traffic tunnels in the United States

References	Tunnel	Year of measurement	NO_x (g-NO_2/kg-fuel)	CO (g/kg-fuel)	OC (mg-C/kg-fuel)	EC (mg-C/kg-fuel)	BC (mg/kg-fuel)	$PM_{2.5}$ (mg/kg-fuel)
Pierson et al.[61]	Fort McHenry Tunnel, MD, Downhill	1992	29.9 ± 0.9[a]	21.0 ± 4.6[a]	-	-	-	-
Pierson et al.[61]	Fort McHenry Tunnel, MD, uphill	1992	33.0 ± 1.5[a]	21.0 ± 8.0[a]	-	-	-	-
Pierson et al.[61]	Tuscarora Mountain Tunnel, PA, level	1992	34.6 ± 1.5[a]	10.8 ± 2.8[a]	-	-	-	-
Miguel et al.[178]	Caldecott Tunnel, CA	1996	-	-	-	-	1440 ± 160	
Kirchstetter et al.[63]	Caldecott Tunnel, CA	1997	57 ± 7[b]	-	421.4 ± 57.1[bc]	1400 ± 600[b]	-	2700 ± 300[b]
Allen et al.[64]	Caldecott Tunnel, CA	1997	-	-	495.0 ± 105.0[d]	788.0 ± 332.0[d]	-	1285.0 ± 237.0[d]
McGaughey et al.[65]	Washburn Tunnel, TX	2000	28.3 ± 4.4[e]	-	-	-	-	
Gëller et al.[66]	Caldecott Tunnel, CA	2004	-	-	-	709 ± 76[f]	-	1015.0 ±127.0[f]
Grieshop et al.[67]	Squirrel Hill Tunnel, PA	2002 and 2004	43 ± 5.5	-	269 ± 118	439 ± 109	-	1060 ± 160
Ban-Weiss et al.[68]	Caldecott Tunnel, CA	2006	40 ± 3	-	292.9 ± 50[g]	860 ± 70	920 ± 70	1400 ± 300
Dallmann et al.[69]	Caldecott Tunnel, CA	2010	28.0 ± 1.5	8.0 ± 1.2	-	-	540 ± 70	-
This work	Fort Pitt Tunnel, PA	2013 and 2014	11.9 ± 15.7[i]	6.4 (0.5-18.0)[i]	167.8 ± 36.3[h]	196.8 ± 41.0[h]	153.5 ± 37.0[h]	-
Difference with Grieshop et al.(%)			-72.3 ± 39.8	-	-37.6 ± 48.8	-55.2 ± 29.9	-	-

a. I assumed one gallon of gasoline weighs 2.80 kg and one gallon of diesel weighs 3.24 kg to convert unit.
b. Data calculated by Ban-Weiss et al.[68] using the revised regression method are reported here.
c. A factor of 1.4 is used to convert Organic Matter (OM) concentration to OC concentration.
d. Data reported here are for $PM_{1.9}$.
e. I assumed the carbon fraction of diesel equals to 0.87 to convert unit. The diesel vehicle emission factor reported here are calculated based on the linear regression results presented in Table 4 in McCaughey et al.[65]
f. Data reported here are for $PM_{2.5}$.
g. A factor of 1.4 is used to convert OM concentration to OC concentration.
h. Results from linear regression of winter data are reported here.
i. Results of peak integration are reported here. The NO_x emission factor is reported as median value (interquartile range).

Table 3.4 Ratio of HDDV-to-LDV emission factors measured in traffic tunnels in the United States

References	Tunnel	Year of measurement	NO_x	OC	EC	BC
Pierson et al.[61]	Fort McHenry Tunnel, MD, Downhill	1992	4.0 ± 0.4[a]	-	-	-
Pierson et al.[61]	Fort McHenry Tunnel, MD, uphill	1992	3.2 ± 0.5[a]	-	-	-
Pierson et al.[61]	Tuscarora Mountain Tunnel, PA, level	1992	6.9 ± 5.0[a]	-	-	-
Miguel et al.[178]	Caldecott Tunnel, CA	1996	-	-	-	48.0 ± 6.2
Kirchstetter et al.[63]	Caldecott Tunnel, CA	1997	6.3 ± 0.8[b]	11.8 ± 2.8[bc]	40.0 ± 17.7[b]	-
Allen et al.[64]	Caldecott Tunnel, CA	1997	-	12.7 ± 7.6[d]	52.5 ± 249.6[d]	-
McGaughey et al.[65]	Washburn Tunnel, TX	2000	3.1 ± 5.1[e]	-	-	-
Gëller et al.[66]	Caldecott Tunnel, CA	2004	-	-	24.1 ± 4.4[f]	-
Grieshop et al.[67]	Squirrel Hill Tunnel, PA	2002 and 2004	13.0 ± 7.7	8.6 ± 9.7	16.5 ± 18.9	-
Ban-Weiss et al.[68]	Caldecott Tunnel, CA	2006	13.3 ± 1.3	13.3 ± 3.1[g]	39.1 ± 7.8	35.4 ± 6.1
Dallmann et al.[69]	Caldecott Tunnel, CA	2010	14.7 ± 1.0[h]	-	-	54.0 ± 12.9[h]
This work	Fort Pitt Tunnel, PA	2013 and 2014	6.0 ± 8.0[i]	11.4 ± 4.5[j]	8.1 ± 2.5[j]	8.0 ± 2.9[j]
	Difference with Grieshop et al.(%)		-53.8 ± 91.2	+32.6 ± 129.6	-50.9 ± 129.4	-

a. I assumed one gallon of gasoline weighs 2.80 kg and one gallon of diesel weighs 3.24 kg to convert unit.
b. Data calculated by Ban-Weiss et al.[68] using the revised regression method are reported here.
c. A factor of 1.4 is used to convert Organic Matter (OM) concentration to OC concentration.
d. Data reported here are for $PM_{1.9}$.
e. I assumed the carbon fraction of diesel equals to 0.87 to convert unit. I assumed the density of gasoline equals to 0.74 kg/L to convert unit. The diesel vehicle emission factor reported here are calculated based on the linear regression results presented in Table 4 in McCaughey et al. [65]
f. Data reported here are for $PM_{2.5}$.
g. A factor of 1.4 is used to convert OM concentration to OC concentration.
h. I used adjusted light-duty-vehicle emission factors reported in Dallmann et al.[70] as the LDV emission factor to calculate these ratios.
i. Gasoline vehicle emission factor was estimated by conducting linear regression to the winter data. Diesel vehicle emission factor was estimated by integrating truck plumes.
j. Results from linear regression of winter data are reported here.

Chapter 4
Size distribution of vehicle emitted primary particles measured in a traffic tunnel

4.1 Introduction

On-road gasoline and diesel vehicles are a major source of particulate matter (PM) in the urban environment [24,48,85], and to better quantify the size distribution of vehicle emitted PM can help better constrain the global CCN concentrations [87] and better estimate the health effect of vehicle emitted ultrafine particles. Many previous studies measured the size distributions of vehicle emitted particles on-road [93–95] or in the traffic tunnel [66,96–99]. Since the vehicle emission standards in US become stricter in recent years [100], and the application of after-treatment technology can potentially change the size-distribution of vehicle emitted particles [101,102], the size distribution of vehicle emitted particles needs to be monitored over time in order to understand the effectiveness and the potential influence of new standards and technology on reducing vehicle emissions.

Vehicle emitted particles are mostly fractal particles, which are nanoparticle aggregates composed of small spherical primary particles, as reported by both vehicle engine tests [92,189–191] and near-road and tunnel studies [192–194]. Assuming the vehicle emitted particle is spherical and has a unit density (1 g/cc) could potentially overestimate mass emissions [191,195]. Among all tunnel studies that measured the size-distribution of vehicle emitted particles, very few studies reported the volume or the mass size distributions. Ban-Weiss et al.[98] conducted measurement in the Caldecott tunnel and reported size-resolved particle volume emission factors of both gasoline and diesel vehicles. However, the particle volume calculated by Ban-Weiss et al.[98] was under the assumption that all particles emitted by vehicles are spherical, and thus could be potentially overestimated. No tunnel studies have compared the particle mass calculated from the size-distribution measurement with direct particle mass measurements.

As shown by previous studies, once entering the atmosphere from the tailpipe, the vehicle emitted primary particles will experience gas-particle patitioning [105,113,114] and evolved organic vapors can react to form secondary organic aerosol (SOA) [49,50]. Therefore, in order to better quantify the contribution of vehicle emissions to the total

particle burden in the atmosphere, it is necessary to have a better quantification of both the particle size and the particle chemical composition or volatility of vehicle emitted particles. Numerous studies measured the chemical composition and the volatility of vehicle emitted particles [82,83,92,113,114,118,196,197], but very few studies reported size-dependent chemical composition or volatility. Kleeman et al. [83] reported size-dependent chemical composition of particles larger than ~50 nm for both gasoline and diesel vehicles, and Lu et al. [92] measured the size-dependent volatile and non-volatile component of particles emitted by diesel vehicles. Those studies were lab engine tests on a limited number of vehicles and may not represent emissions from the much larger real-world fleet.

In this work, we measured the size distribution of vehicle emitted primary particles in the Fort Pitt Tunnel in Pittsburgh, PA with a pair of Scanning Mobility Particle Sizers (SMPS). We report both number-size distribution and mass-size distribution of vehicle emitted particles. To better quantify the size-dependent mass concentration of vehicle emitted particles, we assume they are fractal and re-analyzed the SMPS data with the Nanoparticle Aggregate Mobility Analysis Software Module built in the Aerosol Instrument Manager Software for SMPS. The particle mass measured by the SMPS was compared to other concurrent direct particle mass measurement. A thermodenuder (TD) was deployed in the sampling line to periodically remove the volatile particle component with high temperature (250 °C) to determine the size-dependent volatility of vehicle emitted particle. A size-resolved volatile-to-non-volatile component ratio of vehicle emitted particles is reported based on the SMPS-TD measurement. Finally, we calculated the size-resolved emission factors of particles emitted by the mixed fleet in the tunnel, apportioned the contribution from both gasoline and diesel vehicles, and compared the apportioned size-resolved gasoline and diesel vehicle emission factors with previous studies.

4.2 Methods

4.2.1 Size distribution measurement

Information about the Fort Pitt Tunnel, the traffic conditions in the tunnel, and the measurement station can be found in Chapter 2. The size distribution measurements were conducted from Jan 31 to Feb 4, 2014. During the measurements, approximately 140,000 LDV and 3,600 HDDV passed by the tunnel.

Particle size distributions were measured with a pair of SMPS (TSI Inc.). Particles with a diameter of 4 – 120 nm were measured by a nano-SMPS, which consisted of a nano Differential Mobility Analyzer (DMA, model 3085) and an ultrafine Condensation Particle Counter (CPC, model 3025A). In order to minimize the diffusion loss of smaller particles, the ultrafine CPC was run under high-flow mode. Particles with a diameter of 12 – 550 nm were measured by a long-SMPS, which includes a long-DMA (model 3081) and a CPC (model 3772). The particle number concentrations measured by the nano-SMPS and the long-SMPS are consistent in the size range of 20 to 120 nm (Figure B.1).

For particles with a diameter less than 15nm, particle number concentrations measured by nano-SMPS are 3-1000 times larger than the particle concentrations measured by the long-SMPS (Figure B.2). The higher particle number measurement of the nano-SMPS over the long-SMPS was also seen in other ambient measurement [198]. A recent lab study [199] reported that for particles below 20 nm, the penetration efficiencies are much higher in the nano-DMA compared with in the long-DMA. Compared with the long-DMA, the design of the nano-DMA is modified to optimize the measurement of particles below 20 nm [200]. The ultrafine CPC is also designed to minimize the diffusion loss of the smaller particles [201]. Therefore, for particles below 20nm, number concentrations measured by the nano-SMPS is more reliable compared with long-SMPS.

We collected 60 hours of particle size-distributions in the tunnel at 2-minute resolution, for a total of 1329 scans. I divided these data into three time periods: weekday high traffic time (7:00 – 21:00, 28 total hours), weekday low traffic time (22:00 – 6:00, 22 total

hours), and weekend (14:00 – 23:00, 10 total hours). Among all three time periods, the weekday low traffic time has the lowest traffic volume but highest $\%fuel_D$. The traffic volume and $\%fuel_D$ in weekend are both slightly lower than the traffic volume and $\%fuel_D$ in weekday high traffic time.

4.2.2 Thermodenuder (TD)

To measure the non-volatile component of the vehicle emitted particles, a thermodenuder (TD) was placed in the particle sampling line to remove the volatile component of particles. The design of the TD is described in An et al. [202]. The temperature inside the heating zone of the TD was held constant at 250 ºC; therefore, the 'non-volatile component' in this manuscript is defined as particle component that would not evaporate upon heating under 250 °C. These non-volatile components are mostly EC, and may contain some extremely low volatility organic compounds (ELVOC). The particle residence time at 250 °C inside the TD was about 2.6 seconds with a flow rate of 8.5 LPM. Two electrically-actuated three-way valves (MS-142ACX; Swagelok Co., Solon, OH) were placed at the inlet and outlet of the TD to make instruments sample through either TD or directly from the tunnel through a bypass line. In every 30 min, particles were sampled through bypass line for 20 min, and through TD for 10 min. In total 44 hours of TD measurement data were collected among all 60 hours of particle size distribution measurements.

I tested the particle loss inside the TD in the lab with NaCl particles as described in section B.1 in Appendix B (Figure B.3 and B.4) and in previous studies [52,196]. All TD data presented in this manuscript are corrected for particle loss.

4.2.3 Nanoparticle aggregates correction

As introduced in the previous section, vehicle emitted primary particles are mostly fractal particles. The Aerosol Instrument Manager Software for SMPS (TSI Inc.) assumes all measured particles are spherical by default. However, assuming these fractal particles as spherical particles will lead to an overestimation of the particle mass measured by SMPS. In Figure 4.1(a) and (b) I compare the equivalent spherical particle

mass measured by the SMPS through the bypass line and the TD with the particle mass measured by the OC/EC analyzer and the Black Carbon (BC) measured by the Aethalometer, respectively. The particle mass measured by the OC/EC is calculated using OC concentrations multiplied by an OM (organic mass)/OC ratio of 1.2 [167] and then plus the EC concentrations. Results show that the spherical-particle assumption makes particle mass measured by SMPS 3 times and 5 times higher than particle mass measured by the OC/EC analyzer and the Aethalometer.

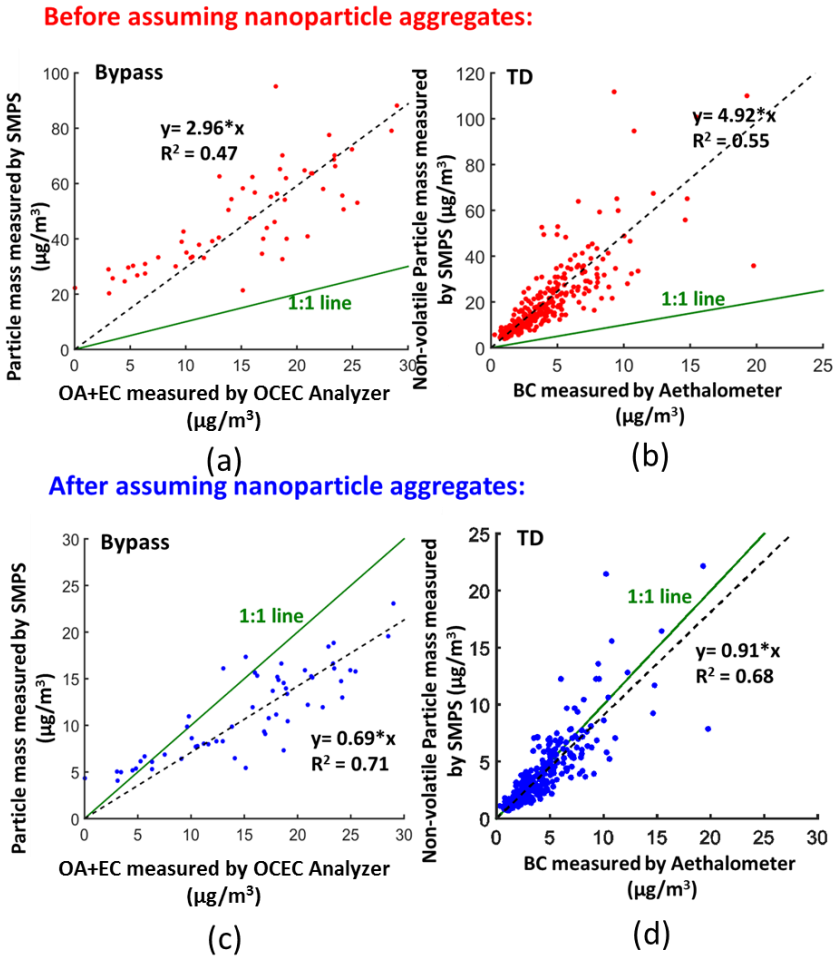

Figure 4.1 Comparison of the particle mass concentrations measured by SMPS and (a) OC/EC analyzer through bypass line, and (b) Aethalometer through TD in the tunnel, assuming particles are spherical. And comparison of the particle mass concentrations measured by SMPS and (c) OC/EC analyzer through bypass line, and (d) Aethalometer through TD in the tunnel, assuming particles are nanoparticle aggregates.

In order to better estimate the number and the mass of these nanoparticle aggregates, I reanalyzed the data with the Nanoparticle Aggregate Mobility Analysis Software Module built in the Aerosol Instrument Manager Software for SMPS (TSI Inc.), assuming the orientation of the aggregates are parallel with respect to the electric field, and the diameter of the primary particle is 30 nm. Several near road studies [193], tunnel studies [192], and vehicle engine tests [189,190] reported that the primary particles of vehicle emitted nanoparticle aggregates have an average size of about 30 nm, and I further discussed the choice of the primary particle size in section B.2 (Table B.1) in Appendix B. A detailed description of the nanoparticle aggregates correction of SMPS data can be found in Lall et al. [195,203]. To briefly summarize here, the correction firstly calculates the number of primary particles (N_p) in an aggregate with a mobility diameter D_p assuming that the aggregate composed of N_p particles of radius *a* = 15 nm has the same drag force with a spherical particle of diameter d_m, both have unit charge. Then the correction uses N_p and *a* to calculate the charging efficiencies of aggregates, which are different with the spherical particles. Particles with a diameter (D_p) less than the size of the primary particles (30 nm) are treated as spheres, and their mass ($m(D_p)$) is calculated using the following equiation:

$$m(D_p) = n(D_p) \cdot (\pi / 6) \cdot {D_p}^3 \cdot \rho \quad (1)$$

Where $n(D_p)$ is the particle number concentration measured by the nano-SMPS, and ρ is the density of the particle, which I assume is 1.2 g/cc [204]. Particles with $D_p \geq 30$ nm are treated as the nanoparticle aggregates, and their mass is calculated as [195]:

$$m(D_p) = n_{agg}(D_p) \cdot N_p(D_p) \cdot (4\pi a^3 / 3) \cdot \rho \quad (2)$$

Where $n_{agg}(D_p)$ is the corrected number concentration measured by the long-SMPS, $N_p(D_p)$ is the number of primary particles in a nanoparticle aggregates with a diameter of D_p (Table B.2).

Compared with the spherical particle assumption, this nanoparticle aggregates correction does not significantly change the measured particle number size distribution, but the corrected particle mass is about 4 times lower, as shown in Figure B.5. Figure 4.1(c) and (d) compare the corrected SMPS mass measured from the bypass line and

the TD with the particle mass measured by the OC/EC analyzer and the BC mass measured by the Aethalometer, respectively. For the bypass measurement, the correction changed the ratio of SMPS-to-OC/EC-mass from 3.0 to 0.7. I would not expect perfect agreement in the bypass measurements because that the OC/EC measurements has a larger particle size cut (2.5 μm). The correlation between the particle mass measured by the SMPS and the OC/EC analyzer is also improved after the correction, the R^2 increased from 0.47 to 0.71. Similarly, for the TD measurements, the nanoparticle aggregates correction decreased the ratio of the SMPS-to-Aethalometer-mass from 5.0 to 0.9, and improved their correlation (R^2 increased from 0.55 to 0.68).

4.2.4 Size-resolved particle emission factors

Following Ban-Weiss et al.,[98] the particle number emission factor, EF_N (the number of emitted particles per kg fuel burned), is calculated using the following equation:

$$EF_N = \frac{\Delta[N]}{\Delta[CO_2] + \Delta[CO]} w_c \cdot 10^{12} \quad (3)$$

where Δ[N] is the background-subtracted particle number concentration in #/cm^3, Δ[CO_2] and Δ[CO] are background-subtracted CO_2 and CO concentrations in mg-C/m^3, and w_c is the carbon mass fraction in the fuel, 0.85 for gasoline and 0.87 for diesel. The particle mass emission factor, EF_M (grams of emitted particles per kg fuel burned), is calculated by simply replacing Δ[N] in Equation 3 with the background-subtracted particle mass concentration, Δ[M], in μg/cm^3. To calculate the size-dependent particle emission factor, $dEF_N/dlogDp$, I applied Equation 3 to each of the 140 SMPS size bins (4 nm to 550 nm).

The ambient background particle size distribution was measured on the campus of Carnegie Mellon University from Sept. 17, 2017 to Sept. 25, 2017. Particles with a size range of 7 nm – 260 nm were continuously measured by a long-SMPS (DMA 3081 and CPC 3772, TSI Inc.). Measured ambient size-distributions were fitted with log-normal distributions to assess particle size distributions in the size range of the tunnel measurements (4 nm – 550 nm). I calculated hourly diurnal ambient background particle

size-distributions for both weekday and weekend. In Figure 4.2(a) I compare the particle size distribution measured in the tunnel and in the ambient. The average total particle number of the ambient background is about 3% of the averaged total particle number measured in the tunnel. In the particle size range of 4-35nm, where over 90% of the total particle number lies, the fraction of background particle number in each size bin is less than 5%.

In this manuscript, I report size-dependent vehicle emission factors of particles measured from the bypass line, and non-volatile particles measured from the TD. For the bypass line emission factor, I subtracted the diurnal ambient background from the particle number concentrations measured in the tunnel to get Δ[N]. For the non-volatile particle emission factor, since we did not apply the TD in the ambient measurements and no background data is available, I directly used the TD measurements in the tunnel as the Δ[N]. This may potentially overestimate the non-volatile particle emission factors of vehicles. However, since the ambient background only takes about 3% of the total particle number measured in the tunnel through the bypass line, I expect the influence of the ambient background on the non-volatile particle sampled through the TD would be also very small.

4.3 Result and discussion

4.3.1 Size distribution of vehicle emitted particles

The averaged particle number-size distribution and mass-size distribution are presented in Figure 4.2, and the time series of the particle number-size distribution are presented in Figure B.6 (a). The particle number-size distributions have an averaged median diameter of 16.5 nm, with an interquartile range of 12.6 – 19.5 nm. This median diameter range is similar with previous tunnel measurements [66,98,99]. The integrated particle number concentration in the tunnel has a mean value of 3.6×10^5 #/cc, with an interquartile range of $2.5 – 6.1 \times 10^5$ #/cc.

The averaged particle mass-size distribution showed two modes, one 30 nm and another one at 146 nm. The particle mass show a sudden jump at 30 nm. It is because

that the nanoparticle aggregate correction made the mass of 30 nm particles increased by about 30% compared with the spherical particle assumption. The averaged integrated particle mass measured in the tunnel is 11.2 μg/m^3, with an interquartile range of 27 – 57 μg/m^3.

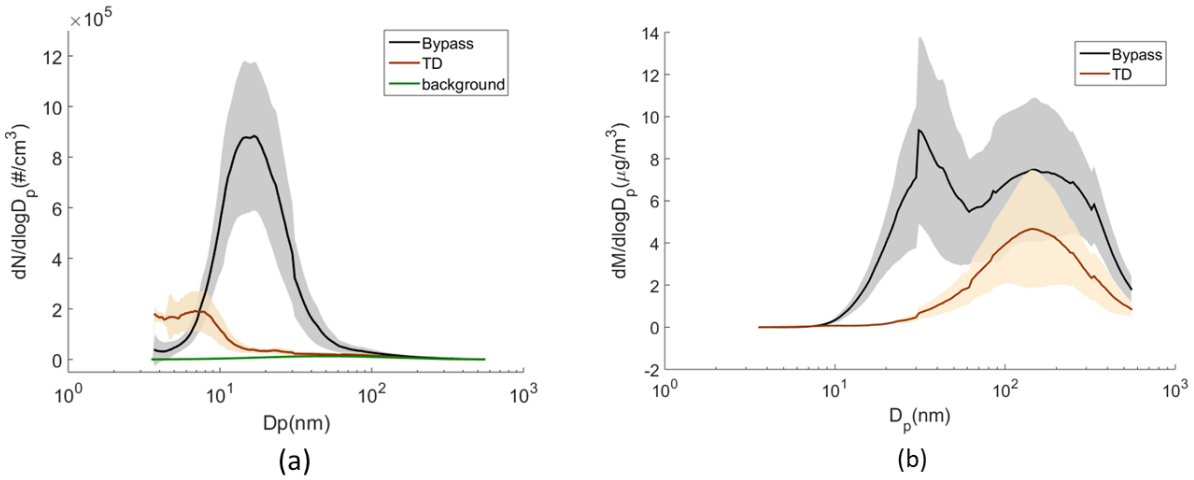

Figure 4.2 Averaged particle (a) number and (b) mass size distributions measured in the tunnel. Solid lines represent the mean value, and the shaded regions represent the standard deviation of 4-h averaged data. The averaged background particle number distribution is shown in (a) as the solid green line.

To show the influence of traffic composition on the particle size-distribution measured in the tunnel, I compare the averaged particle size distributions measured during the weekday high traffic time, the weekday low traffic time, and the weekends in Figure 4.3. The particle number-size distributions of all three time periods all have one mode at 16 nm, while the weekday high traffic time has the highest integrated number concentrations, 5.8 × 10^5 #/cc, and the weekends show the lowest integrated number concentrations, 2.6 × 10^5 #/cc. The particle number concentration inside the tunnel was influenced by both the total traffic volume and the %fuel$_D$. The weekday low traffic time and weekends having lower particle number concentration was mainly because that the traffic volume during these two time periods were lower. The traffic volume on weekends was higher than the weekday low traffic time, but the particle number concentration was lower because the %fuel$_D$ during the weekday low traffic time was over 4 times as the %fuel$_D$ during weekends, and HDDV emit significantly more

particles compared with the LDV. The particle mass-size distributions measured during all three time periods all show two modes, with the smaller mode all at about 30 nm. The larger mode of the mass size-distribution measured during weekday was around 120 – 150 nm, while in weekends it shifted to 334 nm. The integrated particle mass concentrations measured during these time periods show the same trend as the integrated number concentrations.

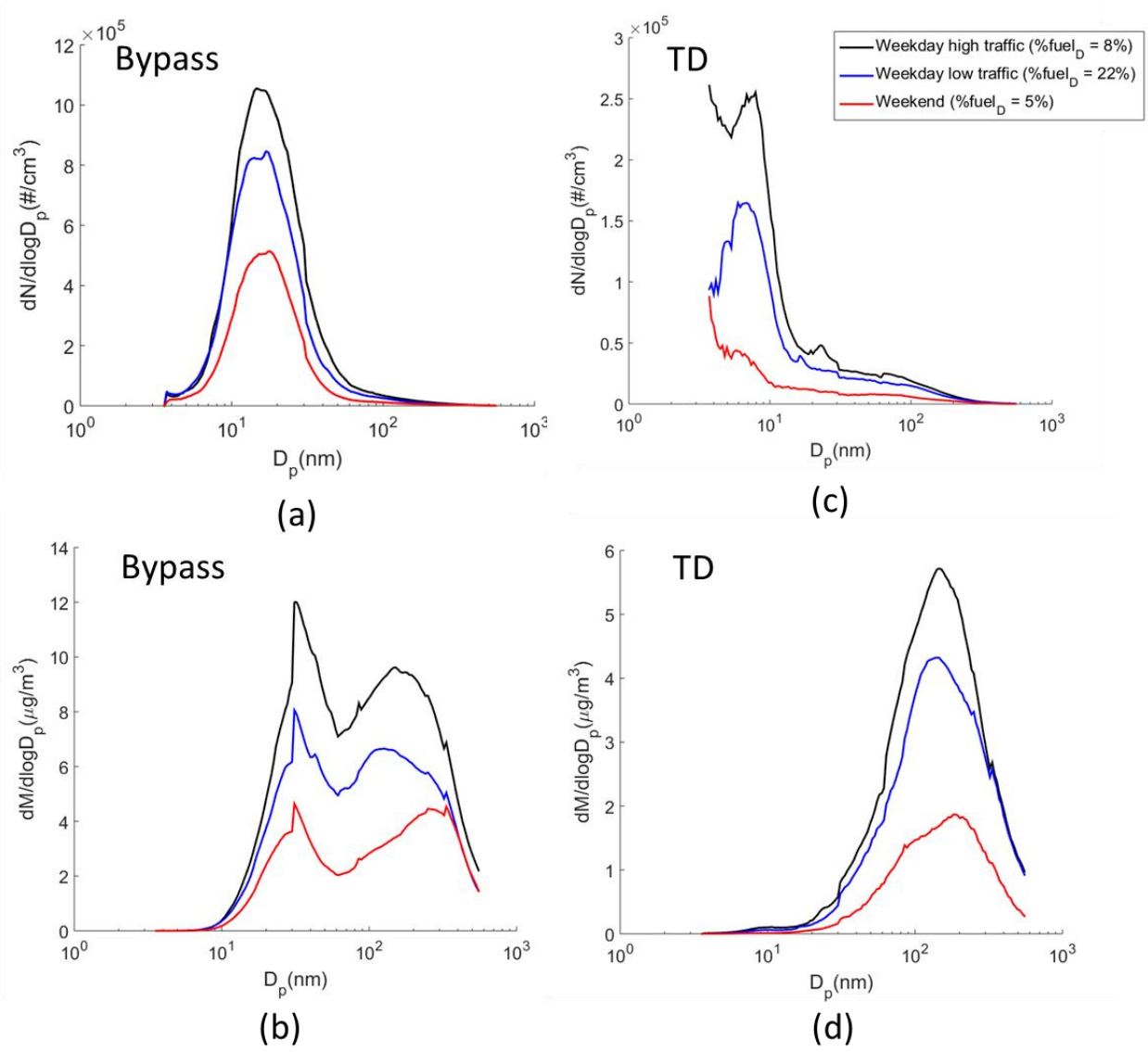

Figure 4.3 Averaged particle size distributions measured in the tunnel in different time periods. (a) and (b) are particle number and mass concentrations, respectively, measured through the bypass line; and (c) and (d) are non-volatile particle number and mass concentrations, respectively, measured through the TD.

4.3.2 Size distribution of vehicle emitted non-volatile particles

The averaged number-size and mass-size distributions of the non-volatile particles are shown in Figure 4.2, and the time series of the number-size distribution of the non-volatile particles are shown in Figure B.6 (b). After evaporation under 250 ºC inside the TD, the median diameter of the particle number-size distribution shifted from 16 nm to 7 nm. The chemical compositions of those 7 nm non-volatile particles remain uncertain. They could be small EC cores, or nucleated particles formed by ELVOC [196]. Rönkkö et al. reported that during the engine brake, the diesel vehicles can produce a significant number of 3 – 7 nm non-volatile particles, which can take up to 20 - 30% of the total particle number concentration and contains heavy metal from the lubricant oil. Since the tunnel where we conducted the measurement has a 2.5% upward grade, braking may not be a likely source. As shown in Figure B.6 (b), during some morning or afternoon rush hours, the number concentrations 20 – 100 nm particles were higher. These 20 – 100 nm non-volatile particles are mostly composed of EC [83] and were dominantly contributed by diesel vehicles.

In order to better understand the source of these non-volatile particles, in Figure 4.4 (a) and (b), I show the correlation of EF_N of smaller non-volatile particles (4 - 15 nm) and EF_N of larger non-volatile particles (20 - 100 nm) to the $\%fuel_D$, respectively. Results show that the EF_N of larger non-volatile particles has better correlation ($R^2 = 0.8$) with $\%fuel_D$ compared with the smaller non-volatile particles ($R^2 = 0.6$), indicating that the larger non-volatile particles are dominantly contributed by HDDV, while the smaller non-volatile particles are majorly emitted by HDDV but may also be contributed by the LDV in the tunnel.

Unlike the averaged mass-size distribution of particles measured through the bypass line in the tunnel, the averaged mass-size distribution of the non-volatile particles measured through TD showed only one mode at 146 nm. The averaged integrated mass concentration of non-volatile particles measured in the tunnel is 4.1 $\mu g/m^3$, with an interquartile range of 1.8 – 5.4 $\mu g/m^3$.

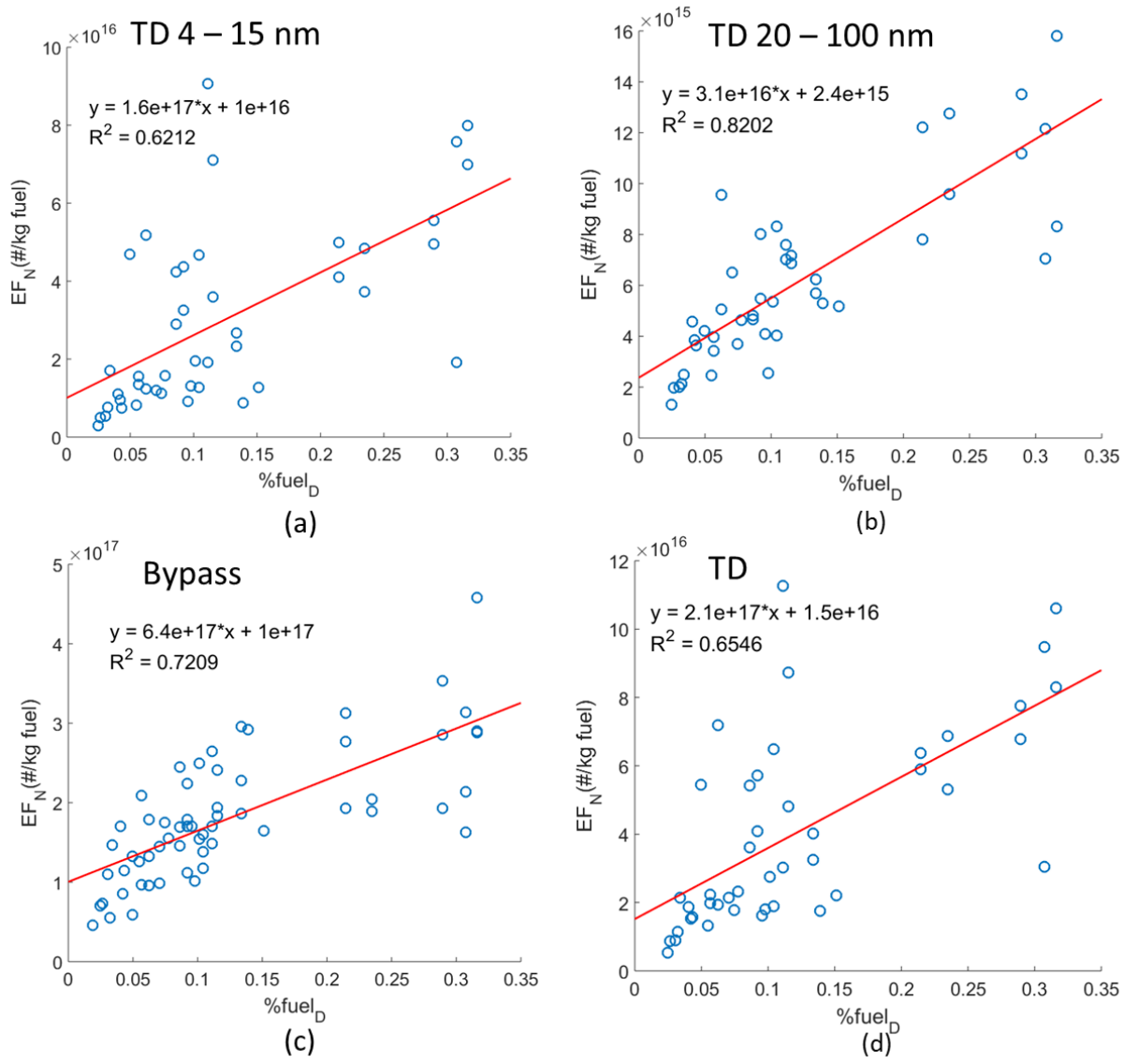

Figure 4.4 Correlation between (a) EF_N of 4 - 15 nm nonvolatile particles and $\%fuel_D$, (b) EF_N of 20 - 100 nm nonvolatile particles and $\%fuel_D$, (c) EF_N of particles measured through the bypass line and $\%fuel_D$, and (d) EF_N of non-volatile particles measured through the TD and $\%fuel_D$. Circles represent the measurement data, and red lines represent the linear regression fitting.

Similar with the previous section, the averaged mass and number size distributions of non-volatile particles in different time periods are presented in Figure 4.3 (c) and (d). Both number and mass size-distributions of non-volatile particles measured through TD during these three time periods have the same trend with the particle size-distribution measured through the bypass line. The highest concentrations of non-volatile particles

was observed during the weekday high traffic time, with an averaged integrated number concentrations of 1.4×10^5 #/cc and mass concentrations of 4.2 μg/m^3; and the lowest concentrations of non-volatile particles was observed at the weekends, with an averaged integrated number concentration of 2.9×10^4 #/cc and mass concentration of 1.4 μg/m^3.

The size distributions of the vehicle emitted particles and non-volatile particles are compared in Figure 4.2 and Figure B.6. After evaporation under 250 ºC inside the TD, the total particle number on average lost 69%, and 72% of the total particle mass evaporated. Particles in the size range of 10 - 80 nm account for over 90% of the total number drop. Concentrations of particles less than 10 nm increased, and it is potentially because of the shrinking of larger particles. The significant decrease of particle number concentrations over a wide size range after heating inside the TD indicates that the vehicle emitted particles could be largely externally mixed, and a large fraction of vehicle emitted particles may be purely composed of volatile component, such as organics and sulfate.

4.3.3 Volatile-to-non-volatile-component ratio of vehicle emitted particles

Using the concurrent mass-size distribution measured through the bypass line and TD, I calculate an averaged volatile-to-non-volatile-component-ratio (Figure 4.5). The volatile component mass is calculated using the particle mass concentration measured through the bypass line minus the non-volatile particle mass concentration measured through the TD.

All particle mass-size distributions measured by the SMPS were re-binned into 10 logarithmically evenly spaced bins from 6.3 nm to 631 nm. These bins are the same as the particle bins used in the TwO-Moment Aerosol Sectional (TOMAS) microphysics package[205] developed for the GEOS-Chem chemical transport model and the ratio reported in Figure 4.5 can be directly applied to the model. Particles with a diameter less than 6.3 nm were all binned into the smallest bins (centered at 8 nm). The largest size bin, which has a size range of 398 – 631 nm and centered at 501 nm, included particles up to the upper size cut of the measurements (398 – 550 nm).

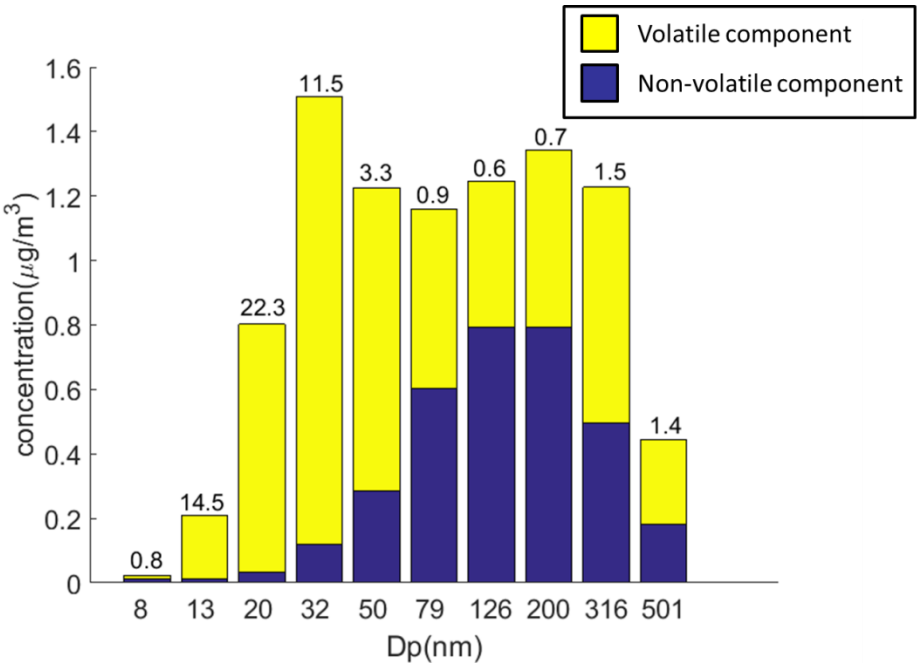

Figure 4.5 The size-resolved mass ratio of volatile-to-non-volatile-component of vehicle emitted particles. Numbers on top of bars are the mass ratio of each size bins. The tick labels on x-axis are the center D_p of each size bins.

Figure 4.5 shows that for particles in the size range of 10 – 63 nm, the mass of the volatile component is significantly higher than the mass of the non-volatile component. Lu et al. [92] tested particles emitted from a diesel engine under lower load and also reported that the mass of the volatile component is higher than the non-volatile component for particles less than 56 nm, but the volatile-to-non-volatile-component-ratio measured in this work is much larger than Lu et al. [92], and it is potentially because that Lu et al. [92] tested only diesel engines, but we measured emissions from a mixed fleet of LDV and HDDV, and the particles emitted by LDV tend to be more volatile.[83]

For 251 - 550 nm particles, the mass of the volatile component was 40-50% higher than the non-volatile component. Kleeman et al. [83] reported that for particle in this size range, the diesel vehicle emitted particles are dominated by EC, and the gasoline vehicle emitted particles are dominated by other volatile component. The ratio we measured in the tunnel is a combined contribution from both gasoline and diesel vehicles.

For particles in the size range of 3 – 10 nm and 63 – 251 nm, the non-volatile component has larger mass concentrations compared with the volatile component. Lu et al.[92] reported that the non-volatile component takes a larger share than the volatile component for particles in the size range of 56 – 320 nm for diesel vehicles running under lower load; and Kleeman et al.[83] found that for diesel vehicle emitted particles, in the size range of 65-350 nm, the EC takes a larger share in the total particle mass than the sum of all other chemical components. Both studies are consistent with our measurement.

The measurement uncertainty is presented in Figure B.7, and it is defined as the standard deviation of hourly averaged volatile-to-non-volatile-component-ratio. The particles in the size range of 10-63 nm showed a larger uncertainty compared with particles in other size range.

There are two major sources of uncertainty for the measured particle volatile-to-non-volatile-component-ratio. First, particles could partially evaporate in the TD and shift to smaller size bins, and for the non-volatile particles measured through TD, I do not know exactly know their original size. Secondly, for each size bin, I do not exactly know how much percentage of the particles are externally mixed and purely composed of volatile component. I am not able to accurately account for these two sources of uncertainty. To re-bin all the particles from finer-spaced bins to coarser-spaced bins can to some extent reduce the uncertainties caused by the shift of size bins after evaporation inside TD. It should also be noticed that the volatile-to-non-volatile-component-ratios reported in Figure 4 are bulk ratios for the entire particle populations in a certain size bin. Since our measurements indicate that a large fraction of vehicle emitted particles could be externally mixed, these mass ratios should be applied to single particles cautiously.

4.3.4 Size-resolved particle emission factors

The average size-resolved particle and non-volatile particle EF_N and EF_M measured at different time periods are shown in Figure 4.6. The shape of these emission factor size distributions are similar with the number and mass size distributions reported in previous section, but the trend in different time periods changed. For both particles and

non-volatile particles, we observed the highest emission factors during the weekday low traffic time, and the lowest emission factors during the weekends. This is consistent with the trend of $\%fuel_D$ of these time periods. The weekday low traffic time has a much higher $\%fuel_D$ (22%), while the weekday high traffic time has a slightly higher $\%fuel_D$ compared with the weekends (8% and 5%, respectively).

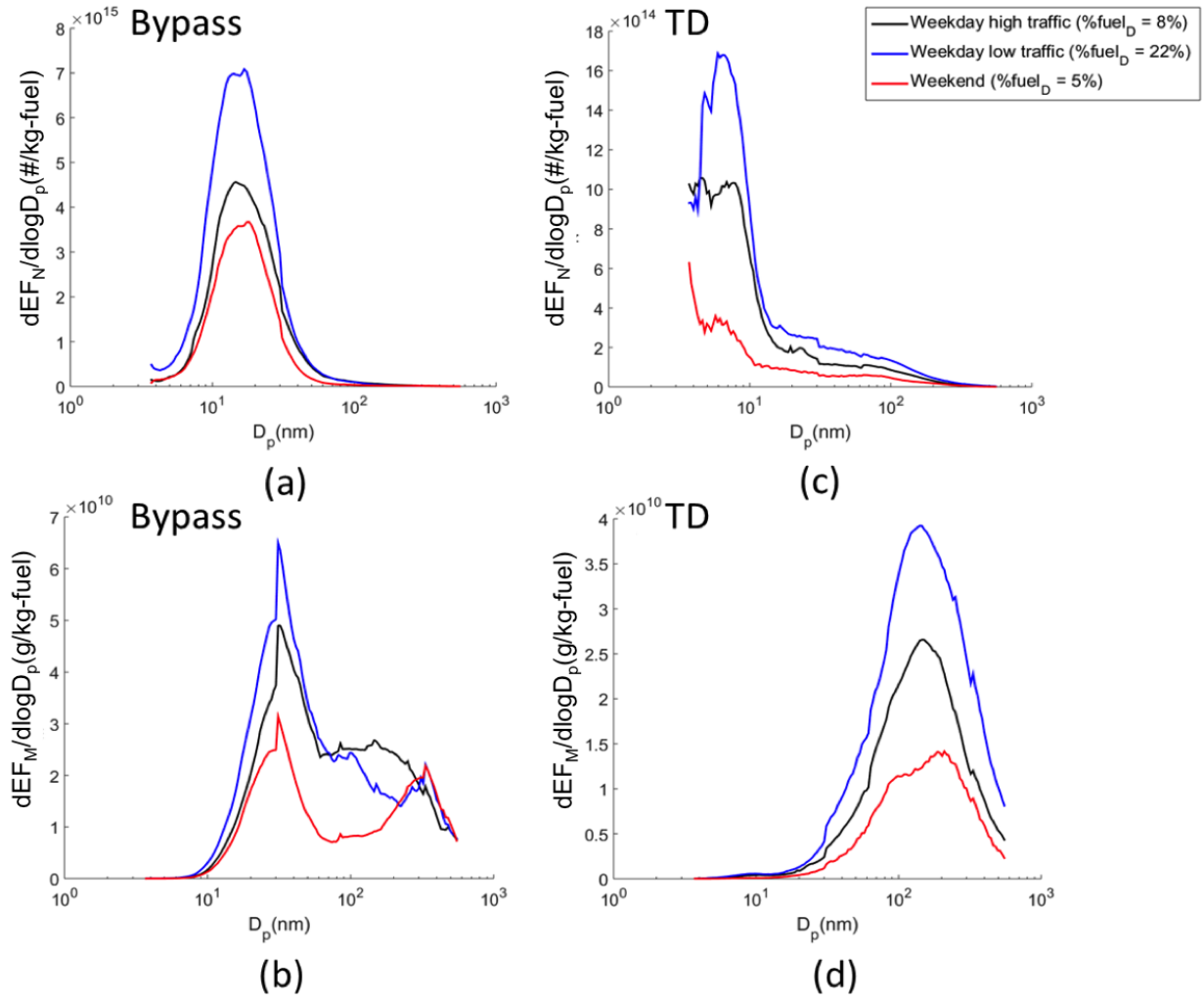

Figure 4.6 Averaged size-resolved particle emission factors measured in the tunnel in different time periods. (a) and (b) are particle number and mass emission factors, respectively, measured through the bypass line; and (c) and (d) are non-volatile particle number and mass emission factors, respectively, measured through the TD.

As shown in Figure 4.4 (c), since there is a strong correlation between the particle number emission factor measured in the tunnel and the $\%fuel_D$, following previous studies [108,182,206], I apportioned the particle emission factor of LDV and HDDV by performing a linear regression of particle emission factors as a function of the $\%fuel_D$. I applied this source apportionment to each of the 140 size bins to get size-dependent particle emission factors for LDV and HDDV. Since the EF_N of non-volatile particles are also strongly correlated with $\%fuel_D$ (Figure 4.4(d)), similar analysis is also performed for the TD measurement to apportion the non-volatile particle emission factors of LDV and HDDV. I randomly select half of our measurement data to perform the linear regression, and the rest of the data are used to test the quality of the source apportionment. The random sampling are repeated for 3000 times, and the mean value and the standard deviation of results from all 3000 samplings are regarded as the mean value and uncertainty range of the apportioned size-resolved emission factors. Details about the source apportionment methods are further described in section B.3 in Appendix B (Figure B.8 and B.9).

The apportioned size-resolved particle and non-volatile particle emission factors of gasoline (LDV) and diesel (HDDV) vehicles are presented in Figure 4.7, and the data are summarized in Table B.3. For the EF_N of vehicle emitted particles (Figure 4.7(a)), in the size range of 4 – 10 nm, the diesel EF_N in each bin is over one order of magnitude higher than the gasoline EF_N; in the size range of 10 – 550 nm, the diesel EF_N in each bin is about 1 – 7 times higher than the gasoline EF_N. Both gasoline and diesel EF_N-size distributions show one mode at 16 nm. Previous studies [66,98] reported that the relative importance of gasoline vehicles increased with decreasing D_p. I did not see the same trend in our measurements. Our results show that the contribution of diesel vehicles kept increasing as D_p decreased.

For the EF_N of non-volatile particles (Figure 4.7(c)), in all size bins, diesel vehicle emissions are over one order of magnitude higher than gasoline vehicle emissions. The non-volatile particle EF_N size distribution of the diesel vehicles peaks around 5 -7 nm. For gasoline vehicles, the highest number concentration appeared at 4 nm, and it may probably have a mode that is smaller than 4 nm.

For particle EF_M (Figure 4.7(b)) of gasoline and diesel vehicles, both EF_M-size distributions peak at 30 nm. For the non-volatile particle EF_M(Figure 6(d)), both gasoline and diesel vehicle EF_M-size distributions showed only one mode at 150 nm. Similar with the trend of EF_N, the EF_M of diesel vehicles are significantly higher than the gasoline vehicles for both volatile and non-volatile particles.

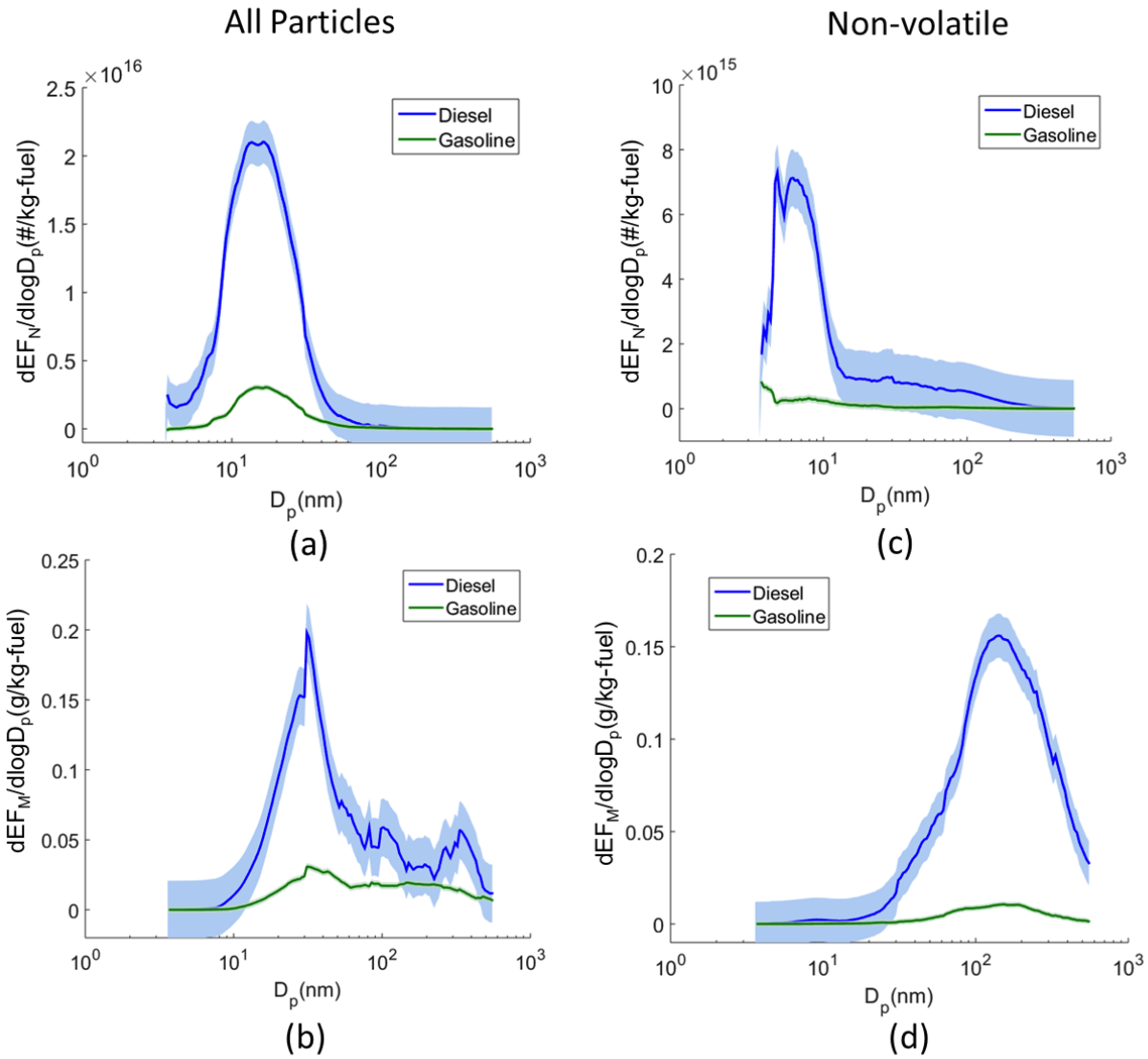

Figure 4.7 Apportioned EF_N and EF_M of vehicle emitted particles and non-volatile particles of gasoline and diesel vehicles. (a) and (b) are emission factors of particles measured through bypass line, and (c) and (d) are emission factors of non-volatile particles measured through TD. Shaded areas represent the uncertainty ranges. The uncertainty ranges of the gasoline emission factors are not visible because of the scale of y-axis.

The integrated EF_N and EF_M of particles and non-volatile particles for both gasoline and diesel vehicles, together with the diesel/gasoline ratio, are summarized in Table 4.1. For both EF_N and EF_M, the diesel/gasoline ratios of vehicle emitted non-volatile particles are about 2-3 times as the diesel/gasoline ratio of vehicle emitted particles, indicating that the importance of gasoline vehicles is relatively higher on contributing volatile particle component, while the importance of diesel vehicles is higher on contributing non-volatile particle component.

4.3.5 Comparison with previous studies

In Figure 4.8 I compare our measured size-resolved EF_N and EF_M of gasoline and diesel vehicles with size-resolved emission factors reported by Ban-Weiss et al. [98]. In order to compare the EF_M, I recalculated the particle volume of Ban-Weiss et al. [98] assuming the EF_N-size distribution they measured is for fractal particles composed of 30 nm primary particles, rather than spherical particles. This assumption is valid since the nanoparticle aggregates correction I used in this study will not significantly change the measured number-size distributions (Figure B.5). I assumed a particle density of 1.2 g/cc to calculate EF_M of Ban-Weiss et al [98].

Figure 4.8 (a) shows that for gasoline vehicles, for 10 – 50 nm particles, our measured EF_N in each size bin are about an order of magnitude higher than Ban-Weiss et al. [98]; EF_N of particles larger than 50 nm measured in this work are similar with Ban-Weiss et al. [98]. The EF_M of gasoline vehicles measured in this work is slightly higher in the size range of 10 - 30 nm and 140 – 290 nm than Ban-Weiss et al (Figure 4.8(b)). [98].

For diesel vehicle emitted particles (Figure 4.8(c)), our measured EF_N is about 5 times larger than Ban-Weiss et al. [98] in the size range of 10 – 40 nm; but for particles with a D_p of 40 -290 nm, our measured EF_N is lower than Ban-Weiss et al. [98] For the EF_M of diesel vehicle emitted particles (Figure 4.8(d)), our measurement at 10-30 nm are slightly higher, while our measurement at 30 -290 nm are over 80% lower than Ban-Weiss et al. [98].

There are several reasons why we observed much higher EF_N of smaller particles (10 – 40 nm) than Ban-Weiss et al. [98]. First, as discussed in the method section, compared

with the long-SMPS, the nano-SMPS is more reliable on measuring particles less than 20 nm, and the particle number concentration measured by nano-SMPS could be up to a factor of 1000 higher than long-SMPS for particles less than 20 nm. Ban-Weiss et al. [98] deployed only a long-SMPS, while in this work we used a nano-SMPS to measure particles smaller than 30 nm. Second, Ban-Weiss et al. [98] conducted the measurement at the tunnel exit, while our measurement was conducted inside the tunnel. The vehicle exhaust sampled in our measurement was less diluted compared with Ban-Weiss et al. [98], and previous studies [105] showed that particle emission factors measured in more diluted conditions would be smaller because of the gas-particle partitioning happened during the dilution. Third, Ban-Weiss et al.[98] conducted measurements in 2006, when effectively zero on-road diesel vehicles were equipped with SCR to reduce NO_x emissions than in 2014. Lehtoranta et al.[101] tested a ship diesel engine and found that the application SCR could potentially increase the emissions of 25-30 nm particles.

The comparison of the integrated EF_N and EF_M for gasoline and diesel vehicles measured in our study with other previous studies is summarized in Table 2. Although our measured EF_N is about 3-5 times larger than reported by Ban-Weiss et al. [98] for both gasoline and diesel vehicles, for gasoline vehicles, our measured EF_N is 77% and 36% lower than it reported by Kittelson et al. [93] and Geller et al. [66], respectively. For diesel vehicles, our measured EF_N is about 7% lower than Kittelson et al. [93]. Kittelson et al. [93] and Geller et al. [66] conducted their measurements in 2006 and 2004, respectively, which are close to the measurement year of Ban-Weiss et al. [98]. Our measured EF_M of diesel vehicles is ~65% lower than Ban-Weiss et al., [98] but our measured EF_M of gasoline vehicles is 2 times as Ban-Weiss et al. [98] However, our measured EF_M of gasoline vehicles is significantly(66%) lower than the $PM_{2.5}$ emission factors of gasoline vehicles measured by Strawa et al. [97] in the tunnel in 2004-2006.

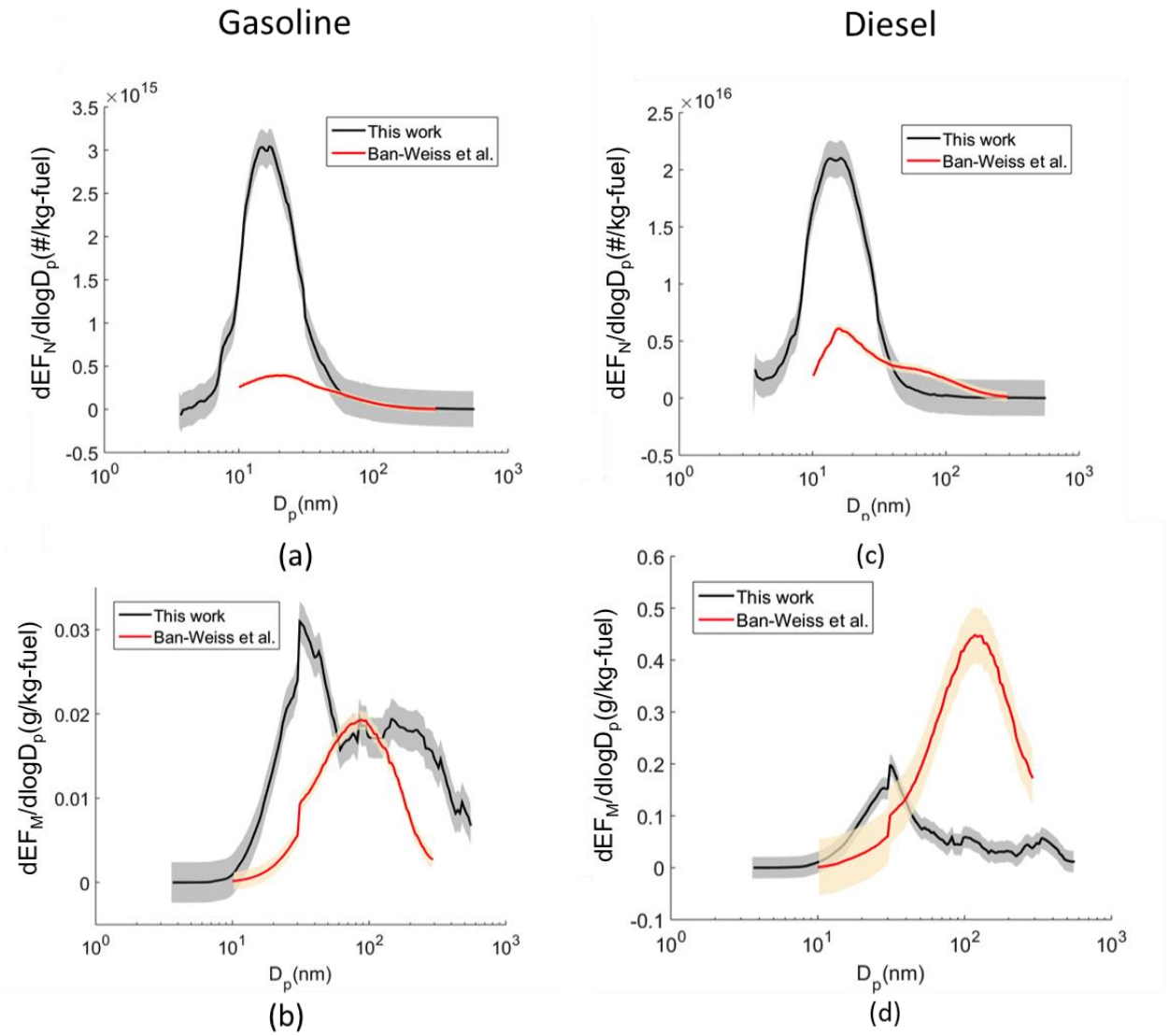

Figure 4.8 Comparison of the size-resolved EF_N and EF_M of gasoline (a and b) and diesel vehicles (c and d) measured in this study and by Ban-Weiss et al. [98].

The diesel/gasoline ratio of the PM emission factors measured in this study and previous studies are also summarized in Table 4.2. The diesel/gasoline ratio for EF_M in this study is much lower than previous studies, indicating that the particle emissions of diesel vehicles decreased much faster than the gasoline vehicles in recent years. It suggests that stricter diesel vehicle emission standards and the deployment of the DPF are effective on regulating particle emissions from diesel vehicles.

4.4 Conclusion

The number-size distribution and mass-size distribution of vehicle emitted particles were measured in a traffic tunnel. I assumed the vehicle emitted particles are nanoparticle aggregates composed of 30 nm spherical primary particles to calculate the size-dependent particle mass, and the particle mass measured by the SMPS was consistent with the particle mass concurrently measured by the OCEC analyzer and the Aethalometer. The number-size distribution of vehicle emitted particles showed only one mode at 16 nm, while the mass-size distribution of vehicle emitted particles showed one mode at ~30 nm, and another one at ~150 nm.

After evaporating under 250 °C inside the TD, the median diameter of the number-size distribution of the vehicle emitted particles shifted from 16 nm to ~7 nm. The total particle number has a significant decrease (69%) after evaporating inside the TD, indicating that the vehicle emitted particles may be largely externally mixed, and a large fraction of vehicle emitted particles may be purely composed of volatile component.

Based on the SMPS-TD measurements, I reported a size-resolved volatile-to-non-volatile-component-ratio for vehicle emitted particles, which could be directly implemented into the TOMAS aerosol microphysics model in GEOS-Chem. Our results show that the non-volatile component takes a large share (over 50%) of the mass of particles in the size range of 60 - 400 nm, while for particles in the size range of 10 – 60 nm, they are dominantly (over 75%) composed of volatile component.

I also apportioned contribution of LDV and HDDV on the particle emissions measured in the tunnel and reported size-resolved particles and non-volatile particles mass and number emission factors for both LDV and HDDV. The HDDV emitted significantly higher (over an order of magnitude higher on number) ultrafine particles and non-volatile particles compared with the LDV. The apportioned LDV and HDDV size-resolved particle emission factors were compared with previous work, and the result indicates that for the number of fine particles (50 - 290nm), the gasoline vehicles emit similar amount compared with 8 years ago, and the diesel vehicles have a lower emission compared with 8 years ago. However, for the number of ultrafine particles (10 – 50 nm), both gasoline and diesel vehicles may have higher emissions compared with

8 years ago. This may potentially pose concerns on the increase of human exposure of ultrafine particles near traffic. As for the EF_M, the diesel vehicles emit about 65% less particle mass than 8 years ago, and the EF_M of gasoline vehicles is still significantly lower (~80%) than the diesel vehicles. Compared with previous studies, the diesel/gasoline ratio of EF_M reported in this work is much lower, indicating that the diesel vehicle emissions decreased more significantly than gasoline vehicles over the past years.

The size-resolved emission factors and the size-resolved volatile-to-non-volatile-ratio of vehicle emitted particles reported in this work can be implemented into the chemical transport model to better estimate the contribution of the vehicle emissions on the total particle burden in the atmosphere, and to better estimate the effect of vehicle primary emissions on climate change. The size-resolved emission factors reported in this work can also be used in the epidemiological models to estimate the human exposure on ultrafine particles. Recently, the increase of the Corporate Average Fuel Economy (CAFE) standards has led to an increased application of gasoline direct-injection (GDI) by the on-road gasoline vehicle. Recent studies showed that the GDI engine could potentially emit more particles and also have a different shape of number-size distribution compared with the port fuel injection (PFI) engine [187,188]. Therefore, it is necessary to continue measuring the size-distribution of particles emitted by on-road vehicles in the future in order to understand how the change of vehicle technologies could potentially influence the contribution of vehicles to the PM in the atmosphere.

Table 4.1 EF_N and EF_M of vehicle emitted particles and non-volatile particles measured in the tunnel

Emission Factor	Particle or Non-volatile particle	LDV	HDDV	Diesel/gasoline ratio
EF_N(#/kg fuel)	Particle	$(1.6\pm0.4)\times10^{15}$	$(1.2\pm0.3)\times10^{16}$	7.5±2.7
	Non-volatile Particle	$(2.4\pm1.6)\times10^{14}$	$(3.5\pm1.1)\times10^{15}$	14.6±10.8
EF_M(g/kg fuel)	Particle	0.02±0.01	0.11±0.06	5.5±4.1
	Non-volatile Particle	0.008±0.003	0.120±0.026	15.0±6.5

Table 4.2 Summary of EF_N and EF_M reported in this study and previous studies

Emission factor	Reference	Size range	Year measured	Type of measurements	LDV	HDDV	Diesel/gasoline ratio
EF_N(#/kg fuel)	This work	3 - 550 nm	2014	Tunnel	$(1.6\pm0.4)\times10^{15}$	$(1.2\pm0.3)\times10_{16}$	7.5±2.7
	Ban-Weiss et al. [98]	10 - 290 nm	2006	Tunnel	$(2.8\pm0.4)\times10^{14}$	$(4\pm1)\times10^{15}$	14±4
	Ban-Weiss et al. [98]	> 3 nm	2006	Tunnel	$(3.9\pm1.4)\times10^{14}$	$(3.3\pm1.3)\times10_{15}$	8±5
	Kittelson et al. [94]	> 3 nm	2006	On-road	7.1×10^{15}	1.3×10^{16}	1.8
	Kirchstetter et al. [207]	> 10 nm	1997	Tunnel	$(2.9\pm0.5)\times10^{14}$	$(7.1\pm3.3)\times10_{15}$	15±8
	Gëller et al. [66]	7 - 270 nm	2004	Tunnel	$(2.5\pm1.4)\times10^{15}$	$(8.2\pm1.5)\times10_{15}$	3.3
EF_M(g/kg fuel)	This work	3 - 550 nm	2014	Tunnel	0.02±0.01	0.11±0.06	5.5±4.1
	Ban-Weiss et al. [98] before correction	10 - 290 nm	2006	Tunnel	0.04±0.01	1.03±0.33	25.8±10.5
	Ban-Weiss et al. [98] after correction	10 - 290 nm	2006	Tunnel	0.01±0.002	0.30±0.10	30.0±11.7
	Strawa et al.[97]	PM2.5	2004-2006	Tunnel	0.07±0.02	1.4±0.3	20
	Gëller et al. [66]	PM2.5	2004	Tunnel	0.067	1.015	15.1

a. The correction here refers to the nanoparticle aggregates correction.

Chapter 5

Gas-particle partitioning of vehicle emitted primary organic aerosol measured in a traffic tunnel[1]

[1]Published as Li, X., Dallmann, T. R., May, A. A., Tkacik, D. S., Lambe, A. T., Jayne, J. T., Croteau, P. L., and Presto, A. A., 2016, "Gas-Particle Partitioning of Vehicle Emitted Primary Organic Aerosol Measured in a Traffic Tunnel," Environ. Sci. Technol., **50**(22), pp. 12146–12155.

5.1 Introduction

Gasoline and diesel vehicles are a significant source of ambient fine particulate matter (PM) [24,48,85]. Vehicle emitted PM mainly consists of elemental carbon (EC) and primary organic aerosol (POA) [53,82–84]. Traditionally, chemical transport models treated POA as non-volatile, which contributed to a discrepancy between modeled and measured PM mass [103,104]. We know now that a substantial fraction of POA from combustion exhaust is semivolatile [105–114] and actively partitions between the vapor and condensed phases. Accurate accounting of POA mass therefore requires knowledge of both the emission rate of condensable material and the volatility of the emissions.

Gas-particle partitioning of POA is a sorption process. Organics in the gas phase partition into the particle phase either by absorbing into the organic condensed phase or adsorbing onto nonvolatile, often EC, cores. Whether absorption or adsorption is the dominant mechanism depends on the relative abundance of organic carbon (OC) and EC.[208] Absorption dominates under most atmospheric conditions.[209,210] The fraction of organic mass in the particle phase can be calculated as:[211,212]

$$X_p = \sum_i f_i \left(1 + \frac{C_i^*(T)}{C_{OA}}\right)^{-1} \quad (1)$$

Where X_p is the fraction of organic mass in the particle phase; f_i is the fraction of species *i* among total organics (particle + gas phase); $C_i^*(T)$ is the effective saturation concentration of species *i* at temperature T; and C_{OA} is the mass concentration of organic aerosol (OA). The emission factor of the POA can be determined by:[213]

$$\mathrm{EF_{OA}} = X_p \cdot \mathrm{EF}_{tot} \quad (2)$$

Where EF_{tot} is the emission factor of total organics (particle + gas phase); and $\mathrm{EF_{OA}}$ is the emission factor of the POA.

Determining X_p requires knowing f_i and $C_i^*(T)$ of all species in the POA. However, no measurement techniques can fully speciate POA.[53,118] Therefore equation (1) is often applied semi empirically using a set of surrogate compounds.[105,112–114,118,212,214] This set of surrogate compounds can be presented with the one-dimensional volatility basis set,[212] which spreads the semivolatile organics over a logarithmically spaced set of C* bins. The set of f_i is the volatility distribution. Several studies have used the volatility basis set to simulate semivolatile POA in chemical transport models (CTMs), [119,215,216] and improve model-measurement agreement.[105]

Numerous studies have investigated gas-particle partitioning of vehicle emitted POA through both field measurements and laboratory studies [84,113–118], but very few studies provide a volatility distribution. Among those studies [113–115,118] that provide POA volatility distributions, conflict of opinion still exists on whether a single volatility distribution can be used to describe the POA gas-particle partitioning of all vehicles. Besides, no studies have been published to demonstrate whether laboratory-derived POA volatility distributions [113–115] can be applied to describe POA gas-particle partitioning of a larger mixed vehicle fleet operating under real-world driving conditions.

In this work we measured the gas-particle partitioning of POA in a traffic tunnel with three independent methods: 1) a thermodenuder (TD), 2) quartz filter sets analyzed by thermal-optical OCEC and 3) analysis of quartz filters with thermal desorption gas chromatography mass spectrometry (TD-GC-MS) to determine volatility distributions. This chapter is intended to show that POA emitted from a large and real-world driving fleet is semivolatile under a wide range of ambient conditions, the POA volatility distribution derived from the dynamometer studies can be applied to explain gas-particle partitioning of ambient POA, and that gas-particle partitioning of the POA measured in the traffic tunnel does not have large diurnal or seasonal variations.

5.2 Methods

5.2.1 Measurement of POA volatility

The Fort Pitt Tunnel, traffic conditions in the tunnel, and air quality measurement stations are described in section 2.1. The results presented in this chapter focus on two time periods. The spring measurement was conducted in May 2013 together with the work presented in Tkacik et al. [50] During this period an Aerosol Chemical Speciation Monitor (ACSM, Aerodyne Research Inc.) [217] measured non-refractory particle phase organic aerosol mass. The time resolution of ACSM is typically 15-30 min but was operated here at 1-min resolution due to high organic aerosol concentrations in the tunnel. A thermodenuder (TD) [218] was also deployed to study the POA gas-particle partitioning under different temperatures. We continuously measured CO_2, CO, and NO_x concentrations. Particulate OC and EC were measured with a semi-continuous OC/EC analyzer (Model 4F, Sunset Laboratory Inc.).

Winter measurements were conducted during January and February 2014. In addition to measuring CO_2, CO, NO_x, OC, and EC, we collected quartz filter sets and analyzed them offline with a Sunset OCEC analyzer (Model 3) and the TD-GC-MS, described in section 5.2.3. All the NO_x and CO data used in this manuscript are subtracted for ambient background to show only the enhancement caused by the vehicles inside the tunnel.

5.2.2 Thermodenuder (TD)

The TD used in this study is the same as the one used in May et al. [113,114] and a detailed description of the instrument can be found there. The TD uses high temperatures to drive the gas-particle partitioning of OA. It consists of a stainless steel heating section (2.7 cm ID x 65 cm L) followed by an activated carbon filled stripper/denuder. The flowrate inside the TD was 4.2 SLPM and the centerline residence time in the heating section was 5.3 seconds at 298 K. Tunnel air was alternately sampled through the TD and an ambient temperature bypass line.

I present the TD data using the mass fraction remaining (MFR):

$$MFR = \frac{C_{TD}}{C_{\text{bypass}}} \quad (3)$$

C_{TD} is the OA concentration measured downstream of the TD by the ACSM. C_{bypass} is the OA concentration measured through the unheated bypass line. The MFR represents the fraction of OA that survived the high temperature inside the TD. In this work the TD was operated at a series of fixed temperatures (25, 40, 60, 100, 150 °C; Figure C.1 and section C.1). I define one TD scan as the time period when the TD temperature increased from 25 ºC to 150 ºC.

As discussed in Ng et al. [217] the collection efficiency (CE) of the ACSM is similar with the CE of the Aerosol Mass Spectrometer (AMS). Following previous AMS measurements [113,117] I assume unity CE for OA measured by the ACSM. Particle number loss inside the TD is discussed in section C.2 (Figure C.2).

OA partitioning does not necessarily reach thermodynamic equilibrium in thermodenuders with short residence time, such as the one used here [219,220]. I used the mass transfer model of Riipinen et al. [219] to compare our TD measurements to predictions of OA evaporation using volatility distributions derived in previous dynamometer and tunnel studies. The TD model does not explicitly include other processes such as nucleation, chemical reaction, or condensation. Inputs to the model include the TD dimensions and temperature, the volatility distribution of POA, the OA concentrations (C_{OA}) and particle mass-median diameter (d_p), and the mass accommodation coefficient (α). I used an accommodation coefficient of 1.[221] A full description of parameters used in the model is summarized in section C.3, Table C.1, and Table C.2.

5.2.3 Quartz filter sets

During the winter measurement we simultaneously sampled tunnel air onto a bare-quartz filter (bare-Q) and a quartz-behind-Teflon filter (QBT). Quartz filters were 47-mm Tissuquartz (2500QAT-UP, Pall Corp.). Teflon filters were 47-mm Teflon membranes

(Pall Corp). The majority (15 out of 18) of the quartz filter sets were collected during weekdays; the remainder were collected on weekends. Filters were collected either during midday (12:00 – 14:00) or in the afternoon rush hour (15:00 – 18:00). During these time periods conditions in the tunnel crossed a wide range: the ambient temperature in the tunnel (same as the filter sampling temperature) ranged from -2 to 6 °C; and the $\%\,fuel_D$ ranged from 2% to 9%.

Sample flow rates were 46 SLPM. Two sharp cut $PM_{2.5}$ cyclones were placed upstream of filters. Fourteen out of 18 filter sets were sampled for 45 min and another 4 were sampled for 90 min. Before sampling all quartz filters were baked at 550 °C overnight to remove all residual organics. All quartz filter samples were kept in a freezer at -18 °C prior to analysis.

We also collected 2 sets of handling blanks in the tunnel. For both bare-Q and QBT, the handling blank represents about 4% of the OC collected onto the filter (Section C.4 and Figure C.3). Therefore, I did not correct quartz filter OC concentrations for handling blanks.

Quartz filters were analyzed using a Sunset Laboratories OCEC Aerosol Analyzer (Model 3) following the IMPROVE-A protocol [170]. OC and EC are defined as the carbon that is thermally desorbed up to 550 ºC in a helium atmosphere and 550 ºC – 800 ºC in a helium-oxygen atmosphere, respectively; both are corrected for pyrolyzed OC.[170] I assume the bare-Q filter captures both particle phase organics and absorbed organic vapors, which is considered the positive artifact. This positive artifact is quantified by the QBT filter, which is assumed to only absorb gas phase organics [167,171]. Therefore, the particle phase OC concentration can be derived from the artifact-corrected bare-Q (bare-Q minus QBT). The particle phase fraction of organics (X_p) can be determined by:

$$X_p = \frac{bare\text{-}Q - QBT}{bare\text{-}Q} \quad (4)$$

In this work I assume an organic-mass-to-organic-carbon ratio of 1.2 to convert OC into OA [222].

Quartz filters were also analyzed by the TD-GC-MS. It has a thermal extraction and injection system (Gerstel, Inc) followed with a gas chromatograph / mass spectrometer (GC/MS, Agilent 6891 GC / 5975 MS). OC collected onto the quartz filter was thermally desorbed inside the Gerstel desorption unit (TDS3); then it is concentrated at -120 °C by the Gerstel cooled injection system (CIS4); and finally the concentrated sample was thermally injected into GC/MS for anaylsis.

Volatility distributions were determined from TD-GC-MS analysis of 18 bare-Q filters following the method of Presto et al. [112]. The mass fragment (*m/z*) 57 is used to derive the POA volatility distribution. The relative abundance of *m/z* 57 signal in the total organics was not strongly affected by the $\%\,fuel_D$ and the OC concentrations in the tunnel (Section C.4 and Figure S6). Therefore, the POA volatility distribution determined from *m/z* 57 is not strongly influenced by the dilution of OA in the tunnel. The method uses a set of surrogate compounds (C_{15}-C_{40} n-alkanes) to develop a relationship between C* (10^{-2} – 10^{6} μg/m^3) and the GC retention time. The set of f_i are calculated using the fraction of the total *m/z* 57 signal in each of a series of logarithmically spaced C* bins. The *m/z* 57 signal in each volatility bin was corrected with the recovery of a set of deuterated standards (C_{16}-C_{36} n-alkanes).

5.3 Result and discussion

5.3.1 Quartz filter measurements

OC/EC analysis of quartz filter samples shows that there is substantial organic mass present in both the condensed and vapor phases. Organic concentrations from all quartz filter samples (C_Q) are shown as the total bar height in Figure 5.1(a). C_Q measured in the tunnel ranges from 8 to 38 μg/m^3.

C_Q shown in Figure 5.1(a) are not corrected for ambient background concentrations. Thus while I expect the filter samples to be dominated by fresh emissions, as shown by the ACSM data in Figure 5.2, there are likely contributions from background OA as well. On weekdays the C_Q were roughly two times higher than the C_Q on the weekends. C_Q

measured at midday (12:00 -14:00) and during the afternoon rush hour (15:00 – 18:00) do not exhibit a large difference on weekdays.

The positive artifact (organic vapors) measured by QBT filters are shown as open areas of the bars in Figure 5.1(a). Artifact corrected particle phase OA concentration (bare-Q minus QBT) are shown as filled areas of bars. The particle phase fractions of organics (X_p) are shown in the lower panel of Figure 5.1(a). X_p in the tunnel ranged from 40 – 60% and on average about half of the organics collected onto the bare-Q filter are organic vapors.

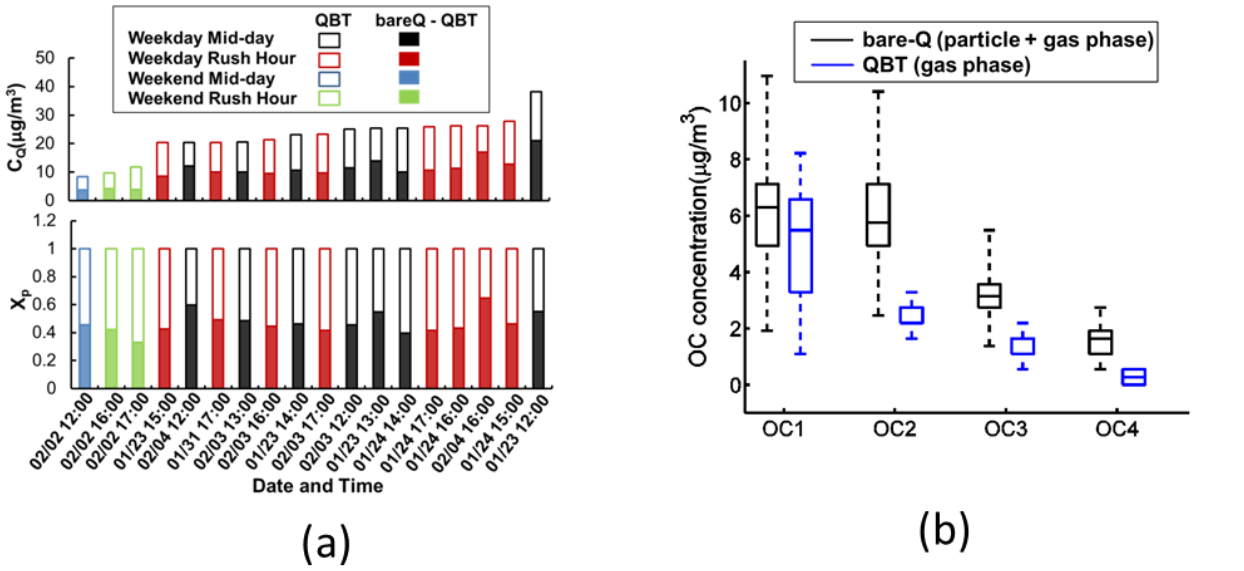

Figure 5.1 a) Organic concentrations (C_Q) and organic particle phase mass fraction (X_p) determined from quartz filter samples. Organic concentrations are sorted from the lowest to the highest C_Q. Data are colored based on the sampling periods. Filled areas represent the particle phase organics (bareQ-QBT) and open areas represent the gas phase organics (QBT). All C_Q are OC concentrations multiplied by an organic-mass-to-organic-carbon ratio of 1.2. b) Box-whisker plot of OC concentrations desorbed at different temperature stages during the OCEC analysis. OC1- OC4 represent OC desorbed at 140 °C, 280 °C, 480 °C and 580 °C, respectively. Results from bare-Q and QBT filters are in black and blue, respectively. The ends of the box represent the first and third quartiles. The center line inside the box is the median. The length of the whiskers covers 99.3 percent assuming the data are normally distributed. For OC2 and OC3 measured from QBT filters the median values overlap with the 25th percentile.

Figure 5.1(b) presents concentrations of OC (μg/m^3) evolved in different temperature stages of the OCEC analysis. Using the IMPROVE-A OC analysis protocol, the desorption temperature of the sample in a Helium environment gradually increases from 140 °C to 560 °C. OC1 – OC4 represent the OC evolved from the lowest to the highest temperature stages. Ma et al. [223] recently showed that OC1-OC4 can be linked to volatility, with higher volatility organics evaporating at lower temperature.

Results for both bare-Q (vapor plus particle) and QBT (vapors only) filters in Figure 5.1(b) show organic mass spread across all OC temperature stages. Organic material captured by the QBT filters (mostly vapor) is clearly more volatile than organics captured on the bare-Q filters (vapor plus particle). The majority (80%) of the vapor phase organics collected onto QBT filters are more volatile OC1 and OC2, whereas 40% of the artifact-corrected particle phase organics (bare-Q minus QBT) consists of less volatile OC3 and OC4.

About 10% and 50% of the OC1 and OC2 mass on the bare-Q filters, respectively, exists in the particle phase. Even for the least volatile OC4 there is still a small fraction (10-20%) present in the vapor phase. The OC/EC analysis indicates that organic mass evolving across the range of OC/EC temperature stages readily partitions between the vapor and condensed phases. Therefore the quartz filters suggest that POA sampled in the tunnel is semivolatile.

5.3.2 Direct measurements of gas-particle partitioning: Thermodenuder data

The analysis of quartz filters presented in the previous section lacks chemical specificity, and cannot directly separate fresh emissions from background organic aerosol that may enter the tunnel. Our analysis assumes that OA in the tunnel is dominated by fresh POA, but is ultimately indirect. In this section, I use ACSM data to more rigorously separate fresh POA from aged background aerosol. The time series of OA concentration measured in the bypass line by the ACSM is shown in Figure 5.2; the TD data are excluded.

I separated the measured OA into two components, Hydrocarbon-like Organic Aerosol (HOA) and Oxygenated Organic Aerosol (OOA), using the principle component analysis

of Zhang et al. [224]. This method uses the fraction of OA mass at *m/z* 57 (f_{57}) to apportion HOA and the mass fraction at *m/z* 44 (f_{44}) to apportion OOA. HOA is indicative of fresh emissions, such as POA, [225] and OOA is representative of more aged, regional OA.[226] Since vehicles are the only emission source in the traffic tunnel, the HOA measured in the tunnel is a good surrogate for vehicle-emitted POA. The POA mass spectrum measured in the tunnel is highly similar with the HOA mass spectrum measured by the AMS [224] (Figure C.6). HOA has a stronger correlation with background corrected CO and NO_x concentrations (Figure C.7), which are indicators of gasoline and diesel vehicle volume in the tunnel, than OOA.[52]

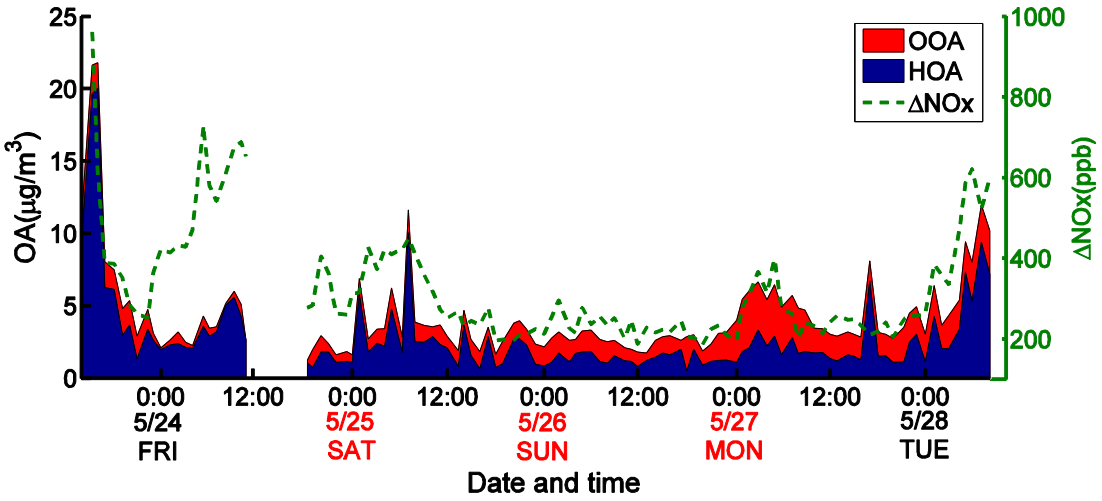

Figure 5.2 Organic aerosol (OA) time series measured by the Aerosol Chemical Speciation Monitor (ACSM). OA has been classified into Hydrocarbon-like Organic Aerosol (HOA, blue areas) and Oxygenated Organic Aerosol (OOA, red areas). The background corrected NO_x data (green dash line) are also presented. All data in the figure are 1-hour averages. The dates colored with red were weekends. The Monday during the sampling period was the Memorial Day holiday so I considered it as a weekend day here.

The trend of OA concentration generally follows the background corrected NO_x concentration.[52] The average OA concentration was higher on weekdays compared with weekends, and the weekend OA time series shows less variation than weekdays. The OA time series showed high peaks around midday and during the afternoon rush hour during weekdays. On weekends a single, smaller OA peak was observed during the early morning hours. These weekday/weekend patterns were also observed over

longer time periods in the semi-continuous OC/EC measurements (Figure C.5). During weekday daylight hours HOA accounted for 70-90% of total OA mass. In both absolute concentration and as a fraction of total OA mass, HOA peaked during the weekday midday and afternoon rush hour periods (>80% OA mass). This high HOA fraction indicates that the majority of the sampled OA on weekdays was POA from vehicle fresh emissions rather than the OA from the background air.

The HOA fraction on weekends was lower than on weekdays. During the weekend HOA made up 30-80% of the total OA, with higher contributions (60-80%) when OA was elevated during morning hours on Saturday. During Sunday and Monday when the OA concentration was low (~3-6 μg m^{-3}) the HOA fraction was approximately 30-40%. In order to assure that gas-particle partitioning results focus on vehicle emitted POA rather than the OA from the background air, our analysis of TD data focuses only on the HOA fraction.

The effect of temperature on the gas-particle partitioning of HOA is shown in Figure 5.3. All TD measurements are presented using box-whisker plots. The median HOA MFR is close to unity when the TD is held near ambient temperature (25 °C). MFR values greater than unity may exist due to temporal variability between samples collected through the TD and the bypass line. When the TD was heated up to higher temperature (40-60 °C) the median HOA MFR dropped to 70-80%, indicating that about 20-30% of the POA evaporated with mild heating. About half of the HOA evaporated when the TD temperature reached 80-90 °C. When the TD temperature reached highest stages (100-150 °C) about 80-85% of the POA evaporated. The trend of median HOA MFRs clearly show that the HOA MFR decreases as the TD temperature increases, indicating that the POA is semivolatile and evaporates upon heating.

The change of the MFR as a function of TD temperature is not linear. The MFR drops quickly for TD temperatures between 25 °C and 100 °C. However when the TD temperature is higher than 100 °C the MFR levels off. From 100 °C to 150 °C the HOA MFR changed from 0.25 to about 0.15. This reduction in the slope under conditions of higher TD temperature and low MFR is commonly observed.[108,109,113,114,202,227] Incomplete evaporation at high TD temperatures (>100 °C) is often explained by a

transition from a purely absorptive environment to one where organics are adsorbed to soot cores.[112–114] Adsorption incurs an additional enthalpy,[211] the enthalpy of adsorption, in addition to enthalpy of vaporization, and this additional enthalpy is often invoked to explain the incomplete evaporation at high TD temperatures.

Adsorption is expected to be important for OC:EC ratio <2.[208] The OC:EC ratio we measured in the unperturbed bypass line is 1.9 ± 0.4 (Figure C.5). This suggests that adsorption should be important under all TD temperatures sampled here, and further implies that adsorption alone cannot explain the small decrease in MFR between 100 and 150 °C.

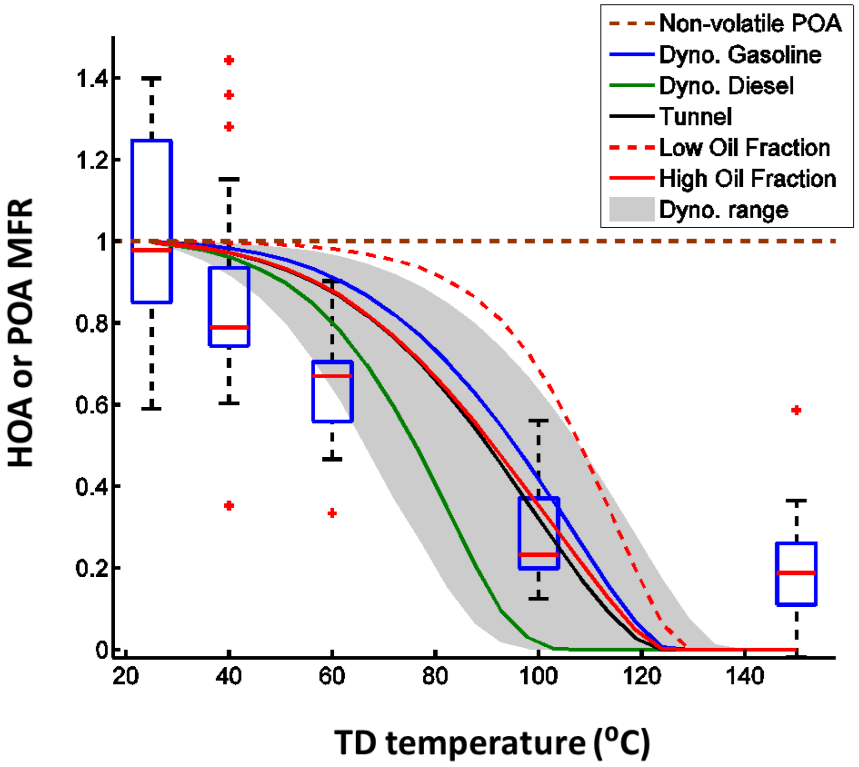

Figure 5.3 Thermodenuder (TD) measurements of the HOA mass fraction remaining (MFR) as a function of TD temperature. I use the box-whisker plot to present tunnel measurements. Each box represents the HOA MFR measured under a certain TD temperature stage. The length of the whiskers covers 99.3 percent assuming the data are normally distributed. Data outside of this range are considered as outliers, which are presented with red crosses. Brown dash line shows the HOA MFR under non-volatile POA assumption. Blue lines and green lines are the TD model results based on the gasoline and the diesel POA volatility distributions measured during the dynamometer testing [113,114]. The black line is the modeled HOA MFR based on the volatility distribution measured in this tunnel study. Red lines are modeled HOA MFR based on the parameterization from Kuwayama et al. [115]. The solid red line represents the higher motor oil fraction case while the dashed red line represents the lower motor oil fraction case. All lines

in the figure are simulations based on median volatility distribution, averaged OA concentration (C_{OA}) and averaged particle mass-median diameter (d_p). The shaded region represents the variation of modeled MFR caused by the variation of both gasoline and diesel volatility distributions and the variations of the C_{OA} and the d_p in the tunnel.

An alternative explanation for non-zero MFR at high TD temperature is the presence of material with extremely low volatility ($C^* \leq 10^{-3}$ μg m^{-3}). Cappa [228] modeled the evaporation of multi-component aerosol with compounds having C* ranging from 10^{-3} to 10^3 ug/m^3 and found that about 10% of organics remained in the particle phase at a TD temperature of 200 °C. Gkatzelis et al. [229] heated ambient particles up to 400 °C inside a TD and found that some fraction of combustion-generated OA still remained in the particle phase, which they explained as extremely low volatile organics. To first order, the observed median MFR of 0.15 at 150 °C (MFR reached zero in less than 10% of all measurements at 150 °C) indicates that fresh exhaust may contain up to 15% nonvolatile or extremely low volatility organic material.

5.3.3 Volatility distributions from TD-GC-MS

Results from the TD-GC-MS show another piece of evidence that the majority of the vehicle emitted POA measured in the traffic tunnel was semivolatile. I classified all organics collected onto the bare-Q filter into logarithmically spaced C* bins ranging from 10^{-2} to 10^6 μg m^{-3}.The organic mass fraction (f_i) in each C* bin is shown in Figure 5.4 (data are in Table C.3). Box-whisker plots are used to show the variability of measured f_i within each C* bin.

Figure 5.1 showed that the total organics loading on all bare-Q filters (C_Q) covered a range of 8 - 38 μg/m^3. The variations in the TD-GC-MS derived volatility distributions are much smaller than the variation of the C_Q. Figure 5.4 shows that within each C* bin the interquartile range is generally less than a factor of 2. The coefficient of variation for the C* bins ranges from 13% to 59%. The variation of the POA volatility distributions is also less than the diurnal variation of the $\%\,fuel_D$ (2-9%). Thus Figure 5.4 suggests that the volatility distribution under different $\%\,fuel_D$ may not be significantly different.

The median volatility distribution in Figure 5.4 shows that 49% of the organic mass collected onto bare-Q filters in the tunnel consists of semivolatile organic compounds (SVOC, $10^{-1} \leq C^* \leq 10^2$ μg/m^3). The mass distribution peaks in the SVOC range, specifically the C* = 10 and 100 μg/m^3 bins. SVOC exist in both particle and vapor phase in the atmosphere. Intermediate-volatile organic compounds (IVOC, $10^2 \leq C^* \leq 10^6$ μg/m^3) contribute about 37% of the total organic mass measured on bare-Q filters. IVOC only exist as vapors in the atmosphere. Only about 12% of organics measured on bare-Q filters consist of low volatility organic compounds (LVOC, $10^{-3} \leq C^* \leq 10^{-1}$ μg/m^3). LVOCs exist almost entirely in the particle phase in the atmosphere.

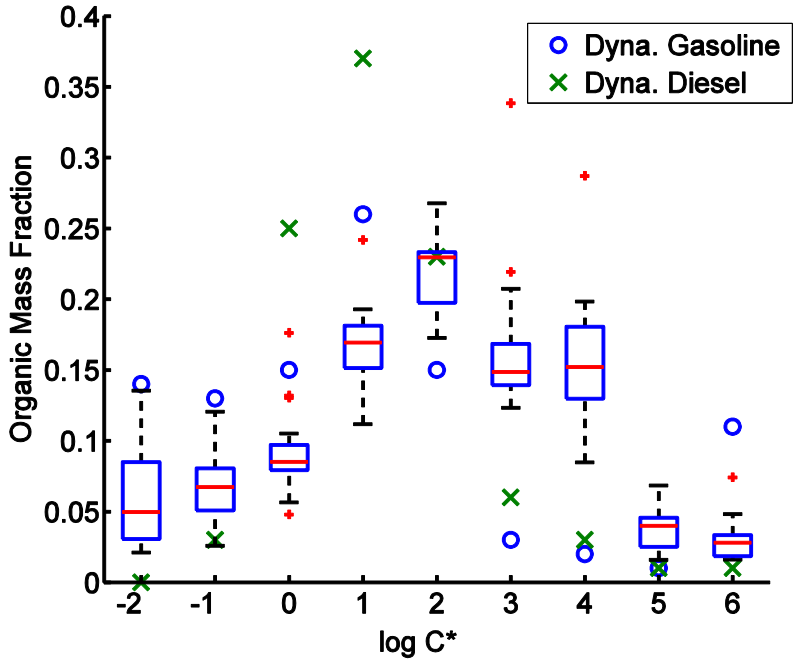

Figure 5.4 The volatility distribution derived from all bare-Q filters. Each box-whisker represents organic mass fractions (f_i) measured from all bare-Q filters in each C* bin. The center line is the median, and the top and bottom of the box are 25th and 75th percentile, respectively. The blue and green symbols represent the gasoline and the diesel POA volatility distributions, respectively, from dynamometer studies of May et al.[22,23] The upper and lower ranges of f_i considering the propagated uncertainties are presented in Figure S13 and are not shown here.

In Figure 5.4 I directly compare tunnel volatility distributions to median POA volatility distributions of gasoline (blue circles) and diesel vehicles (green crosses) measured in dynamometer studies by May et al. [113,114] The volatility distributions reported by May

et al [113,114] were determined using the same TD-GC-MS analysis of bare-Q filters as we used here. Overall there is good agreement between the volatility distributions obtained in the tunnel and the dynamometer tests. The f_i in all three volatility distributions peak in the SVOC region and gradually decreased towards lower and higher C*. Volatility distributions from both tunnel and dynamometer study suggest that the majority (60-80%) of the POA mass is SVOC.

A major difference between the tunnel- and dynamometer-derived volatility distributions is the contribution of IVOCs. Dynamometer studies show that IVOC contributed 17% of gasoline vehicle POA and 11% of diesel vehicle POA, which are 54-70% lower than the tunnel samples.

IVOC exist almost exclusively as vapors in both the atmosphere and in source tests.[212,230,231] Quartz filters capture IVOC vapors, but with less than 100% efficiency.[231] I expect that the collection efficiency of IVOCs onto quartz filters depends at least in part on the sampling temperature. In May et al. [113,114], all quartz filters were collected at 47 °C. Filters collected in this study were collected between -2 °C and 6 °C. The lower sampling temperature in the traffic tunnel made IVOC collection onto quartz filters more efficient.

While the tunnel- and dynamometer-derived volatility distributions differ in the fraction of mass attributable to IVOCs, this difference should have a minor impact on predicted partitioning. I predicted the particle phase fraction (X_p) using all volatility distributions measured in the dynamometer studies and in the tunnel (Figure C.8). Under tunnel conditions and most ambient conditions the X_p predicted by tunnel and dynamometer volatility distributions agree within 20-25%.

5.3.4 Predictions of gas-particle partitioning

I used the TD data, measured volatility distributions, and the TD model of Riipinen et al. [219] to evaluate the ability of different volatility distributions to describe observed POA evaporation in the TD. Figure 5.3 shows the modeled POA MFR as a function of TD temperature for gasoline and diesel vehicles, using the median volatility distributions of May et al. [113,114] and the C_{OA} and d_p during all the TD scans in the tunnel. I also

simulated each TD scan separately using the highest, lowest, and median volatility distributions to provide a full range of TD model predictions (Figure C.9). This range shows the influence of the varied C_{OA}, d_p and volatility distributions on the predictions of TD MFR. The combined range of MFR predictions using both gasoline and diesel volatility distributions from dynamometer studies of May et al. [113,114] is presented as the shaded area in Figure 5.3.

The MFR predicted using median volatility distributions generally captured the trend of the HOA evaporation when the TD temperature was less than 100 °C. The median value of the measured HOA MFR at 25 °C and 100 °C are well predicted, and the median HOA MFR at 40 °C falls into the prediction range. However for TD temperature of 60 °C, MFR is overpredicted, and lies near the 90th percentile of observed MFR.

The volatility distributions of May et al. [113,114] predict complete evaporation of OA between 100 °C (diesel) and 125 °C (gasoline), and therefore predict more evaporation than observed. As noted above, the discrepancy between modeled and observed MFR at high temperatures may indicate processes not explicitly included in the model (e.g., adsorption or chemical reactions), or the presence of extremely low volatility material not quantified by the TD-GC-MS method used to determine volatility distributions.

I also modeled MFR using the median volatility distribution derived from the tunnel bare-Q samples and the average C_{OA} and d_p during all TD scans. It is shown as the black solid line in Figure 5.3. The median tunnel prediction falls between the median gasoline and diesel lines from May et al. [113,114] and is closer to the gasoline line. The fact that the median tunnel MFR prediction falls into the range of median dynamometer MFR predictions provides another piece of evidence that the POA volatility distribution measured in the dynamometer studies can adequately describe the gas-particle partitioning of POA in the tunnel. A full range of TD MFR predictions based on the volatility distributions measured in the tunnel is provided in Figure C.9.

Neither the tunnel-derived nor dynamometer-derived volatility distributions perfectly describe the observed TD MFR. However, the modeled HOA MFRs using volatility distributions are better at predicting the trend of TD measurements than the non-volatile

POA assumption (brown dashed line in Figure 5.3), which equals unity under all TD temperatures.

One possible reason for the discrepancy between modeled and observed MFR at high TD temperature may be the presence of additional low volatility material not quantified here. Kuwayama et al. [115] presented a dual volatility distribution reflecting contributions from more-volatile lubricating oil POA and less-volatile ($C^* = 10^{-2}$ and 10^{-3} $\mu g/m^3$) combustion derived POA. I use this two-component volatility distribution to test the sensitivity of predicted MFR to the presence of additional low volatility material.

I modeled MFR using the Kuwayama et al. [115] volatility distribution for two bounding cases of the oil POA fraction: 86% and 24% by mass (Figure 5.3). The 86% motor oil case is nearly identical to the tunnel case, except for temperatures from 100 -120 °C. At this high temperature range the additional low volatility mass in the Kuwayama et al. [115] combustion derived POA leads to a higher predicted MFR than the tunnel volatility distribution. The POA from the 86% oil case is predicted to evaporate completely by 125 °C, and therefore underpredicts the observed MFR at 150 °C.

The 24% oil POA case is worse at describing the observed MFR data. The increased contribution of low-volatility combustion derived POA increases MFR at TD temperatures below 100 °C. The predicted MFR for this case remains above 0.9 until approximately 90 °C, and 50% evaporation is predicted at T > 110 °C. The POA in the 24% oil case is predicted to evaporate completely at T = 130 °C, and therefore does not describe the observed MFR at T = 150 °C. Agreement at the highest TD temperatures could be improved if the combustion POA consisted of even lower volatility material (e.g., $C^* < 10^{-3}$ $\mu g/m^3$), but would still over predict MFR at nearly all lower temperatures.

This suggests that the vehicle emitted POA in the traffic tunnel is more likely dominated by the motor oil POA rather than the low-volatile fuel-combustion POA.

I also tested the sensitivity of predicted MFR to the presence of additional high volatility material by comparing the TD MFR predictions using the volatility distributions from Zhao et al. [230,231] Zhao et al expanded the volatility distributions of May et al. [113,114] to include IVOCs. The addition of IVOCs to the volatility distribution is expected to have little impact on predicted partitioning, as IVOCs exist as vapors under

all but the most concentrated conditions. As shown in Figure C.10, this is the case. The MFR predictions based on Zhao et al. [230,231] are either within the range or slightly lower than the predictions of May et al. [113,114].

5.3.5 Temporal variations in POA volatilty

The data presented here allow us to investigate variations in POA volatility over daily and seasonal time scales. The data and modeling presented in Figure 5.3 suggest that POA composition and volatility do not show a large seasonal variation. The quartz filters used to determine the volatility distributions were collected in winter at ambient temperatures below 6 °C. The TD data were collected during the spring, when ambient temperatures were approximately 20 °C. As shown in Figure C.9 and Figure 5.3, there is reasonable agreement between the TD data, the predicted MFR based on our filters collected in the winter, and predicted MFR from filters collected by May et al. [113,114] in a temperature-controlled dynamometer.

The composition of the vehicle fleet in the tunnel changes over the course of each day. As shown in Figure 5.4, variation of the volatility distribution derived from the TD-GC-MS is much less than the diurnal variation of $\%fuel_D$.This suggests that POA emissions from gasoline and diesel vehicles have similar volatility, and may have similar composition.

I can also use the TD to investigate sub-daily variations in POA partitioning and volatility. In Figure 5.5 I separated all measured TD MFR in the tunnel into 4 different time periods: high-traffic daytime periods and overnight on either weekdays or weekends. The $\%fuel_D$ ranged from 5% -20% and the $\%fuel_D$ in the high-traffic time is roughly 60% lower than overnight. Results show the same trend in MFR for each of the four time periods. Quantitatively, the mean MFRs at each temperature agree within 20%, and there is significant overlap (error bars indicate the standard deviation of MFR). I compared time-temperature MFR pairs with the Mann-Whitney U-test (Table C.5) and found that the majority (25 out of 30) of sample pairs are not statistically different. Exceptions occurred at 25 and 150 °C. The results in Figure 5.5 therefore

indicate that variations in MFR between time periods are smaller than variations within a given time period.

The variations of MFR can be influenced by C_{OA}, d_p and the POA volatility distribution in the tunnel. I modeled the TD MFR using the median volatility distribution measured in the tunnel and the average C_{OA} and d_p of each different time period, and I compared the variation of modeled TD MFR with the variation of average measured TD MFR in different time periods (Table C.7-1 and Table C.7-2). The result suggests that compared with the POA volatility distribution, the variations of C_{OA} and d_p have a minor impact on the TD MFR. Therefore, the limited temporal variation of MFR further suggests that there are not substantial diurnal changes in POA volatility.

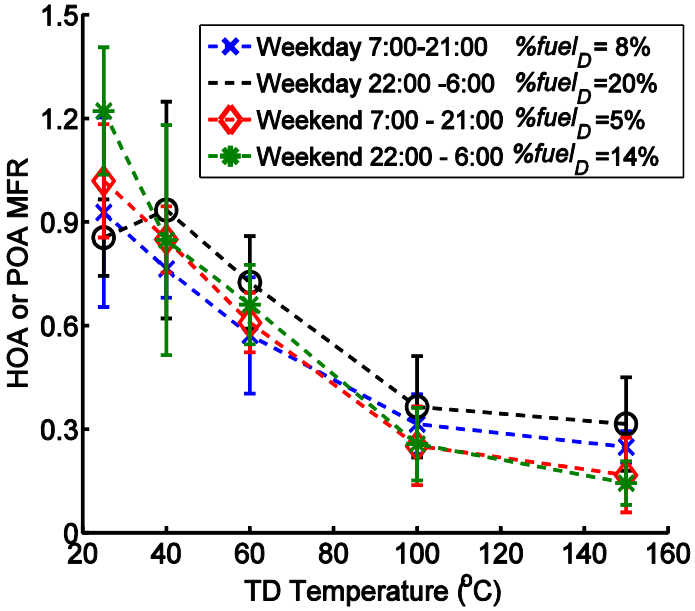

Figure 5.5 Thermodenuder measurements of HOA evaporation in different time periods with different HDDV fuel fractions. Colors indicate different time periods. Bars represent standard deviation of all measurements under a certain TD temperature and time period.

Quartz filters cannot capture all gas phase organics in the atmosphere. Thus our discussion on the temporal variation of POA volatility regards only the material collected onto the quartz filter under tunnel ambient conditions. For those gas phase organics that have not been collected onto the quartz filter, I quantify neither the temporal variability nor the contribution to total organic emissions. I therefore do not know how those gas

phase organics that broke through the bare-Q filter would influence the POA volatility distribution. However, as these vapors are expected to be IVOCs or more volatile, their impact on partitioning should be minimal.

5.4 Conclusion

Data from three independent methods all indicate that a significant portion of the vehicle emitted POA is semivolatile and actively partitions between the vapor and condensed phases. The results presented here also indicate that the volatility distributions for gasoline and diesel vehicles determined in a dynamometer setting adequately describe observed partitioning in the tunnel, and that POA partitioning in the ambient atmosphere can be described by a single volatility distribution.

Our results further suggest that lubricating oil is the major component of vehicular POA, echoing the results of Worton et al. [118] If lubricating oil, rather than combustion products, truly dominates vehicle POA emissions, it may explain why seasonal variations in POA volatility seem to be minor. Formulations of lubricating oil composition do not vary seasonally, unlike fuel composition variations between summer and winter in many locations [232,233].

While the lubricating oil dominated volatility distributions provide reasonable predictions of observed TD data, none capture the ~15% of apparently very low volatility OA mass that does not evaporate at 150 °C. The implication is that the volatility distributions may be too volatile, and therefore overpredict evaporation.

As noted above, this disagreement between TD observations and predicted evaporation at high temperatures is commonly observed [113,114]. Simply adding additional nonvolatile or extremely low volatility material to the volatility distribution does not reconcile the discrepancy, as the low volatility material persists at lower TD temperatures, leading to over predictions in MFR. Adsorption of organics to soot cores may play a role in creating higher than expected MFR at high temperatures. However the data collected here, all of which had OC/EC < 2, should have been impacted by adsorption at all TD temperatures. This suggests that other factors may also be at play, and deserve future consideration.

Chapter 6

Volatile Organic Compound Emissions from Natural Gas Production Facilities Measured in the Denver-Julesburg Basin, the Uintah Basin, and the Marcellus Shale

6.1 Introduction

In recent years, the rapid increase of unconventional O&NG production has raised concerns on the increase of emissions of greenhouse gases [30–34] and Volatile Organic Compounds (VOC) [35–38], including the BTEX, which are detrimental to local air quality [39–44] and public health [45–47]. The raw natural gas is mainly composed of CH_4 (45-98%), ethane (4-21%), a mixture of VOCs, including alkanes and aromatics, inorganic gases like H_2S and SO_2, and water [125]. During all stages of the natural gas exploration and production, the O&NG facilities may emit CH_4 and VOC through fugitive emissions, venting, flaring, accidental release, or storage losses [126]. Many previous studies have shown that the CH_4 and VOC emissions from the O&NG production system in U.S. have been underestimated by state and national emission inventories [37,127,128].

Many previous studies[35,37,38,129,130] measured the VOC concentrations and quantified the regional VOC emissions associated with O&NG production in some major gas production regions with ground and aircraft measurements. However, the VOCs emissions estimated by these studies are all top-down estimations of total VOCs emissions from all O&NG production facilities in the entire region; no facility-level VOCs emissions were reported in these studies. It is important to understand the characteristic of facility-level VOCs emissions in order to better control the VOCs emissions from O&NG production facilities. Also, since the Environmental Protection Agency (EPA) started to regulate the CH_4 and VOCs emissions of O&NG production facilities since Aug. 2016, it is necessary to have facility-level VOCs emission measurements before and after the regulations to test the effectiveness of the policy.

In this work, we measured the VOC concentrations downwind of individual natural gas production well pads and compressor stations in the Denver-Julesburg Basin, the Uintah Basin, and the Marcellus Shale in 2015 and 2016. All these regions are major O&NG production fields in the United States. In Dec. 2015, there are in total about 21,000 active O&NG well pads in the Denver-Julesburg Basin and the Uintah Basin, which contribute to ~4% of the total on-shore natural gas production in US [174]. The

majority of the gas production facilities in the Denver-Julesburg Basin and the Uintah Basin are conventional gas wells [174]. In the Marcellus Shale, there are more than 140,000 active conventional natural gas well pads and more than 3400 active unconventional well pads in Dec. 2015, which accounts for ~30% of the total on-shore natural gas production in US [174]. We specifically focused on measuring O&NG production facilities in the northeastern PA (NEPA) in the Marcellus Shale, where most gas production wells are unconventional. About 1/3 of the unconventional gas production wells in the Marcellus Shale are located in the NEPA, which contribute to ~40% of the total unconventional natural gas production in the Marcellus shale in Dec. 2015 [174].

In this manuscript, I report VOC concentrations and facility-level VOCs emission rates. VOCs emissions from different types of facilities, specifically gas wells vs. compressor stations, and unconventional vs. conventional gas wells, are compared. I also tested the hypothesis that VOCs emission rates of O&NG production facilities in different regions are different. Methane emissions measurements are discussed elsewhere [137,138].

6.2 Methods

6.2.1 Site selection

A suite of 13 VOCs ranging from C3 to C12, together with the CH_4 and ethane concentration, were measured ~50 – 1000 m downwind of the natural gas production well pads and compressor stations in the Denver-Julesburg Basin in March – April 2015, in the Uintah Basin in April – May 2015, and in the NEPA in May – June 2016. We conducted measurement at 32 well pads and 10 compressor stations and collected in total 47 samples. A detailed site count in each region is summarized in Table 6.1, and the locations of all measured sites are presented in Figure 6.1.

A detailed description of the site selection criteria can be found in Omara et al. [128]. To briefly summarize here, the selected sites must have a downwind road access within 50 – 1000 m. The terrain near the selected site must be relatively flat, and there must be

no other VOC and CH_4 sources near the selected site that could potentially interfere with the VOC and CH_4 measured from the site.

Table 6.1 The number of gas production sites measured in the Denver-Julesburg Basin, the Uintah Basin, and the NEPA

Denver-Julesburg Basin	Gas well	Site count	15
		Sample count	18
	Compressor Station	Site count	1
		Sample count	2
Uintah Basin	Gas well	Site count	9
		Sample count	10
	Compressor Station	Site count	8
		Sample count	8
Northeastern PA (NEPA)	Gas well	Site count	8
		Sample count	8
	Compressor Station	Site count	1
		Sample count	1
Total	Gas well	Site count	32
		Sample count	36
	Compressor Station	Site count	10
		Sample count	11

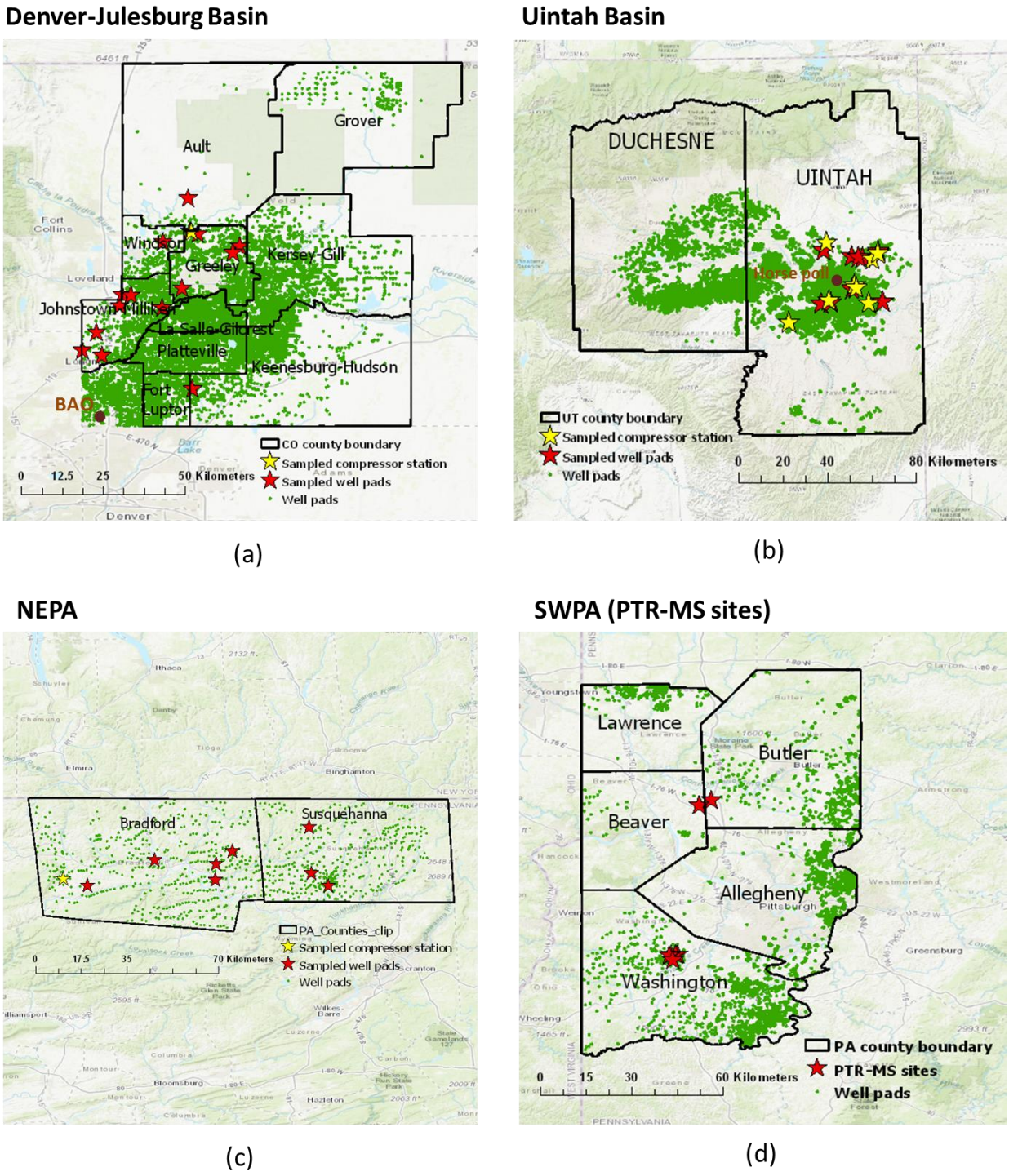

Figure 6.1 Locations of gas production well pads and compressor stations measured in (a) the Denver-Julesburg Basin, (b) the Uintah Basin, and (c) Northeastern PA (NEPA) with GC-FID, and (d) locations of gas production well pads measured in the Marcellus Shale with PTR-MS. Locations of the Boulder Atmospheric Observatory (BAO) and the ground site in Horse Poll are also shown in (a) and (b), respectively.

6.2.2 VOC measured by GC-FID

In total 13 VOCs species, including the BTEX, were measured by a GC-FID (gas chromatography with flame ionization detection; SRI model 8610C). The methane and ethane concentration were measured with a Picarro cavity ring-down spectrometer and a Tunable Infrared Laser Differential Absorption Spectrometer (TILDAS; Aerodyne Research Inc.), respectively, at a time resolution of 1Hz or higher. All instruments were placed in a mobile air quality laboratory. We firstly drive the mobile lab downwind of the target site to find the methane emission plume, and then the mobile lab will sit still inside the methane plume to collect the GC-FID sample. The GC-FID firstly samples the air for 20 min and pre-concentrate VOC from the air sample using an activated carbon trap. Then the trapped VOCs were thermally desorbed and injected into the GC column for analysis for another 20 min. An example of the chromatograph of the GC analysis cycle is presented in Figure 6.2, and all measured VOC species are also shown in the figure. During the 20-min sampling of GC-FID, the wind directions may change and the methane plumes may shift away from our sampling inlet.

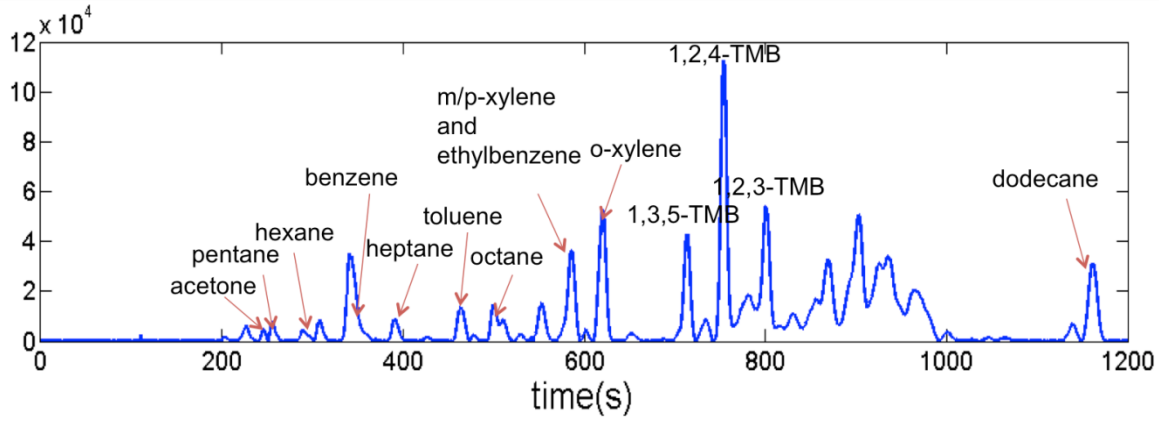

Figure 6.2 Example chromatogram of the analyzing stage of the GC-FID measurement. Identified species are labeled.

The response factor of the GC, defined as the integrated peak area of the chromatograph per unit mass of the VOCs, was calibrated shortly before or after each field campaign. For each measured species, 5, 10, 100 and 1000 ng of the standards were injected into the GC column at the beginning of the analysis cycle, and the

response factor was determined as the slope of the linear regression of the integrated peak area and the mass of the standards. Since the response factors of all measured VOCs species have a difference within 5%, one averaged response factor was used to calculate the concentration of all VOCs species. The retention time calibration of the GC-FID was performed daily in the field. A concentrated standard that contains all the measured VOC species was injected into the GC at the beginning of the analysis cycle to track the potential shifting of the retention time for each species.

6.2.3 PTR-MS and canister samples

We also measured the benzene and toluene concentrations using a PTR-MS downwind of natural gas production well pads in the Southwestern PA (SWPA) in Aug. – Sept. 2015. The PTR-MS collected data at a time resolution of 30 s. Locations of the PTR-MS sites are shown in Figure 4.1(d). We sampled at 5 locations and measured VOC emission from in total 6 well pads. Measurements at each location lasted for 22 – 29 hours. At each sampling location, our mobile lab and the mobile lab from RJ Lee group, Inc. equipped with the PTR-MS were sitting still side by side at a distance of 200 – 800 m downwind of the site. An Airmar 200WX weather station and a Gamin GPS were also deployed in our mobile lab to record the wind speed, the wind angle and the GPS location at the same time at 1Hz.

We also collected canister air samples upwind, downwind, and on site of individual gas production well pads in the SWPA in Aug. 2014. The VOC concentrations of these canister air samples were analyzed with a GC-MS (gas chromatography-mass spectrometry) in our lab. We collected canister samples at in total 6 sites. Among all 6 sites, only one site showed higher downwind VOC concentrations than the upwind measurements. For all other sites, the VOC concentrations were either non-detected, or the downwind measurements were lower than the upwind measurements.

6.2.4 Calculation of the VOC-to-CH_4-ratio

In order to compare the facility-level VOCs emissions in different natural gas production regions, I calculated the background corrected VOC-to-CH_4-ratio (molar ratio, ppb/ppb).

The ambient background methane and ethane concentrations were calculated as the baseline fitting of the 1Hz measurement data, as indicated in Figure D.1. I use the baseline fitting function of MATLAB R2015a [234]. It firstly estimates the baseline points within several shifted windows of a certain width, and then does a regression to these baseline points using a spline approximation to get the baseline. The window widths I used to estimate the baseline of the CH_4 and ethane measurements are ranged from 80 – 500 s.

For the VOCs measured by the GC-FID, in each sampled gas production region, we collected regional background samples at locations where no natural gas production facilities or other methane and VOCs sources are around, or at locations upwind of natural gas well pads. During the sampling of the ambient GC samples, the methane concentrations were measured concurrently at 1 Hz to confirm that no methane plume was sampled.

In the Denver-Julesburg Basin and NEPA, only one ambient background sample was collected in each region. In the Uintah Basin, we collected 3 ambient background samples, and the minimum VOC concentrations among these three samples were taken as the ambient background VOC concentrations. In case that the concentration of a certain VOC species measured downwind of the site was lower than ambient background concentrations, I assumed the site does not emit that species and the background subtracted concentration of that VOC species equals zero.

For benzene and toluene concentrations measured by the PTR-MS, I conducted baseline fittings to determine the ambient background concentration. For VOCs measured from the canister samples, the background subtracted VOCs concentrations were calculated using the downwind concentration minus the upwind concentration.

6.2.5 Calculation of the VOCs emission rates

For a subpart of the sties at which we measured the VOCs with GC-FID, we also measured the methane emission rates at the same time. For those sites that we have both the VOCs measurement and the methane emission rate measurement, the VOCs emission rates were calculated by scaling the concurrently measured methane emission

rates with the background corrected VOCs-to-CH_4-ratio. It assumes that VOCs and methane were co-emitted by the measured sites and were well mixed in the downwind air parcel that we sampled. We measured the methane emission rates of these natural gas production sites by using either tracer-flux methods [128,139,235], EPA OTM(other test method) 33A [236], or the drive-by plume method [237]. Details about the methane emission rate measurement will be presented in two upcoming publications [137,138]. The methane emission rate measurement was conducted at the same time with the VOCs measurement. Only the mean values of the measured methane emission rates were used in this work to calculate the VOCs emission rates.

6.3 Result and discussion

6.3.1 VOC concentration

All VOC (in ppb) and methane (in ppm) concentrations (not background corrected) measured downwind of natural gas production well pads and compressor stations in the Denver-Julesburg Basin, the Uintah Basin, and NEPA are presented in Figure 6.3 using box-whisker plots. The ambient background VOC concentrations in each basin and VOC concentrations reported by previous studies [35,38,238] are also shown in Figure 6.3.

The methane concentrations measured downwind of the facilities are in general around 1.8 ppm, and sometimes it reaches 5-10 ppm. The ethane concentrations are in the range of 2-30 ppb. For all VOC species, the concentrations downwind of sites are close to or lower than 1 ppb. Compared with the Uintah Basin and the NEPA, the xylene and trimethylbenzene concentrations are slightly higher in Denver-Julesburg Basin. The median benzene concentration measured in the Denver-Julesburg Basin is about 7 and 2 times higher than concentrations measured in the Uintah Basin and the NEPA, respectively. The dodecane concentration measured in NEPA is about an order of magnitude lower than it in the Denver-Julesburg Basin and the Uintah Basin. For all other VOC species, the concentrations measured in all regions are similar. All three basins have a similar total BTEX concentration. The variations of VOCs concentrations

in NEPA are smaller compared with it in the Denver-Julesburg Basin and the Uintah Basin.

At all measured sites, the methane concentrations are about 10 ppb – 2.7 ppm higher than the regional background, and the ethane concentrations are about 1 ppb – 350 ppb higher than the regional background. The VOC concentrations measured downwind of the natural gas well pads and compressor stations were in general not significantly higher than the ambient background. In the Denver-Julesburg Basin, except for ethane, pentane, hexane, benzene, and heptane, which have an ambient background concentrations close to or lower than the 25th percentile of concentrations measured downwind of sites, all other VOCs species have an ambient background concentrations close to the median value of concentrations measured downwind of sites. In the Uintah Basin, the ethane ambient background is close to the median value of the site measurements, and the benzene and toluene ambient background concentrations are close to the 75th percentile of the site measurements. All other VOCs species have an ambient background concentrations that are close to or lower than the 25th percentile of concentrations measured downwind of sites. It can be noticed that the median ehylbenzene concentration measured downwind of sites in the Uintah Basin are an order of magnitude higher than the ambient background. In the NEPA, the acetone has an ambient background that close to the 75th percentile of the sites, and the median concentrations of benzene and octane measured downwind of sites are much higher than the ambient background. For all other VOCs species, their ambient background concentrations are close to the median value of the site downwind measurements. For the total BTEX concentration, in Denver-Julesburg Basin, the background concentration is close to the median value of the site measurements; while in the Uintah Basin and the NEPA, it is close to the 25th percentile of the site measurements.

As shown in Figure 6.3(a), we captured in total 2 high VOC emitters in the Denver-Julesburg Basin. The VOC concentrations measured at these high emitters are about 2-3 orders of magnitude higher than the other sites. Both high emitters are natural gas production well pads, but they showed different characteristics for methane and VOCs emissions. The methane and ethane concentrations measured at high emitter #1 are similar with the median value of other sites, but VOC concentrations were significantly

higher, and the heavier compounds (C8 – C12) compounds showed a much higher concentrations compared with the lighter compounds (C3 – C8). For the high emitter #2, the methane and lighter VOCs compounds (C3 – C8) were significantly higher than other sites, and the heavier compounds (C8 – 12) have a much lower concentration compared with the lighter compounds (C3 - C8). The reason for the different VOC emission characteristics of these two high emitters is uncertain. It should be noticed that the high emitter #2 was measured in the night, and the significantly elevated methane and VOCs concentrations were mainly caused by the stagnation of the air in the night. For all other sites, measurements of VOCs and methane were conducted at daytime before sunset.

The VOC-to-CH_4 ratios of these two high emitters are compared with the averaged VOC-to-CH_4 ratio measured at all other gas wells in the Denver-Julesburg Basin in Figure D.2. For all VOC species, the VOC-to-CH_4 ratios of the high emitter #1 are much higher than the averaged ratio measured at other gas wells, while the high emitter #2 has similar or lower VOC-to-CH_4 ratios compared with other sites. It indicates that the high emitter #2 may not be a real ‘high emitter’; the significantly higher concentration we observed was mainly caused by the stagnation of air rather than the significantly higher VOC emissions from the site. In order to make sure the comparison between different gas production fields is not biased by the high emitters, these high emitters are excluded for the calculation of averaged VOC-to-CH_4 ratio and VOC emission rates in the Denver-Julesburg Basin.

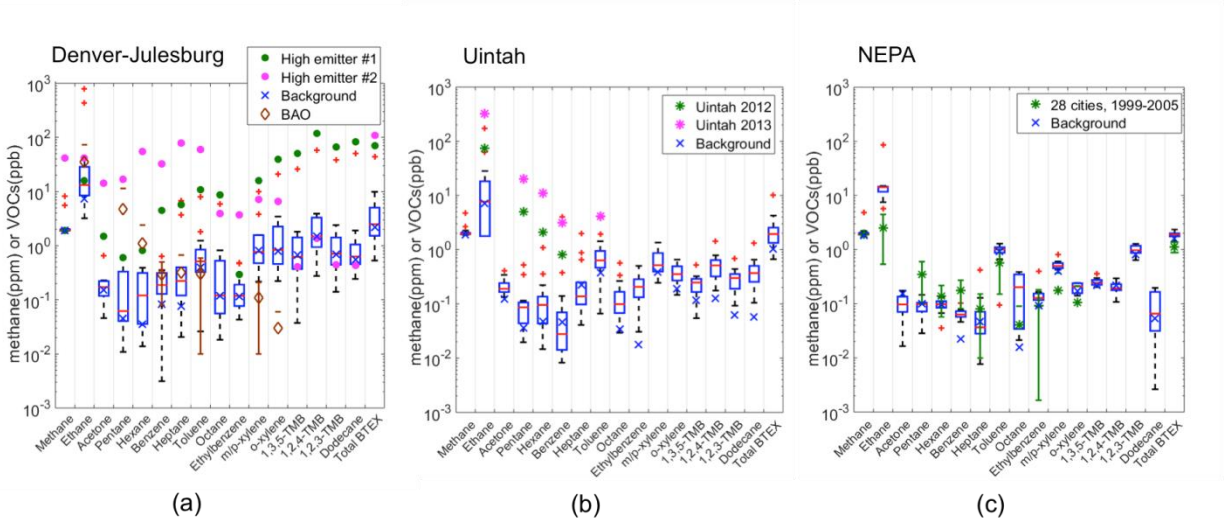

Figure 6.3 All VOC concentrations (in ppb) and methane concentrations (in ppm) measured in (a) the Denver-Julesburg Basin, (b) the Uintah Basin, and (c) Northeastern PA. I use box-and-whisker plots to represent all measurements at gas production facilities for each species. The red line in the middle of the box represents the median concentration; the top and the bottom of the box represent 75th and 25th percentile, respectively. The background measurements of each basin are shown as blue crosses. Measurements from other studies [35,38,238] are also presented to compare with our results.

The downwind BTEX concentrations were 57 ppb and 110 ppb for high emitter #1 and #2, respectively. These high BTEX concentrations detected in Denver-Julesburg Basin pose a potential concern of high BTEX exposure for people working and living on/near natural gas production facilities. In order to show the potential health impact of exposing at the VOC concentrations measured downwind of these high emitters, the VOC hazardous ratio (HR) of these two high emitters are summarized in Table 6.2. The hazardous ratio is calculated using the VOC concentration measured downwind of high emitters divided by the reference concentration (RfC). The RfC used here are reported in the US EPA Integrated Risk Information System (IRIS) [239], and a continuous inhalation exposure to VOC concentrations no larger than the RfC has likely no appreciable risk of adverse health effect during the lifetime. As shown in Table 6.2, the HR of benzene measured at high emitter #2 and the o-xylene and trimethylbenzene measured at high emitter #1 are larger than 1, indicating people working and living on/near these high emitters may potentially have elevated risk of adverse health effect.

Table 6.2 Hazardous Ratio (HR) of VOC measured downwind of two high emitters in Denver-Julesburg basin

VOC species	HR of high emitter #1	HR of high emitter #2
Hexane	0.00	0.28
Benzene	0.46	3.43
Toluene	0.01	0.04
Ethylbenzene	0.00	0.02
m/p-xylene	0.52	0.27
o-xylene	1.28	0.25
1,3,5-trimethylbenzene	3.07	0.00
1,2,4-trimethylbenzene	7.08	0.00
1,2,3-trimethylbenzene	4.24	0.00

In Figure 6.3 I compare the VOC concentrations measured downwind of natural gas production wells and compressor stations with the VOC concentrations in 28 cities in U.S. in 1999-2005.[238] The median ethane concentrations measured in all three gas production regions are about an order of magnitude higher than the 28-city average. For VOC species, the general trend is the lighter compounds (acetone and pentane) have a lower concentrations measured downwind of natural gas sites than the city average, while the heavier compounds (toluene, octane, ethylbenzene and xylene) have higher concentrations downwind of the natural gas sites. The median benzene concentration measured in the Denver-Julesburg Basin is higher than the 28-city average, while benzene in Uintah and the NEPA are lower. The median heptane concentrations measured in the Denver-Julesburg Basin and the NEPA are higher than the 28-city average, while in the NEPA it is lower. The median total BTEX concentrations measured in all three basins are about 70% - 1.3 times higher than the 28-city averaged BTEX concentration. This comparison suggests that that compared with in the cities, people work or live near/on natural gas production sites may potentially have higher exposures to BTEX.

In Figure 6.3, the VOC concentrations measured in this work are also compared with the regional VOC concentrations measured previously in Boulder Atmospheric Observatory (BAO) [35] and in a ground site in Horse Poll in Uintah County [38]. The locations of BAO and the Horse Poll ground site are shown in Figure 6.1 (a) and (b). As shown in Figure 6.3 (a), compared with the BAO measurement, the pentane and

hexane concentrations measured downwind of gas facilities in the Denver-Julesburg Basin are about 1-2 order of magnitude lower, but xylene concentrations are 1-2 order of magnitude higher. The ethane concentrations measured in BAO are close to the 75th percentile of our facility downwind measurement, both studies measured similar benzene, heptane, and toluene concentrations. All VOC concentrations measured in Horse Poll in winter 2012 and winter 2013 (Figure 6.3(b)) are consistently about 1-2 order of magnitude higher than our measurement in the Uintah basin. Since our measurement was conducted in spring/summer time, this difference reveals the seasonal trend of the VOC concentrations in the Uintah Basin. The lower temperature in the winter causes inversion events that can last for several days and leads to a stable atmospheric condition, which accumulates ground emissions and leads to a high VOC concentration in the atmosphere.

6.3.2 Correlations between VOC and methane concentrations

I quantified the correlation between background corrected methane (ΔCH_4) and background corrected VOC concentrations (ΔVOC) using the correlation coefficient (R), which quantifies the linear dependence of two variables. I did this analysis for gas wells and compressor stations measured in different regions separately, and results are summarized in Table D.1. For each species measured in each region, the outliers, which are defined as values more than three standard deviations from the mean, were excluded from the analysis.

The correlation between ΔCH_4 and ΔEthane and the correlation between ΔCH_4 and ΔBTEX measured at gas wells and compressor stations in the Uintah Basin are presented in Figure 6.4. As shown in the figure, the ΔCH_4 and ΔEthane has a strong correlation (R^2 larger than 0.9), but the correlations between ΔCH_4 and ΔBTEX are weak. For the compressor stations in the Uintah Basin, although the R^2 of ΔCH_4 and ΔBTEX equals to 0.81, it is largely influenced by one single data point with much higher ΔCH_4 and ΔBTEX. This trend is similar for other regions, the correlation between ΔCH_4 and ΔEthane is much better than the correlation between ΔCH_4 and ΔVOC. The strong correlation between ΔCH_4 and ΔEthane is because that the CH_4 plumes we sampled

are emitted by natural gas production sites, and raw natural gas contains 1-21% of ethane [125]. The weak correlation between ΔCH_4 and ΔVOC could potentially be because that there are other VOC emission sources besides the natural gas production facilities, or the VOC-to-methane ratio of the natural gas production facilities are highly site dependent. Since the regions where we conducted the measurement are all rural regions, and no other industrial processes or landfills are near the sites we visited, the chance that we had interference of VOC emissions from other sources is low. Previous regional measurements that covered a wider range of CH_4 concentrations (2 - 15 ppm) in Uintah Basin [38] showed that the VOC concentrations have a good correlation with CH_4 concentrations, and natural gas production facilities are a major source of VOC in gas production regions. Therefore, I assume that the major reason of the weak correlation between ΔCH_4 and ΔVOC is that the VOC-to-methane ratio in different sites are highly variable, and I scaled up the methane emission rates with the VOC-to-methane ratio to estimate the facility-level VOC emission rates.

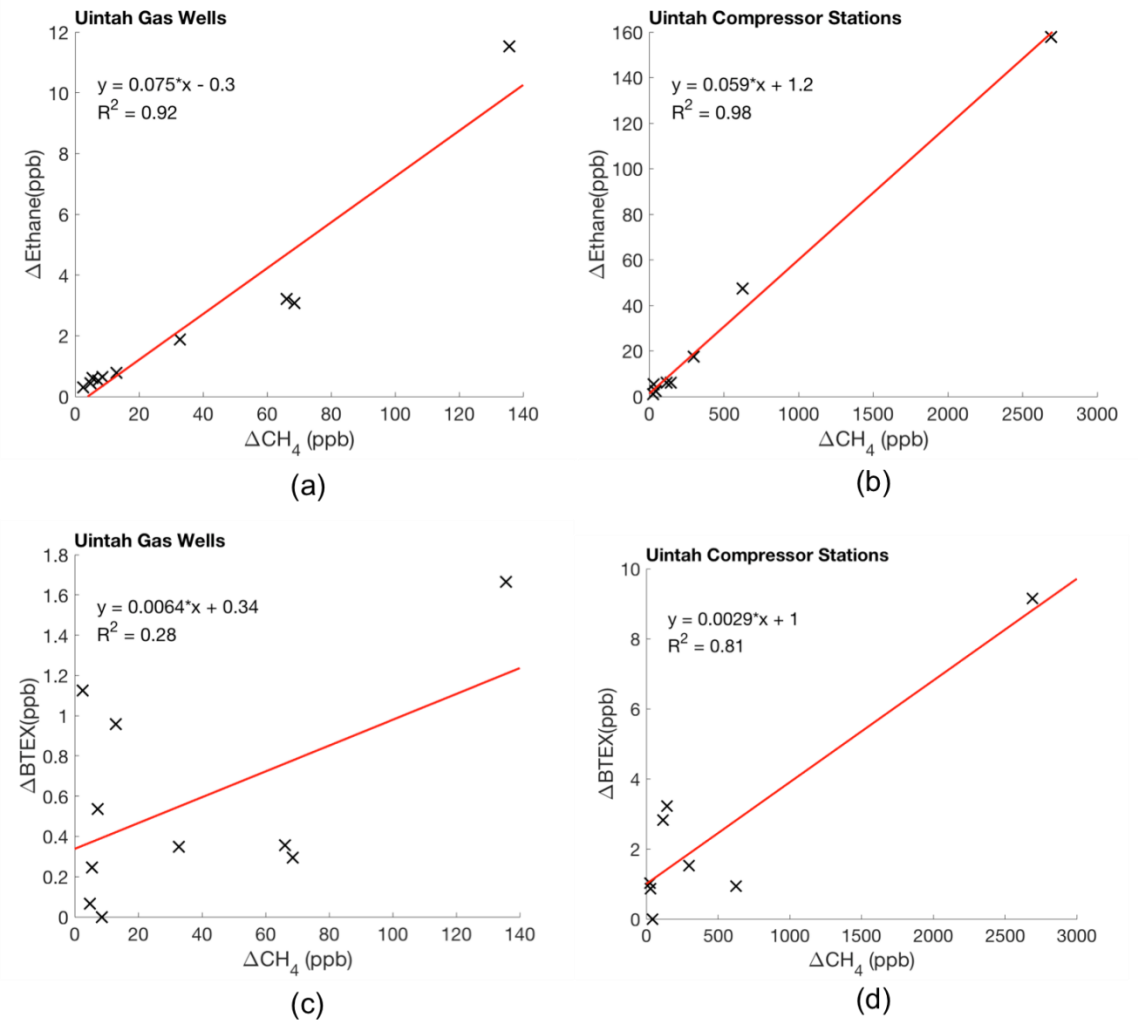

Figure 6.4 Correlations between background corrected ethane concentrations (ΔEthane) and background corrected CH_4 concentrations (ΔCH_4) measured at (a) natural gas production wells and (b) compressor stations in the Uintah Basin, and correlations between background corrected BTEX concentrations (ΔBTEX) and ΔCH_4 measured at (c) natural gas production wells and (d) compressor stations in the Uintah Basin. Crosses represent the measurement data, and red lines are linear regression results.

6.3.3 Facility-level VOC emission rates

All VOC emission rates measured at gas wells in the Denver-Julesburg Basin, the Uintah Basin, and the NEPA, and the VOCs emission rates measured at compressor stations in the Uintah Basin, are presented using the box-whisker plot in Figure 6.5. Results show that the facility-level VOC emissions measured downwind of the gas

production sites are highly variable. For all VOC species measured in all regions, their emission rates generally crossed a range of ~2-3 orders of magnitude. The large variability of measured facility-level VOC emission rates suggests that a single VOC emission profiles with a small uncertainty range may not be adequate to characterize VOC emissions for all gas production sites in a certain region, which makes it highly challenging to estimate the total VOC emission rates by surveying individual sites in a certain gas production region. The data of the median and the interquartile range of the VOC emission rates measured in each region are summarized in Table D.2.

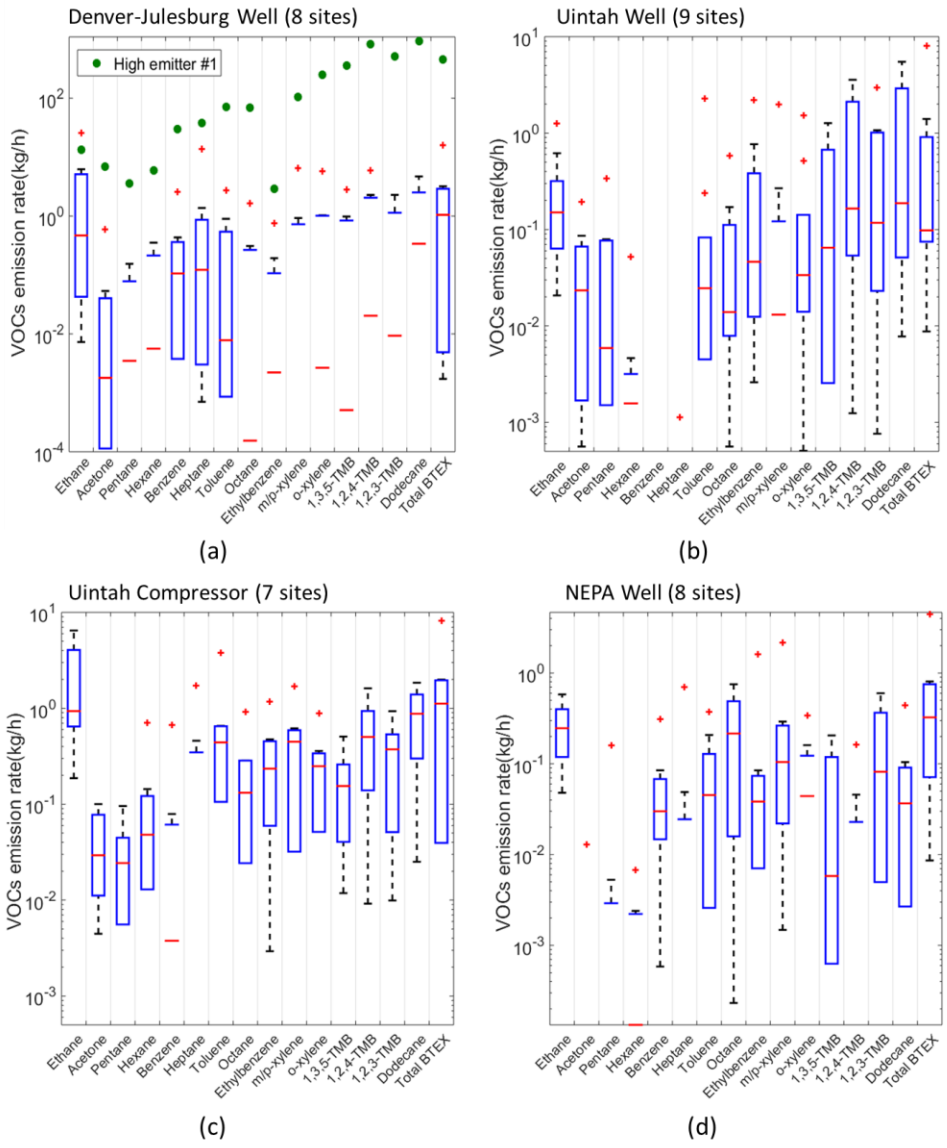

Figure 6.5 Facility-level VOC emission rates measured at (a) gas wells in the Denver-Julesburg Basin, (b) gas wells in the Uintah Basin, (c) compressor stations in the Uintah Basin, and (d)

gas wells in the NEPA. The emission rates of each VOC species are presented with the box-whisker plot. The red line in the middle of the box represents the median emission rate; the top and the bottom of the box represent 75th and 25th percentile, respectively.

The VOC emission rates of the high emitter #1 in the Denver-Julesburg Basin are also presented in Figure 7(a). The VOC emission rates of the high emitter #1 are about 1-2 order of magnitude higher than the 75th percentile of all VOC emission rates measured at gas wells in the Denver-Julesburg Basin for almost all VOC species. It is because that it has a much higher VOC-to-methane ratio than other sites.

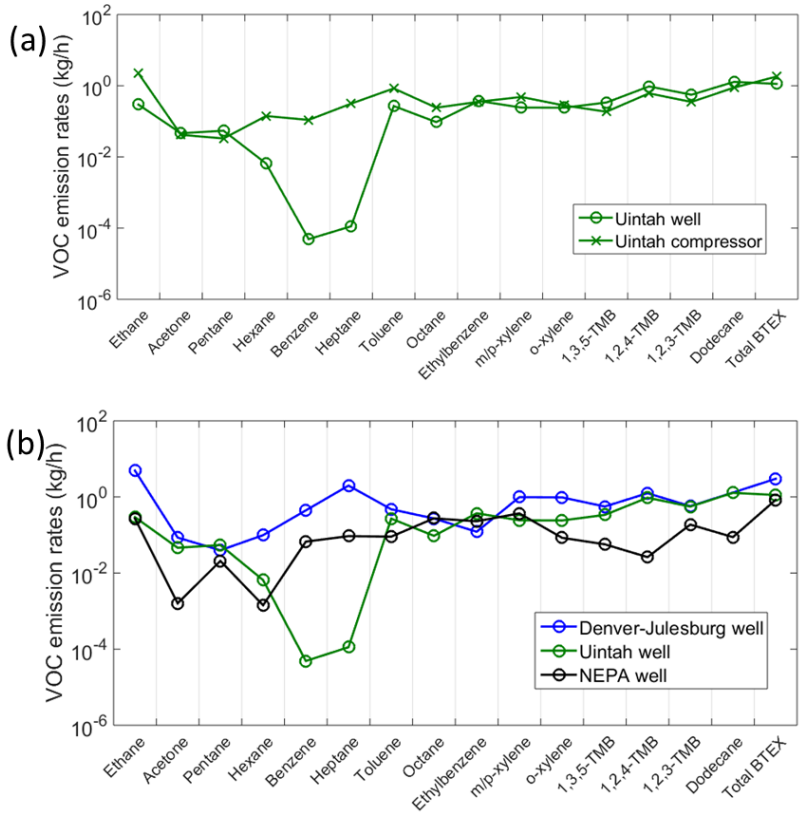

Figure 6.6 (a) Averaged facility-level VOC emission rate measured in the Uintah Basin, and (b) the comparison of the averaged facility-level VOC emission rate measured at gas wells in the Denver-Julesburg Basin, the Uintah Basin, and the NEPA.

We measured VOC emission rates at 9 gas production well pads and 7 compressor stations in the Uintah Basin, and it offers a chance to compare VOC emission rates from different types of sites (gas wells vs. compressor stations). In Figure 6.6 (a), I compared

the averaged VOC emission rates measured at gas wells and compressor stations in Uintah Basin. The ethane emission rate of compressor stations are about 2 times as it of gas wells, but the VOC emission rates of gas wells and compressor stations are in general similar. The ethane and hexane emission rates measured at the compressor stations are about 6 and 20 times higher than they measured at the gas wells, respectively. The benzene and heptane concentrations measured at the gas wells in the Uintah Basin are about 3 orders of magnitude lower than they measured at compressor stations, but they may be highly uncertain because of the choice of background concentrations, and it is further discussed in section D.2 in Appendix D.

Since the gas wells we sampled in the Denver-Julesburg Basin and the Uintah Basin are mostly conventional gas well pads, while the gas wells we sampled in the NEPA are mostly unconventional gas well pads, I compared the averaged VOC emission rates measured at gas wells in all three regions to study the difference of VOC emissions of conventional and unconventional gas wells, and results are shown in Figure 6.6 (b). In general, the VOC emission rates measured in the Denver-Julesburg Basin and in the Uintah Basin are similar, while the VOC emission rates measured in the NEPA are lower than other two regions. It suggests that the unconventional wells may potentially have a lower facility-level VOC emissions compared with the conventional wells. The benzene and heptane emission rates measured in the Uintah Basin are significantly lower than other regions. The averaged ethane emission rates measured in the Uintah Basin and NEPA are similar, while it measured at the Denver-Julesburg Basin is about 16 times larger. For the total BTEX, the averaged emission rate measured in the Uintah Basin is about 30% higher than it measured in the NEPA, and the averaged BTEX emission rate measured in the Denver-Julesburg Basin is about 1.7 times higher than it measured in the Uintah Basin.

6.3.4 PTR-MS and canister measurements

Since we did not measure the CH_4 emission rates during the PTR-MS and canister measurements, I cannot calculate the methane emission rates using PTR-MS and canister data, and only the VOC-to-CH_4 ratios measured by PTR-MS and canister

samples are reported in this work. In Figure 6.7, I compared the VOC-to-CH_4 ratio measured by PTR-MS and canister samples in SWPA with the VOC-to-CH_4 ratio measured by GC-FID at gas wells in NEPA. The VOC-to-CH_4 ratio measured by GC-FID is further described in section D.1 in Appendix D. The ethane-to-CH_4 ratio measured at the canister site in the SWPA is about 4 times as the averaged ethane-to-CH_4 ratio measured in the NEPA, and the o-xylene-to-CH_4 ratio measured in the canister site is similar with it measured in the NEPA. However, for benzene, toluene, ethylbenzene, and the m/p-xylene, the VOC-to-CH_4 ratios measured from the canister sample are much lower (~1-2 order of magnitude lower) than the VOC-to-CH_4 ratios measured in the NEPA. The benzene-to-CH_4 ratio and the toluene-to-CH_4 ratio measured with PTR-MS in the SWPA are about 1-2 order of magnitude higher than the canister measurements in the Marcellus Shale, and is also much higher than they measured in the NEPA with the GC-FID. It is potentially because that the high time resolution of the PTR-MS measurements makes it able to capture more high VOC emission events compared with the GC-FID and the canister measurement. Figure D.3 shows the toluene concentrations concurrently measured by the PTR-MS and the GC-FID at one PTR-MS site in the Marcellus Shale for over 24 hours. The toluene concentrations measured by both instruments are well agreed. However, for all toluene peaks showed up during the measurements, the GC-FID measurements can capture the increasing trend, but the peak concentrations measured by the GC-FID is much lower than the peak concentrations measured by the PTR-MS.

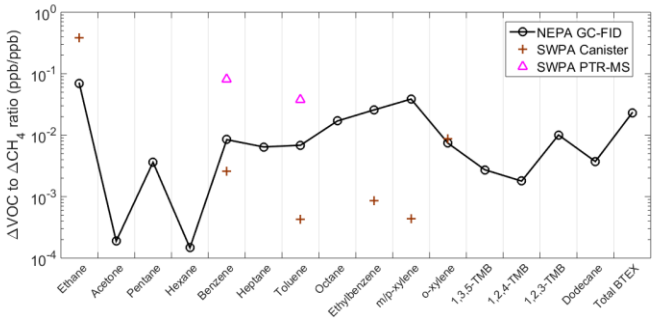

Figure 6.7 Comparison of averaged VOC-to-CH_4 ratio measured by the GD-FID at gas wells in the NEPA with the VOC-to-CH_4 ratio measured with PTR-MS and canisters samples in SWPA.

6.3.5 Comparison with previous studies

As discussed in section 1.4.1, since no previous studies reported the facility-level VOC emission rates, I compare our results with previous studies [36–38,129] by comparing the VOC-to-CH_4 ratio, and results are summarized in Table 6.3. The VOC-to-CH_4 ratios reported by previous studies are also presented in Figure D.2. Since only Warneke et al. [36] reported VOC-to-CH_4 ratios measured downwind of oil and gas production facilities, and all other studies [37,38,129] reported regional VOC-to-CH_4 ratio, the comparisons between our study and previous studies are mostly the comparison between the VOC-to-CH_4 ratios measured at individual facilities and the regional VOC-to-CH_4 ratios.

In the Denver-Julesburg Basin, the regional benzene-to-CH_4 ratio measured by Pétron et al.[37] is about 90% lower than the mean benzene-to-CH_4 ratio we measured at wells, but about 1 order of magnitude higher than it measured at compressor stations. It should be noticed that we only collected two GC-FID samples at one compressor stations in Denver-Julesburg Basin, and it may not be representative for all compressor stations in the region.

In the Uintah Basin, the regional ethane-to-CH_4 ratio reported by Helmig et al. [38] is slightly lower than the ethane-to-CH_4 ratio we measured downwind of natural gas facilities, and the regional toluene-to-CH_4 ratio is about an order of magnitude lower than it measured at gas facilities. For pentane, hexane, and benzene, the regional VOC-to-CH_4 ratios lie between the VOC-to-CH_4 ratios measured downwind of gas wells and compressor stations. Warneke et al. [36] measured VOC-to-CH_4 ratios downwind of natural gas production facilities in Uintah Basin, and the benzene-to-CH_4 ratio they measured is close to what we measured at compressor stations, but over one order of magnitude higher than we measured at gas wells.

In the Marcellus Shale, Yuan et al. [129] reported the regional benzene-to-CH_4 ratio measured in the NEPA, and it lies between the benzene-to-CH_4 ratios measured at gas wells and compressor stations, but is much closer to the gas well measurements. The regional benzene-to-CH_4 ratio reported by Yuan et al. [129] is about 70% lower than it

measured at gas wells in NEPA. We only collected one sample at one compressor station in the NEPA, and it may not represent all compressor stations in the region.

These comparisons in all three gas production fields in general show that the VOC-to-CH_4 ratios measured downwind of gas wells are higher than the regional VOC-to-CH_4 ratios. The enhanced VOC-to-CH_4 ratio at gas wells indicates that the VOC we measured downwind of individual facilities are dominantly emitted by the gas production facilities.

6.4 Conclusion

The VOC concentrations and the facility-level VOC emission rates measured downwind at individual natural gas production well pads and compressor stations in the Denver-Julesburg Basin, the Uintah Basin, and the NEPA are reported in this work. The VOC concentrations measured near facilities are in general not significantly higher than the regional background and the city ambient concentrations, except in the Denver-Julesburg Basin, we observed significantly enhanced VOC concentrations, which are about 2-3 order of magnitude higher than other sites, at two gas production well pads. It poses potential concerns on high BTEX exposure for people working and living on/near natural gas production sites.

The facility-level VOC emission rates measured at gas production facilities in all three gas production fields are highly variable and cross a range of ~2-3 order of magnitudes. It suggests that a single VOC emission profile may not be able to characterize VOC emissions from all natural gas production facilities, and to use a single emission factor to estimate the total VOC emissions from all gas production facilities in a region may yield highly uncertain result.

The VOC emission rates of the natural gas production well pads and the compressor stations measured in the Uintah Basin are similar, except for the benzene and heptane, the emission rates of the gas wells are much lower than compressor stations. The VOC emission rates measured at gas wells in the NEPA are in general lower than they measured in the Denver-Julesburg Basin and the Uintah Basin, indicating that the

unconventional gas wells have a lower VOC emission rate compared with the conventional wells.

Results of this work suggest that it is highly challenging to estimate VOC emissions of the entire O&NG production sector by surveying individual gas production facilities, and the top-down estimation may be a better way to constrain VOC emissions from all gas production facilities in a region. Since our measurements were conducted before EPA started to regulate VOC emissions from the O&NG production facilities, the facility-level VOC emission rates reported in this work can serve as the basis for future studies to test the effectiveness of the regulation policies.

Table 6.3 Comparison of the VOC-to-CH4 ratio (ppb/ppb) reported in this study and previous studies

Gas production regions	VOC species	VOC-to-CH_4 ratio of gas wells	VOC-to-CH_4 ratio of compressor stations	VOC-to-CH_4 ratio reported by previous study	Reference
Denver-Julesburg	Benzene	1.95E-02 ± 3.04E-02	1.27E-05 ± 1.79E-05	1.36E-03	Petron et al.[37]
Uintah	Ethane	7.62E-02 ± 2.47E-02	7.03E-02 ± 4.53E-02	6.30E-02	Helmig et al. [38]
	Pentane	1.00E-02 ± 1.84E-02	6.07E-04 ± 9.28E-04	3.20E-03	
	Hexane	3.72E-03 ± 9.84E-03	1.11E-03 ± 1.26E-03	1.80E-03	
	Benzene	1.05E-05 ± 3.31E-05	8.99E-04 ± 1.24E-03	5.80E-04	
	Toluene	2.12E-02 ± 4.27E-02	6.19E-03 ± 5.76E-03	6.40E-04	
	Benzene	1.05E-05 ± 3.31E-05	8.99E-04 ± 1.24E-03	6.73E-04	Warneke et al. [36]
Marcellus Shale	Benzene	7.51E-03 ± 1.62E-02 (GC-FID in NEPA)	2.04E-05 (GC-FID in NEPA)	1.95E-03 (NEPA)	Yuan et al. [129]

Chapter 7

Constructing a Spatially Resolved Methane Emission Inventory of Natural Gas Production and Distribution over Contiguous United States

7.1 Introduction

Methane is the second most powerful greenhouse gas (GHG) after carbon dioxide [14]. The natural gas production and distribution is a major source of methane emissions in US [126]. Since 2010, the unconventional oil and natural gas (O&NG) production increased dramatically in United States [23], and it has raised concerns on the increase of methane emissions [30,31,33,34,240]. The Edgar v4.2 [134] and the EPA GHGI [135,136] are the two most commonly used methane emission inventories in US, and both inventories are spatially resolved across the contiguous US [136]. However, previous modeling and measurement studies [136,144] consistently show that both inventories may underestimate methane emissions from the natural gas production and distribution.

In recent years, our research team at Carnegie Mellon University and other research teams have conducted many field measurements across the contiguous US to quantify methane emissions from natural gas production and distribution [128,137–143]. The EPA GHGI has already included results from recent ground measurements [142,143] for methane emissions from the natural gas transmission and distribution systems. However, for the natural gas production system, EPA GHGI still uses emission factors from the 1996 EPA/GRI (Gas Research Institute) studies [145]. Omara et al. [137] combined results from all these studies and provided a spatial distribution of methane emissions from onshore natural gas production over contiguous US, but no spatially resolved and up-to-date methane emission inventory for the entire natural gas production and distribution sector over the contiguous US exists at this moment.

In this chapter, I constructed a gridded methane emission inventory of the natural gas production and distribution over the contiguous US using facility-level methane emissions reported by recent ground measurements in US [128,137,140,142,143]. The annual total methane emissions and the spatial pattern of our constructed inventory are compared with the EPA GHGI and the Edgar v4.2. In order to explore whether my inventory could potentially improve

the prediction of methane concentrations in the atmosphere, I modified the GEOS-Chem default methane emission inventory with my inventory and the EPA GHGI, and then run the GEOS-Chem methane simulations with either my inventory or the EPA GHGI. The simulated methane concentrations are compared with the GOSAT measurements to determine whether the simulation with my inventory or the simulation with the EPA GHGI could better represent the actual methane concentrations in the atmosphere.

7.2 Method

7.2.1 Inventory construction

My built methane emission inventory of natural gas production and distribution is an annual inventory and has a spatial resolution of 0.1° latitude × 0.1° longitude over the contiguous United States. The base year of the inventory is 2015. The methane emissions of natural gas production and distribution are calculated as the product of emission factors and the activities. The emission factors I used to construct the inventory are methane emissions per gas well or methane emissions per facility reported by previous field measurement studies [128,137,140,142,143] and the EPA Greenhouse Gas Reporting Program (GHGRP) [173]. The activity data are number and locations of the natural gas facilities in the Contiguous United states, and the data are obtained from Drillinginfo [174], U.S. Energy Information Administration (EIA) [175], and EPA GHGRP [173]. The known locations of the natural gas facilities allow us to spatially distribute the methane emissions from the natural gas production and distribution processes.

Following the EPA GHGI [126], the methane emissions of the natural gas production and distribution are composed of 4 sectors: the natural gas production, processing, transmission and distribution. Methane emission from the natural gas production consists of methane emissions from the on-shore natural gas production, the offshore natural gas production, the coalbed methane production,

and the natural gas gathering facilities. For methane emissions from the on-shore natural gas production, Omara et al.[137] estimated the averaged facility-level methane emissions in 48 basins/regions in United States. Since the methane emission factors of EPA GHGI for on-shore natural gas production are per-well basis, in order to compare with the EPA GHGI, I converted the methane emissions per-facility reported by Omara et al. [137] into per-well basis. For each basin/region, I obtained the total number of on-shore natural gas production facilities and the location and the number of gas wells in each production facility from the Drillinginfo [174]. I firstly calculated the total methane emissions in each basin/region using the facility-level methane emission and the total facility count, and then estimated the methane emissions per well in each basin/region using the total methane emission dividing by the total well count. The methane emissions from each facility are then calculated as the methane emissions per gas well multiplying by the number of gas wells of each natural gas production facility. It should also be noticed that the methane emissions reported by Omara et al. [137] are for Dec. 2015, and only gas wells that were active in production in Dec. 2015 are included in the estimation of methane emissions. To calculate methane emissions in the entire 2015, I assume the on-shore gas production facilities in other months in 2015 have the same emission rate as in Dec. 2015, and the zero-production gas wells in Dec. 2015 were not included in my inventory. The total number of zero-production gas wells is only about 6% of the total number of non-zero-production gas wells [174].

For the methane emissions from offshore natural gas production, following EPA GHGI [126], I used the platform-level methane emission data from the 2011 Gulfwide Emission Inventory constructed by the Bureau of Ocean Energy Management (BOEM) [241]. The database also has location information of each platform, and it only has offshore natural gas facilities in the Gulf of Mexico. The total annual offshore methane emissions estimated by the EPA GHGI are the same from 2011-2015. Therefore, I assume the offshore methane emissions in 2015 are the same as it in 2011. Methane emissions from the coalbed methane wells are estimated using the emission factors reported in EPA GHGI [126] and

the well count and location data are obtained from the Drillinginfo [174]. The EPA GHGI reported methane emissions per gallon-produced-water in Powder River, and methane emissions per well in Black Warrior. For coalbed methane production facilities in other regions, I assume they have the same methane emissions per-well as facilities in Black Warrior. Methane emissions from the natural gas gathering facilities are estimated using the facility-level methane emissions and the gathering station locations reported by Marchese et al. [140]. Marchese et al. [140] provided the location information of only a subpart of the extrapolated gathering stations in 8 states. I scaled up the facility-level methane emissions of these gathering stations with known locations to make sure that the total methane emissions from gathering facilities in each sate matches the estimation of Marchese et al. [140]. These 8 states in total are account for 84% of the methane emissions from all gathering facilities in U.S.

For the processing plant, I calculated the methane emissions using the facility-level methane emissions reported by Marchese et al. [140]. Data from EPA GHGRP [173] and EIA natural gas processing plant survey [175] are combined to get the locations of all processing plants in U.S. For processing plants that reported only to EIA, there are no latitude and longitude information available, and the zip code was used to determine the location of the plant. I identified in total 751 processing plants, which is about 13% higher than the processing plant count used by the EPA GHGI. [126].

For methane emissions from the natural gas transmission and distribution sectors, since the EPA GHGI has already included the emission factors reported by recent ground measurement [142,143], I kept them the same as gridded EPA methane emission inventory constructed by Maasakkers et al. [136].

7.2.2 GEOS-Chem simulation

I ran the GEOS-Chem (version 11-01) methane simulation with my built methane emission inventory or the gridded EPA GHGI built by Maasakkers et al. [136] to explore whether my built methane emission inventory of natural gas production

and distribution can potentially improve the predictions of methane concentrations in the atmosphere. The current version of GEOS-Chem (version 11-01) uses the Edgar v4.2 [134] as the default methane emission inventories for all anthropogenic sources. I used HEMCO (Harvard-NASA Emission Component) to replace the methane emissions from natural gas production and distribution sector (1B2b) of Edgar 4.2 with my built inventory or the gridded methane emission inventory of natural gas production and distribution built by Maasakkers et al. [136]. For all other anthropogenic and natural methane emission sources, I kept the same with the default setting of GEOS-Chem version 11-01. The Edgar v4.2 has gridded methane emission data available up to the year of 2008. If no methane emission data is available for the current simulation year, GEOS-Chem methane simulation will use the emission data from the latest previous years.

I ran the GEOS-Chem methane simulation over the nested North American domain (10° - 70 ° latitude, -140° - -40° longitude) at a spatial resolution of 0.5° latitude × 0.625° longitude over 47 vertical layers to get the daily methane concentration predictions for Feb. 2015. The MERRA-2 (Modern-Era Retrospective analysis for Research and Applications, Version 2) data was used as the meteorological field of the simulation. Results from global GEOS-Chem methane simulations (2° latitude × 2.5° longitude) were taken as the boundary conditions of the nested grid simulations over North American.

In order to determine which simulation better represent the actual methane concentrations in the atmosphere, I compared the simulation results with methane concentrations measured by GOSAT (Greenhouse Gases Observing Satellite) in Feb. 2015. The GOSAT [242] was launched by the Japanese Aerospace Exploration Agency (JAXA) in Jan. 2009. It measures the absorption of the backscattered solar radiance in shortwave infrared (SWIR) to determine the methane abundance in the atmosphere. GOSAT has a pixel resolution of 10 km × 10 km, but its coverage over the Contiguous U.S. is sparse over a month, as shown in Figure 7.3 (a). I used the University of Leicester version 7.0 GOSAT product [243] obtained from the European Space Agency Greenhouse GAS Climate Change Initiative (ESA GHG-CCI) data product site [244]. It provides the

daily column mixing ratio of methane (X_{CH4}) retrieved from the GOSAT measurements, and the retrievals of X_{CH4} have already validated with the ground measurements from the Total Carbon Column Observing Network (TCCON). To compare the GEOS-Chem simulations with the GOSAT X_{CH4} retrievals, I used the code written by Dr. Melissa Sulprizio and Dr. Joannes Maasakkers in Harvard University to calculate X_{CH4} from the GEOS-Chem simulation results. This function will be described in detail in an upcoming publication. The averaging kernels of the GOSAT data were applied while calculating the X_{CH4} from the GEOS-Chem simulations. I calculated the GEOS-Chem simulated X_{CH4} only for those GEOS-Chem grid cells that has GOSAT X_{CH4} retrieval available during the time period of the simulation. For those GEOS-Chem grid cells that were not covered by GOSAT measurements, since no satellite averaging kernels are available, I did not calculate the X_{CH4} of the GEOS-Chem simulations.

7.3 Result and discussion

Figure 7.1 shows the gridded methane emissions (0.1° × 0.1°) over the contiguous U.S. for each sector of the natural gas production and distribution described in the method part, and the total annual methane emissions of each natural gas production and distribution sector are summarized in Table 7.1. Figure 7.1 (a) – (d) are the four subparts of the natural gas production sector showing in Figure 7.1 (e). Methane emissions from the on-shore natural gas production (Figure 7.1(a)) show hot spot in the major natural gas production basin/region across U.S., including the Marcellus Shale (Appalachian Basin) in Pennsylvania and West Virginia, Western Gulf in Texas and Louisiana, Fort Worth and Permian in Texas, and Anadarko in Oklahoma. The offshore methane emissions (Figure 7.1(b)) are only in the Gulf of Mexico. Methane emissions from coalbed methane production (Figure 7.1(c)) show hot spot in major coalbed methane production regions, including the Powder River Basin in Wyoming, the Balck Warrior Basin in Alabama, San Juan Basin and Raton Basin in northern New Mexico and Southern Colorado, and the Cherokee Platform in Kansas and

Oklahoma. Methane emissions from the gathering stations (Figure 7.1(d)) are high in some major gas production basin/region such as the northern part of the Marcellus Shale, Fort Worth Basin, Anadarko, San Juan Basin, and the Powder River Basin. Among all four sectors of natural gas production, the on-shore natural gas production dominates the methane emissions from the entire natural gas production sector (Figure 7.1(e)). It contributes to about 88% of the methane emissions from the natural gas production. Methane emissions from the natural gas processing (Figure 7.1(f)) follow the spatial distribution of the gas processing plants and are mostly in Texas, Louisiana, Oklahoma and Wyoming.

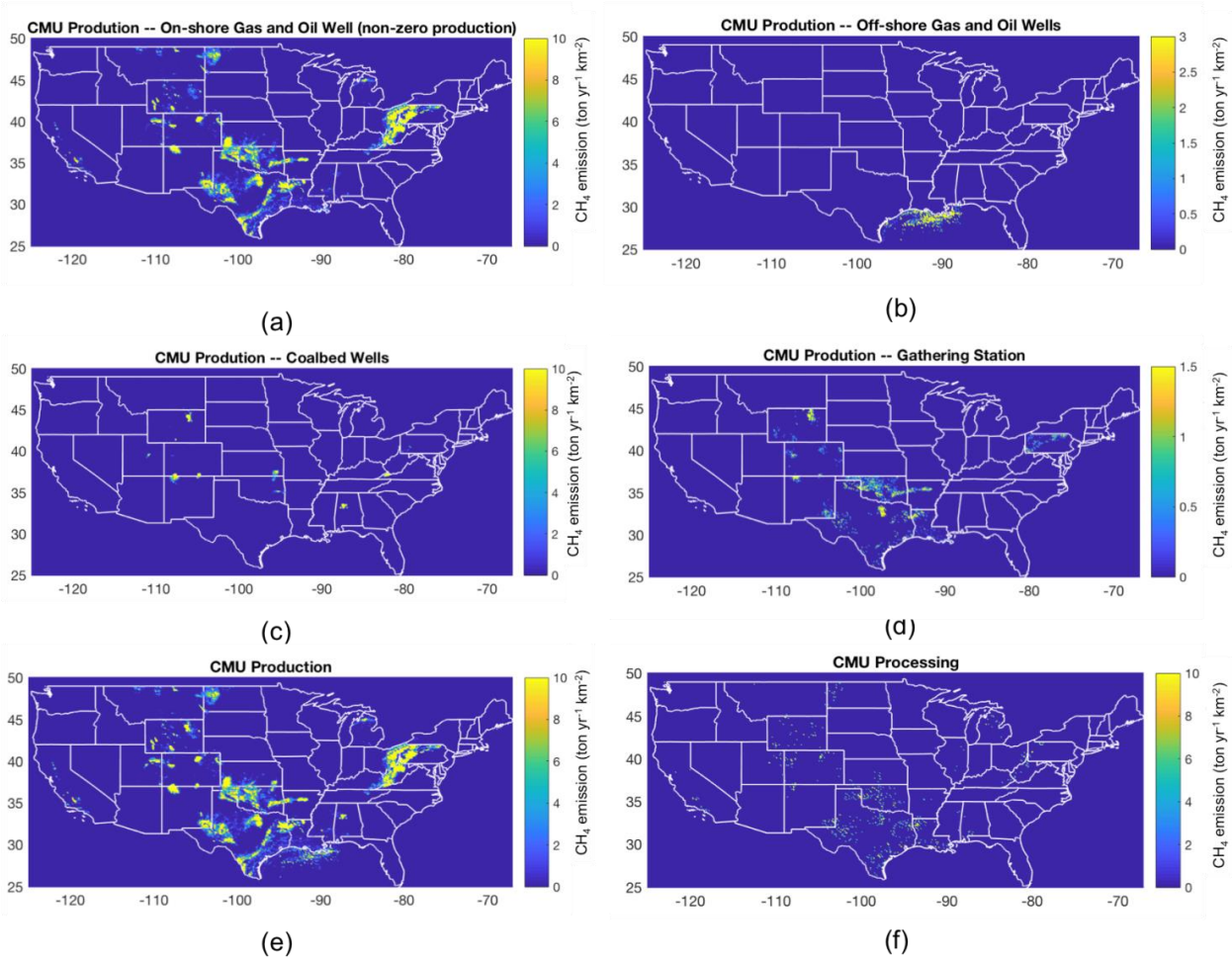

Figure 7.1 Gridded (0.1° × 0.1°) annual methane emissions of (a) on-shore natural gas production, (b) off-shore natural gas production, (c) coalbed methane production, (d) natural gas gathering, (e) natural gas production, and (f) natural gas processing over the contiguous US.

The gridded methane emissions (0.1° × 0.1°) of the entire natural gas production and distribution sector in contiguous U.S. are presented in Figure 7.2(a). As shown in Table 7.1, the natural gas production contributes to 73% of the methane emissions from the entire natural gas production and distribution sector, and the on-shore natural gas production alone contributes to 64% of the total methane emissions. Since the natural gas production dominates the methane emissions from the entire sector, the spatial trend of methane emissions from the natural gas production and distribution generally follows the spatial trend of the natural gas production and shows hot spot in major gas production fields including the Marcellus Shale in Pennsylvania and West Virginia, Western Gulf, Fort Worth, and Permian in Texas, and Anadarko in Oklahoma.

I compared my built methane emission inventory with the methane emissions from natural gas production and distribution estimated by Edgar v4.2 [134] and EPA GHGI [126], and the total methane emissions estimated by these inventories are summarized in Table 7.1. For the entire natural gas production and distribution sector, the total annual methane emissions estimated by my inventory are 74% and 20% higher than the Edgar v4.2 and the EPA GHGI. Turner et al. [133] conducted inverse modeling using the Edgar v4.2 as the a priori emission field and the GOSAT X_{CH4} retrieval and concluded that the actual methane emissions from the oil and gas sectors in Contiguous U.S. could be 61% - 148% higher than the estimation of Edgar v4.2, and the methane emissions estimated my inventory are within this range. My inventory also indicates that the natural gas production has a higher contribution to the total methane emissions from the natural gas production and distribution than it estimated by the EPA GHGI (73% vs. 64%). It is mainly because that for the natural gas production, the current EPA GHGI still uses the emission factors reported by EPA and Gas Research Institute in 1996, while recent ground measurements suggest that the methane emission factors of the natural gas production facilities should be much higher [137]. Methane emissions from the natural gas processing estimated by my inventory are about 22% lower than the EPA GHGI. It is because that the

methane emissions per processing plant estimated by Marchese et al. [140] based on the recent field measurement is ~38% lower than it estimated by the EPA GHGI, although I identified more processing plants than the EPA GHGI.

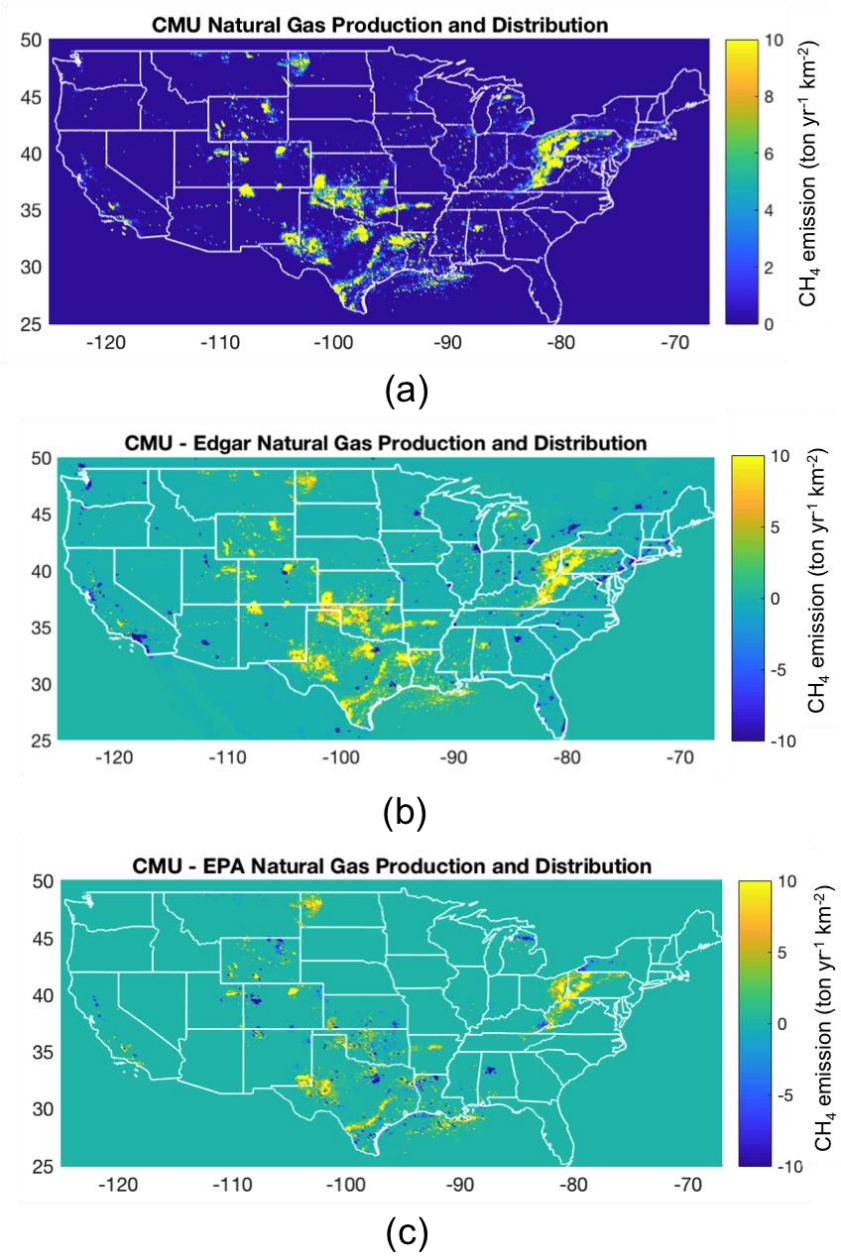

Figure 7.2 (a) Gridded (0.1° × 0.1°) methane emission inventory of natural gas production and distribution over the contiguous U.S., and the spatial difference of my inventory with the methane emissions of natural gas production and distribution estimated by (b) Edgar v4.2 and (c) EPA GHGI.

The spatial differences of my built methane emission inventory with the Edgar v4.2 and the EPA GHGI for the natural gas production and distribution are shown in Figure 7.2(b) and 2(c). Compared with my built inventory, methane emissions estimated the Edgar v4.2 are significantly lower in major gas production fields over the entire contiguous U.S (Figure 7.2(b)), which is similar with the comparison of EPA GHGI and Edgar v4.2 [136]. As shown in Figure 7.2(c), my built methane emission inventory also shows higher methane emissions in major gas production region than the gridded EPA GHGI, but the difference between my inventory and the EPA GHGI are smaller than the difference between my inventory and the Edgar v4.2. It can be also noticed that the methane emissions estimated by my inventory are lower than the EPA GHGI in some coalbed methane production regions, such as the Powder River Basin, the Black Warrior Basin, the Piceance Basin in Colorado, and the Southwestern Coal Region in Texas. It is probably because that the methane emission factor I used for coalbed methane wells in this work is lower that it used in Maasakkers et al. [136], or I may have missing coalbed wells compared with Maasakkers et al. [136]. But since the coalbed methane production only contribute to about 4% of the methane emissions from the entire natural gas production and distribution sector, it has a minor impact on the overall spatial trend of the methane emissions.

The comparison of the GEOS-Chem simulated X_{CH4} and the GOSAT X_{CH4} retrievals are presented in Figure 7.3. Results suggest that compared with the EPA GHGI, my methane emission inventory improves the agreement between simulated and satellite measured X_{CH4}, but the improvement is very limited. All grid cells presented in Figure 7.3 are nested GEOS-Chem grid that has a spatial resolution of 0.5° latitude × 0.625° longitude. Figure 7.3(a) shows the monthly averaged X_{CH4} retrieved from the GOSAT measurement in Feb. 2015. The GOSAT measurement has a relatively sparse coverage over the contiguous U.S. in Feb. 2015. The GOSAT X_{CH4} retrievals in the eastern and southern U.S. are in general higher than the central and western U.S. (~ 1830 ppb v.s. ~1800 ppb), except in central California, the X_{CH4} could reach ~1900 ppb. The spatial differences of GOSAT X_{CH4} retrievals and the simulated X_{CH4} with EPA GHGI are

shown in Figure 7.3(b). The GEOS-Chem simulated methane concentrations are systematically ~20-60 ppb higher than the GOSAT X_{CH4} retrievals. In order to better compare the trend of satellite measurements and GEOS-Chem simulations, in Figure 7.3 and Figure 7.4, I added the average difference between GOSAT X_{CH4} retrievals and GEOS-Chem simulations, 44 ppb, to all GEOS-Chem simulated X_{CH4}. The satellite and model differences are higher in some of the natural gas production fields, such as in the southwest Pennsylvania, Texas, and the northern Wyoming. Particularly, in the San Joaquin Basin in central California, the satellite and model have the highest difference. Figure 7.1(c) shows the spatial comparison of the simulated X_{CH4} with my inventory and the simulated X_{CH4} with EPA GHGI. The two simulations are in general similar. The simulated X_{CH4} with my inventory are higher than the simulated X_{CH4} with EPA GHGI over some gas production fields, including the Marcellus Shale (Pennsylvania and West Virginia) and Fort Worth and Western Gulf in Texas, but the differences are only about 0.5 – 2 ppb, which is much smaller than the difference of GOSAT X_{CH4} retrievals and simulated X_{CH4} with EPA GHGI (~10 ppb in Texas). In Figure 7.4 I compared the GOSAT X_{CH4} retrievals with the simulated X_{CH4} in each GEOS-Chem grid, and results show that the simulated X_{CH4} are well correlated with satellite measurements (R^2 = 0.4). Compared with the model simulations with the EPA GHGI, the model simulations with my inventory slightly improved the model and satellite agreement (R^2 = 0.4105 v.s. R^2 = 0.4093).

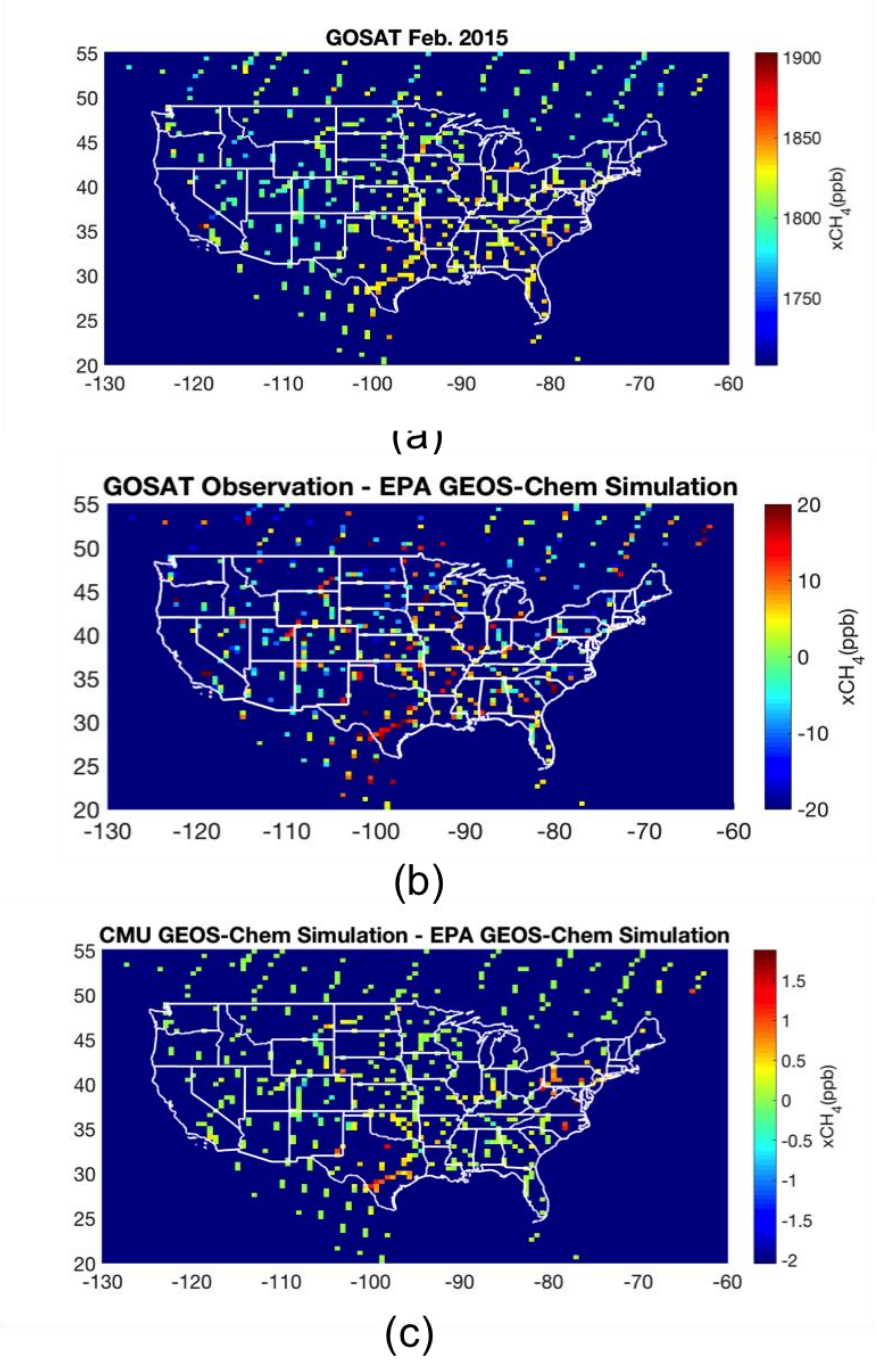

Figure 7.3 (a) The GOSAT X_{CH4} retrievals in the Contiguous US in Feb. 2015, (b) the spatial difference of the GOSAT X_{CH4} retrievals and the GEOS-Chem simulated X_{CH4} with EPA GHGI, and (c) the spatial difference of simulated X_{CH4} with my inventory and simulated X_{CH4} with the EPA GHGI.

The spatial differences of my inventory with the gridded EPA GHGI presented in Figure 7.2(c) show that the two inventories have large differences over some natural gas production regions. To further study how these regional differences of methane emissions could influence the regional methane concentrations, in Figure 7.5, I specifically focused on the methane emissions and the GEOS-Chem simulated X_{CH4} in the Marcellus Shale, where ~30% of the total U.S. on-shore natural gas are produced [174]. Figure 7.5 (a) show the spatial difference of methane emissions estimated by my inventory and the EPA GHGI for natural gas production and distribution in the Marcellus Shale, and Figure 7.5(b) show the difference of the simulated X_{CH4} with my inventory and the simulated X_{CH4} with EPA GHGI in the Marcellus Shale. Only 23 GEOS-Chem grid cells were cover by GOSAT measurement in Feb. 2011 in the Marcellus Shale region. The results show that although the methane emissions estimated by my inventory are over 600 Gg/year higher than the EPA GHGI in the Marcellus Shale, the increase of the simulated X_{CH4} are small. The highest difference of the simulated X_{CH4} in a single grid cell is ~2ppb, and the averaged difference of X_{CH4} for all grid cells is 0.46 ppb.

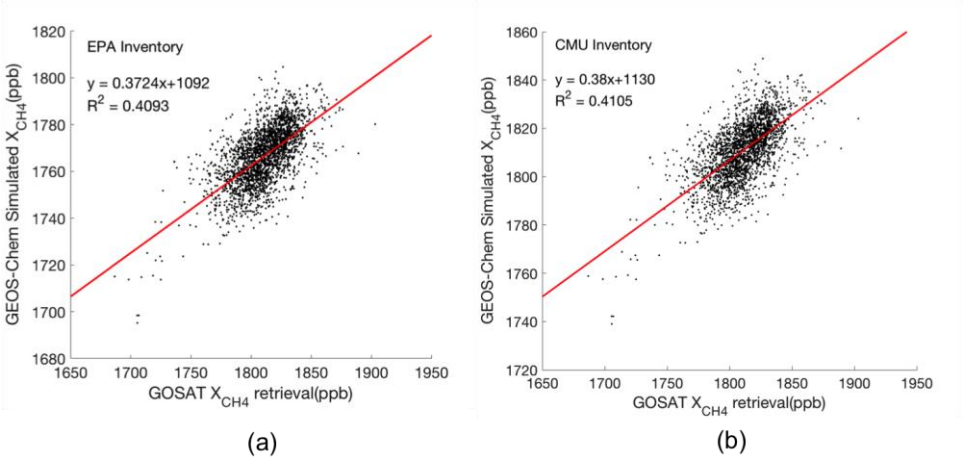

Figure 7.4 Comparison of the GOSAT X_{CH4} retrievals with (a) the GEOS-Chem simulated X_{CH4} with the EPA GHGI, and (b) the GEOS-Chem simulated X_{CH4} with our constructed inventory.

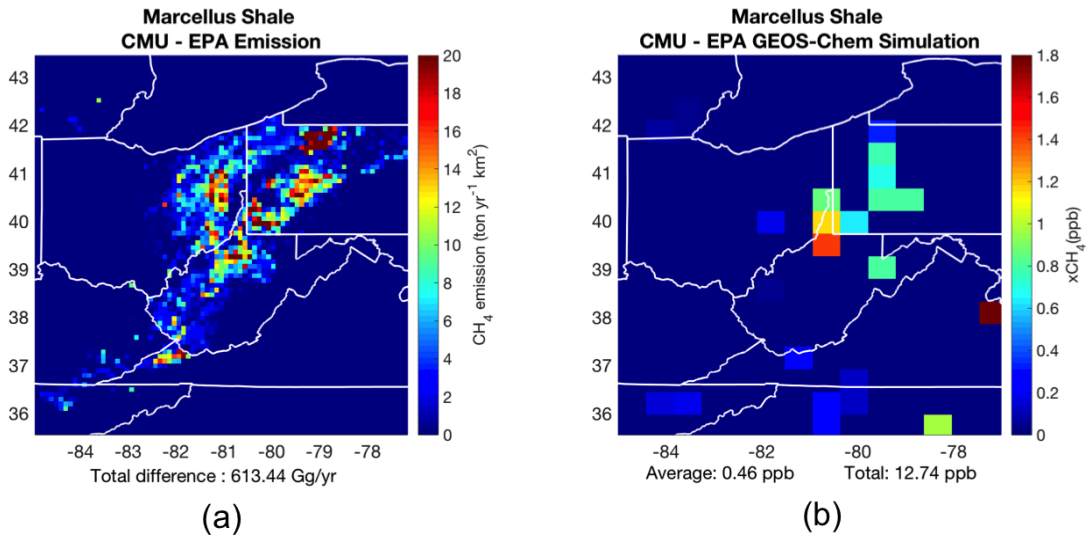

Figure 7.5 (a) The spatial difference of methane emissions from the natural gas production and distribution in the Marcellus Shale estimated by my inventory and the EPA GHGI, and (b) the spatial difference of simulated X_{CH4} with my inventory and simulated X_{CH4} with the EPA GHGI in the Marcellus Shale.

7.4 Conclusions

I constructed a gridded (0.1° × 0.1°) methane emission inventory of the natural gas production and distribution over the contiguous US based on the facility-level methane emissions of natural gas production facilities reported by recent ground measurements. Compared with the EPA GHGI and the Edgar v4.2, my inventory show higher methane emissions over major natural gas production fields, and the total methane emissions of the natural gas production and distribution sector estimated by my inventory are 74% and 20% higher than the Edgar v4.2 and EPA GHGI, respectively. The total methane emissions from the natural gas production and distribution are dominantly (73%) contributed by the natural gas production sector.

I also ran the GEOS-Chem methane simulation with either methane emission inventory of natural gas production and distribution constructed in this study or the gridded EPA GHGI and compared the results with the GOSAT measurements. Results show that my inventory can improve the model and

satellite comparison, but the improvement is very limited. The GEOS-Chem simulations with my inventory and EPA GHGI are similar, with small differences (0.5-2 ppb) over some major gas production fields.

The spatially resolved methane emission inventory of natural gas production and distribution constructed in this work can be applied to update the current default methane emission inventory of GEOS-Chem, and the updated methane emission inventory can be used as a better a priori emission field for top-down studies that inversely estimate methane emissions from atmospheric methane observation.

Table 7.1 Methane emissions from natural gas production and distribution estimated by this study, the EPA GHGI, and the Edgar v4.2

	CMU(2015)		EPA GHGI(2012)		Edgar v4.2 (2008)
	Emission (Gg/yr)	Percentage in total emission (%)	Emission (Gg/yr)	Percentage in total emission (%)	
Natural Gas Total	8271	-	6906	-	4758
Production	6007	73	4442	64	-
On-shore gas and oil wells	5254	64	-	-	-
Coalbed methane	319	4	-	-	-
Off-shore wells	271	3	-	-	-
Gathering station	162	2	-	-	-
Processing	691	8	890	13	-
Transmission	1116	13	1116	16	-
Distribution	457	6	457	7	-

Chapter 8
Conclusions and future work

8.1 Conclusions

In this work, we conducted multi-seasonal measurements in the Fort Pitt Tunnel in Pittsburgh, PA to characterize the gaseous and particulate air pollutants emitted from the on-road gasoline and diesel vehicles, which is a major energy use process that largely contributes to the air pollution in the urban area. And we also conducted mobile measurements in the Denver-Julesburg Basin, the Uintah Basin, and the Marcellus Shale to characterize the greenhouse gas and air pollutant emissions from the natural gas production system, which is a major energy production process that has increased dramatically in recent years and is expected to have a long-lasting impact in the future.

I report the fuel-based vehicle emission factors of gaseous and particulate pollutants (NO_x, CO, OC, EC, BC, PAH) measured in the traffic tunnel. The strong dependence of the fleet average vehicle emission factors to the $\%fuel_D$ allows us to perform linear regression to apportion the gasoline and diesel vehicle emission factors. Since there are several sources of uncertainties for the linear regression method that are hard to quantify, for NO_x, PAH and CO, which are measured at 1 Hz in the tunnel, I use the 1 Hz data and integrate peaks of individual truck plumes to estimate emission factors of HDDV. The emission factors measured in this study are compared with emission factors measured by Greishop et al. [67] ~10 years ago in the Squirrel Hill Tunnel in Pittsburgh, and I found that the NO_x, OC and EC emission factors of diesel vehicles and the NO_x and OC emission factors of gasoline vehicles significantly dropped (~50 - 70%) over the past 10 years, while the EC emission factors of gasoline vehicles measured in both studies are similar. To further confirm this long-term trend, I summarized emission factors measured in previous tunnel studies in U.S. since 1990s and compared them with the change of vehicle emission standards in U.S. Results show that the stricter emission standards were effective on regulating NO_x and PM emissions of diesel vehicles and the NO_x, CO and PM emissions of gasoline vehicles, while the EC emissions of gasoline vehicles did not change too much over the past three decades. By studying the trend of HDDV-to-LDV emission factor ratios measured in the tunnel since 1990s, I found that the relative importance of HDDV on NO_x and EC emissions

decreased, but the NO_x, OC and EC emissions of HDDV remain significantly higher (~5-10 times) than the LDV.

The number-size distribution and mass-size distribution of vehicle emitted particles measured in the traffic tunnel are also reported in this work. I assumed the vehicle emitted particles are nanoparticle aggregates composed of 30 nm spherical primary particles to calculate the size-dependent particle mass. The number-size distribution of vehicle emitted particles showed only one mode at 16 nm. After evaporating under 250 °C inside the TD, the median diameter of the number-size distribution of the vehicle emitted particles shifted from 16 nm to ~7 nm. The total particle number has a significant decrease (69%) after evaporating inside the TD, indicating that the vehicle emitted particles may be largely externally mixed, and a large fraction of vehicle emitted particles may be purely composed of volatile component. I also report a size-resolved volatile-to-non-volatile-component-ratio for vehicle emitted particles, which could be directly implemented into the TOMAS aerosol microphysics model in GEOS-Chem. It shows that the non-volatile component takes a large share (over 50%) of the mass of particles in the size range of 60 - 400 nm, while for particles in the size range of 10 – 60 nm, they are dominantly (over 75%) composed of volatile component. I also conduct source apportionment to get the size-resolved particles and non-volatile particles mass and number emission factors for both gasoline and diesel vehicles.

We measured the gas-particle partitioning of vehicle emitted POA in the traffic tunnel with three independent methods: artifact corrected bare-quartz filters, TD-ACSM measurements, and bare-Q filters analyzed with TD-GC-MS. Results from all methods consistently show that vehicle emitted POA measured in the traffic tunnel is semivolatile under a wide range of fleet compositions and ambient conditions. I compared the gas-particle partitioning of POA measured in both tunnel and dynamometer studies and found that volatility distributions measured in the traffic tunnel are similar to volatility distributions measured in the dynamometer studies, and predict similar gas-particle partitioning in the TD. These results suggest that the POA volatility distribution measured in the dynamometer studies can be applied to describe gas-particle partitioning of ambient POA emissions. The POA volatility distribution measured in the

tunnel does not have significant diurnal or seasonal variations, which indicate that a single volatility distribution is adequate to describe the gas-particle partitioning of vehicle emitted POA in the urban environment.

The VOC concentrations and the facility-level VOC emission rates measured downwind at individual natural gas production well pads and compressor stations in the Denver-Julesburg Basin, the Uintah Basin, and the NEPA are reported in this work. The VOC concentrations measured near facilities are in general not significantly higher than the regional background and the city ambient concentrations, except at two gas production well pads the Denver-Julesburg Basin, we observed significantly enhanced VOC concentrations, which are about 2-3 order of magnitude higher than other sites. It poses potential concerns on high BTEX exposure for people working and living on/near natural gas production sites. The facility-level VOC emission rates measured at gas production facilities in all three gas production fields are highly variable and cross a range of ~2-3 order of magnitudes. It suggests that a single VOC emission profile may not be able to characterize VOC emissions from all natural gas production facilities, and to use a single emission factor to estimate the total VOC emissions from all gas production facilities in a region may yield highly uncertain result. The VOC emission rates of the natural gas production well pads and the compressor stations measured in the Uintah Basin are similar. The VOC emission rates measured at gas wells in the NEPA are in general lower than they measured in the Denver-Julesburg Basin and the Uintah Basin, suggesting that the unconventional gas wells have a lower VOC emission rate compared with the conventional wells.

I construct a gridded (0.1° × 0.1°) methane emission inventory of the natural gas production and distribution over the contiguous US based on the facility-level methane emissions of natural gas production facilities reported by recent ground measurements. Compared with the EPA GHGI and the Edgar v4.2, my inventory show higher methane emissions over major natural gas production fields, and the total methane emissions of the natural gas production and distribution sector estimated by my inventory are 74% and 20% higher than the Edgar v4.2 and EPA GHGI, respectively. The total methane emissions from the natural gas production and distribution are dominantly (73%)

contributed by the natural gas production sector. I also ran the GEOS-Chem methane simulation with either methane emission inventory constructed in this study or the gridded EPA GHGI and compared the results with the GOSAT measurements. Results show that my inventory can improve the model and satellite comparison, but the improvement is very limited. The GEOS-Chem simulations with my inventory and EPA GHGI are similar, with small differences (0.5-2 ppb) over some major gas production fields.

The size-resolved emission factors of vehicle emitted particles and POA volatility distribution reported in this work can be applied by the chemical transport models to better quantify the contribution of vehicle emissions to the PM in the atmosphere.

Since our measurement of VOC emissions of natural gas production facilities were conducted before EPA started to regulate VOC emissions from the O&NG production facilities in Aug. 2016, the facility-level VOC emission rates reported in this work can serve as the basis for future studies to test the effectiveness of the regulation policies. The spatially resolved methane emission inventory of natural gas production and distribution constructed in this work can be applied to update the current default methane emission inventory of GEOS-Chem, and the updated methane emission inventory can be used as a better a priori emission field for top-down studies that inversely estimate methane emissions from atmospheric methane observation.

8.2 Future work

8.2.1 Continuous measurement of on-road gasoline and diesel vehicle emissions

Since the vehicle emission standards become stricter in US [100], and the application of new vehicle technology, such as the gasoline direct injection (GDI) engine, may alter the characteristic of on-road vehicle emissions [187,188], it is necessary to conduct on-road studies to continuously monitoring vehicle emissions in the future in order to test the effectiveness of policies on regulating vehicle emissions, and to get up-to-date vehicle emission factors.

8.2.2 Continuous measurement of VOC emissions from natural gas production facilities

Since US EPA started to regulate CH_4 and VOC emissions from the natural gas production facilities since 2016, it is necessary to measure facility-level VOC emissions afterwards and compare with our measurement to see the effectiveness of the regulations. Also, more field surveys are needed to better estimate the fraction of VOC ‘super emitters’ among all gas production facilities, and their contribution to the total VOC emissions from natural gas production systems.

References

[1] OMS, 2012, “Burden of Disease from Ambient and Household Air Pollution,” Public Heal. Environ. Soc. Determ. Heal. [Online]. Available: http://www.who.int/phe/health_topics/outdoorair/databases/en/.

[2] WHO, 2009, “Global Health Risks: Mortality and Burden of Disease Attributable to Selected Major Risks,” Bull. World Health Organ., **87**, pp. 646–646.

[3] Congress, 2004, “Clean Air Act - As Amended Through P.L. 108-201,” US Gov. Print. Off., **2**(5707), pp. 16–17.

[4] U.S. Environmental Protection Agency, 2010, “National Ambient Air Quality Standards (NAAQS),” http://www.epa.gov/air/criteria.html [Online]. Available: http://www.epa.gov/air/criteria.html.

[5] US EPA, OCSPP,OPPT, N., 2017, “Asbestos National Emissions Standard for Hazardous Air Pollutants (NESHAP),” U.S. EPA [Online]. Available: https://www.epa.gov/asbestos/asbestos-national-emissions-standard-hazardous-air-pollutants-neshap.

[6] Zhang, Q., Jimenez, J. L., Canagaratna, M. R., Allan, J. D., Coe, H., Ulbrich, I., Alfarra, M. R., Takami, A., Middlebrook, A. M., Sun, Y. L., Dzepina, K., Dunlea, E., Docherty, K., DeCarlo, P. F., Salcedo, D., Onasch, T., Jayne, J. T., Miyoshi, T., Shimono, A., Hatakeyama, S., Takegawa, N., Kondo, Y., Schneider, J., Drewnick, F., Borrmann, S., Weimer, S., Demerjian, K., Williams, P., Bower, K., Bahreini, R., Cottrell, L., Griffin, R. J., Rautiainen, J., Sun, J. Y., Zhang, Y. M., and Worsnop, D. R., 2007, “Ubiquity and Dominance of Oxygenated Species in Organic Aerosols in Anthropogenically-Influenced Northern Hemisphere Midlatitudes,” Geophys. Res. Lett., **34**(13).

[7] Kanakidou, M., Seinfeld, J. H., Pandis, S. N., Barnes, I., Dentener, F. J., Facchini, M. C., Van Dingenen, R., Ervens, B., Nenes, A., Nielsen, C. J., Swietlicki, E., Putaud, J. P., Balkanski, Y., Fuzzi, S., Horth, J., Moortgat, G. K., Winterhalter, R., Myhre, C. E. L., Tsigaridis, K., Vignati, E., Stephanou, E. G., and Wilson, J., 2005, “Organic Aerosol and Global Climate Modelling: A Review,” Atmos. Chem. Phys., **5**, pp. 1053–1123.

[8] Seinfeld, J. H., and Pandis, S. N., 2006, *Atmospheric Chemistry and Physics:*

From Air Pollution to Climate Change.

[9] Cheng, M. T., and Tsai, Y. I., 2000, “Characterization of Visibility and Atmospheric Aerosols in Urban, Suburban, and Remote Areas,” Sci. Total Environ., **263**(1-3), pp. 101–114.

[10] Cao, J. J., Wang, Q. Y., Chow, J. C., Watson, J. G., Tie, X. X., Shen, Z. X., Wang, P., and An, Z. S., 2012, “Impacts of Aerosol Compositions on Visibility Impairment in Xi’an, China,” Atmos. Environ., **59**, pp. 559–566.

[11] Zhao, H., Che, H., Zhang, X., Ma, Y., Wang, Y., Wang, H., and Wang, Y., 2013, “Characteristics of Visibility and Particulate Matter (PM) in an Urban Area of Northeast China,” Atmos. Pollut. Res., **4**(4), pp. 427–434.

[12] Dockery, D. W., Pope, C. A., Xu, X., Spengler, J. D., Ware, J. H., Fay, M. E., Ferris, B. G., and Speizer, F. E., 1993, “An Association between Air Pollution and Mortality in Six U.S. Cities,” N. Engl. J. Med., **329**(24), pp. 1753–1759.

[13] West, J., Cohen, A., Dentener, F., Brunekreef, B., Zhu, T., Armstrong, B., Bell, M., Brauer, M., Carmichael, G. R., Costa, D., Dockery, D., Kleeman, M. J., Krzyzanowski, M., Kunzli, N., Liousse, C., Lung, S.-C., Martin, R. V, Pöschl, U., Pope, C. A., Roberts, J. M., Russell, A. G., and Wiedinmyer, C., 2016, “What We Breathe Impacts Our Health: Improving Understanding of the Link between Air Pollution and Health,” Environ. Sci. Technol., p. acs.est.5b03827.

[14] IPCC, 2013, “IPCC Fifth Assessment Report (AR5),” IPCC, p. s. 10–12.

[15] Lohmann, U., and Feichter, J., 2004, “Global Indirect Aerosol Effects: A Review,” Atmos. Chem. Phys. Discuss., **4**(6), pp. 7561–7614.

[16] Bond, T. C., Doherty, S. J., Fahey, D. W., Forster, P. M., Berntsen, T., Deangelo, B. J., Flanner, M. G., Ghan, S., K??rcher, B., Koch, D., Kinne, S., Kondo, Y., Quinn, P. K., Sarofim, M. C., Schultz, M. G., Schulz, M., Venkataraman, C., Zhang, H., Zhang, S., Bellouin, N., Guttikunda, S. K., Hopke, P. K., Jacobson, M. Z., Kaiser, J. W., Klimont, Z., Lohmann, U., Schwarz, J. P., Shindell, D., Storelvmo, T., Warren, S. G., and Zender, C. S., 2013, “Bounding the Role of Black Carbon in the Climate System: A Scientific Assessment,” J. Geophys. Res. Atmos., **118**(11), pp. 5380–5552.

[17] Stavrakou, T., Müller, J. F., Boersma, K. F., Van Der A., R. J., Kurokawa, J.,

Ohara, T., and Zhang, Q., 2013, “Key Chemical NOx Sink Uncertainties and How They Influence Top-down Emissions of Nitrogen Oxides,” Atmos. Chem. Phys., **13**(17), pp. 9057–9082.

[18] NEI EPA, 2016, “National Emissions Inventory (NEI),” US Environ. Prot. Agency [Online]. Available: https://www.epa.gov/air-emissions-inventories.

[19] Xu, L., Guo, H., Boyd, C. M., Klein, M., Bougiatioti, A., Cerully, K. M., Hite, J. R., Isaacman-VanWertz, G., Kreisberg, N. M., Knote, C., Olson, K., Koss, A., Goldstein, A. H., Hering, S. V., de Gouw, J., Baumann, K., Lee, S.-H., Nenes, A., Weber, R. J., and Ng, N. L., 2015, “Effects of Anthropogenic Emissions on Aerosol Formation from Isoprene and Monoterpenes in the Southeastern United States.,” Proc. Natl. Acad. Sci. U. S. A., **112**(1), pp. 37–42.

[20] Goldstein, A. H., Koven, C. D., Heald, C. L., and Fung, I. Y., 2009, “Biogenic Carbon and Anthropogenic Pollutants Combine to Form a Cooling Haze over the Southeastern United States.,” Nature, **106**(22), pp. 8835–40.

[21] Heo, J., de Foy, B., Olson, M. R., Pakbin, P., Sioutas, C., and Schauer, J. J., 2015, “Impact of Regional Transport on the Anthropogenic and Biogenic Secondary Organic Aerosols in the Los Angeles Basin,” Atmos. Environ., **103**, pp. 171–179.

[22] Moan, J. L., and Smith, Z. A., 2007, “Energy Use Worldwide: A Reference Handbook,” ABC-CLIO, p. 337.

[23] Doe/Eia, 2012, *Annual Energy Review 2011*.

[24] Dallmann, T. R., and Harley, R. A., 2010, “Evaluation of Mobile Source Emission Trends in the United States,” J. Geophys. Res. Atmos., **115**(14), pp. 1–12.

[25] United States Department of Transportation, 2017, “National Transportation Statistics” [Online]. Available: www.rita.dot.gov/bts/sites/rita.dot.gov.bts/files/publications/national_transportation_statistics/index.html.

[26] US Environmental Protection Agency, “History of Reducing Air Pollution from Transportation in the United States” [Online]. Available: https://www.epa.gov/air-pollution-transportation/accomplishments-and-success-air-pollution-transportation.

[27] U.S. Energy Information Administration, 2017, *August 2017 Monthly Energy Review*.

[28] EIA, 2016, “Annual Energy Outlook 2016,” U.S. Energy Inf. Adm., p. ES–5.

[29] U.S. Energy Information Administration, 2017, “Short-Term Energy Outlook (STEO),” Short-Term Energy Outlook (STEO), (September 2017), p. 49.

[30] Brandt, A. R., Heath, G. A., Kort, E. A., O’Sullivan, F., Pétron, G., Jordaan, S. M., Tans, P., Wilcox, J., Gopstein, A. M., Arent, D., Wofsy, S., Brown, N. J., Bradley, R., Stucky, G. D., Eardley, D., and Harriss, R., 2014, “Methane Leaks from North American Natural Gas Systems,” Science (80-.)., **343**(6172), pp. 733–735.

[31] Alvarez, R. A., Pacala, S. W., Winebrake, J. J., Chameides, W. L., and Hamburg, S. P., 2012, “Greater Focus Needed on Methane Leakage from Natural Gas Infrastructure.,” Proc. Natl. Acad. Sci. U. S. A., **109**(17), pp. 6435–40.

[32] Turner, A. J., Jacob, D. J., Benmergui, J., Wofsy, S. C., Maasakkers, J. D., Butz, A., Hasekamp, O., and Biraud, S. C., 2016, “A Large Increase in U.S. Methane Emissions over the Past Decade Inferred from Satellite Data and Surface Observations,” Geophys. Res. Lett., **43**(5), pp. 2218–2224.

[33] Pétron, G., Frost, G., Miller, B. R., Hirsch, A. I., Montzka, S. A., Karion, A., Trainer, M., Sweeney, C., Andrews, A. E., Miller, L., Kofler, J., Bar-Ilan, A., Dlugokencky, E. J., Patrick, L., Moore, C. T., Ryerson, T. B., Siso, C., Kolodzey, W., Lang, P. M., Conway, T., Novelli, P., Masarie, K., Hall, B., Guenther, D., Kitzis, D., Miller, J., Welsh, D., Wolfe, D., Neff, W., and Tans, P., 2012, “Hydrocarbon Emissions Characterization in the Colorado Front Range: A Pilot Study,” J. Geophys. Res. Atmos., **117**(4).

[34] Howarth, R. W., Santoro, R., and Ingraffea, A., 2011, “Methane and the Greenhouse-Gas Footprint of Natural Gas from Shale Formations,” Clim. Change, **106**(4), pp. 679–690.

[35] Gilman, J. B., Lerner, B. M., Kuster, W. C., and De Gouw, J. a., 2013, “Source Signature of Volatile Organic Compounds from Oil and Natural Gas Operations in Northeastern Colorado,” Environ. Sci. Technol., **47**(3), pp. 1297–1305.

[36] Warneke, C., Geiger, F., Edwards, P. M., Dube, W., Pétron, G., Kofler, J., Zahn, A., Brown, S. S., Graus, M., Gilman, J. B., Lerner, B. M., Peischl, J., Ryerson, T. B., de Gouw, J. A., and Roberts, J. M., 2014, "Volatile Organic Compound Emissions from the Oil and Natural Gas Industry in the Uintah Basin, Utah: Oil and Gas Well Pad Emissions Compared to Ambient Air Composition," Atmos. Chem. Phys., **14**(20), pp. 10977–10988.

[37] Pétron, G., Karion, A., Sweeney, C., Miller, B. R., Montzka, S. A., Frost, G. J., Trainer, M., Tans, P., Andrews, A., Kofler, J., Helmig, D., Guenther, D., Dlugokencky, E., Lang, P., Newberger, T., Wolter, S., Hall, B., Novelli, P., Brewer, A., Conley, S., Hardesty, M., Banta, R., White, A., Noone, D., Wolfe, D., and Schnell, R., 2014, "A New Look at Methane and Nonmethane Hydrocarbon Emissions from Oil and Natural Gas Operations in the Colorado Denver-Julesburg Basin," J. Geophys. Res. Atmos., pp. 1–17.

[38] Helmig, D., Thompson, C. R., Evans, J., Boylan, P., Hueber, J., and Park, J. H., 2014, "Highly Elevated Atmospheric Levels of Volatile Organic Compounds in the Uintah Basin, Utah," Environ. Sci. Technol., **48**(9), pp. 4707–4715.

[39] Katzenstein, A. S., Doezema, L. A., Simpson, I. J., Blake, D. R., and Rowland, F. S., 2003, "Extensive Regional Atmospheric Hydrocarbon Pollution in the Southwestern United States.," Proc. Natl. Acad. Sci., **100**(21), pp. 11975–11979.

[40] Kemball-Cook, S., Bar-Ilan, A., Grant, J., Parker, L., Jung, J., Santamaria, W., Mathews, J., and Yarwood, G., 2010, "Ozone Impacts of Natural Gas Development in the Haynesville Shale," Environ. Sci. Technol., **44**(24), pp. 9357–9363.

[41] Schnell, R. C., Oltmans, S. J., Neely, R. R., Endres, M. S., Molenar, J. V., and White, A. B., 2009, "Rapid Photochemical Production of Ozone at High Concentrations in a Rural Site during Winter," Nat. Geosci., **2**(2), pp. 120–122.

[42] Roy, A. A., Adams, P. J., Robinson, A. L., Roy, A. A., Adams, P. J., Air, A. L. R., Roy, A. A., Adams, P. J., and Robinson, A. L., 2014, "Air Pollutant Emissions from the Development , Production , and Processing of Marcellus Shale Natural Gas Air Pollutant Emissions from the Development , Production , and Processing of Marcellus Shale Natural Gas," **2247**(May 2017).

[43] Roohani, Y. H., Roy, A. A., Heo, J., Robinson, A. L., and Adams, P. J., 2017, "Impact of Natural Gas Development in the Marcellus and Utica Shales on Regional Ozone and Fi Ne Particulate Matter Levels," Atmos. Environ., **155**, pp. 11–20.

[44] Vinciguerra, T., Yao, S., Dadzie, J., Chittams, A., Deskins, T., Ehrman, S., and Dickerson, R. R., 2015, “Regional Air Quality Impacts of Hydraulic Fracturing and Shale Natural Gas Activity : Evidence from Ambient VOC Observations,” Atmos. Environ., **110**, pp. 144–150.

[45] McKenzie, L. M., Witter, R. Z., Newman, L. S., and Adgate, J. L., 2012, “Human Health Risk Assessment of Air Emissions from Development of Unconventional Natural Gas Resources,” Sci. Total Environ., **424**, pp. 79–87.

[46] Colborn, T., Kwiatkowski, C., Schultz, K., and Bachran, M., 2011, “Natural Gas Operations from a Public Health Perspective,” Hum. Ecol. Risk Assess. An Int. J., **17**(5), pp. 1039–1056.

[47] Adgate, J. L., Goldstein, B. D., and McKenzie, L. M., 2014, “Potential Public Health Hazards, Exposures and Health Effects from Unconventional Natural Gas Development,” Environ. Sci. Technol., **48**(15), pp. 8307–8320.

[48] U.S. EPA, “The 2011 National Emissions Inventory.” [Online]. Available: http://www3.epa.gov/ttnchie1/net/2011inventory.html.

[49] Gentner, D. R., Jathar, S. H., Gordon, T. D., Bahreini, R., Day, D. A., El Haddad, I., Hayes, P. L., Pieber, S. M., Platt, S. M., de Gouw, J., Goldstein, A. H., Harley, R. A., Jimenez, J. L., Prévôt, A. S. H., and Robinson, A. L., 2017, “Review of Urban Secondary Organic Aerosol Formation from Gasoline and Diesel Motor Vehicle Emissions,” Environ. Sci. Technol., **51**(3), pp. 1074–1093.

[50] Tkacik, D. S., Lambe, A. T., Jathar, S., Li, X., Presto, A. A., Zhao, Y., Blake, D., Meinardi, S., Jayne, J. T., Croteau, P. L., and Robinson, A. L., 2014, “Secondary Organic Aerosol Formation from In-Use Motor Vehicle Emissions Using a Potential Aerosol Mass Reactor.,” Environ. Sci. Technol., **48**(19), pp. 11235–42.

[51] Nam, E., Kishan, S., Baldauf, R. W., Fulper, C. R., Sabisch, M., and Warila, J., 2010, “Temperature Effects on Particulate Matter Emissions from Light-Duty, Gasoline-Powered Motor Vehicles.,” Environ. Sci. Technol., **44**(12), pp. 4672–4677.

[52] May, A. A., Nguyen, N. T., Presto, A. a., Gordon, T. D., Lipsky, E. M., Karve, M., Gutierrez, A., Robertson, W. H., Zhang, M., Brandow, C., Chang, O., Chen, S., Cicero-Fernandez, P., Dinkins, L., Fuentes, M., Huang, S. M., Ling, R., Long, J.,

Maddox, C., Massetti, J., McCauley, E., Miguel, A., Na, K., Ong, R., Pang, Y., Rieger, P., Sax, T., Truong, T., Vo, T., Chattopadhyay, S., Maldonado, H., Maricq, M. M., and Robinson, A. L., 2014, “Gas- and Particle-Phase Primary Emissions from In-Use, On-Road Gasoline and Diesel Vehicles,” Atmos. Environ., **88**, pp. 247–260.

[53] Schauer, J. J., Kleeman, M. J., Cass, G. R., and Simoneit, B. R. T., 2002, “Measurement of Emissions from Air Pollution Sources. 5. C1-C32 Organic Compounds from Gasoline-Powered Motor Vehicles.,” Environ. Sci. Technol., **36**(6), pp. 1169–1180.

[54] Durant, J. L., Ash, C. A., Wood, E. C., Herndon, S. C., Jayne, J. T., Knighton, W. B., Canagaratna, M. R., Trull, J. B., Brugge, D., Zamore, W., and Kolb, C. E., 2010, “Short-Term Variation in near-Highway Air Pollutant Gradients on a Winter Morning,” Atmos. Chem. Phys., **10**(17), pp. 8341–8352.

[55] Gouriou, F., Morin, J. P., and Weill, M. E., 2004, “On-Road Measurements of Particle Number Concentrations and Size Distributions in Urban and Tunnel Environments,” Atmos. Environ., **38**(18), pp. 2831–2840.

[56] Kam, W., Liacos, J. W., Schauer, J. J., Delfino, R. J., and Sioutas, C., 2012, “On-Road Emission Factors of PM Pollutants for Light-Duty Vehicles (LDVs) Based on Urban Street Driving Conditions,” Atmos. Environ., **61**, pp. 378–386.

[57] Zhu, Y., Hinds, W. C., Kim, S., Shen, S., and Sioutas, C., 2002, “Study of Ultrafine Particles near a Major Highway with Heavy-Duty Diesel Traffic,” Atmos. Environ., **36**(27), pp. 4323–4335.

[58] Massoli, P., Fortner, E. C., Canagaratna, M. R., Williams, L. R., Zhang, Q., Sun, Y., Schwab, J. J., Trimborn, A., Onasch, T. B., Demerjian, K. L., Kolb, C. E., Worsnop, D. R., and Jayne, J. T., 2012, “Pollution Gradients and Chemical Characterization of Particulate Matter from Vehicular Traffic near Major Roadways: Results from the 2009 Queens College Air Quality Study in NYC,” Aerosol Sci. Technol., **46**(11), pp. 1201–1218.

[59] Liggio, J., Gordon, M., Smallwood, G., Li, S. M., Stroud, C., Staebler, R., Lu, G., Lee, P., Taylor, B., and Brook, J. R., 2012, “Are Emissions of Black Carbon from Gasoline Vehicles Underestimated? Insights from near and on-Road Measurements,” Environ. Sci. Technol., **46**(9), pp. 4819–4828.

[60] Canagaratna, M. R., Jayne, J. T., Ghertner, D. a., Herndon, S., Shi, Q., Jimenez,

J. L., Silva, P. J., Williams, P., Lanni, T., Drewnick, F., Demerjian, K. L., Kolb, C. E., and Worsnop, D. R., 2004, “Chase Studies of Particulate Emissions from in-Use New York City Vehicles,” Aerosol Sci. Technol., **38**(6), pp. 555–573.

[61] Pierson, W. R., Gertler, A. W., Robinson, N. F., Sagebiel, J. C., Zielinska, B., Bishop, G. A., Stedman, D. H., Zweidinger, R. B., and Ray, W. D., 1996, “Real-World Automotive Emissions - Summary of Studies in the Fort McHenry and Tuscarora Mountain Tunnels,” Atmos. Environ., **30**(12), pp. 2233–2256.

[62] Miguel, A. H., Kirchstetter, T. W., Harley, R. A., and Hering, S. V., 1998, “On-Road Emissions of Particulate Polycyclic Aromatic Hydrocarbons and Black Carbon from Gasoline and Diesel Vehicles,” Environ. Sci. Technol., **32**(4), pp. 450–455.

[63] Kirchstetter, T. W., Harley, R. a., Kreisberg, N. M., Stolzenburg, M. R., and Hering, S. V., 1999, “On-Road Measurement of Fine Particle and Nitrogen Oxide Emissions from Light- and Heavy-Duty Motor Vehicles,” Atmos. Environ., **33**(18), pp. 2955–2968.

[64] Allen, J. O., Mayo, P. R., Hughes, L. S., Salmon, L. G., and Cass, G. R., 2001, “Emissions of Size-Segregated Aerosols from on-Road Vehicles in the Caldecott Tunnel,” Environ. Sci. Technol., **35**(21), pp. 4189–4197.

[65] McGaughey, G. R., Desai, N. R., Allen, D. T., Seila, R. L., Lonneman, W. A., Fraser, M. P., Harley, R. A., Pollack, A. K., Ivy, J. M., and Price, J. H., 2004, “Analysis of Motor Vehicle Emissions in a Houston Tunnel during the Texas Air Quality Study 2000,” Atmos. Environ., **38**(20), pp. 3363–3372.

[66] Gëller, M. D., Sardar, S. B., Phuleria, H., Fine, P. M., and Sioutas, C., 2005, “Measurements of Particle Number and Mass Concentrations and Size Distributions in a Tunnel Environment,” Environ. Sci. Technol., **39**(22), pp. 8653–8663.

[67] Grieshop, A. P., Lipsky, E. M., Pekney, N. J., Takahama, S., and Robinson, A. L., 2006, “Fine Particle Emission Factors from Vehicles in a Highway Tunnel: Effects of Fleet Composition and Season,” Atmos. Environ., **40**, pp. 287–298.

[68] Ban-Weiss, G. A., McLaughlin, J. P., Harley, R. A., Lunden, M. M., Kirchstetter, T. W., Kean, A. J., Strawa, A. W., Stevenson, E. D., and Kendall, G. R., 2008, “Long-Term Changes in Emissions of Nitrogen Oxides and Particulate Matter from on-Road Gasoline and Diesel Vehicles,” Atmos. Environ., **42**(2), pp. 220–232.

[69] Dallmann, T. R., Demartini, S. J., Kirchstetter, T. W., Herndon, S. C., Onasch, T. B., Wood, E. C., and Harley, R. a., 2012, “On-Road Measurement of Gas and Particle Phase Pollutant Emission Factors for Individual Heavy-Duty Diesel Trucks,” Environ. Sci. Technol., **46**(15), pp. 8511–8518.

[70] Dallmann, T. R., Kirchstetter, T. W., Demartini, S. J., and Harley, R. A., 2013, “Quantifying on-Road Emissions from Gasoline-Powered Motor Vehicles: Accounting for the Presence of Medium- and Heavy-Duty Diesel Trucks,” Environ. Sci. Technol., **47**(23), pp. 13873–13881.

[71] Ho, J., and Winer, A. M., 1998, “Effects of Fuel Type, Driving Cycle, and Emission Status on in-Use Vehicle Exhaust Reactivity.,” J. Air Waste Manag. Assoc., **48**(7), pp. 592–603.

[72] Singer, B. C., Kirchstetter, T. W., Harley, R. A., Kendall, G. R., and Hesson, J. M., 1999, “A Fuel-Based Approach to Estimating Motor Vehicle Cold-Start Emissions,” J. Air Waste Manag. Assoc., **49**(2), pp. 125–135.

[73] Sternbeck, J., Sjödin, Å., and Andréasson, K., 2002, “Metal Emissions from Road Traffic and the Influence of Resuspension - Results from Two Tunnel Studies,” Atmos. Environ., **36**(30), pp. 4735–4744.

[74] Hsu, Y. C., Tsai, J. H., Chen, H. W., and Lin, W. Y., 2001, “Tunnel Study of on-Road Vehicle Emissions and the Photochemical Potential in Taiwan,” Chemosphere, **42**(3), pp. 227–234.

[75] Smit, R., Kingston, P., Wainwright, D. H., and Tooker, R., 2017, “A Tunnel Study to Validate Motor Vehicle Emission Prediction Software in Australia,” Atmos. Environ., **151**, pp. 188–199.

[76] Zhang, Y., Wang, X., Wen, S., Herrmann, H., Yang, W., Huang, X., Zhang, Z., Huang, Z., He, Q., and George, C., 2016, “On-Road Vehicle Emissions of Glyoxal and Methylglyoxal from Tunnel Tests in Urban Guangzhou, China,” Atmos. Environ., **127**, pp. 55–60.

[77] Pérez-Martínez, P. J., Miranda, R. M., Nogueira, T., Guardani, M. L., Fornaro, A., Ynoue, R., and Andrade, M. F., 2014, “Emission Factors of Air Pollutants from Vehicles Measured inside Road Tunnels in S??o Paulo: Case Study Comparison,” Int. J. Environ. Sci. Technol., **11**(8), pp. 2155–2168.

[78] Popa M., E., Vollmer M., K., Jordan, A., Brand W., A., Pathirana S., L., Rothe, M., and Röckmann, T., 2014, “Vehicle Emissions of Greenhouse Gases and Related Tracers from a Tunnel Study: CO:CO2, N2O:CO2, CH4:CO2, O2:CO2 Ratios, and the Stable Isotopes 13C and 18O in CO2 and CO,” Atmos. Chem. Phys., **14**(4), pp. 2105–2123.

[79] Alves, C. A., Gomes, J., Nunes, T., Duarte, M., Calvo, A., Custódio, D., Pio, C., Karanasiou, A., and Querol, X., 2015, “Size-Segregated Particulate Matter and Gaseous Emissions from Motor Vehicles in a Road Tunnel,” Atmos. Res., **153**, pp. 134–144.

[80] Neeft, J. P. A., Makkee, M., and Moulijn, J. A., 1996, “Diesel Particulate Emission Control,” Fuel Process. Technol., **47**(1), pp. 1–69.

[81] Forzatti, P., 2001, “Present Status and Perspectives in de-NOx SCR Catalysis,” Appl. Catal. A Gen., **222**(1-2), pp. 221–236.

[82] Maricq, M. M., 2007, “Chemical Characterization of Particulate Emissions from Diesel Engines: A Review,” J. Aerosol Sci., **38**(11), pp. 1079–1118.

[83] Kleeman, M. J., Schauer, J. J., and Cass, G. R., 2000, “Size and Composition Distribution of Fine Particulate Matter Emitted from Motor Vehicles,” Environ. Sci. Technol., **34**(7), pp. 1132–1142.

[84] Fujitani, Y., Saitoh, K., Fushimi, A., Takahashi, K., Hasegawa, S., Tanabe, K., Kobayashi, S., Furuyama, A., Hirano, S., and Takami, A., 2012, “Effect of Isothermal Dilution on Emission Factors of Organic Carbon and N-Alkanes in the Particle and Gas Phases of Diesel Exhaust,” Atmos. Environ., **59**, pp. 389–397.

[85] Zhang, R., Wang, G., Guo, S., Zamora, M. L., Ying, Q., Lin, Y., Wang, W., Hu, M., and Wang, Y., 2015, “Formation of Urban Fine Particulate Matter,” Chem. Rev., **115**(10), pp. 3803–3855.

[86] Pierce, J. R., and Adams, P. J., 2008, “Uncertainty in Global CCN Concentrations from Uncertain Aerosol Nucleation and Primary Emission Rates,” Atmos. Chem. Phys. Discuss., **8**, pp. 16291–16333.

[87] Lee, L. A., Pringle, K. J., Reddington, C. L., Mann, G. W., Stier, P., Spracklen, D.

V., Pierce, J. R., and Carslaw, K. S., 2013, “The Magnitude and Causes of Uncertainty in Global Model Simulations of Cloud Condensation Nuclei,” Atmos. Chem. Phys., **13**(17), pp. 8879–8914.

[88] Hinds, W. C., 1999, *Aerosol Technology: Properties, Behavior, and Measurement of Airborne Particles.*

[89] Brown, J. S., Zeman, K. L., and Bennett, W. D., 2002, “Ultrafine Particle Deposition and Clearance in the Healthy and Obstructed Lung,” Am. J. Respir. Crit. Care Med., **166**(9), pp. 1240–1247.

[90] Oberdörster, G., 2000, “Pulmonary Effects of Inhaled Ultrafine Particles,” Int. Arch. Occup. Environ. Health, **74**(1), pp. 1–8.

[91] Peters, A., Wichmann, H. E., Tuch, T., Heinrich, J., and Heyder, J., 1997, “Respiratory Effects Are Associated with the Number of Ultrafine Particles.,” Am. J. Respir. Crit. Care Med., **155**(September 1990), pp. 1376–1383.

[92] Lu, T., Cheung, C. S., and Huang, Z., 2012, “Size-Resolved Volatility, Morphology, Nanostructure, and Oxidation Characteristics of Diesel Particulate,” Energy and Fuels, **26**(10), pp. 6168–6176.

[93] Kittelson, D. B., Watts, W. F., Johnson, J. P., Schauer, J. J., and Lawson, D. R., 2006, “On-Road and Laboratory Evaluation of Combustion Aerosols-Part 2:. Summary of Spark Ignition Engine Results,” J. Aerosol Sci., **37**(8), pp. 931–949.

[94] Kittelson, D. B., Watts, W. F., and Johnson, J. P., 2006, “On-Road and Laboratory Evaluation of Combustion Aerosols-Part1: Summary of Diesel Engine Results,” J. Aerosol Sci., **37**(8), pp. 913–930.

[95] Johnson, J. P., Kittelson, D. B., and Watts, W. F., 2005, “Source Apportionment of Diesel and Spark Ignition Exhaust Aerosol Using on-Road Data from the Minneapolis Metropolitan Area,” Atmos. Environ., **39**(11), pp. 2111–2121.

[96] Imhof, D., Weingartner, E., Prévôt, A. S. H., Ordóñez, C., Kurtenbach, R., Wiesen, P., Rodler, J., Sturm, P., McCrae, I., Sjödin, Å., and Baltensperger, U., 2005, “Aerosol and NOx Emission Factors and Submicron Particle Number Size Distributions in Two Road Tunnels with Different Traffic Regimes,” Atmos. Chem. Phys. Discuss., **5**, pp. 5127–5166.

[97] Strawa, A. W., Kirchstetter, T. W., Hallar, A. G., Ban-Weiss, G. A., McLaughlin, J. P., Harley, R. A., and Lunden, M. M., 2010, “Optical and Physical Properties of Primary on-Road Vehicle Particle Emissions and Their Implications for Climate Change,” J. Aerosol Sci., **41**(1), pp. 36–50.

[98] Ban-Weiss, G. A., Lunden, M. M., Kirchstetter, T. W., and Harley, R. A., 2010, “Size-Resolved Particle Number and Volume Emission Factors for on-Road Gasoline and Diesel Motor Vehicles,” J. Aerosol Sci., **41**(1), pp. 5–12.

[99] Abu-Allaban, M., Gillies, J. A., and Gertler, A. W., 2003, “Application of a Multi-Lag Regression Approach to Determine on-Road PM10 and PM2.5 Emission Rates,” Atmos. Environ., **37**(37), pp. 5157–5164.

[100] Agency, U. S. E. P., 2014, “Tier 3 Motor Vehicle Emission and Fuel Standards,” Off. Transp. Air Qual. EPA-420-F-14-009, (March), pp. 5–9.

[101] Lehtoranta, K., Vesala, H., Koponen, P., and Korhonen, S., 2015, “Selective Catalytic Reduction Operation with Heavy Fuel Oil: NOx, NH3, and Particle Emissions,” Environ. Sci. Technol., **49**(7), pp. 4735–4741.

[102] Caroca, J. C., Millo, F., Vezza, D., Vlachos, T., De Filippo, A., Bensaid, S., Russo, N., and Fino, D., 2011, “Detailed Investigation on Soot Particle Size Distribution during DPF Regeneration, Using Standard and Bio-Diesel Fuels,” Ind. Eng. Chem. Res., **50**(5), pp. 2650–2658.

[103] Hodzic, A., Jimenez, J. L., Madronich, S., Canagaratna, M. R., Decarlo, P. F., Kleinman, L., and Fast, J., 2010, “Modeling Organic Aerosols in a Megacity: Potential Contribution of Semi-Volatile and Intermediate Volatility Primary Organic Compounds to Secondary Organic Aerosol Formation,” Atmos. Chem. Phys., **10**(12), pp. 5491–5514.

[104] Shrivastava, M. K., Lane, T. E., Donahue, N. M., Pandis, S. N., and Robinson, A. L., 2008, “Effects of Gas Particle Partitioning and Aging of Primary Emissions on Urban and Regional Organic Aerosol Concentrations,” J. Geophys. Res. Atmos., **113**(18), pp. 1–16.

[105] Robinson, A. L., Donahue, N. M., Shrivastava, M. K., Weitkamp, E. a, Sage, A. M., Grieshop, A. P., Lane, T. E., Pierce, J. R., and Pandis, S. N., 2007, “Rethinking Organic Aerosols: Semivolatile Emissions and Photochemical Aging.,” Science, **315**(5816), pp. 1259–1262.

[106] Kuhn, T., Biswas, S., Fine, P. M., Geller, M., and Sioutas, C., 2005, “Physical and Chemical Characteristics and Volatility of PM in the Proximity of a Light-Duty Vehicle Freeway,” Aerosol Sci. Technol., **39**(4), pp. 347–357.

[107] Lipsky, E. M., and Robinson, A. L., 2005, “Effects of Dilution on Fine Particle Mass and Partitioning of Semivolatile Organics in Diesel Exhaust and Wood Smoke,” Environ. Sci. Technol., **40**(1), pp. 155–162.

[108] Grieshop, A. P., Miracolo, M. a., Donahue, N. M., and Robinson, A. L., 2009, “Constraining the Volatility Distribution and Gas-Particle Partitioning of Combustion Aerosols Using Isothermal Dilution and Thermodenuder Measurements,” Environ. Sci. Technol., **43**(13), pp. 4750–4756.

[109] Huffman, J. A., Docherty, K. S., Mohr, C., Cubison, M. J., Ulbrich, I. M., Ziemann, P. J., Onasch, T. B., and Jimenez, J. L., 2009, “Chemically-Resolved Volatility Measurements of Organic Aerosol from Different Sources,” Environ. Sci. Technol., **43**(14), pp. 5351–5357.

[110] Verma, V., Pakbin, P., Cheung, K. L., Cho, A. K., Schauer, J. J., Shafer, M. M., Kleinman, M. T., and Sioutas, C., 2011, “Physicochemical and Oxidative Characteristics of Semi-Volatile Components of Quasi-Ultrafine Particles in an Urban Atmosphere,” Atmos. Environ., **45**(4), pp. 1025–1033.

[111] Ranjan, M., Presto, A. A., May, A. A., and Robinson, A. L., 2012, “Temperature Dependence of Gas–Particle Partitioning of Primary Organic Aerosol Emissions from a Small Diesel Engine,” Aerosol Sci. Technol., **46**(1), pp. 13–21.

[112] Presto, A. A., Hennigan, C. J., Nguyen, N. T., and Robinson, A. L., 2012, “Determination of Volatility Distributions of Primary Organic Aerosol Emissions from Internal Combustion Engines Using Thermal Desorption Gas Chromatography Mass Spectrometry,” Aerosol Sci. Technol., **46**(10), pp. 1129–1139.

[113] May, A. A., Presto, A. A., Hennigan, C. J., Nguyen, N. T., Gordon, T. D., and Robinson, A. L., 2013, “Gas-Particle Partitioning of Primary Organic Aerosol Emissions: (1) Gasoline Vehicle Exhaust,” Atmos. Environ., **77**, pp. 128–139.

[114] May, A. A., Levin, E. J. T., Hennigan, C. J., Riipinen, I., Lee, T., Collett, J. L., Jimenez, J. L., Kreidenweis, S. M., and Robinson, A. L., 2013, “Gas-Particle Partitioning of Primary Organic Aerosol Emissions: (2) Diesel Vehicles,” Environ. Sci. Technol., **47**, pp. 8288–8296.

[115] Kuwayama, T., Collier, S., Forestieri, S., Brady, J. M., Bertram, T. H., Cappa, C. D., Zhang, Q., and Kleeman, M. J., 2015, “Volatility of Primary Organic Aerosol Emitted from Light Duty Gasoline Vehicles,” Environ. Sci. Technol., **49**, pp. 1569–1577.

[116] Biswas, S., Ntziachristos, L., Moore, K. F., and Sioutas, C., 2007, “Particle Volatility in the Vicinity of a Freeway With Heavy-Duty Diesel Traffic,” Atmos. Environ., **41**(16), pp. 3479–3493.

[117] Chirico, R., Prevot, A. S. H., DeCarlo, P. F., Heringa, M. F., Richter, R., Weingartner, E., and Baltensperger, U., 2011, “Aerosol and Trace Gas Vehicle Emission Factors Measured in a Tunnel Using an Aerosol Mass Spectrometer and Other On-Line Instrumentation,” Atmos. Environ., **45**(13), pp. 2182–2192.

[118] Worton, D. R., Isaacman, G., Gentner, D. R., Dallmann, T. R., Chan, A. W. H., Ruehl, C., Kirchstetter, T. W., Wilson, K. R., Harley, R. A., and Goldstein, A. H., 2014, “Lubricating Oil Dominates Primary Organic Aerosol Emissions from Motor Vehicles,” Environ. Sci. Technol., **48**(7), pp. 3698–3706.

[119] Fountoukis, C., Megaritis, A. G., Skyllakou, K., Charalampidis, P. E., Pilinis, C., Denier Van Der Gon, H. A. C., Crippa, M., Canonaco, F., Mohr, C., Prévôt, A. S. H., Allan, J. D., Poulain, L., Petäjä, T., Tiitta, P., Carbone, S., Kiendler-Scharr, A., Nemitz, E., O’Dowd, C., Swietlicki, E., and Pandis, S. N., 2014, “Organic Aerosol Concentration and Composition Over Europe: Insights from Comparison of Regional Model Predictions With Aerosol Mass Spectrometer Factor Analysis,” Atmos. Chem. Phys., **14**(17), pp. 9061–9076.

[120] Koo, B., Knipping, E., and Yarwood, G., 2014, “1.5-Dimensional Volatility Basis Set Approach for Modeling Organic Aerosol in CAMx and CMAQ,” Atmos. Environ., **95**, pp. 158–164.

[121] Levi, M., 2013, “Climate Consequences of Natural Gas as a Bridge Fuel,” Clim. Change, **118**(3-4), pp. 609–623.

[122] Zhang, X., Myhrvold, N. P., Hausfather, Z., and Caldeira, K., 2016, “Climate Benefits of Natural Gas as a Bridge Fuel and Potential Delay of near-Zero Energy Systems,” Appl. Energy, **167**, pp. 317–322.

[123] Hausfather, Z., 2015, “Bounding the Climate Viability of Natural Gas as a Bridge

Fuel to Displace Coal," Energy Policy, **86**, pp. 286–294.

[124] Encana, 2013, "Completed Well Pads and Equipment Fact Sheet" [Online]. Available: https://www.encana.com/pdf/communities/usa/CompletedWellPadsandEquipment(DJ).pdf.

[125] Lyons, W. C., Plisga, G. J., and Lorenz, M. D., 2015, *Standard Handbook of Petroleum and Natural Gas Engineering*.

[126] "EPA. Inventory of US Greenhouse Gas Emissions and Sinks: 1990−2014, 2016" [Online]. Available: https://www.epa.gov/ghgemissions/usgreenhouse-gas-inventory-report-1990-2014.

[127] Brandt, A. R., Heath, G. A., Kort, E. A., O'Sullivan, F., Petron, G., Jordaan, S. M., Tans, P., Wilcox, J., Gopstein, a M., Arent, D., Wofsy, S., Brown, N. J., Bradley, R., Stucky, G. D., Eardley, D., and Harriss, R., 2014, "Supplementary Materials for Methane Leaks from North American Natural Gas Systems," Science (80-.)., **343**(6172), pp. 733–735.

[128] Omara, M., Sullivan, M. R., Li, X., Subramanian, R., Robinson, A. L., and Presto, A. A., 2016, "Methane Emissions from Conventional and Unconventional Natural Gas Production Sites in the Marcellus Shale Basin," Environ. Sci. Technol., p. acs.est.5b05503.

[129] Yuan, B., Kaser, L., Karl, T., Graus, M., Peischl, J., Campos, T. L., Shertz, S., Apel, E. C., Hornbrook, R. S., Hills, A., Gilman, J. B., Lerner, B. M., Warneke, C., Flocke, F. M., Ryerson, T. B., Guenther, A. B., and Gouw, J. A. De, 2015, "Airborne Flue Measurements of Methane and Volatile Organic Compounds over the Haynesville and Marcellus Shale Gas Production Regions," J. Geophys. Res. Atmos., **120**, pp. 6271–6289.

[130] Thompson, C. R., Hueber, J., and Helmig, D., 2014, "Influence of Oil and Gas Emissions on Ambient Atmospheric Non-Methane Hydrocarbons in Residential Areas of Northeastern Colorado," Elem. Sci. Anthr., **2**, p. 000035.

[131] Goetz, J. D., Avery, A., Werden, B., Floerchinger, C., Fortner, E. C., Wormhoudt, J., Massoli, P., Herndon, S. C., Kolb, C. E., Knighton, W. B., Peischl, J., Warneke, C., Gouw, J. A. De, Shaw, S. L., and Decarlo, P. F., 2017, "Analysis of Local-Scale Background Concentrations of Methane and Other Gas-Phase Species in the Marcellus Shale," pp. 1–20.

[132] Goetz, J. D., Floerchinger, C., Fortner, E. C., Wormhoudt, J., Massoli, P., Knighton, W. B., Herndon, S. C., Kolb, C. E., Knipping, E., Shaw, S. L., and Decarlo, P. F., 2015, “Atmospheric Emission Characterization of Marcellus Shale Natural Gas Development Sites.”

[133] Turner, a. J., Jacob, D. J., Wecht, K. J., Maasakkers, J. D., Lundgren, E., Andrews, a. E., Biraud, S. C., Boesch, H., Bowman, K. W., Deutscher, N. M., Dubey, M. K., Griffith, D. W. T., Hase, F., Kuze, a., Notholt, J., Ohyama, H., Parker, R., Payne, V. H., Sussmann, R., Sweeney, C., Velazco, V. a., Warneke, T., Wennberg, P. O., and Wunch, D., 2015, “Estimating Global and North American Methane Emissions with High Spatial Resolution Using GOSAT Satellite Data,” Atmos. Chem. Phys., **15**(12), pp. 7049–7069.

[134] Edgar, 2011, “EDGAR - Emission Database for Global Atmospheric Research,” Glob. Emiss. EDGAR v4.2 (November 2011), p. 3720.

[135] “EPA. Inventory of US Greenhouse Gas Emissions and Sinks: 1990−2014, 2016.”

[136] Maasakkers, J. D., Jacob, D. J., Sulprizio, M. P., Turner, A. J., Weitz, M., Wirth, T., Hight, C., DeFigueiredo, M., Desai, M., Schmeltz, R., Hockstad, L., Bloom, A. A., Bowman, K. W., Jeong, S., and Fischer, M. L., 2016, “Gridded National Inventory of U.S. Methane Emissions,” Environ. Sci. Technol., p. acs.est.6b02878.

[137] Omara, M., Zimmerman, N., Sullivan, M. R., Li, X., Ellis, A., Cesa, R., Subramanian, R., Robinson, A. L., and Presto, A. A., 2017, “On Site-Level Methane Emissions Characteristics and Prevalence of High Emitters among U.S. Gas Production Sites,” Prep.

[138] Zimmerman, N., Omara, M., Li, X., Ellis, A., Sullivan, M. R., Subramanian, R., Presto, A. A., and Robinson, A. L., 2017, “Inverse Gaussian Modelling as an Effective Surveying Tool for Quantifying Fugitive Methane from Natural Gas Production,” In prep. for Atmos. Meas. Tech.

[139] Roscioli, J. R., Yacovitch, T. I., Floerchinger, C., Mitchell, A. L., Tkacik, D. S., Subramanian, R., Martinez, D. M., Vaughn, T. L., Williams, L., Zimmerle, D., Robinson, A. L., Herndon, S. C., and Marchese, A. J., 2015, “Measurements of Methane Emissions from Natural Gas Gathering Facilities and Processing Plants: Measurement Methods,” Atmos. Meas. Tech., **8**(5), pp. 2017–2035.

[140] Marchese, A. J., Vaughn, T. L., Zimmerle, D. J., Martinez, D. M., Williams, L. L., Robinson, A. L., Mitchell, A. L., Subramanian, R., Tkacik, D. S., Roscioli, J. R., and Herndon, S. C., 2015, “Methane Emissions from United States Natural Gas Gathering and Processing,” Environ. Sci. Technol., **49**(17), pp. 10718–10727.

[141] Mitchell, A. L., Tkacik, D. S., Roscioli, J. R., Herndon, S. C., Yacovitch, T. I., Martinez, D. M., Vaughn, T. L., Williams, L., Sullivan, M., Floerchinger, C., Omara, M., Subramanian, R., Zimmerle, D., Marchese, A. J., and Robinson, A. L., 2015, “Measurements of Methane Emissions from Natural Gas Gathering Facilities and Processing Plants: Measurement Results,” Environ. Sci. Technol., **49**(20), p. 12602.

[142] Zimmerle, D. J., Williams, L. L., Vaughn, T. L., Quinn, C., Subramanian, R., Duggan, G. P., Willson, B., Opsomer, J. D., Marchese, A. J., Martinez, D. M., and Robinson, A. L., 2015, “Methane Emissions from the Natural Gas Transmission and Storage System in the United States.,” Environ. Sci. Technol., **49**(15), pp. 9374–83.

[143] Lamb, B. K., Edburg, S. L., Ferrara, T. W., Howard, T., Harrison, M. R., Kolb, C. E., Townsend-small, A., Dyck, W., Possolo, A., and Whetstone, J. R., 2015, “Direct Measurements Show Decreasing Methane Emissions from Natural Gas Local Distribution Systems in the United States.”

[144] Brandt, A. R., Heath, G. A., Kort, E. A., O’Sullivan, F., Pétron, G., Jordaan, S. M., Tans, P., Wilcox, J., Gopstein, A. M., Arent, D., Wofsy, S., Brown, N. J., Bradley, R., Stucky, G. D., Eardley, D., and Harriss, R., 2014, “Methane Leaks from North American Natural Gas Systems,” Science (80-.)., **343**(6172), pp. 733–735.

[145] Kirchgessner, D. A., Lott, R. A., Cowgill, R. M., Harrison, M. R., and Shires, T. M., 1997, “Estimate of Methane Emissions from the U.S. Natural Gas Industry,” Chemosphere, **35**(6), pp. 1365–1390.

[146] Brantley, H. L., Thoma, E. D., Squier, W. C., Guven, B. B., and Lyon, D., 2014, “Assessment of Methane Emissions from Oil and Gas Production Pads Using Mobile Measurements,” Environ. Sci. Technol., **48**(24), pp. 14508–14515.

[147] Rella, C. W., Tsai, T. R., Botkin, C. G., Crosson, E. R., and Steele, D., 2015, “Measuring Emissions from Oil and Natural Gas Well Pads Using the Mobile Flux Plane Technique.”

[148] Yacovitch, T. I., Herndon, S. C., Pétron, G., Kofler, J., Lyon, D., Zahniser, M. S.,

and Kolb, C. E., 2015, “Mobile Laboratory Observations of Methane Emissions in the Barnett Shale Region,” Environ. Sci. Technol., **49**(13), pp. 7889–7895.

[149] Lan, X., Talbot, R., Laine, P., and Torres, A., 2015, “Characterizing Fugitive Methane Emissions in the Barnett Shale Area Using a Mobile Laboratory.”

[150] Eastern Research Group, Inc., Sage Environmental Consulting, L. P., 2011, “City of Fort Worth Natural Gas Air Quality Study,” Report.

[151] Lyon, D. R., Zavala-Araiza, D., Alvarez, R. A., Harriss, R., Palacios, V., Lan, X., Talbot, R., Lavoie, T., Shepson, P., Yacovitch, T. I., Herndon, S. C., Marchese, A. J., Zimmerle, D., Robinson, A. L., and Hamburg, S. P., 2015, “Constructing a Spatially Resolved Methane Emission Inventory for the Barnett Shale Region,” Environ. Sci. Technol., **49**(13), pp. 8147–8157.

[152] Allen, D. T. ., Cardoso-Saldaña, F. J. ., and Kimura, Y., 2017, “Variability in Spatially and Temporally Resolved Emissions and Hydrocarbon Source Fingerprints for Oil and Gas Sources in Shale Gas Production Regions,” Environ. Sci. Technol.

[153] Littlefield, J. A., Marriott, J., Schivley, G. A., and Skone, T. J., 2017, “Synthesis of Recent Ground-Level Methane Emission Measurements from the U.S. Natural Gas Supply Chain,” J. Clean. Prod., **148**, pp. 118–126.

[154] Wecht, K. J., Jacob, D. J., Frankenberg, C., Jiang, Z., and Blake, D. R., 2014, “Mapping of North American Methane Emissions with High Spatial Resolution by Inversion of SCIAMACHY Satellite Data,” J. Geophys. Res. Atmos., (119), pp. 7741–7756.

[155] Wecht, K. J., Jacob, D. J., Sulprizio, M. P., Santoni, G. W., Wofsy, S. C., Parker, R., B??sch, H., and Worden, J., 2014, “Spatially Resolving Methane Emissions in California: Constraints from the CalNex Aircraft Campaign and from Present (GOSAT, TES) and Future (TROPOMI, Geostationary) Satellite Observations,” Atmos. Chem. Phys., **14**(15), pp. 8173–8184.

[156] Environmental Protection Agency (EPA), 1998, “NOx How Nitrogen Oxides Affect The Way We Live And Breathe,” Epa-456/F-98-005, (September), p. 6.

[157] US Environmental Protection Agency, “Health and Environmental Effects of Particulate Matter (PM)” [Online]. Available: https://www.epa.gov/pm-

pollution/health-and-environmental-effects-particulate-matter-pm.

[158] IPCC, 2013, *Climate Change 2013: The Physical Science Basis. Contribution of Working Group I to the Fifth Assessment Report of the Intergovernmental Panel on Climate Change.*

[159] Epstein, S. A., and Nizkorodov, S. A., 2012, "A Comparison of the Chemical Sinks of Atmospheric Organics in the Gas and Aqueous Phase," Atmos. Chem. Phys., **12**(17), pp. 8205–8222.

[160] Tox Town, 2017, "Environmental Health Concerns of Volatile Organic Compounds (VOCs)" [Online]. Available: https://toxtown.nlm.nih.gov/text_version/chemicals.php?id=31.

[161] The U.S. Environmental Protection Agency (EPA), "Health Effects of Ozone Pollution."

[162] The U.S. Environmental Protection Agency (EPA), "Ecosystem Effects of Ozone Pollution."

[163] Voulgarakis, A., Naik, V., Lamarque, J. F., Shindell, D. T., Young, P. J., Prather, M. J., Wild, O., Field, R. D., Bergmann, D., Cameron-Smith, P., Cionni, I., Collins, W. J., Dalsøren, S. B., Doherty, R. M., Eyring, V., Faluvegi, G., Folberth, G. A., Horowitz, L. W., Josse, B., MacKenzie, I. A., Nagashima, T., Plummer, D. A., Righi, M., Rumbold, S. T., Stevenson, D. S., Strode, S. A., Sudo, K., Szopa, S., and Zeng, G., 2013, "Analysis of Present Day and Future OH and Methane Lifetime in the ACCMIP Simulations," Atmos. Chem. Phys., **13**(5), pp. 2563–2587.

[164] Tox Town, 2017, "Environmental Health Concerns of Methane."

[165] Bureau of Transporation Statistics, "Average Age of Automobiles and Trucks in Operation in the United States" [Online]. Available: http://www.rita.dot.gov/bts/sites/rita.dot.gov.bts/files/publications/national_transportation_statistics/html/table_01_26.html_mfd.

[166] Subramanian, R., Khlystov, A. Y., Cabada, J. C., and Robinson, A. L., 2004, "Positive and Negative Artifacts in Particulate Organic Carbon Measurements With Denuded and Undenuded Sampler Configurations," Aerosol Sci. Technol., **38**(S1), pp. 27–48.

[167] Turpin, B. J., Saxena, P., and Andrews, E., 2000, “Measuring and Simulating Particulate Organics in The Atmosphere: Problems and Prospects,” Atmos. Environ., **34**(18), pp. 2983–3013.

[168] Arnott, W. P., Hamasha, K., Moosmüller, H., Sheridan, P. J., and Ogren, J. a., 2005, “Towards Aerosol Light-Absorption Measurements with a 7-Wavelength Aethalometer: Evaluation with a Photoacoustic Instrument and 3-Wavelength Nephelometer,” Aerosol Sci. Technol., **39**(September 2015), pp. 17–29.

[169] Kirchstetter, T. W., and Novakov, T., 2007, “Controlled Generation of Black Carbon Particles from a Diffusion Flame and Applications in Evaluating Black Carbon Measurement Methods,” Atmos. Environ., **41**(9), pp. 1874–1888.

[170] Chow, J. C., Watson, J. G., Chen, L. W. A., Chang, M. C. O., Robinson, N. F., Trimble, D., and Kohl, S., 2007, “The IMPROVE_A Temperature Protocol for Thermal/optical Carbon Analysis: Maintaining Consistency With a Long-Term Database.,” J. Air Waste Manag. Assoc., **57**(9), pp. 1014–1023.

[171] Subramanian, R., Khlystov, A. Y., Cabada, J. C., and Robinson, A. L., 2004, “Positive and Negative Artifacts in Particulate Organic Carbon Measurements with Denuded and Undenuded Sampler Configurations,” Aerosol Sci. Technol., **38**, pp. 27–48.

[172] US Environmental Protection Agency, 2017, “Air Quality System (AQS),” n.d. [Online]. Available: http://www.epa.gov/aqs.

[173] “EPA. Greenhouse Gas Reporting Program, 2015.”

[174] “DrillingInfo, DI Desktop, 2015.”

[175] “EIA. EIA-757 Natural Gas Processing Plant Survey, 2013.”

[176] Lippmann, M., 1991, “Health Effects of Tropospheric Ozone,” Environ. Sci. Technol., **25**(12), pp. 1954–1962.

[177] Turns, S. R., 2000, *An Introduction to Combustion: Concepts and Applications*.

[178] Miguel, A. H., Kirchstetter, T. W., Harley, R. a., and Hering, S. V., 1998, “On-Road Emissions of Particulate Polycyclic Aromatic Hydrocarbons and Black Carbon

from Gasoline and Diesel Vehicles," Environ. Sci. Technol., **32**(4), pp. 450–455.

[179] Jeong, C. H., Hopke, P. K., Kim, E., and Lee, D. W., 2004, "The Comparison between Thermal-Optical Transmittance Elemental Carbon and Aethalometer Black Carbon Measured at Multiple Monitoring Sites," *Atmospheric Environment*, pp. 5193–5204.

[180] Salako, G. O., Hopke, P. K., Cohen, D. D., Begum, B. A., Biswas, S. K., Pandit, G. G., Chung, Y. S., Rahman, S. A., Hamzah, M. S., Davy, P., Markwitz, A., Shagjjamba, D., Lodoysamba, S., Wimolwattanapun, W., and Bunprapob, S., 2012, "Exploring the Variation between EC and BC in a Variety of Locations," Aerosol Air Qual. Res., **12**(1), pp. 1–7.

[181] Briggs, N. L., and Long, C. M., 2016, "Critical Review of Black Carbon and Elemental Carbon Source Apportionment in Europe and the United States," Atmos. Environ., **144**, pp. 409–427.

[182] Gertler, A. W., Gillies, J. A., Pierson, W. R., Rogers, C. F., Sagebiel, J. C., Abu-Allaban, M., Coulomb, W., Tarnay, L., and Cahill, T. A., 2002, *Real-World Particulate Matter and Gaseous Emissions From Motor Vehicles in a Highway Tunnel*.

[183] Fraser, M. P., Buzcu, B., Yue, Z. W., McGaughey, G. R., Desai, N. R., Allen, D. T., Seila, R. L., Lonneman, W. A., and Harley, R. A. |, 2003, "Separation of Fine Particulate Matter Emitted from Gasoline and Diesel Vehicles Using Chemical Mass Balancing Techniques," Environ. Sci. Technol., **37**, pp. 3904–3909.

[184] Li, X., Lu, J., Dallmann, T. R., May, A. A., and Presto, A. A., 2017, "Long-Term Trend of on-Road Gasoline and Diesel Vehicle Emission Factors Measured in the Traffic Tunnel," prep. Environ. Sci. Technol.

[185] The U.S. Environmental Protection Agency (EPA), 2014, "Light-Duty Vehicle and Light-Duty Truck -- Tier 0, Tier 1, National Low Emission Vehicle (NLEV), and Clean Fuel Vehicle (CFV) Exhaust Emission Standards," Emiss. Stand. Ref. Guid., (March), p. 2016.

[186] The U.S. Environmental Protection Agency (EPA), 2016, "Light-Duty Vehicles, Light-Duty Trucks, and Medium-Duty Passenger Vehicles: Tier 2 Exhaust Emission Standards and Implementation Schedule (EPA-420-B-16-015, March 2016)," (March), p. 2016.

[187] Saliba, G., Saleh, R., Zhao, Y., Presto, A. A., Lambe, A. T., Frodin, B., Sardar, S., Maldonado, H., Maddox, C., May, A. A., Drozd, G. T., Goldstein, A. H., Russell, L. M., Hagen, F., and Robinson, A. L., 2017, "Comparison of Gasoline Direct-Injection (GDI) and Port Fuel Injection (PFI) Vehicle Emissions: Emission Certification Standards, Cold-Start, Secondary Organic Aerosol Formation Potential, and Potential Climate Impacts," Environ. Sci. Technol., p. acs.est.6b06509.

[188] Zimmerman, N., Wang, J. M., Jeong, C. H., Wallace, J. S., and Evans, G. J., 2016, "Assessing the Climate Trade-Offs of Gasoline Direct Injection Engines," Environ. Sci. Technol., **50**(15), pp. 8385–8392.

[189] B??rub??, K. A., Jones, T. P., Williamson, B. J., Winters, C., Morgan, A. J., and Richards, R. J., 1999, "Physicochemical Characterisation of Diesel Exhaust Particles: Factors for Assessing Biological Activity," Atmos. Environ., **33**(10), pp. 1599–1614.

[190] Kocbach, A., Johansen, B. V., Schwarze, P. E., and Namork, E., 2005, "Analytical Electron Microscopy of Combustion Particles: A Comparison of Vehicle Exhaust and Residential Wood Smoke," Sci. Total Environ., **346**(1-3), pp. 231–243.

[191] Park, K., Cao, F., Kittelson, D. B., and McMurry, P. H., 2003, "Relationship between Particle Mass and Mobility for Diesel Exhaust Particles," Environ. Sci. Technol., **37**(3), pp. 577–583.

[192] Ancelet, T., Davy, P. K., Trompetter, W. J., Markwitz, A., and Weatherburn, D. C., 2011, "Carbonaceous Aerosols in an Urban Tunnel," Atmos. Environ., **45**(26), pp. 4463–4469.

[193] Dye, A. L., Rhead, M. M., and Trier, C. J., 2000, "The Quantitative Morphology of Roadside and Background Urban Aerosol in Plymouth, UK," Atmos. Environ., **34**(19), pp. 3139–3148.

[194] Paoletti, L., De Berardis, B., and Diociaiuti, M., 2002, "Physico-Chemical Characterisation of the Inhalable Particulate Matter (PM10) in an Urban Area: An Analysis of the Seasonal Trend," Sci. Total Environ., **292**(3), pp. 265–275.

[195] Lall, A. A., and Friedlander, S. K., 2006, "On-Line Measurement of Ultrafine Aggregate Surface Area and Volume Distributions by Electrical Mobility Analysis: 1. Theoretical Analysis," J. Aerosol Sci., **37**, pp. 260–271.

[196] Li, X., Dallmann, T. R., May, A. A., Tkacik, D. S., Lambe, A. T., Jayne, J. T., Croteau, P. L., and Presto, A. A., 2016, “Gas-Particle Partitioning of Vehicle Emitted Primary Organic Aerosol Measured in a Traffic Tunnel,” Environ. Sci. Technol., **50**(22), pp. 12146–12155.

[197] Pant, P., and Harrison, R. M., 2013, “Estimation of the Contribution of Road Traffic Emissions to Particulate Matter Concentrations from Field Measurements: A Review,” Atmos. Environ., **77**, pp. 78–97.

[198] Zimmerman, N., Jeong, C., Wang, J. M., Ramos, M., Wallace, J. S., and Evans, G. J., 2015, “A Source-Independent Empirical Correction Procedure for the Fast Mobility and Engine Exhaust Particle Sizers,” Atmos. Environ., **100**, pp. 178–184.

[199] Liu, J., Jiang, J., Zhang, Q., Deng, J., and Hao, J., 2016, “A Spectrometer for Measuring Particle Size Distributions in the Range of 3 Nm to 10 μm,” Front. Environ. Sci. Eng., **10**(1), pp. 63–72.

[200] Inc., T., 2009, *TSI Series 3080 Scanning Mobility Particle Sizer Manual*.

[201] Inc., T., 2002, *TSI Model 3025A Ultrafine Condensation Particle Counter Manual*.

[202] An, W. J., Pathak, R. K., Lee, B. H., and Pandis, S. N., 2007, “Aerosol Volatility Measurement Using an Improved Thermodenuder: Application to Secondary Organic Aerosol,” J. Aerosol Sci., **38**(3), pp. 305–314.

[203] Lall, A. A., Seipenbusch, M., Rong, W., and Friedlander, S. K., 2006, “On-Line Measurement of Ultrafine Aggregate Surface Area and Volume Distributions by Electrical Mobility Analysis: II. Comparison of Measurements and Theory,” J. Aerosol Sci., **37**(3), pp. 272–282.

[204] Rissler, J., Nordin, E. Z., Eriksson, A. C., Nilsson, P. T., Frosch, M., Sporre, M. K., Wierzbicka, A., Svenningsson, B., L??ndahl, J., Messing, M. E., Sjogren, S., Hemmingsen, J. G., Loft, S., Pagels, J. H., and Swietlicki, E., 2014, “Effective Density and Mixing State of Aerosol Particles in a near-Traffic Urban Environment,” Environ. Sci. Technol., **48**(11), pp. 6300–6308.

[205] Trivitayanurak, W., Adams, P. J., Spracklen, D. V., and Carslaw, K. S., 2008, “Tropospheric Aerosol Microphysics Simulation with Assimilated Meteorology: Model Description and Intermodel Comparison,” Atmos. Chem. Phys., **8**(12), pp. 3149–3168.

[206] Fraser, M. P., Buzcu, B., Yue, Z. W., McGaughey, G. R., Desai, N. R., Allen, D. T., Seila, R. L., Lonneman, W. A., and Harley, R. A., 2003, “Separation of fine Particulate Matter Emitted from Gasoline and Diesel Vehicles Using Chemical Mass Balancing Techniques,” Environ. Sci. Technol., **37**(17), pp. 3904–3909.

[207] Kirchstetter, T. W., Harley, R. A., Kreisberg, N. M., Stolzenburg, M. R., and Hering, S. V., 1999, “On-Road Measurement of Fine Particle and Nitrogen Oxide Emissions from Light- and Heavy-Duty Motor Vehicles,” Atmos. Environ., **33**(18), pp. 2955–2968.

[208] Roth, C. M., Goss, K. U., and Schwarzenbach, R. P., 2005, “Sorption of a Diverse Set of Organic Vapors To Diesel Soot and Road Tunnel Aerosols,” Environ. Sci. Technol., **39**(17), pp. 6632–6637.

[209] Roth, C. M., Goss, K. U., and Schwarzenbach, R. P., 2005, “Sorption of a Diverse Set of Organic Vapors to Urban Aerosols,” Environ. Sci. Technol., **39**(17), pp. 6638–6643.

[210] Liang, C., Pankow, J. F., Odum, J. R., and Seinfeld, J. H., 1998, “Gas/particle Partitioning of Semivolatile Organic Compounds to Model Inorganic, Organic, and Ambient Smog Aerosols,” Environ. Sci. Technol., **31**(11), pp. 3086–3092.

[211] Pankow, J. F., 1994, “An Absorption Model of Gas/particle Partitioning of Organic Compounds in the Atmosphere,” Atmos. Environ., **28**(2), pp. 185–188.

[212] Donahue, N. M., Robinson, A. L., Stanier, C. O., and Pandis, S. N., 2006, “Coupled Partitioning, Dilution, and Chemical Aging of Semivolatile Organics,” Environ. Sci. Technol., **40**(8), pp. 2635–2643.

[213] Robinson, A. L., Grieshop, A. P., Donahue, N. M., and Hunt, S. W., 2010, “Updating the Conceptual Model for Fine Particle Mass Emissions from Combustion Systems,” J. Air Waste Manage. Assoc., **60**(10), pp. 1204–1222.

[214] Shrivastava, M. K., Lipsky, E. M., Stanier, C. O., and Robinson, A. L., 2006, “Modeling Semivolatile Organic Aerosol Mass Emissions from Combustion Systems.,” Environ. Sci. Technol., **40**(8), pp. 2671–2677.

[215] Murphy, B. N., and Pandis, S. N., 2009, “Simulating the Formation of Semivolatile

Primary and Secondary Organic Aerosol in a Regional Chemical Transport Model.," Environ. Sci. Technol., **43**(13), pp. 4722–8.

[216] Fountoukis, C., Racherla, P. N., Denier Van Der Gon, H. a C., Polymeneas, P., Charalampidis, P. E., Pilinis, C., Wiedensohler, A., Dall'Osto, M., O'Dowd, C., and Pandis, S. N., 2011, "Evaluation of a Three-Dimensional Chemical Transport Model (PMCAMx) in the European Domain During the EUCAARI May 2008 Campaign," Atmos. Chem. Phys., **11**(20), pp. 10331–10347.

[217] Ng, N. L., Herndon, S. C., Trimborn, A., Canagaratna, M. R., Croteau, P. L., Onasch, T. B., Sueper, D., Worsnop, D. R., Zhang, Q., Sun, Y. L., and Jayne, J. T., 2011, "An Aerosol Chemical Speciation Monitor (ACSM) for Routine Monitoring of the Composition and Mass Concentrations of Ambient Aerosol," Aerosol Sci. Technol., **45**(7), pp. 780–794.

[218] Huffman, J. A., Ziemann, P. J., Jayne, J. T., Worsnop, D. R., and Jimenez, J. L., 2008, "Development and Characterization of a Fast-Stepping/Scanning Thermodenuder for Chemically-Resolved Aerosol Volatility Measurements," Aerosol Sci. Technol., **42**(5), pp. 395–407.

[219] Riipinen, I., Pierce, J. R., Donahue, N. M., and Pandis, S. N., 2010, "Equilibration Time Scales of Organic Aerosol Inside Thermodenuders: Evaporation Kinetics Versus Thermodynamics," Atmos. Environ., **44**(5), pp. 597–607.

[220] Saleh, R., Shihadeh, A., and Khlystov, A., 2011, "On Transport Phenomena and Equilibration Time Scales in Thermodenuders," Atmos. Meas. Tech., **4**(3), pp. 571–581.

[221] Julin, J., Winkler, P. M., Donahue, N. M., Wagner, P. E., and Riipinen, I., 2014, "Near-Unity Mass Accommodation Coefficient of Organic Molecules of Varying Structure," Environ. Sci. Technol., (48), pp. 12083–12089.

[222] Turpin, B. J., and Lim, H.-J., 2001, "Species Contributions to PM2.5 Mass Concentrations: Revisiting Common Assumptions for Estimating Organic Mass," Aerosol Sci. Technol., **35**(1), pp. 602–610.

[223] Ma, J., Li, X., Gu, P., Dallmann, T. R., Presto, A. A., and Donahue, N. M., 2016, "Estimating Ambient Particulate Organic Carbon Concentrations and Partitioning Using Thermal Optical Measurements and the Volatility Basis Set," Aerosol Sci. Technol.

[224] Zhang, Q., Rami Alfarra, M., Worsnop, D. R., Allan, J. D., Coe, H., Canagaratna, M. R., and Jimenez, J. L., 2005, “Deconvolution and Quantification of Hydrocarbon-like and Oxygenated Organic Aerosols Based on Aerosol Mass Spectrometry,” Environ. Sci. Technol., **39**(13), pp. 4938–4952.

[225] Mohr, C., Huffman, J. A., Cubison, M. J., Aiken, A. C., Docherty, K. S., Kimmel, J. R., Ulbrich, I. M., Hannigan, M., and Jimenez, J. L., 2009, “Characterization of Primary Organic Aerosol Emissions from Meat Cooking, Trash Burning, and Motor Vehicles With High-Resolution Aerosol Mass Spectrometry and Comparison With Ambient and Chamber Observations,” Environ. Sci. Technol., **43**(7), pp. 2443–2449.

[226] Zhang, Q., Worsnop, D. R., Canagaratna, M. R., and Jimenez, J.-L., 2005, “Hydrocarbon-like and Oxygenated Organic Aerosols in Pittsburgh: Insights into Sources and Processes of Organic Aerosols,” Atmos. Chem. Phys. Discuss., **5**(5), pp. 8421–8471.

[227] Faulhaber, A. E., Thomas, B. M., Jimenez, J. L., Jayne, J. T., Worsnop, D. R., and Ziemann, P. J., 2009, “Characterization of a Thermodenuder-Particle Beam Mass Spectrometer System for the Study of Organic Aerosol Volatility and Composition,” Atmos. Meas. Tech., **2**(1), pp. 15–31.

[228] Cappa, C. D., 2010, “A Model of Aerosol Evaporation Kinetics in a Thermodenuder,” Atmos. Meas. Tech., **3**(3), pp. 579–592.

[229] Gkatzelis, G. I., Papanastasiou, D. K., Florou, K., Kaltsonoudis, C., Louvaris, E., and Pandis, S. N., 2015, “Measurement of Non-Volatile Particle Number Size Distribution,” Atmos. Meas. Tech. Discuss., **8**(6), pp. 6355–6393.

[230] Zhao, Y., Nguyen, N. T., Presto, A. A., Hennigan, C. J., May, A. A., and Robinson, A. L., 2016, “Intermediate Volatility Organic Compound Emissions from On-Road Gasoline Vehicles and Small O Ff -Road Gasoline Engines,” Environ. Sci. Technol., **50**, pp. 4554–4563.

[231] Zhao, Y., Nguyen, N. T., Presto, A. A., Hennigan, C. J., May, A. A., and Robinson, A. L., 2015, “Intermediate Volatility Organic Compound Emissions from On-Road Diesel Vehicles: Chemical Composition, Emission Factors, and Estimated Secondary Organic Aerosol Production,” Environ. Sci. Technol., **49**(19), pp. 11516–11526.

[232] Gentner, D. R., Harley, R. A., Miller, A. M., and Goldstein, A. H., 2009, “Diurnal

and Seasonal Variability of Gasoline-Related Volatile Organic Compound Emissions in Riverside, California.," Environ. Sci. Technol., **43**(12), pp. 4247–4252.

[233] Lough, G. C., Schauer, J. J., Lonneman, W. A., and Allen, M. K., 2005, "Summer and Winter Nonmethane Hydrocarbon Emissions from On-Road Motor Vehicles in the Midwestern United States.," J. Air Waste Manag. Assoc., **55**(5), pp. 629–646.

[234] "MATLAB Correct Baseline of Signal with Peaks" [Online]. Available: https://www.mathworks.com/help/bioinfo/ref/msbackadj.html.

[235] Lamb, B. K., McManus, J. B., Shorter, J. H., Kolb, C. E., Mosher, B., Harriss, R. C., Allwine, E., Blaha, D., Howard, T., Guenther, A., Lott, R. A., Siverson, R., Westberg, H., and Zimmerman, P., 1995, "Development of Atmospheric Tracer Methods to Measure Methane Emissions from Natural Gas Facilities and Urban Areas," Environ. Sci. Technol., **29**(6), pp. 1468–1479.

[236] Brantley, H. L., Thoma, E. D., Squier, W. C., Guven, B. B., and Lyon, D., 2014, "Assessment of Methane Emissions from Oil and Gas Production Pads Using Mobile Measurements," Environ. Sci. Technol., **48**(24), pp. 14508–14515.

[237] Yacovitch, T. I., Herndon, S. C., P??tron, G., Kofler, J., Lyon, D., Zahniser, M. S., and Kolb, C. E., 2015, "Mobile Laboratory Observations of Methane Emissions in the Barnett Shale Region," Environ. Sci. Technol., **49**(13), pp. 7889–7895.

[238] Baker, A. K., Beyersdorf, A. J., Doezema, L. A., Katzenstein, A., Meinardi, S., Simpson, I. J., Blake, D. R., and Sherwood Rowland, F., 2008, "Measurements of Nonmethane Hydrocarbons in 28 United States Cities," Atmos. Environ., **42**(1), pp. 170–182.

[239] U.S. Environmental Protection Agency, U. S. E., ORD, and Assessment, N. C. for E., 2013, "Integrated Risk Information System (IRIS)," U.S. Environ. Prot. Agency, U.S. EPA.

[240] Turner, A. J., Jacob, D. J., Benmergui, J., Wofsy, S. C., Maasakkers, J. D., Butz, A., Hasekamp, O., and Biraud, S. C., 2016, "A Large Increase in U.S. Methane Emissions over the Past Decade Inferred from Satellite Data and Surface Observations," Geophys. Res. Lett., **43**(5), pp. 2218–2224.

[241] Bureau of Ocean Energy Management (BOEM), 2014, "Year 2011 Gulfwide

Emission Inventory Study."

[242] Kuze, A., Suto, H., Nakajima, M., and Hamazaki, T., 2009, "Thermal and near Infrared Sensor for Carbon Observation Fourier-Transform Spectrometer on the Greenhouse Gases Observing Satellite for Greenhouse Gases Monitoring.," Appl. Opt., **48**(35), pp. 6716–6733.

[243] Parker, R., Boesch, H., Cogan, A., Fraser, A., Feng, L., Palmer, P. I., Messerschmidt, J., Deutscher, N., Griffith, D. W. T., Notholt, J., Wennberg, P. O., and Wunch, D., 2011, "Methane Observations from the Greenhouse Gases Observing SATellite: Comparison to Ground-Based TCCON Data and Model Calculations," Geophys. Res. Lett., **38**(15).

[244] European Space Agency (ESA), "European Space Agency Greenhouse Gas Climate Change Initiative Data Products."

[245] Stevanovic, S., Miljevic, B., Madl, P., Clifford, S., and Ristovski, Z., 2015, "Characterisation of a Commercially Available Thermodenuder and Diffusion Drier for Ultrafine Particles Losses," Aerosol Air Qual. Res., **15**(1), pp. 357–363.

Appendices

Appendix A
Supporting Information for
Long-term trend of on-road gasoline and diesel vehicle emission factors measured in traffic tunnels

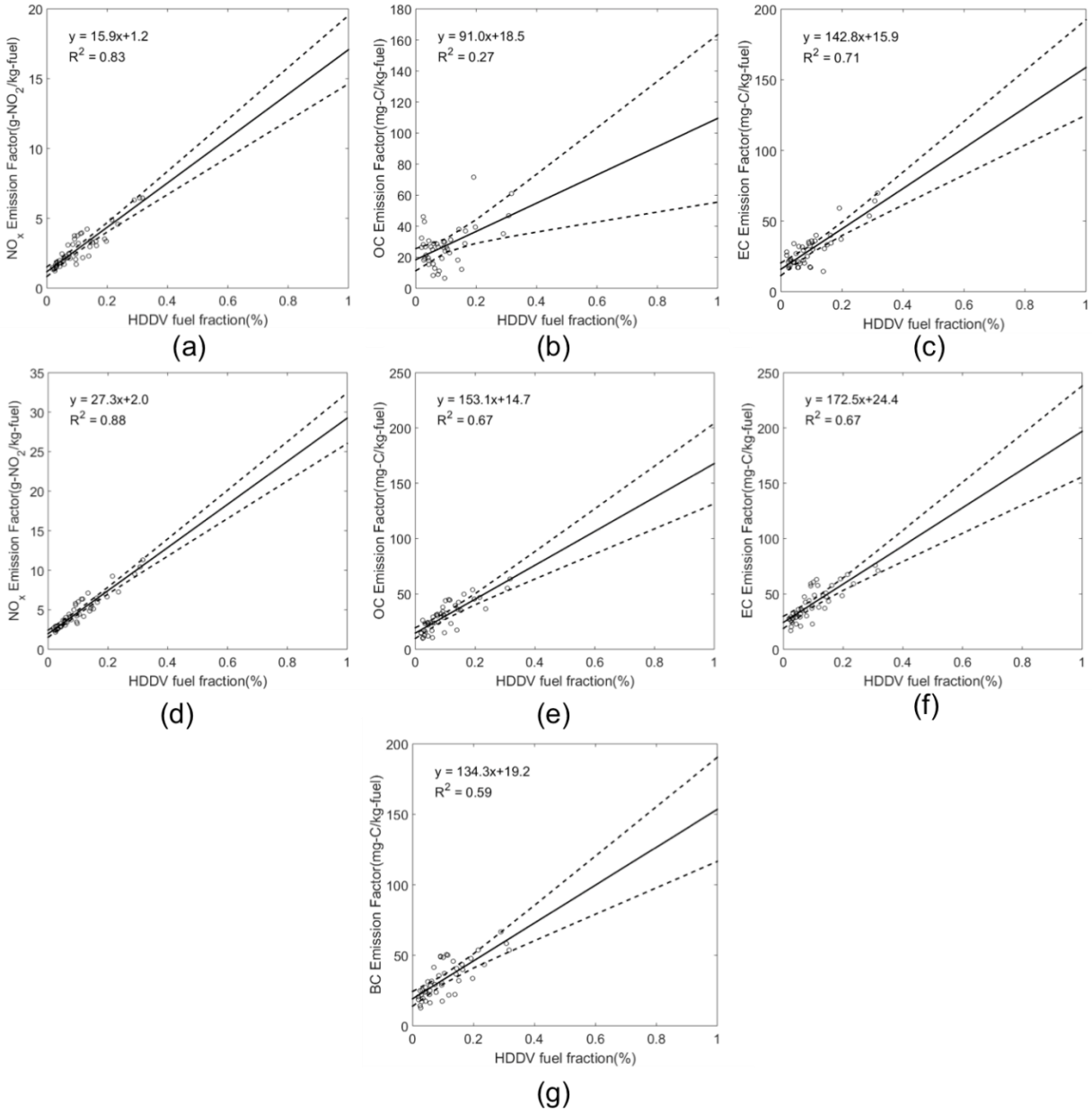

Figure A.1 The uncertainty range of the linear regression fittings of (a) NO_x, (b) OC, and (c) EC emission factors measured in the spring as a function of diesel fuel fractions in the tunnel and (d) NO_x, (e) OC, (f) EC, and (g) BC emission factors measured in the winter as a function of diesel fuel fractions in the tunnel. Circles represent the measurement data. Solid lines are the linear regression fitting of the data, and the dashed lines are the 95% confidence bonds of the fitting.

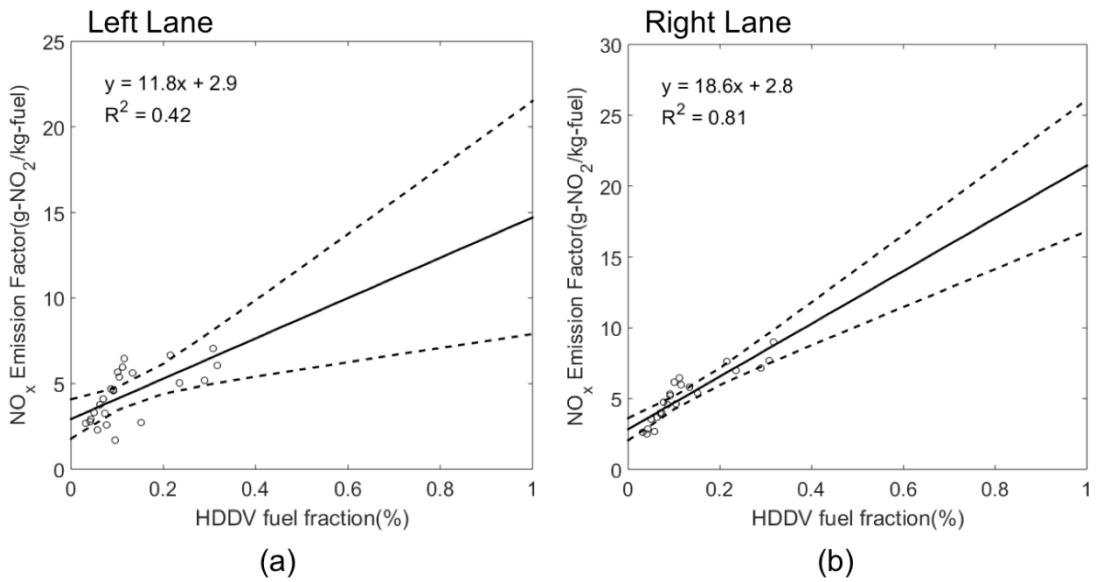

Figure A.2 The uncertainty range of NO_x emission factors as a function of diesel fuel fractions in the tunnel measured over (a) the left lane and (b) the right lane over one single week. Circles represent the measurement data. Solid lines are the linear regression fitting of the data, and the dashed lines are the 95% confidence bonds of the fitting.

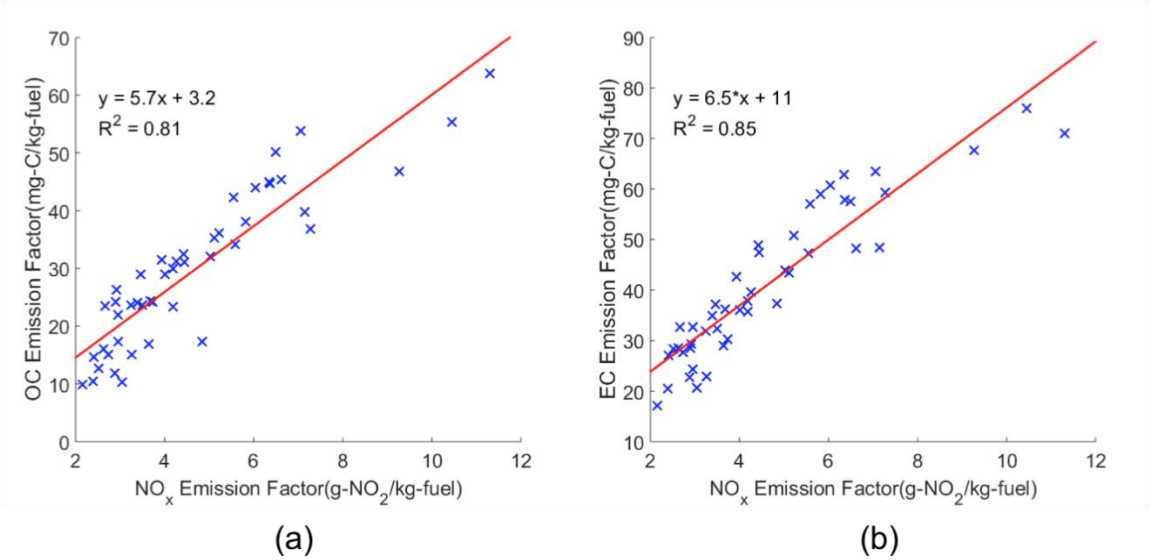

Figure A.3 (a) Comparison of OC emission factors and NO_x emission factors measured in the tunnel. (b) Comparison of EC emission factors and NO_x emission factors measured in the tunnel. Red solid lines are the linear regression fitting of the data.

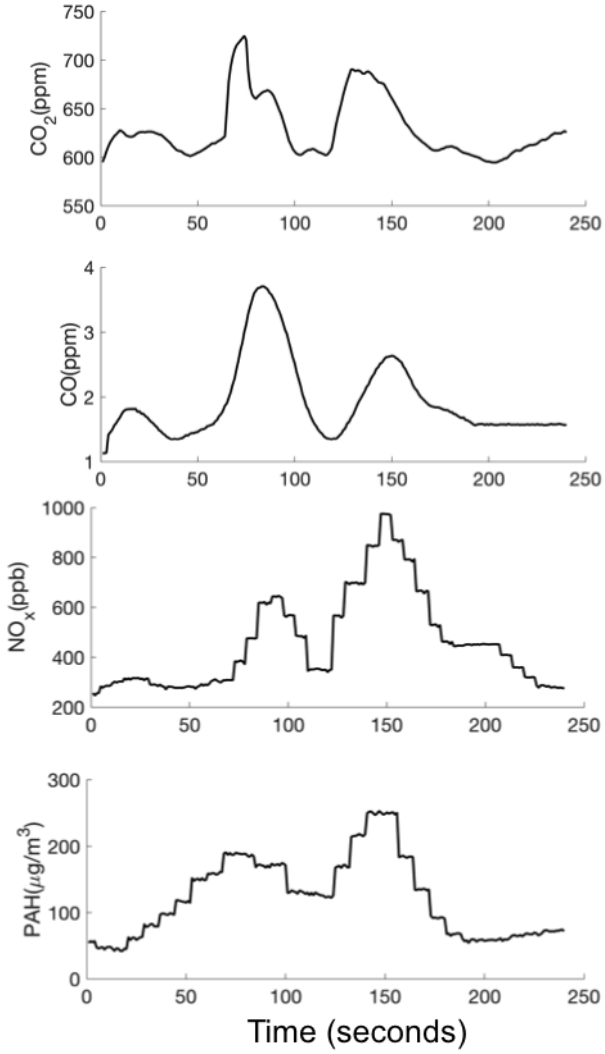

Figure A.4 Example of diesel truck plumes captured in the Ft. Pitt tunnel. The two peaks in CO_2 (centered at approximately t = 70 s and 130 s) indicate exhaust plumes from two passing diesel trucks. Coincident peaks in CO, NO_x, and particle-bound PAHs are evident.

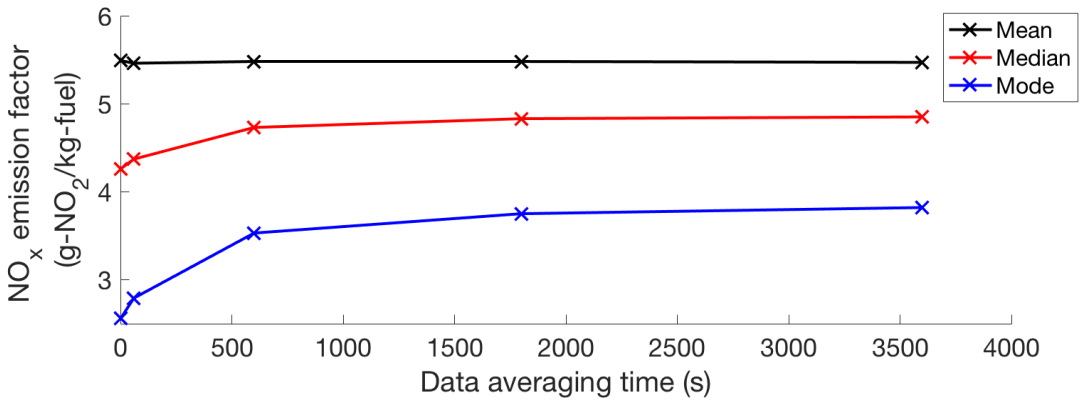

Figure A.5 The influence of the data averaging time on the mean, median, and mode value of the NO_x emission factors measured in the tunnel in winter.

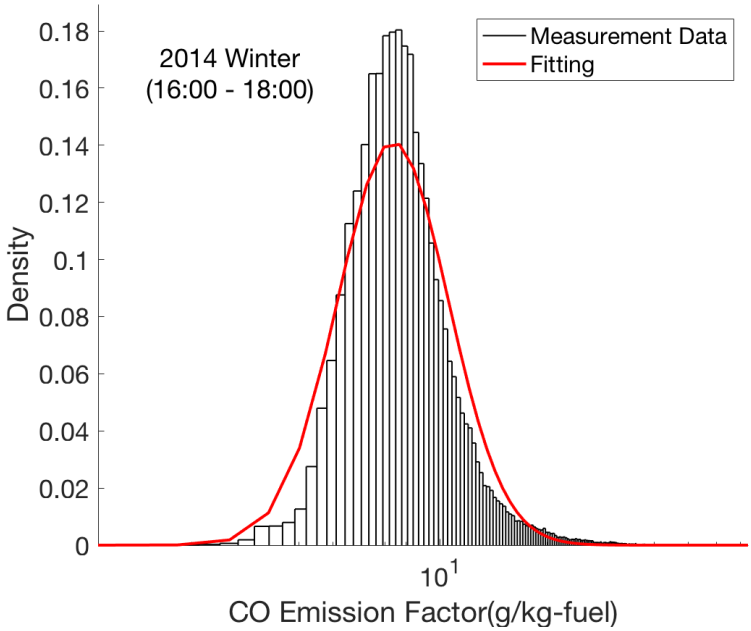

Figure A.6 The frequency density distribution of 1-s CO emission factors measured in the tunnel in winter during the afternoon rush hour (16:00 – 18:00). Red line is the lognormal fitting of the distribution.

Table A.1 Number fractions of pre-LEV, LEV1, and LEV2 vehicles in Allegheny Countyin 2010

Tire	Vehicle Model Year	Vehicle number	Fraction
pre-LEV	before 1994	14961	0.02
LEV1	1994-2003	275100	0.41
LEV2	after 2004	377108	0.57
Total		667169	1.00

Table A.2 The frequency density distributions and mean, median, mode and variance of the NO_x emission factors calculated with different data averaging time

Data averaging time	log(μ)	log(σ)	Mean	Median	Mode	Variance
1s	1.45	0.71	5.49	4.26	2.56	19.88
1min	1.47	0.67	5.46	4.37	2.79	16.88
10min	1.55	0.54	5.48	4.73	3.53	10.22
30min	1.57	0.50	5.48	4.83	3.75	8.65
1h	1.58	0.49	5.47	4.85	3.82	8.05

Appendix B
Supporting Information for
Size distribution of vehicle emitted primary particles measured in a traffic tunnel

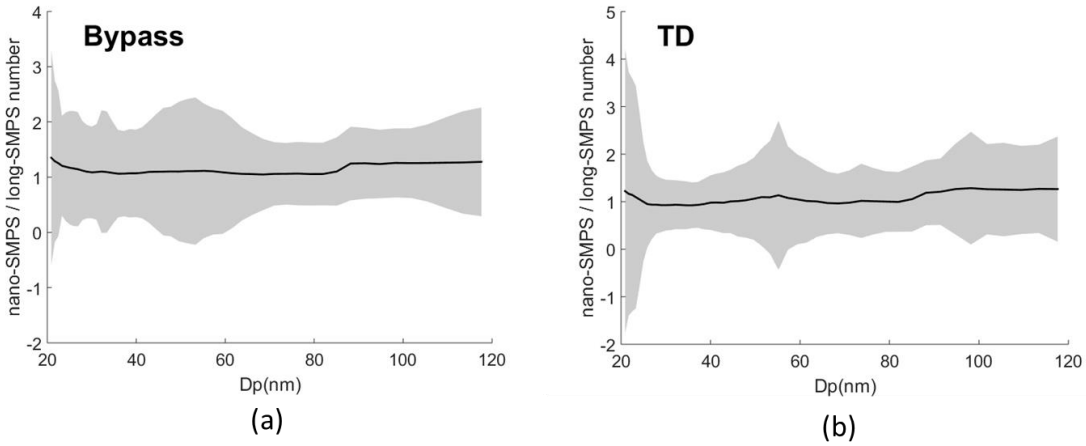

Figure B.1 The ratio of particle number concentrations measured by nano-SMPS and long-SMPS for 20 -120 nm particles sampled through (a) the bypass line and (b) the TD.

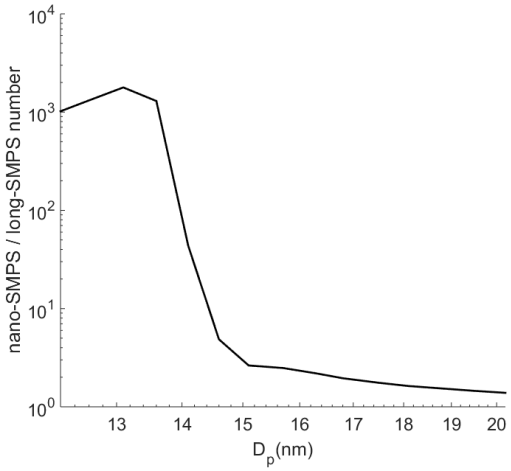

Figure B.2 The ratio of particle number concentrations measured by nano-SMPS and long-SMPS for less than 20 nm particles.

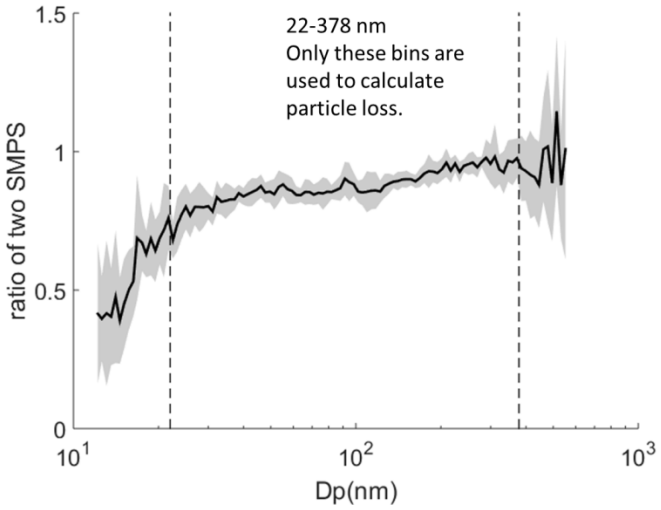

Figure B.3 The ratio of the number concentrations measured by two long-SMPS. Both SMPS were sampling NaCl particles directly from the Teflon chamber.

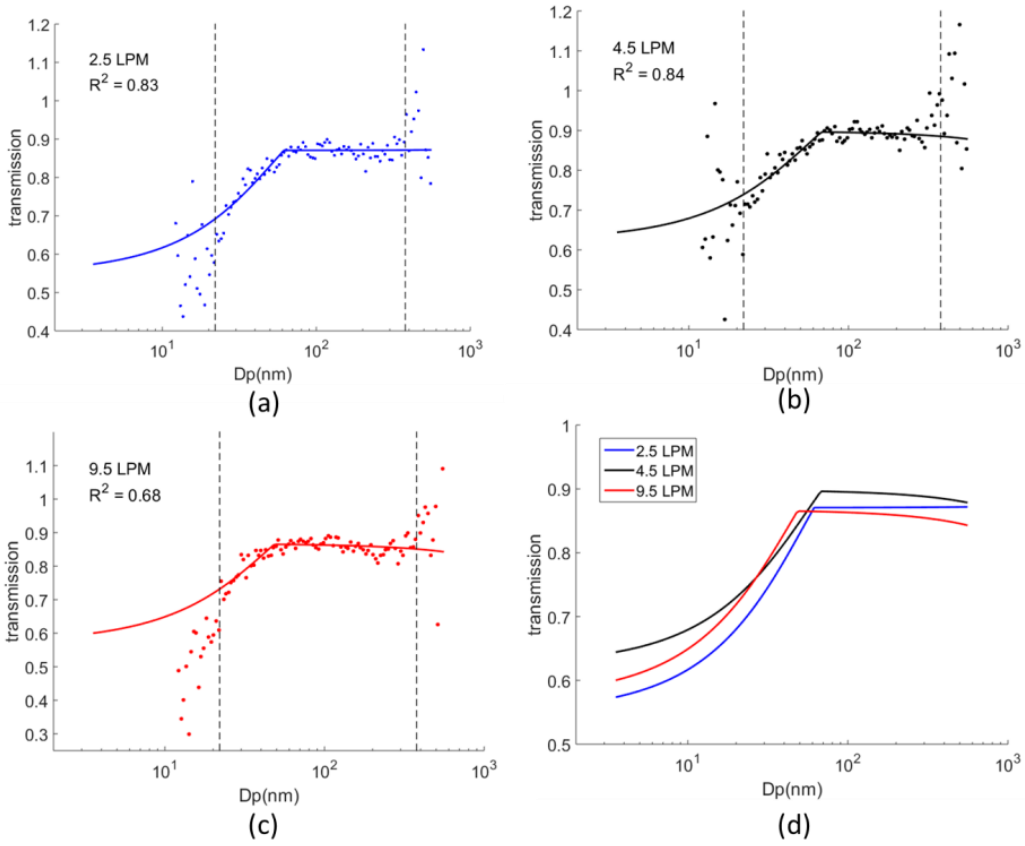

Figure B.4 The size-resolved particle transmissions through the TD under the flow rate of (a) 2.5 LPM, (b) 4.5 LPM, and (c) 9.5 LPM. (d) The comparison of TD particle transmissions under different flow rates. Dots represent the measurement data, and lines represent the fittings.

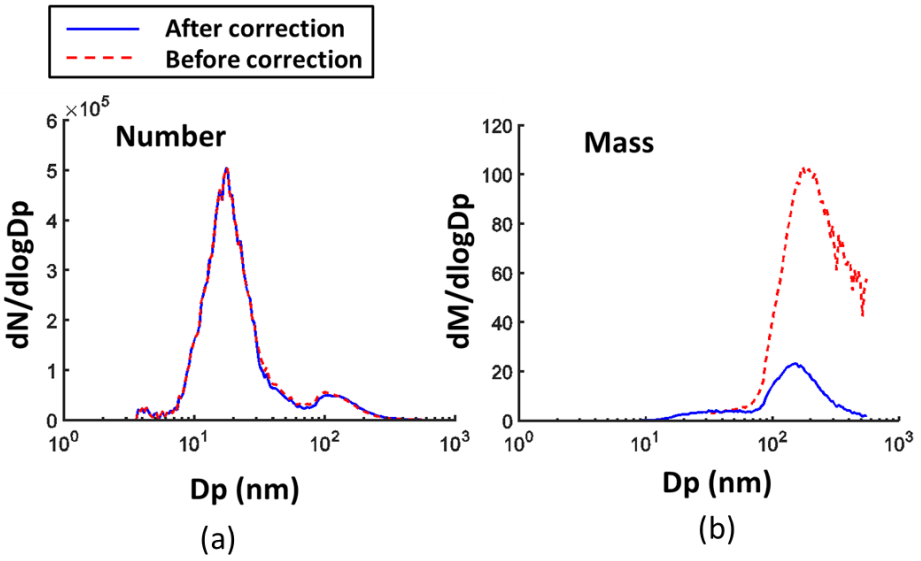

Figure B.5 Example of the particle (a) number and (b) mass size distributions measured by the SMPS before and after the nanoparticle aggregates correction.

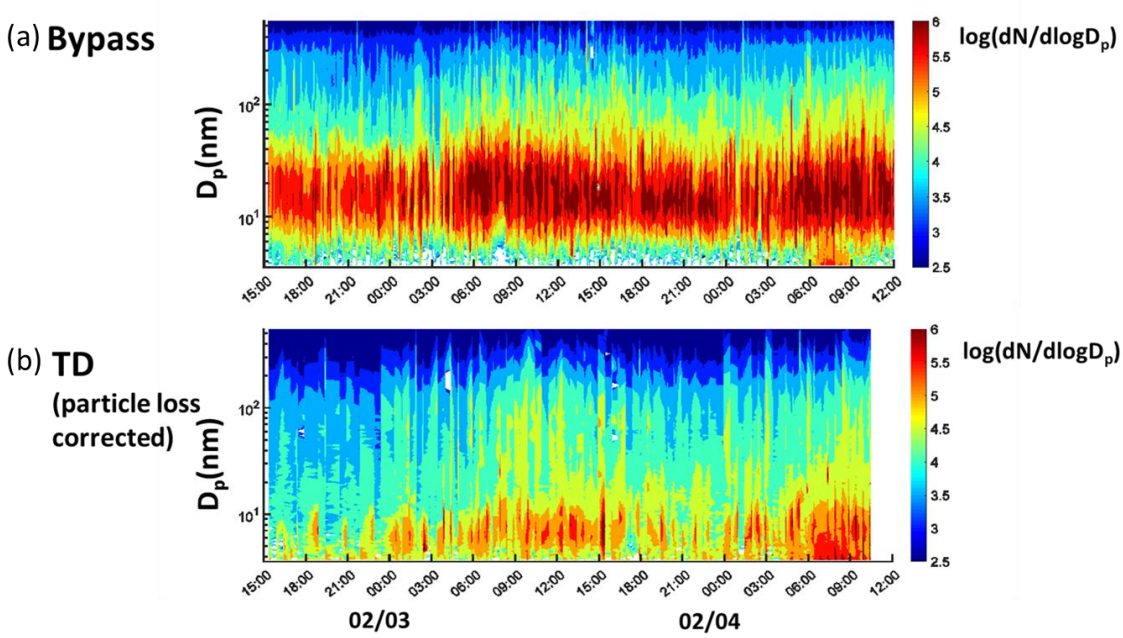

Figure B.6 Time series of the particle number size distributions measured in the tunnel through (a) bypass line and (b) the TD.

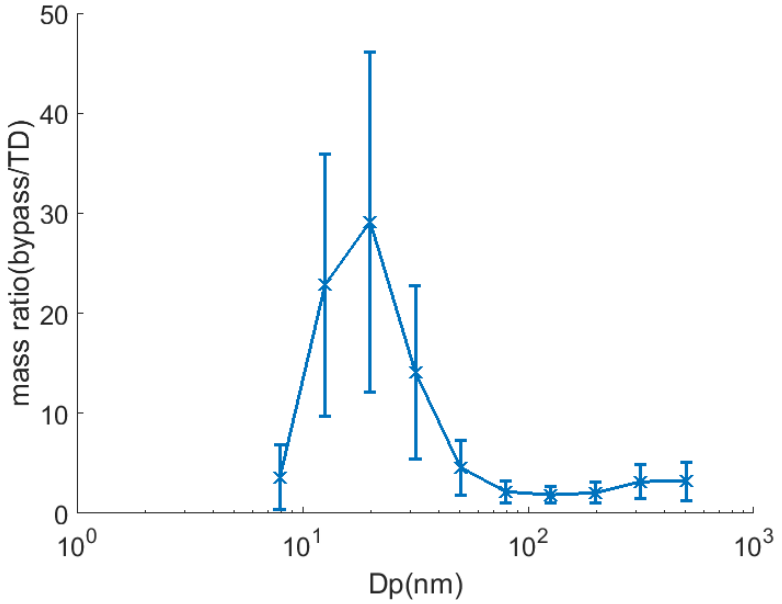

Figure B.7 The size-resolved mass ratio of volatile-to-non-volatile-component of vehicle emitted particles. Symbols represent the mean value, and bars represent the standard deviation of the hourly averaged data.

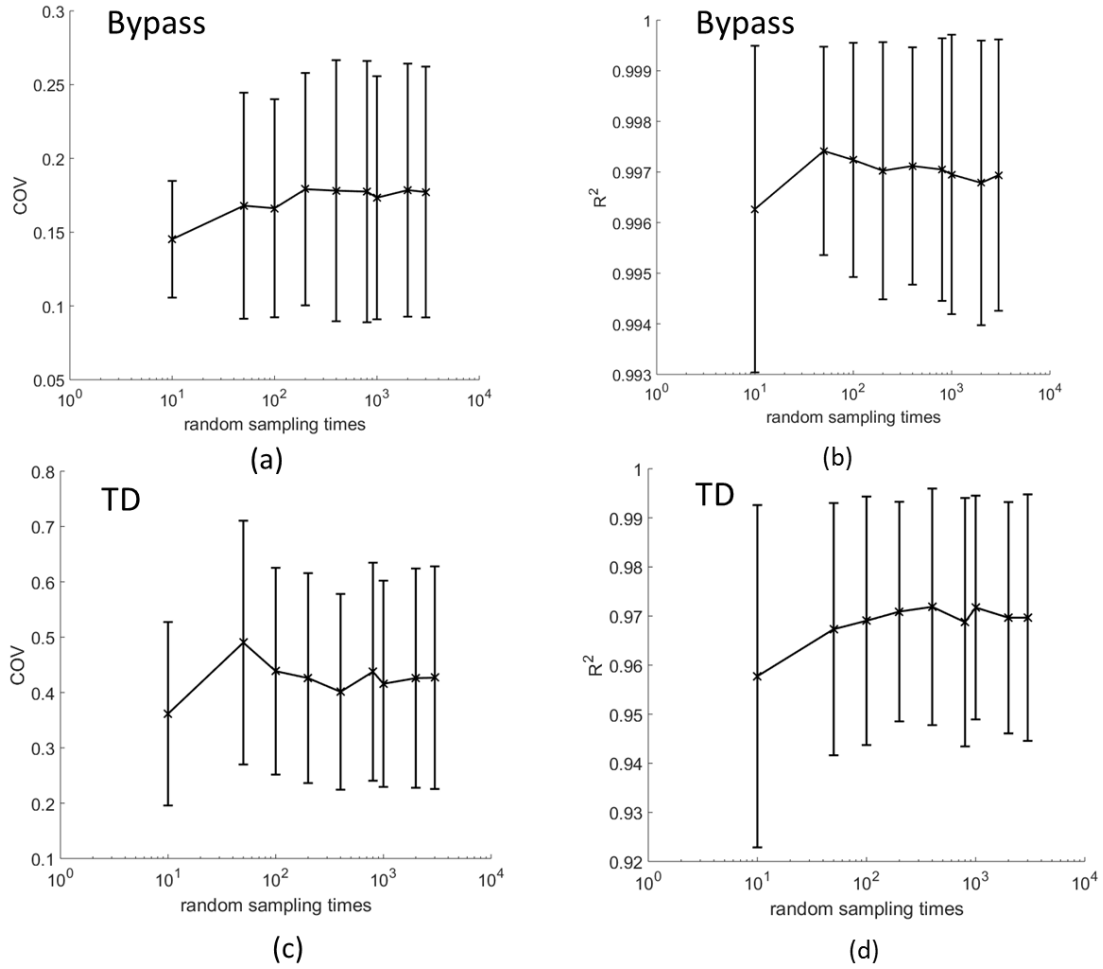

Figure B.8 Influence of the random sampling times on the coefficient of variance (COV) and R^2 of the reconstructed and measured size-resolved EF_N. Symbols represent the mean value, and bars represent the standard deviation of all sampling results.

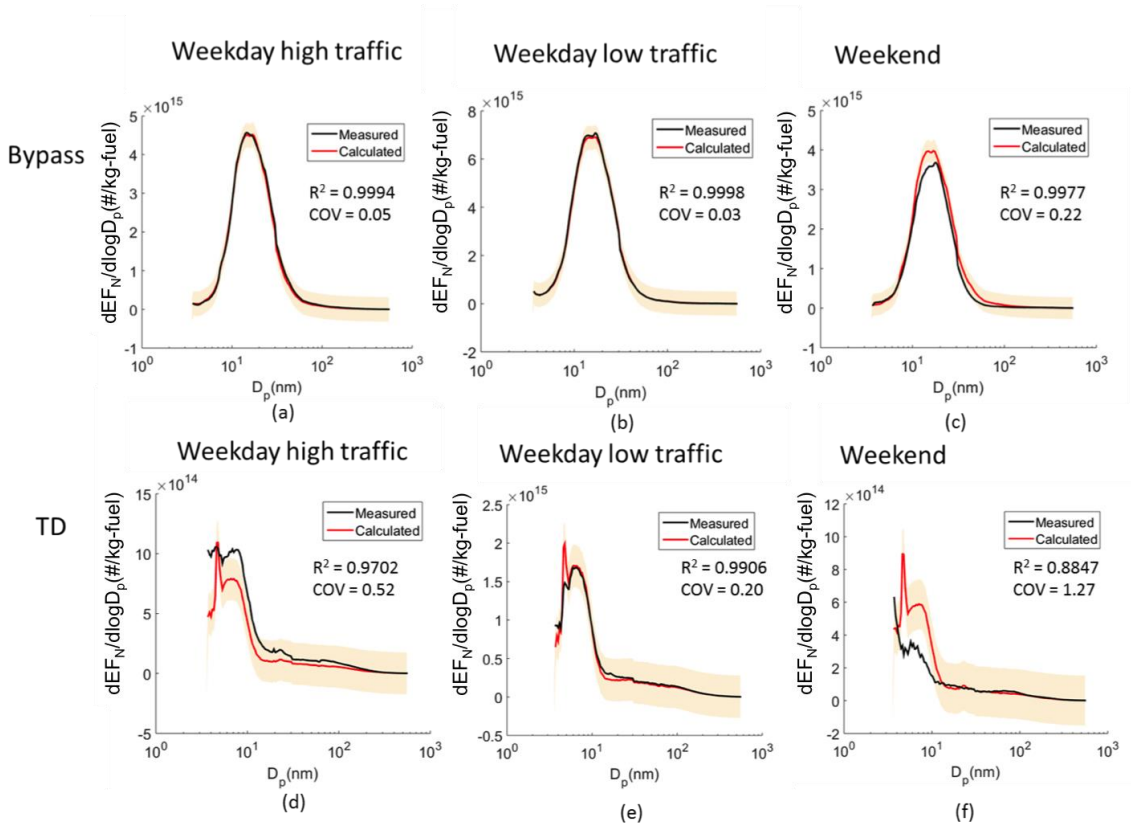

Figure B.9 The measured and calculated size-resolved EF_N of vehicle emitted particles and non-volatile particles measured in different time periods. Shaded areas represent the uncertainty range of the calculated EF_N.

B.1 Particle loss inside the TD

I tested the particle loss inside the TD under different flow rate (2.5, 4.5, and 9.5 LPM) with NaCl particles following the method described in previous studies [52,196]. To briefly summarize here, I generated some NaCl particles and firstly sent them into a 10 m^3 Teflon chamber, and then the particles in the chamber were sent through a TD. Two long-SMPS were sampling at the upstream and the downstream of the TD simultaneously to characterize the particle transmissions trough the TD. Before characterizing the TD particle loss, both SMPS were sampling directly from the chamber at the same time to test the discrepancy of two instruments. As shown in Figure B.3, the ratios of number concentrations measured by these two SMPS are relatively stable at the particle size range of 22 - 378nm. Therefore, I fitted the particle transmission of this size range with the equation proposed by Stevanovic et al. [245] to get the TD transmissions of 4 – 550 nm particles, and the result is shown in Figure B.4. The particle transmissions under different TD flow rate are similar. Therefore, for all TD data presented in this work, I used the TD particle transmission function under the flow rate of 9.5 LPM to correct for the particle loss.

B.2 The size of primary particles of the nanoparticle aggregates measured in the tunnel.

In order to justify the choice of 30 nm as the size of the primary particle of the nanoparticle aggregates measured in the tunnel, I varied the primary particle size (a = 20, 30, 50, 80, and 100 nm) and re-analyzed the SMPS size distribution data using the Nanoparticle Aggregate Mobility Analysis Software Module built in the Aerosol Instrument Manager Software for SMPS, and then performed the same analysis shown in Figure 4.1 to study how the size of the primary particles (a) would influence the comparison of particle mass measured by SMPS and other direct particle mass instruments. Results are shown in Table B.1. For particles measured through bypass line, assuming a = 80 or 100 nm would make SMPS over estimates the particle mass, and a = 20 nm would make SMPS greatly underestimate the particle mass. Although a = 50 nm would make the SMPS

mass closer to the OCEC mass than a = 30 nm, the correlation between SMPS mass and OCEC mass becomes worse. Also, as discussed in the text, since OCEC and SMPS have different size cut (<2.5 μm v.s. 4 – 550 nm), I expect the SMPS measured less mass than the OCEC. For particles measured through the TD, a = 50, 80, and 100nm makes SMPS greatly overestimate the particle mass, while a = 20 nm makes SMPS greatly underestimate the particle mass. The case that a = 30 nm makes the SMPS measured mass matches best with the Athalometer measured mass. Therefore, for both particles measured through the bypass line and the TD, a = 30 nm would make the SMPS measured mass best match other direct particle mass measurements.

Table B.1 The influence of the primary particle size on the comparison between particle mass measured by SMPS and other instruments

Primary particle size(a,nm)	20	30	50	80	100	Assuming Spherical
Ratio of bypass SMPS mass to OCEC mass	0.46	0.71	0.93	1.15	1.31	2.96
Bypass R^2	0.61	0.65	0.57	0.69	0.70	0.47
Ratio of TD SMPS mass to Aethalometer BC mass	0.55	0.91	1.47	1.8	2.12	3.67
TD R^2	0.68	0.68	0.68	0.67	0.66	-0.19

B.3 Source apportionment of size-resolved emission factors of LDV and HDDV

In order to determine the quality of the source apportionment, all measurement data were divided into two sets. Among all 60 hours of data, 30 hours were randomly selected as the training set, and the rest of data were used as the testing set. I performed the linear regression only to the training set to determine the size-dependent particle emission factors of LDV and HDDV (EF_G and EF_D, respectively), and then used use them to reconstruct the averaged size-dependent particle emissions factor of the testing set (EF(t)) using the following equation:

$$EF(t) = EF_G \cdot (1 - \%\, fuel_D(t)) + EF_D \cdot \%\, fuel_D(t) \quad (1)$$

where $\%fuel_D(t)$ is the averaged diesel fuel fraction the testing set. The coefficient of determination (R^2) and the coefficient of variation (COV) were calculated to determine how close the reconstructed size-dependent particle emission factor is to the actual measurement of the testing set. The COV is defined as the following equation:

$$COV = \frac{MSE}{mean(t)} \quad (2)$$

where MSE is the mean-squared error of the reconstructed size-dependent particle emission factor and the averaged measured size-dependent particle emission factor of the testing set, averaged across all size bins. And the mean (t) is the averaged particle number concentration of the testing set across all size bins.

I repeated this random sampling process for n times, and the size-dependent particle emission factors of LDV and HDDV were determined as the average of all source apportionment results from n times of random sampling. The standard deviation of these results was regarded as the uncertainty of the estimated LDV and HDDV emission factors. In order to determine how many random samplings needed to create a representative estimation of LDV and HDDV emission factors, I varied n from 10 to 3000, and the distributions of R^2 and COV with n = 10-3000 are presented in Figure B.8. It shows that when n≥400, the distributions of R^2 and COV became stable. Therefore, 3000 times of random sampling is enough to generate a representative source apportionment result.

As shown in Figure B.8, for the particle emission factors measured through the bypass line, the averaged COV and R^2 of all 3000 times of random sampling processes was 0.17 and 0.997, respectively, indicating that the apportioned gasoline and diesel emission factor size-distributions was able to match the actual measurement. The averaged COV and R^2 for the non-volatile particles emission factors measured through TD are slightly worse (0.4 and 0.97, respectively). To further test the quality of the source apportionment results, the

apportioned averaged LDV and HDDV emission factors size-distributions were used to reconstruct the vehicle emission factors during the weekday high traffic time, the weekday low traffic time, and the weekends (Figure B.9). For the particle emission factors measured through the bypass line, the reconstructed size-distributions well matched the measurement. For the non-volatile particle emission factors measured through the TD, the reconstructed results better matched the weekday measurement than the weekend measurement, which has a higher COV (1.27) and lower R^2 (0.88). In general, the apportioned particle and non-volatile particle emission factors for LDV and HDDV are able to predict the actual measurement with an acceptable uncertainty.

Table B.2 The number of primary particles in the nanoparticle aggregate with a diameter of D_p

Dp(nm)	Number of primary particles(Np(Dp))
31.1	1.7
32.2	1.8
33.4	2
34.6	2.1
35.9	2.3
37.2	2.4
38.5	2.6
40	2.8
41.4	3
42.9	3.2
44.5	3.4
46.1	3.6
47.8	3.9
49.6	4.2
51.4	4.4
53.3	4.8
55.2	5.1
57.3	5.4
59.4	5.8
61.5	6.2
63.8	6.6
66.1	7.1
68.5	7.5
71	8.1
73.7	8.6
76.4	9.2
79.1	9.8

Dp(nm)	Number of primary particles(Np(Dp))
82	10.4
85.1	11.1
88.2	11.8
91.4	12.6
94.7	13.4
98.2	14.3
101.8	15.2
105.5	16.2
109.4	17.2
113.4	18.3
117.6	19.4
121.9	20.6
126.3	21.9
131	23.3
135.8	24.7
140.7	26.2
145.9	27.8
151.2	29.4
156.8	31.2
162.5	33
168.5	34.9
174.7	37
181.1	39.1
187.7	41.3
194.6	43.7
201.7	46.1
209.1	48.7

Dp(nm)	Number of primary particles(Np(Dp))
216.7	51.4
224.7	54.2
232.9	57.2
241.4	60.2
250.3	63.5
259.5	66.8
269	70.3
278.8	74
289	77.8
299.6	81.8
310.6	86
322	90.3
333.8	94.8
346	99.5
358.7	104.4
371.8	109.5
385.4	114.8
399.5	120.3
414.2	126.1
429.4	132.1
445.1	138.3
461.4	144.7
478.3	151.4
495.8	158.4
514	165.7
532.8	173.2
552.3	181.1

Table B.3-1 Size resolved particle emission factors of LDV and HDDV

mean value

Dp(nm)	$dEF_N/dlogDp$(#/kg fuel)		$dEF_M/dlogDp$(g/kg fuel)	
	LDV	HDDV	LDV	HDDV
3.72	-	2.43E+15	-	7.87E-05
3.85	-	1.87E+15	-	6.72E-05
4	-	1.75E+15	-	7.05E-05
4.14	9.92E+12	1.64E+15	4.42E-07	7.32E-05
4.29	1.90E+13	1.57E+15	9.41E-07	7.79E-05
4.45	1.63E+13	1.71E+15	9.04E-07	9.49E-05
4.61	3.25E+13	1.75E+15	2.00E-06	1.08E-04
4.78	5.19E+13	1.80E+15	3.56E-06	1.23E-04
4.96	8.15E+13	1.83E+15	6.25E-06	1.40E-04
5.14	9.34E+13	1.98E+15	7.97E-06	1.69E-04
5.33	9.64E+13	2.20E+15	9.17E-06	2.09E-04
5.52	8.94E+13	2.62E+15	9.45E-06	2.77E-04
5.73	1.12E+14	2.86E+15	1.32E-05	3.38E-04
5.94	1.41E+14	3.05E+15	1.86E-05	4.02E-04
6.15	1.60E+14	3.47E+15	2.34E-05	5.07E-04
6.38	1.90E+14	3.93E+15	3.10E-05	6.42E-04
6.61	2.28E+14	4.59E+15	4.14E-05	8.32E-04
6.85	2.83E+14	5.17E+15	5.72E-05	1.05E-03
7.1	3.95E+14	5.41E+15	8.89E-05	1.22E-03
7.37	6.14E+14	5.58E+15	1.54E-04	1.40E-03
7.64	7.28E+14	6.25E+15	2.04E-04	1.75E-03
7.91	7.74E+14	7.28E+15	2.41E-04	2.26E-03
8.2	8.34E+14	8.48E+15	2.89E-04	2.94E-03
8.51	8.74E+14	1.03E+16	3.38E-04	4.01E-03
8.82	9.24E+14	1.23E+16	3.98E-04	5.28E-03
9.14	1.00E+15	1.39E+16	4.82E-04	6.68E-03
9.47	1.18E+15	1.50E+16	6.31E-04	7.99E-03
9.82	1.37E+15	1.61E+16	8.17E-04	9.57E-03
10.2	1.64E+15	1.70E+16	1.10E-03	1.13E-02
10.6	1.90E+15	1.78E+16	1.42E-03	1.33E-02
10.9	2.16E+15	1.81E+16	1.76E-03	1.47E-02
11.3	2.36E+15	1.88E+16	2.14E-03	1.70E-02
11.8	2.50E+15	1.95E+16	2.58E-03	2.02E-02
12.2	2.63E+15	2.02E+16	3.01E-03	2.31E-02
12.6	2.76E+15	2.06E+16	3.46E-03	2.59E-02
13.1	2.86E+15	2.09E+16	4.03E-03	2.95E-02
13.6	2.93E+15	2.10E+16	4.63E-03	3.32E-02
14.1	3.01E+15	2.09E+16	5.30E-03	3.68E-02
14.6	3.03E+15	2.08E+16	5.93E-03	4.07E-02
15.1	3.03E+15	2.08E+16	6.56E-03	4.50E-02
15.7	3.00E+15	2.09E+16	7.29E-03	5.08E-02
16.3	2.99E+15	2.10E+16	8.14E-03	5.73E-02
16.8	3.04E+15	2.09E+16	9.07E-03	6.24E-02
17.5	3.03E+15	2.07E+16	1.02E-02	6.98E-02
18.1	2.97E+15	2.03E+16	1.11E-02	7.57E-02
18.8	2.88E+15	1.99E+16	1.20E-02	8.32E-02
19.5	2.78E+15	1.93E+16	1.30E-02	8.97E-02
20.2	2.71E+15	1.86E+16	1.40E-02	9.65E-02
20.9	2.62E+15	1.78E+16	1.50E-02	1.02E-01

21.7	2.50E+15	1.70E+16	1.61E-02	1.09E-01
22.5	2.41E+15	1.64E+16	1.72E-02	1.18E-01
23.3	2.36E+15	1.56E+16	1.88E-02	1.24E-01
24.1	2.24E+15	1.47E+16	1.97E-02	1.29E-01
25	2.11E+15	1.38E+16	2.07E-02	1.35E-01
25.9	1.93E+15	1.31E+16	2.11E-02	1.43E-01
26.9	1.77E+15	1.23E+16	2.17E-02	1.50E-01
27.9	1.61E+15	1.12E+16	2.20E-02	1.53E-01
28.9	1.53E+15	1.01E+16	2.32E-02	1.52E-01
30	1.41E+15	8.94E+15	2.39E-02	1.52E-01
31.1	1.06E+15	6.82E+15	3.10E-02	1.98E-01
32.2	9.84E+14	6.24E+15	3.07E-02	1.94E-01
33.4	9.09E+14	5.48E+15	3.03E-02	1.83E-01
34.6	8.26E+14	4.81E+15	2.95E-02	1.72E-01
35.9	7.57E+14	4.12E+15	2.90E-02	1.58E-01
37.2	6.93E+14	3.56E+15	2.84E-02	1.46E-01
38.5	6.27E+14	3.11E+15	2.75E-02	1.36E-01
40	5.67E+14	2.71E+15	2.67E-02	1.27E-01
41.4	5.33E+14	2.31E+15	2.68E-02	1.16E-01
42.9	5.09E+14	1.97E+15	2.74E-02	1.06E-01
44.5	4.60E+14	1.71E+15	2.65E-02	9.83E-02
46.1	4.08E+14	1.47E+15	2.51E-02	9.06E-02
47.8	3.59E+14	1.29E+15	2.37E-02	8.49E-02
49.6	3.21E+14	1.11E+15	2.26E-02	7.85E-02
51.4	2.85E+14	9.74E+14	2.15E-02	7.35E-02
53.3	2.47E+14	9.61E+14	1.99E-02	7.75E-02
55.2	2.24E+14	8.56E+14	1.93E-02	7.38E-02
57.3	1.96E+14	7.84E+14	1.81E-02	7.22E-02
59.4	1.71E+14	6.81E+14	1.69E-02	6.70E-02
61.5	1.5E+14	6.5E+14	1.57E-02	6.84E-02
63.8	1.45E+14	5.58E+14	1.63E-02	6.27E-02
66.1	1.38E+14	4.9E+14	1.66E-02	5.88E-02
68.5	1.32E+14	4.28E+14	1.69E-02	5.47E-02
71	1.24E+14	3.91E+14	1.69E-02	5.34E-02
73.7	1.18E+14	3.25E+14	1.72E-02	4.74E-02
76.4	1.14E+14	2.83E+14	1.77E-02	4.40E-02
79.1	1.04E+14	3E+14	1.73E-02	4.97E-02
82	9.48E+13	3.32E+14	1.68E-02	5.88E-02
85.1	1.04E+14	2.37E+14	1.95E-02	4.46E-02
88.2	9.21E+13	2.25E+14	1.85E-02	4.52E-02
91.4	8.69E+13	2.09E+14	1.86E-02	4.47E-02
94.7	8.17E+13	1.94E+14	1.86E-02	4.42E-02
98.2	7.15E+13	2.39E+14	1.73E-02	5.81E-02
101.8	6.65E+13	2.29E+14	1.72E-02	5.90E-02
105.5	6.26E+13	2.1E+14	1.72E-02	5.76E-02
109.4	5.85E+13	1.96E+14	1.71E-02	5.71E-02
113.4	5.53E+13	1.72E+14	1.72E-02	5.35E-02
117.6	5.19E+13	1.55E+14	1.71E-02	5.11E-02
121.9	4.89E+13	1.4E+14	1.71E-02	4.91E-02
126.3	4.61E+13	1.26E+14	1.71E-02	4.70E-02
131	4.56E+13	1.02E+14	1.80E-02	4.03E-02
135.8	4.36E+13	8.74E+13	1.83E-02	3.66E-02
140.7	4.15E+13	7.66E+13	1.84E-02	3.40E-02
145.9	4.12E+13	5.99E+13	1.94E-02	2.82E-02
151.2	3.86E+13	6.7E+13	1.93E-02	3.35E-02
156.8	3.59E+13	5.86E+13	1.90E-02	3.10E-02

162.5	3.33E+13	5.09E+13	1.86E-02	2.85E-02
168.5	3.11E+13	5.06E+13	1.84E-02	3.00E-02
174.7	2.93E+13	4.92E+13	1.84E-02	3.09E-02
181.1	2.76E+13	4.63E+13	1.83E-02	3.07E-02
187.7	2.57E+13	4.35E+13	1.80E-02	3.05E-02
194.6	2.42E+13	4.4E+13	1.80E-02	3.26E-02
201.7	2.29E+13	3.97E+13	1.80E-02	3.11E-02
209.1	2.16E+13	3.69E+13	1.79E-02	3.05E-02
216.7	2.07E+13	2.99E+13	1.81E-02	2.60E-02
224.7	1.97E+13	2.39E+13	1.81E-02	2.20E-02
232.9	1.83E+13	2.69E+13	1.77E-02	2.61E-02
241.4	1.71E+13	2.84E+13	1.74E-02	2.91E-02
250.3	1.6E+13	3.38E+13	1.73E-02	3.64E-02
259.5	1.4E+13	3.76E+13	1.59E-02	4.26E-02
269	1.33E+13	3.73E+13	1.59E-02	4.45E-02
278.8	1.25E+13	3.24E+13	1.57E-02	4.06E-02
289	1.18E+13	2.83E+13	1.55E-02	3.73E-02
299.6	1.06E+13	3.02E+13	1.47E-02	4.19E-02
310.6	9.73E+12	3.28E+13	1.42E-02	4.79E-02
322	8.88E+12	2.97E+13	1.36E-02	4.56E-02
333.8	9.08E+12	3.55E+13	1.46E-02	5.72E-02
346	7.97E+12	3.29E+13	1.35E-02	5.56E-02
358.7	7.17E+12	2.99E+13	1.27E-02	5.30E-02
371.8	6.25E+12	2.69E+13	1.16E-02	5.00E-02
385.4	5.58E+12	2.39E+13	1.09E-02	4.65E-02
399.5	4.78E+12	2.08E+13	9.77E-03	4.24E-02
414.2	4.21E+12	1.81E+13	9.01E-03	3.86E-02
429.4	3.65E+12	1.55E+13	8.19E-03	3.48E-02
445.1	3.66E+12	1.14E+13	8.60E-03	2.68E-02
461.4	3.35E+12	9.58E+12	8.22E-03	2.35E-02
478.3	3.71E+12	6.33E+12	9.53E-03	1.63E-02
495.8	3.28E+12	5.16E+12	8.82E-03	1.39E-02
514	2.91E+12	4.57E+12	8.19E-03	1.28E-02
532.8	2.64E+12	3.97E+12	7.75E-03	1.17E-02
552.3	2.23E+12	3.82E+12	6.86E-03	1.17E-02

standard deviation

Dp(nm)	$dEF_N/dlogDp$(#/kg fuel)		$dEF_M/dlogDp$(g/kg fuel)	
	LDV	HDDV	LDV	HDDV
3.72	1.66E+14	1.66E+15	5.36E-06	5.37E-05
3.85	1.44E+14	1.42E+15	5.15E-06	5.08E-05
4	1.20E+14	1.10E+15	4.81E-06	4.44E-05
4.14	1.06E+14	9.60E+14	4.71E-06	4.28E-05
4.29	9.60E+13	9.15E+14	4.76E-06	4.54E-05
4.45	9.68E+13	9.32E+14	5.36E-06	5.16E-05
4.61	8.88E+13	8.36E+14	5.47E-06	5.14E-05
4.78	8.70E+13	8.14E+14	5.97E-06	5.59E-05
4.96	9.04E+13	8.42E+14	6.93E-06	6.45E-05
5.14	8.22E+13	7.06E+14	7.01E-06	6.02E-05
5.33	7.89E+13	7.03E+14	7.50E-06	6.69E-05
5.52	9.16E+13	9.02E+14	9.68E-06	9.53E-05
5.73	8.08E+13	7.36E+14	9.56E-06	8.70E-05
5.94	8.82E+13	7.84E+14	1.16E-05	1.03E-04
6.15	9.83E+13	8.25E+14	1.44E-05	1.21E-04
6.38	1.07E+14	9.23E+14	1.75E-05	1.51E-04

6.61	1.30E+14	1.19E+15	2.35E-05	2.16E-04
6.85	1.44E+14	1.33E+15	2.90E-05	2.69E-04
7.1	1.54E+14	1.21E+15	3.47E-05	2.72E-04
7.37	2.87E+14	1.52E+15	7.21E-05	3.83E-04
7.64	3.35E+14	1.70E+15	9.38E-05	4.75E-04
7.91	3.06E+14	1.75E+15	9.50E-05	5.45E-04
8.2	2.81E+14	1.73E+15	9.72E-05	5.98E-04
8.51	2.88E+14	1.96E+15	1.11E-04	7.57E-04
8.82	3.35E+14	2.53E+15	1.44E-04	1.09E-03
9.14	3.70E+14	2.97E+15	1.77E-04	1.43E-03
9.47	3.79E+14	2.91E+15	2.02E-04	1.56E-03
9.82	3.93E+14	2.86E+15	2.34E-04	1.70E-03
10.2	4.55E+14	3.06E+15	3.03E-04	2.04E-03
10.6	5.04E+14	3.30E+15	3.77E-04	2.47E-03
10.9	5.04E+14	3.33E+15	4.10E-04	2.71E-03
11.3	5.13E+14	3.45E+15	4.66E-04	3.13E-03
11.8	5.41E+14	3.77E+15	5.58E-04	3.89E-03
12.2	5.59E+14	3.97E+15	6.38E-04	4.53E-03
12.6	5.76E+14	4.17E+15	7.24E-04	5.24E-03
13.1	5.86E+14	4.36E+15	8.27E-04	6.16E-03
13.6	5.97E+14	4.47E+15	9.43E-04	7.07E-03
14.1	6.00E+14	4.52E+15	1.06E-03	7.96E-03
14.6	5.98E+14	4.55E+15	1.17E-03	8.90E-03
15.1	5.88E+14	4.57E+15	1.27E-03	9.88E-03
15.7	5.72E+14	4.48E+15	1.39E-03	1.09E-02
16.3	5.68E+14	4.53E+15	1.55E-03	1.23E-02
16.8	5.79E+14	4.52E+15	1.73E-03	1.35E-02
17.5	5.83E+14	4.53E+15	1.96E-03	1.53E-02
18.1	5.66E+14	4.45E+15	2.11E-03	1.66E-02
18.8	5.46E+14	4.34E+15	2.28E-03	1.81E-02
19.5	5.26E+14	4.24E+15	2.45E-03	1.97E-02
20.2	5.16E+14	4.15E+15	2.67E-03	2.15E-02
20.9	5.17E+14	4.07E+15	2.97E-03	2.34E-02
21.7	5.01E+14	3.92E+15	3.22E-03	2.52E-02
22.5	5.00E+14	3.96E+15	3.58E-03	2.83E-02
23.3	5.17E+14	4.04E+15	4.11E-03	3.21E-02
24.1	5.08E+14	3.99E+15	4.46E-03	3.51E-02
25	4.90E+14	3.96E+15	4.82E-03	3.89E-02
25.9	4.64E+14	3.86E+15	5.07E-03	4.22E-02
26.9	4.40E+14	3.76E+15	5.39E-03	4.60E-02
27.9	4.07E+14	3.52E+15	5.56E-03	4.81E-02
28.9	3.85E+14	3.36E+15	5.84E-03	5.10E-02
30	3.55E+14	3.09E+15	6.02E-03	5.25E-02
31.1	2.82E+14	2.48E+15	8.18E-03	7.20E-02
32.2	2.66E+14	2.34E+15	8.27E-03	7.28E-02
33.4	2.39E+14	2.09E+15	7.97E-03	6.98E-02
34.6	2.16E+14	1.89E+15	7.71E-03	6.75E-02
35.9	1.93E+14	1.68E+15	7.39E-03	6.42E-02
37.2	1.77E+14	1.54E+15	7.27E-03	6.32E-02
38.5	1.64E+14	1.44E+15	7.20E-03	6.30E-02
40	1.54E+14	1.36E+15	7.22E-03	6.38E-02
41.4	1.50E+14	1.30E+15	7.54E-03	6.54E-02
42.9	1.51E+14	1.24E+15	8.11E-03	6.69E-02
44.5	1.41E+14	1.15E+15	8.11E-03	6.60E-02
46.1	1.25E+14	1.03E+15	7.68E-03	6.37E-02
47.8	1.10E+14	9.31E+14	7.22E-03	6.14E-02

49.6	9.80E+13	8.53E+14	6.91E-03	6.01E-02
51.4	8.75E+13	7.81E+14	6.60E-03	5.89E-02
53.3	7.85E+13	7.16E+14	6.33E-03	5.77E-02
55.2	6.98E+13	6.3E+14	6.01E-03	5.43E-02
57.3	6.15E+13	5.65E+14	5.67E-03	5.20E-02
59.4	5.37E+13	4.98E+14	5.29E-03	4.90E-02
61.5	4.72E+13	4.49E+14	4.96E-03	4.72E-02
63.8	4.01E+13	3.78E+14	4.51E-03	4.24E-02
66.1	3.66E+13	3.37E+14	4.38E-03	4.04E-02
68.5	3.35E+13	3E+14	4.28E-03	3.85E-02
71	3.19E+13	2.83E+14	4.36E-03	3.87E-02
73.7	2.99E+13	2.58E+14	4.36E-03	3.77E-02
76.4	2.8E+13	2.37E+14	4.36E-03	3.68E-02
79.1	2.74E+13	2.35E+14	4.55E-03	3.90E-02
82	2.63E+13	2.3E+14	4.65E-03	4.06E-02
85.1	2.59E+13	2.07E+14	4.87E-03	3.89E-02
88.2	2.75E+13	2.15E+14	5.51E-03	4.31E-02
91.4	2.59E+13	2.02E+14	5.54E-03	4.32E-02
94.7	2.43E+13	1.89E+14	5.54E-03	4.30E-02
98.2	2.32E+13	1.89E+14	5.62E-03	4.57E-02
101.8	2.12E+13	1.74E+14	5.47E-03	4.49E-02
105.5	1.94E+13	1.59E+14	5.32E-03	4.36E-02
109.4	1.75E+13	1.42E+14	5.11E-03	4.15E-02
113.4	1.6E+13	1.28E+14	4.96E-03	3.97E-02
117.6	1.46E+13	1.13E+14	4.80E-03	3.71E-02
121.9	1.33E+13	9.95E+13	4.67E-03	3.48E-02
126.3	1.22E+13	8.77E+13	4.54E-03	3.26E-02
131	1.14E+13	7.62E+13	4.49E-03	3.01E-02
135.8	1.05E+13	6.96E+13	4.39E-03	2.92E-02
140.7	9.85E+12	6.35E+13	4.38E-03	2.82E-02
145.9	9.36E+12	5.91E+13	4.41E-03	2.78E-02
151.2	8.84E+12	5.68E+13	4.41E-03	2.84E-02
156.8	8.15E+12	5.21E+13	4.31E-03	2.76E-02
162.5	7.45E+12	4.86E+13	4.17E-03	2.72E-02
168.5	6.78E+12	4.41E+13	4.02E-03	2.61E-02
174.7	6.21E+12	4.05E+13	3.90E-03	2.54E-02
181.1	5.65E+12	3.77E+13	3.75E-03	2.50E-02
187.7	5.06E+12	3.38E+13	3.55E-03	2.37E-02
194.6	4.67E+12	3.23E+13	3.46E-03	2.39E-02
201.7	4.32E+12	3.08E+13	3.38E-03	2.41E-02
209.1	4.02E+12	2.89E+13	3.32E-03	2.39E-02
216.7	3.84E+12	2.81E+13	3.35E-03	2.45E-02
224.7	3.64E+12	2.77E+13	3.35E-03	2.55E-02
232.9	3.42E+12	2.63E+13	3.31E-03	2.55E-02
241.4	3.23E+12	2.46E+13	3.30E-03	2.52E-02
250.3	3.27E+12	2.47E+13	3.52E-03	2.66E-02
259.5	3.17E+12	2.34E+13	3.59E-03	2.65E-02
269	3.05E+12	2.22E+13	3.64E-03	2.65E-02
278.8	3.03E+12	2.26E+13	3.81E-03	2.84E-02
289	2.96E+12	2.18E+13	3.91E-03	2.87E-02
299.6	2.84E+12	2.04E+13	3.94E-03	2.83E-02
310.6	2.67E+12	1.91E+13	3.89E-03	2.78E-02
322	2.54E+12	1.75E+13	3.90E-03	2.68E-02
333.8	2.58E+12	1.75E+13	4.15E-03	2.82E-02
346	2.4E+12	1.59E+13	4.05E-03	2.69E-02
358.7	2.27E+12	1.5E+13	4.01E-03	2.66E-02

371.8	2.11E+12	1.39E+13	3.93E-03	2.58E-02
385.4	1.93E+12	1.25E+13	3.76E-03	2.43E-02
399.5	1.77E+12	1.13E+13	3.62E-03	2.30E-02
414.2	1.64E+12	1.01E+13	3.50E-03	2.16E-02
429.4	1.51E+12	9.18E+12	3.39E-03	2.06E-02
445.1	1.42E+12	8.2E+12	3.32E-03	1.92E-02
461.4	1.31E+12	7.24E+12	3.21E-03	1.78E-02
478.3	1.23E+12	6.38E+12	3.15E-03	1.64E-02
495.8	1.15E+12	5.64E+12	3.10E-03	1.52E-02
514	1.07E+12	5.05E+12	3.01E-03	1.42E-02
532.8	9.88E+11	4.3E+12	2.90E-03	1.26E-02
552.3	8.85E+11	3.89E+12	2.72E-03	1.20E-02

Table B.3-2 Size resolved non-volatile particle emission factors of LDV and HDDV

mean value

Dp(nm)	$dEF_N/dlogDp$(#/kg fuel)		$dEF_M/dlogDp$(g/kg fuel)	
	LDV	HDDV	LDV	HDDV
3.72	8.10E+14	1.71E+15	2.62E-05	5.53E-05
3.85	6.61E+14	2.47E+15	2.37E-05	8.84E-05
4	6.68E+14	2.19E+15	2.68E-05	8.82E-05
4.14	6.03E+14	2.93E+15	2.69E-05	1.31E-04
4.29	5.87E+14	2.73E+15	2.91E-05	1.36E-04
4.45	4.80E+14	4.06E+15	2.66E-05	2.25E-04
4.61	2.13E+14	7.00E+15	1.31E-05	4.31E-04
4.78	1.75E+14	7.29E+15	1.20E-05	5.00E-04
4.96	2.31E+14	6.65E+15	1.77E-05	5.10E-04
5.14	2.60E+14	6.35E+15	2.22E-05	5.42E-04
5.33	2.61E+14	5.96E+15	2.48E-05	5.67E-04
5.52	2.67E+14	6.55E+15	2.82E-05	6.92E-04
5.73	2.50E+14	6.92E+15	2.95E-05	8.18E-04
5.94	2.53E+14	7.11E+15	3.33E-05	9.37E-04
6.15	2.48E+14	7.13E+15	3.62E-05	1.04E-03
6.38	2.79E+14	7.04E+15	4.54E-05	1.15E-03
6.61	2.69E+14	7.07E+15	4.88E-05	1.28E-03
6.85	3.00E+14	6.94E+15	6.06E-05	1.40E-03
7.1	2.72E+14	6.88E+15	6.12E-05	1.55E-03
7.37	2.94E+14	6.61E+15	7.39E-05	1.66E-03
7.64	3.00E+14	6.54E+15	8.40E-05	1.83E-03
7.91	3.27E+14	6.22E+15	1.02E-04	1.93E-03
8.2	3.03E+14	5.95E+15	1.05E-04	2.06E-03
8.51	2.87E+14	5.71E+15	1.11E-04	2.21E-03
8.82	2.96E+14	5.18E+15	1.27E-04	2.23E-03
9.14	2.55E+14	4.78E+15	1.22E-04	2.29E-03
9.47	2.59E+14	4.19E+15	1.38E-04	2.23E-03
9.82	2.50E+14	3.76E+15	1.49E-04	2.23E-03
10.2	2.40E+14	3.21E+15	1.60E-04	2.14E-03
10.6	2.42E+14	2.72E+15	1.81E-04	2.04E-03
10.9	2.19E+14	2.36E+15	1.78E-04	1.92E-03
11.3	1.95E+14	2.02E+15	1.77E-04	1.83E-03
11.8	1.85E+14	1.74E+15	1.91E-04	1.80E-03
12.2	1.63E+14	1.56E+15	1.86E-04	1.78E-03
12.6	1.65E+14	1.30E+15	2.08E-04	1.63E-03

13.1	1.52E+14	1.21E+15	2.15E-04	1.71E-03
13.6	1.44E+14	1.11E+15	2.27E-04	1.75E-03
14.1	1.38E+14	9.91E+14	2.43E-04	1.75E-03
14.6	1.26E+14	9.59E+14	2.46E-04	1.88E-03
15.1	1.17E+14	9.77E+14	2.53E-04	2.11E-03
15.7	1.11E+14	9.53E+14	2.70E-04	2.32E-03
16.3	1.15E+14	9.38E+14	3.13E-04	2.55E-03
16.8	1.14E+14	9.09E+14	3.41E-04	2.71E-03
17.5	1.01E+14	9.23E+14	3.41E-04	3.11E-03
18.1	9.49E+13	9.29E+14	3.53E-04	3.46E-03
18.8	8.99E+13	9.12E+14	3.75E-04	3.81E-03
19.5	1.01E+14	9.19E+14	4.69E-04	4.28E-03
20.2	8.78E+13	8.91E+14	4.55E-04	4.61E-03
20.9	9.15E+13	8.97E+14	5.25E-04	5.14E-03
21.7	9.70E+13	8.46E+14	6.23E-04	5.43E-03
22.5	9.93E+13	8.79E+14	7.11E-04	6.29E-03
23.3	9.80E+13	8.54E+14	7.79E-04	6.79E-03
24.1	9.35E+13	8.60E+14	8.22E-04	7.57E-03
25	8.20E+13	8.86E+14	8.05E-04	8.70E-03
25.9	6.77E+13	9.48E+14	7.39E-04	1.03E-02
26.9	6.31E+13	9.53E+14	7.72E-04	1.17E-02
27.9	5.65E+13	9.81E+14	7.70E-04	1.34E-02
28.9	5.61E+13	9.51E+14	8.51E-04	1.44E-02
30	4.97E+13	9.85E+14	8.43E-04	1.67E-02
31.1	3.98E+13	8.14E+14	1.16E-03	2.37E-02
32.2	4.25E+13	8.03E+14	1.32E-03	2.50E-02
33.4	3.93E+13	8.26E+14	1.31E-03	2.75E-02
34.6	4.07E+13	7.91E+14	1.45E-03	2.83E-02
35.9	4.00E+13	7.84E+14	1.53E-03	3.00E-02
37.2	3.80E+13	7.99E+14	1.56E-03	3.27E-02
38.5	3.80E+13	7.95E+14	1.67E-03	3.49E-02
40	4.06E+13	7.77E+14	1.91E-03	3.65E-02
41.4	4.15E+13	7.58E+14	2.08E-03	3.81E-02
42.9	3.73E+13	7.70E+14	2.01E-03	4.14E-02
44.5	3.85E+13	7.67E+14	2.22E-03	4.42E-02
46.1	3.89E+13	7.41E+14	2.40E-03	4.56E-02
47.8	4.07E+13	7.02E+14	2.68E-03	4.63E-02
49.6	4.24E+13	6.93E+14	2.99E-03	4.89E-02
51.4	4.21E+13	7.01E+14	3.17E-03	5.29E-02
53.3	4.30E+13	6.75E+14	3.47E-03	5.44E-02
55.2	4.45E+13	6.69E+14	3.83E-03	5.77E-02
57.3	4.32E+13	6.46E+14	3.98E-03	5.95E-02
59.4	4.38E+13	6.05E+14	4.31E-03	5.96E-02
61.5	4.24E+13	5.88E+14	4.46E-03	6.19E-02
63.8	4.80E+13	6.40E+14	5.38E-03	7.19E-02
66.1	4.89E+13	6.27E+14	5.86E-03	7.52E-02
68.5	4.93E+13	6.17E+14	6.31E-03	7.89E-02
71	5.00E+13	5.86E+14	6.84E-03	8.01E-02
73.7	4.95E+13	5.69E+14	7.22E-03	8.29E-02
76.4	4.86E+13	5.59E+14	7.56E-03	8.69E-02
79.1	4.73E+13	5.49E+14	7.85E-03	9.11E-02
82	4.49E+13	5.50E+14	7.94E-03	9.72E-02
85.1	4.46E+13	5.70E+14	8.41E-03	1.07E-01
88.2	4.21E+13	5.67E+14	8.46E-03	1.14E-01
91.4	3.96E+13	5.65E+14	8.47E-03	1.21E-01
94.7	3.74E+13	5.54E+14	8.51E-03	1.26E-01

98.2	3.54E+13	5.43E+14	8.58E-03	1.32E-01
101.8	3.39E+13	5.26E+14	8.74E-03	1.36E-01
105.5	3.20E+13	5.11E+14	8.77E-03	1.40E-01
109.4	3.08E+13	4.95E+14	8.99E-03	1.45E-01
113.4	2.93E+13	4.75E+14	9.10E-03	1.47E-01
117.6	2.82E+13	4.54E+14	9.31E-03	1.50E-01
121.9	2.70E+13	4.37E+14	9.47E-03	1.53E-01
126.3	2.62E+13	4.13E+14	9.75E-03	1.54E-01
131	2.55E+13	3.91E+14	1.01E-02	1.54E-01
135.8	2.43E+13	3.71E+14	1.02E-02	1.56E-01
140.7	2.34E+13	3.51E+14	1.04E-02	1.56E-01
145.9	2.23E+13	3.31E+14	1.05E-02	1.56E-01
151.2	2.13E+13	3.09E+14	1.07E-02	1.54E-01
156.8	1.99E+13	2.91E+14	1.05E-02	1.54E-01
162.5	1.83E+13	2.74E+14	1.03E-02	1.54E-01
168.5	1.74E+13	2.55E+14	1.03E-02	1.51E-01
174.7	1.64E+13	2.36E+14	1.03E-02	1.48E-01
181.1	1.56E+13	2.20E+14	1.04E-02	1.46E-01
187.7	1.49E+13	2.04E+14	1.04E-02	1.43E-01
194.6	1.39E+13	1.90E+14	1.03E-02	1.41E-01
201.7	1.26E+13	1.76E+14	9.87E-03	1.38E-01
209.1	1.15E+13	1.66E+14	9.53E-03	1.37E-01
216.7	1.03E+13	1.53E+14	8.96E-03	1.33E-01
224.7	9.14E+12	1.44E+14	8.41E-03	1.33E-01
232.9	8.22E+12	1.33E+14	7.98E-03	1.29E-01
241.4	7.35E+12	1.22E+14	7.51E-03	1.25E-01
250.3	6.77E+12	1.17E+14	7.28E-03	1.26E-01
259.5	6.23E+12	1.04E+14	7.06E-03	1.18E-01
269	5.37E+12	9.60E+13	6.40E-03	1.15E-01
278.8	4.74E+12	8.72E+13	5.95E-03	1.10E-01
289	4.14E+12	7.86E+13	5.47E-03	1.04E-01
299.6	3.83E+12	7.02E+13	5.31E-03	9.74E-02
310.6	3.24E+12	6.37E+13	4.73E-03	9.29E-02
322	2.90E+12	5.70E+13	4.44E-03	8.73E-02
333.8	2.86E+12	5.66E+13	4.60E-03	9.11E-02
346	2.51E+12	5.07E+13	4.24E-03	8.56E-02
358.7	2.30E+12	4.58E+13	4.07E-03	8.11E-02
371.8	1.89E+12	4.09E+13	3.51E-03	7.59E-02
385.4	1.73E+12	3.69E+13	3.38E-03	7.18E-02
399.5	1.65E+12	3.16E+13	3.37E-03	6.46E-02
414.2	1.41E+12	2.81E+13	3.02E-03	6.02E-02
429.4	1.18E+12	2.49E+13	2.63E-03	5.58E-02
445.1	1.06E+12	2.18E+13	2.49E-03	5.11E-02
461.4	8.42E+11	2.01E+13	2.07E-03	4.94E-02
478.3	8.21E+11	1.72E+13	2.11E-03	4.42E-02
495.8	6.91E+11	1.53E+13	1.86E-03	4.11E-02
514	6.70E+11	1.35E+13	1.88E-03	3.80E-02
532.8	5.84E+11	1.19E+13	1.72E-03	3.51E-02
552.3	4.60E+11	1.07E+13	1.41E-03	3.30E-02

standard deviation

Dp(nm)	dEF_N/dlogDp(#/kg fuel)		dEF_M/dlogDp(g/kg fuel)	
	LDV	HDDV	LDV	HDDV
3.72	3.68E+14	1.45E+15	1.19E-05	4.68E-05
3.85	3.33E+14	1.52E+15	1.20E-05	5.45E-05

4	3.19E+14	1.24E+15	1.28E-05	4.97E-05
4.14	3.24E+14	1.24E+15	1.44E-05	5.52E-05
4.29	3.24E+14	1.40E+15	1.61E-05	6.94E-05
4.45	3.38E+14	1.69E+15	1.87E-05	9.36E-05
4.61	5.59E+14	5.26E+15	3.44E-05	3.24E-04
4.78	5.37E+14	5.23E+15	3.69E-05	3.59E-04
4.96	3.66E+14	3.30E+15	2.81E-05	2.53E-04
5.14	2.79E+14	2.23E+15	2.38E-05	1.90E-04
5.33	2.29E+14	1.88E+15	2.18E-05	1.79E-04
5.52	2.14E+14	1.66E+15	2.26E-05	1.75E-04
5.73	2.07E+14	1.59E+15	2.44E-05	1.88E-04
5.94	2.07E+14	1.57E+15	2.73E-05	2.06E-04
6.15	2.14E+14	1.66E+15	3.13E-05	2.43E-04
6.38	2.17E+14	1.58E+15	3.54E-05	2.58E-04
6.61	2.28E+14	1.72E+15	4.13E-05	3.12E-04
6.85	2.28E+14	1.64E+15	4.60E-05	3.32E-04
7.1	2.42E+14	1.88E+15	5.45E-05	4.23E-04
7.37	2.49E+14	1.91E+15	6.26E-05	4.81E-04
7.64	2.57E+14	2.06E+15	7.20E-05	5.76E-04
7.91	2.57E+14	1.98E+15	7.99E-05	6.16E-04
8.2	2.52E+14	2.04E+15	8.74E-05	7.08E-04
8.51	2.45E+14	2.00E+15	9.48E-05	7.73E-04
8.82	2.23E+14	1.77E+15	9.61E-05	7.63E-04
9.14	2.07E+14	1.76E+15	9.93E-05	8.44E-04
9.47	1.86E+14	1.58E+15	9.92E-05	8.41E-04
9.82	1.66E+14	1.37E+15	9.89E-05	8.12E-04
10.2	1.47E+14	1.20E+15	9.83E-05	8.02E-04
10.6	1.30E+14	9.91E+14	9.76E-05	7.42E-04
10.9	1.11E+14	8.20E+14	9.03E-05	6.67E-04
11.3	9.12E+13	6.85E+14	8.26E-05	6.21E-04
11.8	7.86E+13	5.86E+14	8.12E-05	6.04E-04
12.2	6.88E+13	5.33E+14	7.85E-05	6.09E-04
12.6	5.71E+13	4.23E+14	7.17E-05	5.32E-04
13.1	4.93E+13	3.81E+14	6.96E-05	5.38E-04
13.6	4.33E+13	3.41E+14	6.84E-05	5.39E-04
14.1	3.80E+13	2.92E+14	6.69E-05	5.15E-04
14.6	3.48E+13	2.73E+14	6.80E-05	5.33E-04
15.1	3.04E+13	2.35E+14	6.57E-05	5.08E-04
15.7	2.73E+13	2.05E+14	6.63E-05	4.99E-04
16.3	3.23E+13	2.49E+14	8.79E-05	6.78E-04
16.8	2.98E+13	2.13E+14	8.87E-05	6.35E-04
17.5	2.65E+13	2.01E+14	8.92E-05	6.77E-04
18.1	2.51E+13	2.08E+14	9.33E-05	7.73E-04
18.8	2.39E+13	1.95E+14	9.98E-05	8.15E-04
19.5	3.35E+13	1.90E+14	1.56E-04	8.85E-04
20.2	2.60E+13	1.92E+14	1.35E-04	9.95E-04
20.9	3.35E+13	1.94E+14	1.92E-04	1.12E-03
21.7	4.07E+13	2.17E+14	2.61E-04	1.39E-03
22.5	4.83E+13	2.37E+14	3.46E-04	1.70E-03
23.3	5.00E+13	2.41E+14	3.97E-04	1.92E-03
24.1	4.46E+13	2.53E+14	3.92E-04	2.23E-03
25	3.52E+13	2.37E+14	3.46E-04	2.32E-03
25.9	2.80E+13	2.13E+14	3.06E-04	2.32E-03
26.9	2.51E+13	2.07E+14	3.08E-04	2.53E-03
27.9	2.21E+13	1.95E+14	3.01E-04	2.66E-03
28.9	2.07E+13	1.80E+14	3.13E-04	2.73E-03

30	2.05E+13	2.00E+14	3.47E-04	3.39E-03
31.1	1.59E+13	1.55E+14	4.61E-04	4.51E-03
32.2	1.62E+13	1.61E+14	5.05E-04	5.02E-03
33.4	1.49E+13	1.45E+14	4.97E-04	4.83E-03
34.6	1.55E+13	1.54E+14	5.55E-04	5.50E-03
35.9	1.55E+13	1.51E+14	5.94E-04	5.76E-03
37.2	1.56E+13	1.56E+14	6.40E-04	6.38E-03
38.5	1.45E+13	1.41E+14	6.38E-04	6.20E-03
40	1.53E+13	1.52E+14	7.21E-04	7.12E-03
41.4	1.56E+13	1.54E+14	7.87E-04	7.72E-03
42.9	1.50E+13	1.45E+14	8.09E-04	7.79E-03
44.5	1.45E+13	1.40E+14	8.34E-04	8.04E-03
46.1	1.38E+13	1.27E+14	8.50E-04	7.84E-03
47.8	1.40E+13	1.30E+14	9.24E-04	8.59E-03
49.6	1.38E+13	1.27E+14	9.75E-04	8.96E-03
51.4	1.31E+13	1.15E+14	9.89E-04	8.66E-03
53.3	1.37E+13	1.20E+14	1.10E-03	9.68E-03
55.2	1.49E+13	1.38E+14	1.29E-03	1.19E-02
57.3	1.46E+13	1.28E+14	1.34E-03	1.18E-02
59.4	1.38E+13	1.22E+14	1.36E-03	1.20E-02
61.5	1.40E+13	1.17E+14	1.47E-03	1.23E-02
63.8	1.43E+13	1.17E+14	1.61E-03	1.31E-02
66.1	1.42E+13	1.15E+14	1.70E-03	1.38E-02
68.5	1.46E+13	1.18E+14	1.87E-03	1.51E-02
71	1.44E+13	1.17E+14	1.97E-03	1.59E-02
73.7	1.42E+13	1.14E+14	2.07E-03	1.66E-02
76.4	1.36E+13	1.10E+14	2.11E-03	1.71E-02
79.1	1.33E+13	1.10E+14	2.20E-03	1.82E-02
82	1.31E+13	1.12E+14	2.32E-03	1.98E-02
85.1	1.35E+13	1.20E+14	2.55E-03	2.27E-02
88.2	1.21E+13	9.84E+13	2.44E-03	1.98E-02
91.4	1.18E+13	9.75E+13	2.53E-03	2.09E-02
94.7	1.13E+13	9.37E+13	2.57E-03	2.13E-02
98.2	1.08E+13	8.98E+13	2.63E-03	2.18E-02
101.8	1.06E+13	8.73E+13	2.74E-03	2.25E-02
105.5	1.05E+13	8.63E+13	2.89E-03	2.37E-02
109.4	1.02E+13	8.14E+13	2.98E-03	2.38E-02
113.4	9.96E+12	7.84E+13	3.09E-03	2.43E-02
117.6	9.82E+12	7.63E+13	3.24E-03	2.51E-02
121.9	9.57E+12	7.18E+13	3.35E-03	2.52E-02
126.3	9.40E+12	6.99E+13	3.50E-03	2.60E-02
131	9.03E+12	6.60E+13	3.56E-03	2.60E-02
135.8	8.88E+12	6.60E+13	3.72E-03	2.77E-02
140.7	8.79E+12	6.50E+13	3.91E-03	2.89E-02
145.9	8.42E+12	6.23E+13	3.97E-03	2.94E-02
151.2	8.10E+12	5.90E+13	4.05E-03	2.95E-02
156.8	7.79E+12	5.79E+13	4.12E-03	3.06E-02
162.5	7.51E+12	5.64E+13	4.21E-03	3.16E-02
168.5	7.15E+12	5.31E+13	4.24E-03	3.15E-02
174.7	6.80E+12	5.16E+13	4.26E-03	3.24E-02
181.1	6.52E+12	4.84E+13	4.33E-03	3.21E-02
187.7	6.34E+12	4.75E+13	4.45E-03	3.33E-02
194.6	5.96E+12	4.44E+13	4.41E-03	3.29E-02
201.7	5.68E+12	4.34E+13	4.45E-03	3.40E-02
209.1	5.39E+12	4.16E+13	4.45E-03	3.44E-02
216.7	5.05E+12	3.96E+13	4.40E-03	3.46E-02

224.7	4.77E+12	3.82E+13	4.39E-03	3.51E-02
232.9	4.50E+12	3.68E+13	4.37E-03	3.57E-02
241.4	4.12E+12	3.53E+13	4.21E-03	3.61E-02
250.3	3.87E+12	3.34E+13	4.16E-03	3.59E-02
259.5	3.40E+12	2.94E+13	3.86E-03	3.33E-02
269	3.12E+12	2.73E+13	3.72E-03	3.26E-02
278.8	2.79E+12	2.45E+13	3.50E-03	3.07E-02
289	2.48E+12	2.22E+13	3.27E-03	2.93E-02
299.6	2.19E+12	1.92E+13	3.04E-03	2.67E-02
310.6	1.94E+12	1.72E+13	2.82E-03	2.51E-02
322	1.68E+12	1.47E+13	2.58E-03	2.25E-02
333.8	1.64E+12	1.44E+13	2.64E-03	2.32E-02
346	1.47E+12	1.31E+13	2.48E-03	2.21E-02
358.7	1.30E+12	1.17E+13	2.31E-03	2.07E-02
371.8	1.12E+12	1.02E+13	2.09E-03	1.89E-02
385.4	9.77E+11	8.72E+12	1.90E-03	1.70E-02
399.5	8.71E+11	7.44E+12	1.78E-03	1.52E-02
414.2	7.64E+11	6.53E+12	1.63E-03	1.40E-02
429.4	6.80E+11	5.97E+12	1.52E-03	1.34E-02
445.1	6.03E+11	5.30E+12	1.41E-03	1.24E-02
461.4	5.28E+11	4.84E+12	1.30E-03	1.19E-02
478.3	4.65E+11	4.07E+12	1.20E-03	1.05E-02
495.8	4.17E+11	3.72E+12	1.12E-03	1.00E-02
514	3.80E+11	3.33E+12	1.07E-03	9.37E-03
532.8	3.50E+11	2.97E+12	1.03E-03	8.73E-03
552.3	3.04E+11	2.69E+12	9.34E-04	8.27E-03

Appendix C
Supporting information for
Gas-particle partitioning of vehicle emitted primary organic aerosol measured in a traffic tunnel

C.1 The TD temperature program

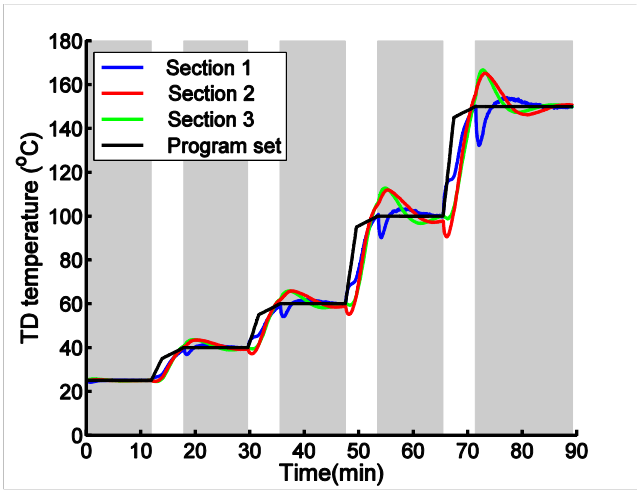

Figure C.1 The TD temperature program during the measurement. The black line shows the program setting temperature and the blue, red and green lines are actual temperature measurements inside different sections of the TD. Section 1 is close to the TD inlet, and section 3 is close to the denuder. Shaded areas represent time periods when instruments were sampling aerosols passing through the TD while during other time periods instruments were directly sampling the tunnel air.

During our spring measurement the temperature of TD was cycling between 25 °C and 150 °C. It firstly followed the program presented in Figure D.1 to increase from 25 °C and 150 °C for 90 min, and then took another 90 min to cool down to 25 °C. Instruments were sampling from the TD only when the temperature of the TD was held constant in a certain temperature stage (shaded time periods in Figure S3); and instruments were sampling the tunnel air through a bypass line during other times. We used a pair of electrically-actuated three-way valves (MS-142ACX; Swagelok Co., Solon, OH) to control whether to sample through TD or to sample through the bypass line. We were using the same TD with May et al. [113]. Figure S6 of May et al. [113] showed a schematic of the TD, and a more

detailed description of the TD and valves can be also found in the online supplemental matarials of May et al. [113].

C.2 Particle loss inside the thermodenuder (TD)

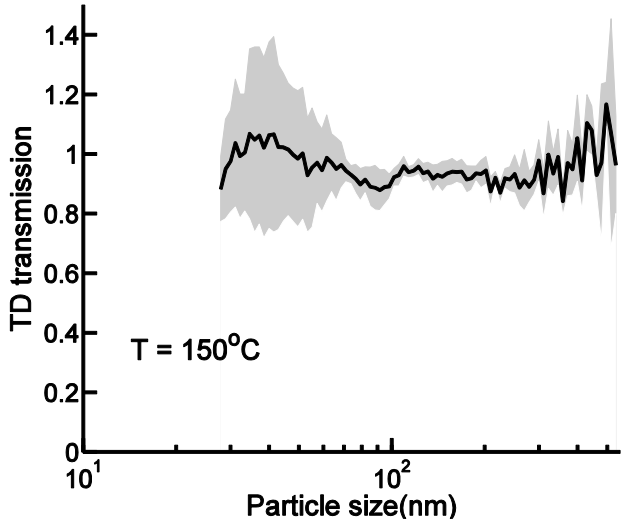

Figure C.2 Size-resolved particle number transmission through the thermodenuder (TD) at 150 °C. The solid line represents averaged transmission and the shaded area represents the stand deviation of all measurements.

Particle losses inside the TD are mainly caused by thermophoresis and diffusion. May et al. [113] characterized the size-resolved particle number transmission through the thermodenuder (TD) from 25 °C up to 120 °C (Figure S8 in May et al. [113]). Results show that for particles with a diameter between 50 nm to 500 nm their penetration through TD was weekly dependent on the particle size thus the size-dependent correction of particle loss inside the TD was unnecessary. And for TD temperature up to 100 °C the particle number transmission was always larger than 0.85. The particle mass losses in these tests were all less than 8%.

Here, following the method used by May et al. [113], I tested the size-dependent particle loss inside the TD under 150 °C. I used an atomizer (TSI 3076; TSI, Inc., Shoreview, MA) and 1 g/L sodium chloride (NaCl) solution to generate particles. Solution was pumped into the atomizer with a syringe pump (BS-300; Braintree Scientific, Inc., Braintree, MA) at a constant rate of 50 ml/hr. Air was pumped into

the atomizer constantly at 25 psi. Generated NaCl particles passed through a diffusion drier and then entered into a 10 m^3 Teflon environmental chamber. Particle number size distribution inside the chamber was continuously measured with a scanning mobility particle sizer (SMPS; TSI 3081/3772). At the same time particles inside the chamber were sent through the TD and then measured by another SMPS (TSI 3081/3010). Particle transmissions were calculated using the particle number concentration at the downstream of the TD divided by number concentration inside the chamber measured at the same time. Before measuring the TD transmission particles inside the chamber were sampled by both SMPS together to characterize the discrepancy of two instruments.

Similar with results of May et al. [113] I found that under TD temperature of 150 °C for particles between 50 nm to 500 nm the particle number transmission was fairly constant in all size bins. The averaged particle number transmission trough the TD was generally higher than 0.9. The mass loss was under 9%.

Therefore, I did not correct the TD MFR for particle losses; this lack of a correction would only have a minor impact on our results and does not impact overall conclusions.

C.3 Parameters used in the TD model

Table C.1 Parameters used in the Thermodenuder (TD) model

Parameter	Value
Mass accommodation coefficient, α	1
Gas-phase diffusivity, D	5×10^{-6} m^2 s^{-1}
Surface tension,	0.05 N m^{-1}
Particle density,	1100 kg m^{-3}
Molecular weight, MW_i	454 – 45 log C_i^* g mol^{-1}
Enthalpy of vaporization, $H_{vap,i}$	85 – 11 log C_i^* kJ mol^{-1}

I used the TD model of Riipinen et al. [219] in this work and a detailed description of the TD model can be found there [219] and also in the online supplemental matarials of May et al. [113].

Table C.2 Aerosol mass concentration (C_{OA}) and Mass-median particle diameter (d_p) used in the Thermodenuder (TD) model

TD measurement starting time	Aerosol Mass Concentration (C_{OA}, in μg/m^3)	Mass-median particle diameter (d_p, in nm)
5/23/13 14:02:32	10.78	231
5/23/13 17:42:40	4.01	234
5/23/13 21:12:19	1.3	271
5/24/13 00:42:51	2.82	255
5/24/13 04:12:13	1.77	258
5/24/13 07:42:29	2.97	247
5/24/13 18:38:03	1.41	427
5/24/13 22:07:17	1.14	397
5/25/13 01:37:22	1.47	283
5/25/13 05:08:21	2.14	310
5/25/13 08:37:18	1.92	270
5/25/13 12:07:09	0.9	226
5/25/13 15:37:05	1.28	199
5/25/13 19:08:01	0.83	198
5/25/13 22:37:55	1.14	219
5/26/13 02:07:45	1.18	252
5/26/13 05:37:32	1.49	238
5/26/13 09:07:17	1.72	219
5/26/13 12:36:59	0.9	220
5/26/13 16:07:45	1.01	238
5/26/13 19:37:31	0.91	240
5/26/13 23:07:16	1.03	234
5/27/13 02:37:07	2.41	162
5/27/13 06:07:03	1.5	155
5/27/13 09:37:57	1.44	190

5/27/13 13:07:43	0.99	172
5/27/13 16:37:26	1.12	176
5/27/13 20:07:11	1.22	177
5/27/13 23:37:56	1.66	183
5/28/13 03:07:36	1.94	198
5/28/13 06:37:21	6.25	241
Average	2.02	236

The C_{OA} and d_p listed in the Table C.2 are averaged HOA concentration measured by ACSM and averaged particle mass median diameter measured by the SMPS when both instruments were sampling from the bypass line during each TD scan.

C.4 Quartz filter handling blank

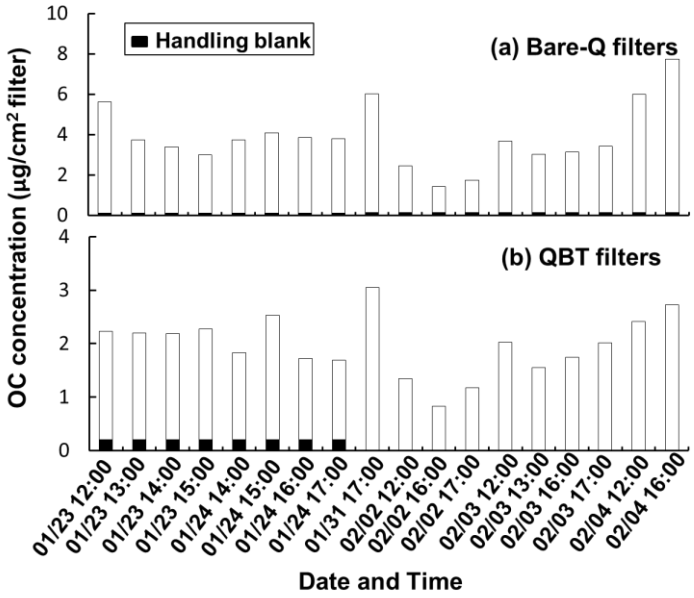

Figure C.3 OC concentration of all (a) bare-Q samples and (b) QBT samples. The total bar height represents the total OC concentration on each filter; and the black filled area represents the handling blank.

We collected 2 quartz filter sets to determine the handling blanks during our winter campaign. These 2 quartz filter sets underwent all of the experiment procedures except actual sampling. One filter set was collected on 01/23 and another one was collected on 02/04. In Figure C.3 I used the blank quartz filter set collected on 01/23 to represent handling blanks of quartz filters collected from 01/23 to 01/24, and the blank quartz filter set collected on 02/04 to represent handling blanks of quartz filters collected from 01/31 to 02/04. The fraction of handling blanks of all bare-Q filters is ranged from 2% to 12% with an average of 4%; for all QBT filters it is ranged from 0 to 12% with an average of 4%.

C.5 Relative abundance of M/Z 57 in total organics

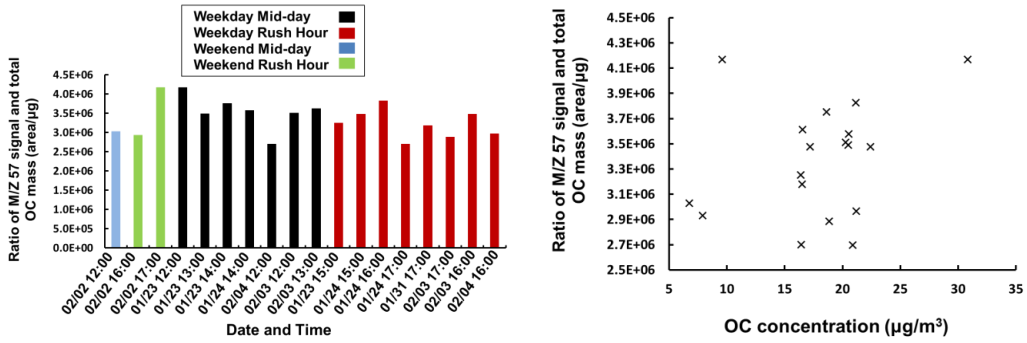

(a) (b)

Figure C.4 The ratio of total integrated GC area of M/Z 57 over the toal OC mass on the bare-Q filter under (a) different time periods, either weekday or weekend, mid-day or rush hour; (b) different OC concentration.

The relative abundance of the m/z 57 in the OC in the tunnel did not change significantly with the changing OA loading or the dilution in the tunnel. In order to show this, I calculated the ratio of m/z 57 signal (total integrated area of GC) over the total OC mass we sampled onto the bare-Q filter and regard it as an indicator of the relative abundance of m/z 57. In Figure C.4(a) I presented this ratio measured in either weekday or weekend, mid-day or rush hour. It shows that although the traffic volume and the traffic composition were different in different time periods, the relative abundance of the m/z 57 did not show a statistically

significant difference. During all time periods it was changing in average within 11% of the averaged value. Figure C.4(b) presented scatter plot of the ratio of total integrated GC area of m/z 57 over the total OC mass and the OC concentration measured from the bare-Q filter. The OC concentration here can be regarded as an indicator of dilution in the tunnel. Figure C.4(b) shows that there is no obvious correlation between the relative abundance of m/z 57 signal and the dilution or OC concentrations in the tunnel.

C.6 OCEC concentration in the Fort Pitt Tunnel

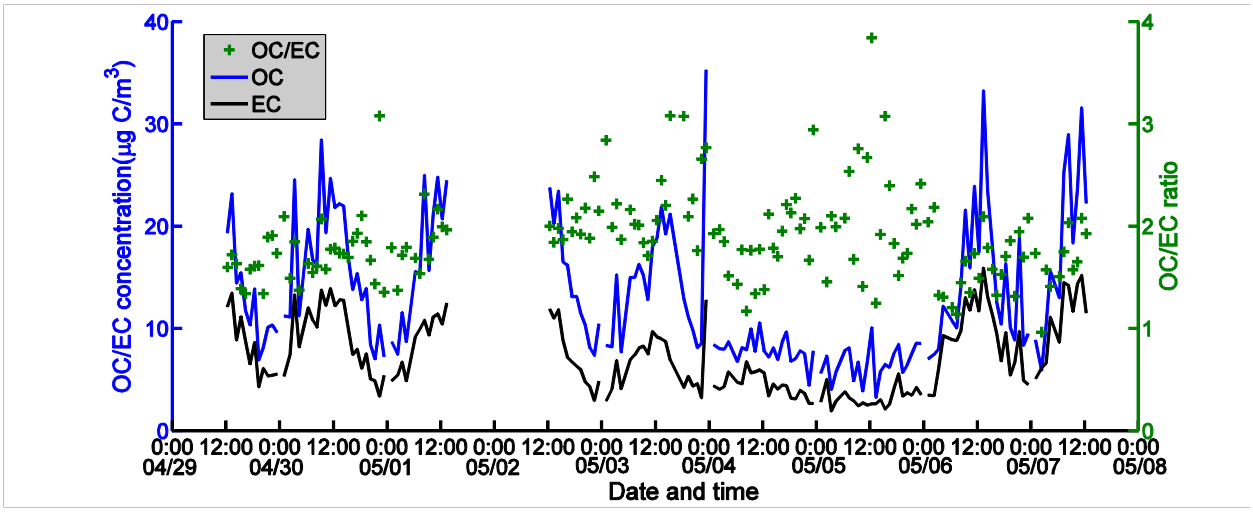

Figure C.5 OC and EC concentration as well as OC-to-EC ratio measured in the Fort Pitt Tunnel in Pittsburgh, PA with Sunset semi-continuous OC/EC analyzer (Model 4).

C.7 Comparison of the POA and the HOA mass spectrum

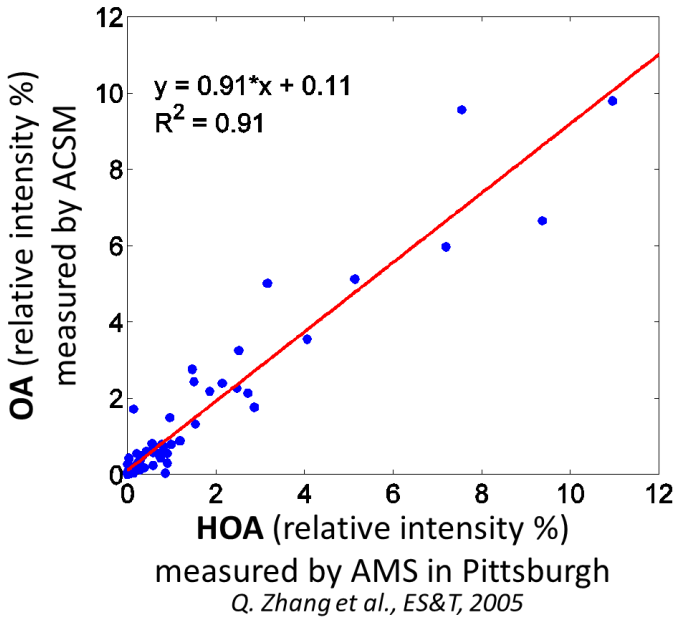

Figure C.6 Comparison of the OA mass spectrum measured by the Aerosol Chemical Speciation Monitor (ACSM) in the Fort Pitt Tunnel, Pittsburgh, PA and the HOA mass spectrum measured by Aerosol Mass Spectrometer (AMS) in Pittsburgh, PA by Zhang et al. [224].

I took the averaged OA mass spectrum measured by the Aerosol Chemical Speciation Monitor (ACSM) during our tunnel campaign and compared it with the mass spectrum of HOA measured by Aerosol Mass Spectrometer (AMS) in Pittsburgh, PA by Zhang et al. [224] (Figure C.6). I choose the afternoon rush hour (15:00-17:00) in 05/23 as the averaging time period of the tunnel OA mass spectrum, and during this time period the POA dominates the total OA concentration (Figure 5.2). The results show that the POA we measured in the traffic tunnel is highly similar with the HOA (R^2 = 0.91).

C.8 Comparison of the HOA or the OOA and the CO or NO_x concentration

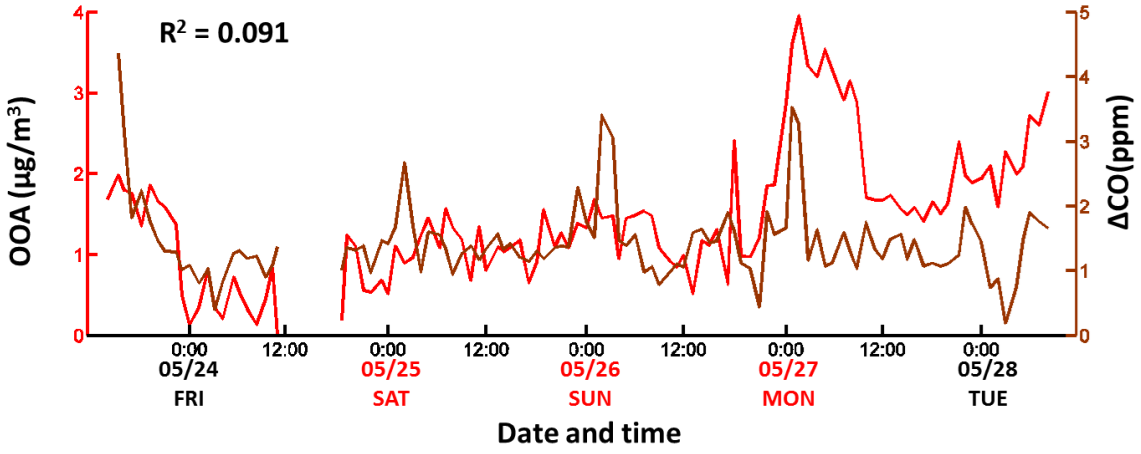
R² = 0.091
OOA (µg/m³)
ΔCO(ppm)
0:00 05/24 FRI
12:00
0:00 05/25 SAT
12:00
0:00 05/26 SUN
12:00
0:00 05/27 MON
12:00
0:00 05/28 TUE
Date and time

(a)

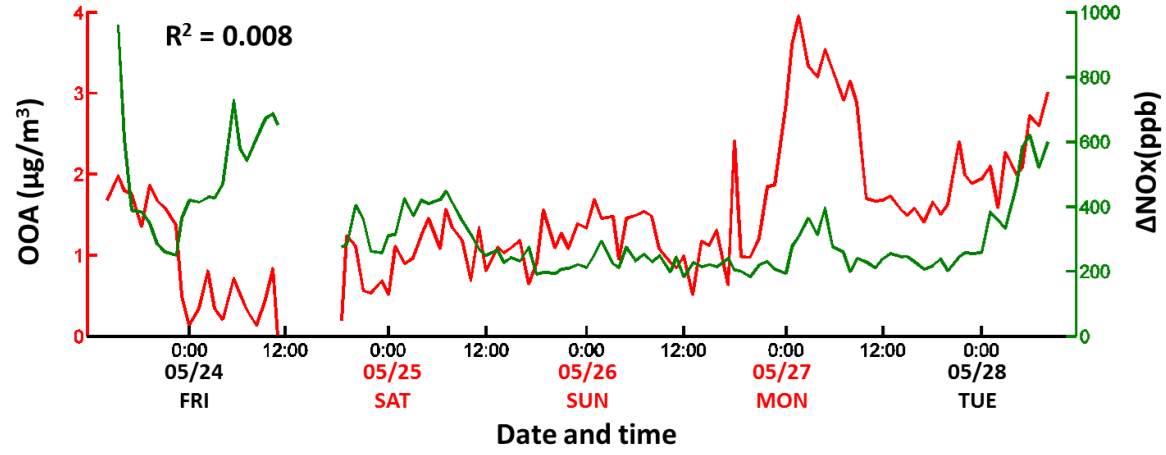
R² = 0.008
OOA (µg/m³)
ΔNOx(ppb)
0:00 05/24 FRI
12:00
0:00 05/25 SAT
12:00
0:00 05/26 SUN
12:00
0:00 05/27 MON
12:00
0:00 05/28 TUE
Date and time

(b)

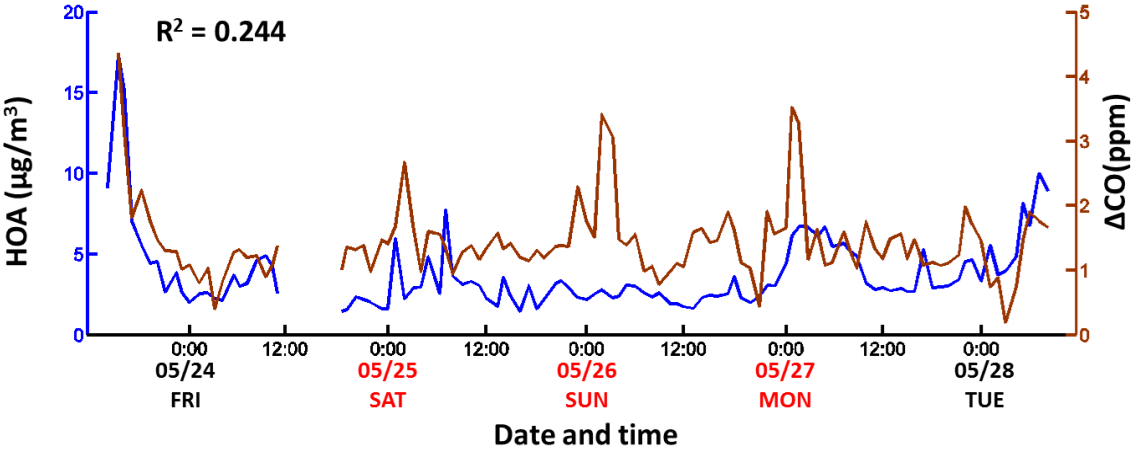
R² = 0.244
HOA (µg/m³)
ΔCO(ppm)
0:00 05/24 FRI
12:00
0:00 05/25 SAT
12:00
0:00 05/26 SUN
12:00
0:00 05/27 MON
12:00
0:00 05/28 TUE
Date and time

(c)

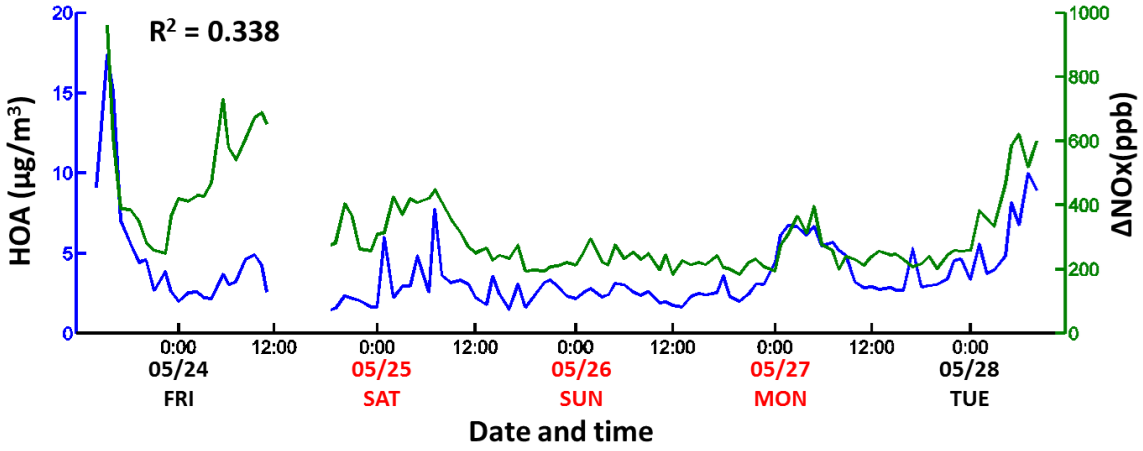

(d)

Figure C.7 Comparisons of the time series of (a) OOA and background corrected CO, (b) OOA and background corrected NO_x, (c) HOA and background corrected CO, and (d) HOA and background corrected NO_x.

Figure C.7 compared the time series of HOA or OOA with either CO or NO_x time series. R^2 is also shown in the plot to show the correlation between the two time series. As pointed out in the main text the background corrected CO and NO_x concentrations are good indicators of the total gasoline and total diesel vehicle volume in the tunnel, respectively. Figure C.7 (a) and (b) shows that there is no correlation between OOA and CO (R^2 = 0.091) or NO_x (R^2 = 0.008), which means that there is no correlation between OOA and the traffic. The correlation between HOA and CO (R^2 = 0.244) is not very strong, but is much better than the OOA versus CO. The correlations between HOA and NO_x is the best in these comparisons (R^2 = 0.338). In the midnight and early morning of 05/24 (0:00 – 12:00), although the changing trend of the HOA and NO_x was similar, but the increase of the NO_x was much higher than the increase of HOA. If I excluded this part of the data from the analysis, the R^2 of the HOA and NO_x could reach up to 0.617. The fact that the correlation between HOA and the traffic is much better than it between OOA and the traffic supports the assumption that the HOA is a good indicator of vehicle emitted POA, and the OOA is representative of more

aged, regional OA.

C.9 Comparison of volatility distributions from tunnel studies and dynamometer studies

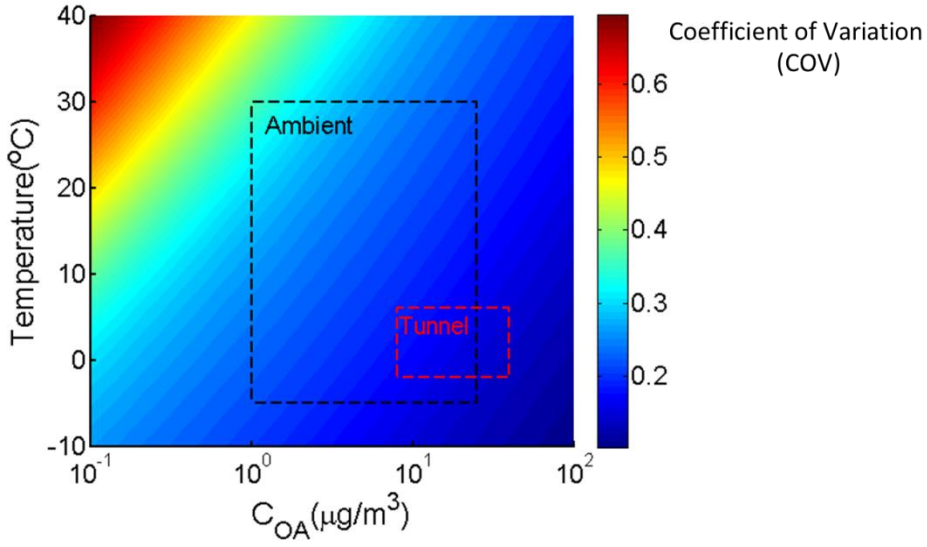

Figure C.8 Variation of gas-particle partitioning of vehicle POA emissions predicted with dynamometer and tunnel volatility distributions as a function of atmospheric conditions (temperature and concentration of Organic Aerosol, C_{OA}).

To construct Figure C.8 I first calculated the organics particle fractions (X_p) based on the partitioning theory (equation 1 in the main text) with each volatility distribution measured in the dynamometer studies and in the tunnel. Then I calculated the coefficient of variation (COV, defined as the standard deviation divided by the mean value) of X_p estimated with all volatility distributions under a certain ambient temperature and $C_{OA.}$ The COV is presented with a color-scale in Figure C.8. I also indicate the range of general ambient conditions (temperature -5 – 30 °C, C_{OA} 1 – 20 μg/m^3) and tunnel conditions in winter (temperature -2 – 6 °C, C_{OA} 8 – 40 μg/m^3). Under ambient conditions the COV of X_p is mostly about 20-25%, while in cleaner (C_{OA} less than 2 μg/m^3) and warmer (temperature higher than 25 °C) environment it could reach up to 30-40%. Under tunnel conditions in winter the COV of X_p is about 20%.

C. 10 Variations of TD model prediction

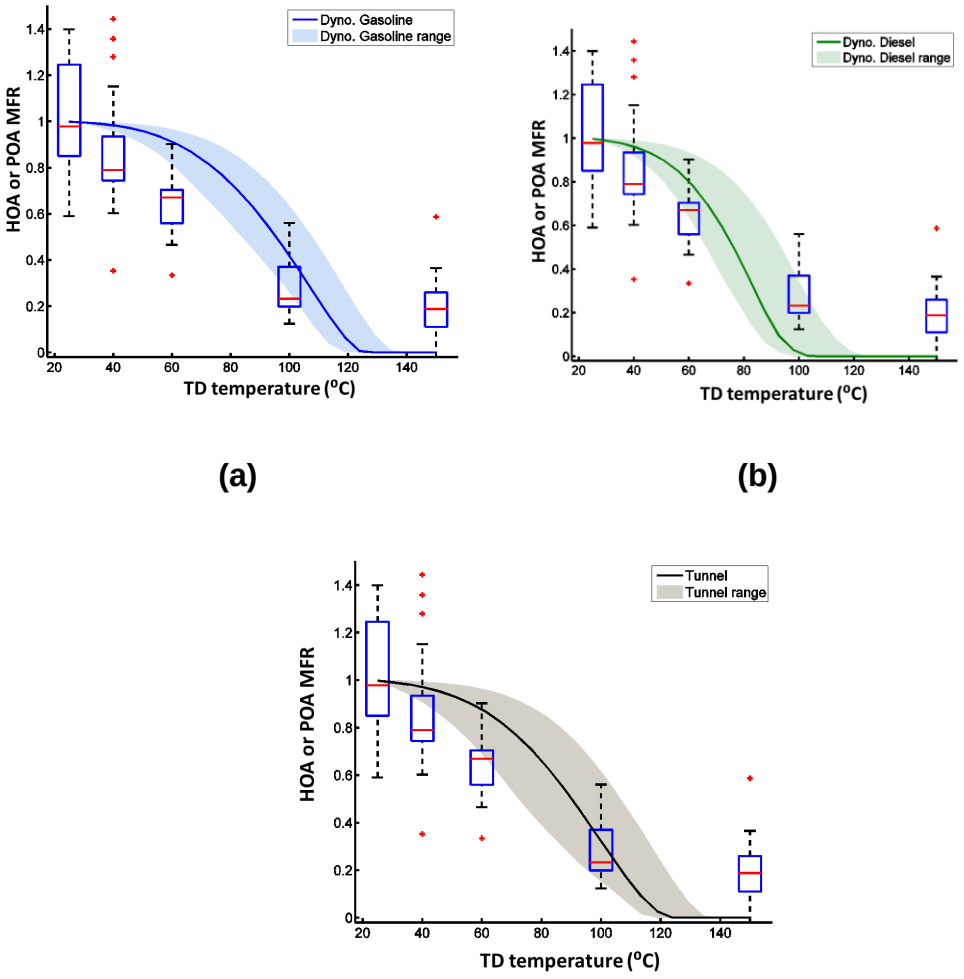

Figure C.9 TD MFR simulations using the volatility distributions of (a) gasoline vehicles from dynamometer studies, (b) diesel vehicles from dynamometer studies and (c) tunnel studies. The shaded range in all figures represent the variation range of TD MFR simulations considering the variation of volatility distributions and the variations of OA concentrations (C_{OA}) and particle mass median diameter (d_p) measured in the tunnel. Similar with Figure 3, all solid lines in Figure S11 are MFR simulations using the median volatility distribution and averaged C_{OA} and d_p in the traffic tunnel. TD measurements are also presented using box-whisker plot to compare with the simulations.

For the dynamometer gasoline simulations, I firstly ran 31 TD similuations using the median volatility distribution reported by May et al.[113] and the 31 sets of C_{OA} and d_p listed in Table C.2; I then ran another 62 TD simulations using the upper or the lower range of the volatility distribution reported by May et al.[113]

together with the 31 sets of C_{OA} and d_p. These in total 93 TD simulations defined the shaded range presented in Figure C.9 (a). The solid blue line in Figure 5.3 and in Figure C.9 (a) is the TD simulation using the median gasoline volatility distribution and an averaged C_{OA} and d_p. I used the same method to provide the range of diesel and tunnel TD simulations in Figure C.9 (b) and Figure C.9 (c), and the averaged diesel and tunnel TD simulations in Figure 5.3, Figure C.9 (b) and Figure C.9(c). The shaded range in Figure 5.3 is defined by the range of both gasoline and diesel simulations and it can be viewed as a simulation range of dynamometer studies. I think the range I provided in Figure 5.3 and Figure C.9 is able to present the influence of the variable C_{OA}, d_p and volatility distributions on the TD MFR prediction.

The highest and lowest range of tunnel volatility distributions used to calculate the MFR range in Figure C.9 (c) are the ranges considering the propagated error of organic mass fractions (f_i, the last column in the Table C.3).

C.11 Comparison of volatility distributions measured by May et al. [113,114] **and Zhao et al.** [230,231]

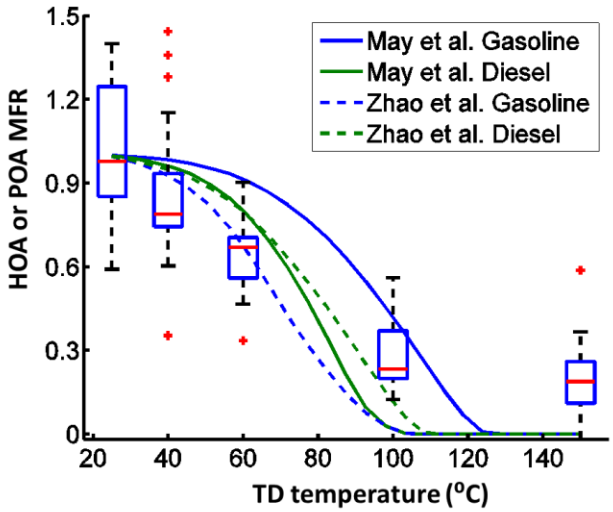

Figure C.10 Comparison of TD MFR simulations using the volatility distributions of gasoline and diesel vehicles from May et al.[113,114] and Zhao et al. [230,231] Only simulations using median volatility distributions and averaged C_{OA} and d_p in the tunnel is shown in the figure. Solid lines are simulations based on May et al. [113,114] and dash lines are simulations based on Zhao et al. [230,231] Blue and green lines represent

results of gasoline and diesel vehicles, respectively. Similar as Figure 3, TD measurements are also presented using box-whisker plot to compare with the simulations.

The volatility distributions of Zhao et al. [230,231] used to calculate dash lines in the Figure C.10 are volatility distributions only measured by the TD-GC-MS. It is not the volatility distributions that corrected the low volatile organics using the OC/EC measurements.

The MFR prediction of diesel vehicles of Zhao et al. [231] falls between the range defined by the gasoline and diesel predictions of May et al. [113,114] The predictions of gasoline vehicles of Zhao et al. [230] are slightly lower than the range of May et al. [113,114] but are close to the diesel predictions of May et al. [114] (largest MFR difference is about 0.1). Similar with predictions based on May et al. [113,114], the predictions based on Zhao et al. [230,231] are able to capture the MFR at 25, 60 and 100 °C but still cannot match with the measurements at 40 and 150 °C. Therefore, I conclude that the volatility distributions of Zhao et al. [230,231] and May et al. [113,114] are similar at predicting the POA gas-particle partitioning.

C.12 Data of the tunnel volatility distribution

Table C.3 POA volatility distributions measured in the traffic tunnel

log C_i^* @ 298 K	Median mass fraction of organics (f_i)	Interquartile range of f_i	Range of f_i considering the propagated error
-2	0.05	0.03 – 0.08	0.02 – 0.16
-1	0.07	0.05 – 0.08	0.02 – 0.15
0	0.09	0.08 – 0.10	0.04 – 0.21
1	0.17	0.15 – 0.18	0.09 – 0.28
2	0.23	0.20 – 0.23	0.15 – 0.30
3	0.15	0.14 – 0.17	0.10 – 0.39
4	0.15	0.13 – 0.18	0.07 – 0.33
5	0.04	0.03 – 0.05	0.01 – 0.08
6	0.03	0.02 – 0.03	0.01 – 0.09

In Table C.3 the median and interquartile range of the organic mass fraction (f_i) were calculated based on all f_i measured by the TD-GC-MS and did not consider the propagated error of f_i. The same data sets were also used to make the box-whisker plot in Figure 5.4 and Figure C.11. Ranges presented in the last column of the Table C.3 are highest and lowest f_i values in each C* bin considering the propagated error of f_i. These ranges are presented as the gray crosses in Figure C.11.

C.13 Uncertainty propagation of the volatility distribution

The organic mass fraction of the C* bin i, f_i is calculated using the following equation:

$$f_i = \frac{A_i / A_{tot}}{R} \quad (1)$$

Where A_i is the integrated GC area of the C* bin i. A_{tot} is the total integrated GC area of a certain bare-Q sample. R is the recovery correction factor of a certain C* bin.

The recover correction factor, R , is calculated using following equation:

$$R = \frac{A_{\text{int}}}{RF_{\text{int}} \times m_{\text{int}}} \quad (2)$$

Where the A_{int} is the integrated GC area of internal standard in each sample. RF_{int} is the response factor of the internal standard. It is the integrated GC area per unit mass of the internal standard. m_{int} is the mass of internal standards I injected onto each bare-Q samples. It is 2 ng for all measured samples.

To determine the error of f_i , I need to determine the error of each term in Equation 1 and Equation 2. The filter sampling process may also induce uncertainty to the f_i and the major sampling uncertainty comes from the uncertainty of the sampling flow. To control the sampling flow at 46 LPM I was

using two mass flow controllers from Alicat Scientific, Tucson, AZ (model MCR-50SLPM-D/5M). I calculated the accuracy of the flow rate based on the equation in the manual and it is very small, only ±1%. Therefore, I ignored the filter sampling process when I estimated the uncertainty of f_i.

i) The uncertainty of the A_i and A_{tot}

a) The uncertainty of the A_i

Here I estimate the uncertainty of the integrated GC area based on some n-alkanes standard samples I measured during the same time when I was also measuring the tunnel samples. The n-alkanes standard contains C15 – C38 and C40 n-alkanes. I put 2 ng n-alkane standards onto the blank quartz filter and measure with the TD-GC-MS, and it was repeated for 3 times. I use the averaged coefficient of variation of the GC area of all n-alkanes in a certain C* bin as the uncertainty of A_i, and it is shown in the Table S4-1.

Table C.4-1 Uncertainties of the integrated GC area of organics in each C* bin, A_i

log C*	-2	-1	0	1	2	3	4	5	6
Uncertainty of the A_i (±)	0.17	0.16	0.06	0.02	0.06	0.13	0.13	0.16	0.23

b) The uncertainty of the A_{tot}

Since A_{tot} is the summation of the A_i of all the C* bins, and I have already estimated the uncertainty of the A_i of all the C* bins in the previous discussion, here the uncertainty of A_{tot} is estimated by propagating the uncertainty of the A_i. Since the error propagation also depends on the total GC area, and the different aerosol loadings caused different total GC areas for each bare-Q sample, I estimated the uncertainty of A_{tot} separately for each bare-Q sample and it is ranged from ±3% to ±5%.

ii) The uncertainty of the R

The internal standard I used was the deuterated n-Alkane standards 3 from Chiron AS, Trondheim, Norway (S-437-K-IO, batch 6208). It contains 7 n-alkanes with carbon numbers of 12, 16, 20, 24, 30, 32 and 36 and concentration of all compounds are 1000 µg/mL. It uses isooctane as solvent.

a) The uncertainty of the A_{int}

The uncertainty of the A_{int} is estimated based on the coefficient of variation of repeated measurements of 2 ng n-alkane standard mentioned in the previous discussion. I estimated the uncertainty of A_{int} separately for each internal standard compound. For example, the uncertainty of A_{int} of C12 n-alkane is estimated by the coefficient of variation of integrated GC areas of C12 n-alkane during all n-alkane standard measurements. Results are shown in Table C.4-2.

Table C.4-2 Uncertainties of the integrated GC area of each internal standard compound, A_{int}

Internal standard n-Alkane carbon number	C36	C32	C30	C24	C20	C16
uncertainty of the A_{int} (±)	0.09	0.16	0.14	0.04	0.01	0.14

b). The uncertainty of the m_{int}

Before each TD-GC-MS measurement I added a known mass (2 ng) of internal standards onto the bare-Q filter to track the recovery of the instrument. I diluted the 1000 µg/mL stock solution of internal standard to 0.2 µg/mL and injected 10 µl to each filter. I do not exactly know the uncertainty of the original stock solution and I assume it is very small and do not significantly influence the uncertainty estimation. The uncertainty estimation for the m_{int} is purely based on the uncertainly of the dilution process.

During the dilution I used the 10 µl (Model 701) and 1 ml (Gastight #1001) syringe from the Hamilton Company. According to the company's Trueness and Precision Statement of Conformance all syringes have an averaged accuracy of

± 1%. I firstly diluted the 1000 µg/mL stock solution to 10 µg/mL. I took 10 µl stock solution with the 10 µl syringe, with an accuracy of ± 1%, and diluted it with 0.99 ml solvent. Since 0.99 ml is very hard to accurately measure with the 1ml syringe, I took 1ml solvent and consider the accuracy as ± 2%. Using the rule of error propagation the accuracy of the first dilution is estimated to be ± 2%.

I then diluted the 10 µg/mL solution to 0.2 µg/mL. I took 10 µl 10 µg/mL solution with the 10 µl syringe, with an accuracy of ± 1%, and diluted it with 0.49 ml solvent. Since 0.49 ml is very hard to accurately measure with the 1ml syringe, we took 0.5ml solvent and consider the accuracy as ± 3%. Using the rule of error propagation the accuracy of the 0.2 µg/mL solution is estimated to be ± 4%.

I took 10 µl 0.2 µg/mL solution (accuracy ± 4%) with the 10 µl syringe (accuracy ± 1%) to put it onto the filter as internal standard. Therefore, using the rule of error propagation, the accuracy of the m_{int} is ± 4%.

c). The uncertainty of the RF_{int}

To determine RF_{int}, I measured the GC peak areas of internal standards with different mass (0.1 ng, 0.3 ng, 1 ng, 2 ng and 5 ng) and did a linear regression fitting of the GC area to mass to get this response factor. The uncertainty of the RF_{int} mainly depends on the fitting process. Therefore, for each internal standard compound, I took the uncertainty of the linear regression slope as the uncertainty of the RF_{int}. The results as well as the R^2 of the linear regression are listed in Table C.4-3.

Table C.4-3 Uncertainties of the response factors of each internal standard compound, RF_{int}

n-Alkane carbon number	C36	C32	C30	C24	C20	C16
uncertainty of response factor (±)	0.07	0.09	0.05	0.07	0.04	0.01
R^2 of linear regression	0.9946	0.9914	0.997	0.9955	0.9987	0.9999

So far I analyzed uncertainties of all the terms in Equation S2 and Equation S3. Follow the rule of error propagation I got the uncertainty of the f_i for each C* bins and for each sample. I assume all terms in Equation S2 and Equation S3 are independent and I ignored the covariance. The uncertainty of f_i is ranged from ± 11% to ± 28%. I summarized the measured f_i of all bare-Q samples together with the uncertainty range in the Table C.8.

The median volatility distribution and the uncertainty range considering the propagated error from the TD-GC-MS analysis is summarized in the Table C.3 and presented in the Figure C.11.

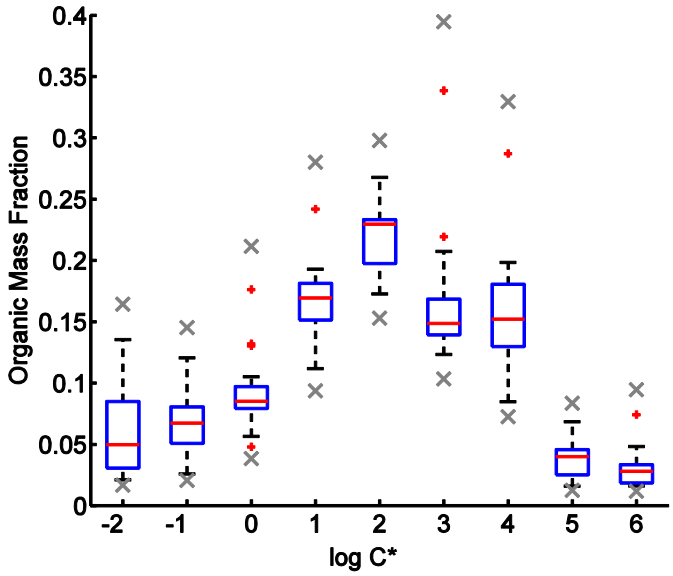

Figure C.11 Volatility distributions measured from the TD-GC-MS analysis of bare-Q filters collected in the traffic tunnel. Similar with Figure 4 the box-whisker plot is used to present volatility distributions measured from all quartz filters. The gray crosses at the top and the bottom of the whiskers show the highest and lowest range of organic mass fraction (f_i) in each C* bin considering the propagated uncertainty.

C.14 Statistical test of thermodenuder data

Table C.5 Results of the Mann-Whitney U-test of all thermodenuder (TD) data

TD Temp. (^oC)	Weekday Day vs. Weekday Night	Weekday Day vs. Weekend Day	Weekend Day vs. Weekday Night	Weekend Night vs. Weekday Day	Weekend Night vs. Weekday Night	Weekend Night vs. Weekday Day
25	FALSE	FALSE	FALSE	FALSE	***TRUE***	***TRUE***
40	FALSE	FALSE	FALSE	FALSE	FALSE	FALSE
60	FALSE	FALSE	FALSE	FALSE	FALSE	FALSE
100	FALSE	FALSE	FALSE	FALSE	FALSE	FALSE
150	FALSE	FALSE	***TRUE***	***TRUE***	***TRUE***	FALSE

Table C.6 The number of TD scans, average OA concentration and particle mass median diameter in each time period

Time period	Number of TD scans	Average Aerosol Mass Concentration (C_{OA}, in $\mu g/m^3$)	Average Mass-median particle diameter (d_p, in nm)
Weekday Daytime	4	4.1	282
Weekday Overnight	6	2.5	270
Weekend Daytime	12	1.2	202
Weekend Overnight	9	1.4	256
Total	31	-	-

In order to show there is no significant sub-daily variations in measured TD MFR in the tunnel I did the Wilcoxon rank sum test on all TD MFR data with MATLAB and presented results in Table C.5. The Wilcoxon rank sum test is equivalent to the Mann-Whitney U-test. The test is to examine whether the null hypothesis, which assumes two independent samples come from the same population, is true or not. If the test returns 'FALSE' it indicates a failure to reject the null hypothesis, which means the two tested samples come from the same distribution. If the test returns 'TURE' it means that the null hypothesis is rejected, which suggests the two tested samples come from different distributions. The Mann-Whitney U-test can be applied to any unknown distributions. I conducted all tests under a significance level of 5%.

As described in the main text I separated all measured TD MFR in the tunnel into 4 different time periods: high-traffic daytime periods (7:00 -21:00) and overnight (22:00 – 6:00) on either weekdays or weekends. The number of TD measurements in each time period is summarized in Table C.6. Under each temperature stage I took MFRs measured in either 2 out of these 4 time periods as 2 independent samples to conduct the statistical test. There are in total 30 tests. The majority (25 out of 30) of these tests returned 'FALSE', which means that the majority of the tested samples come from the same distribution and are not significantly different. There are 2 tests returned 'TURE' for a TD temperature of 25 °C and 3 under 150 °C. At 25 °C the mean MFR measured in weekend overnight was about 20% higher than mean MFRs of other time periods. And under 150 °C mean MFRs measured in weekdays were slightly higher than MFRs measured in weekends.

C.15 Comparison of the volatility distribution of POA and lubricant oil

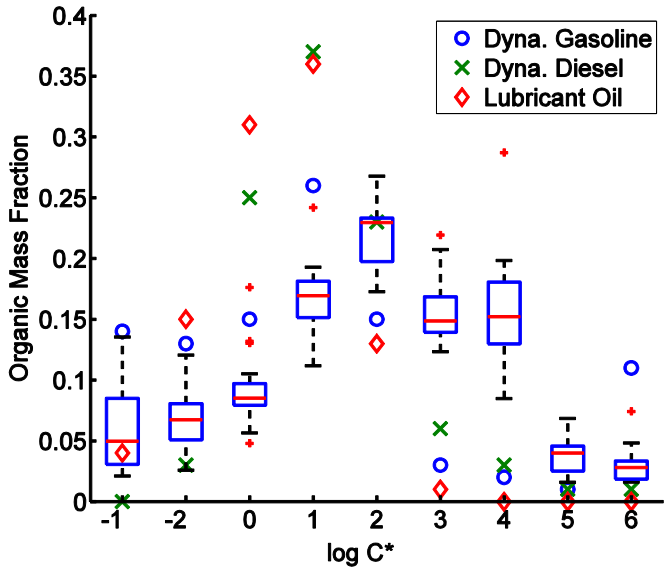

Figure C.12 Comparison of the dynamometer stuides volatility distribution measured by May et al.[113,114] and the tunnel volatility distribution measured in this work with the lubricant oil volatility distribution measured by May et al.[113] Similar with Figure 4 in the main text the tunnel volatility distribution is presented with box-whisker plot. The blue, green and red symbols represent the gasoline POA, the diesel POA and the lubricant oil volatility distributions, respectively, from dynamometer studies of May et al. [113,114].

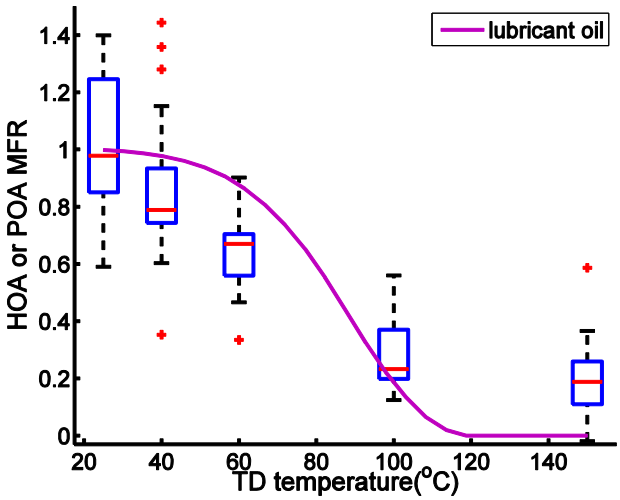

Figure C.13 Comparison of measured TD MFR in the tunnel (presented with box-whisker plot) with the modeled TD MFR based on the lubricant oil volatility distributions measured by May et al.[113] and the average C_{OA} and d_p in the tunnel. (solid magenta line).

C.16 The influence of OA concentrations (C_{OA}) and mass-median diameter (d_p) on the variation of MFR

Table C.7-1 Simulated TD MFR in different time periods

TD temperature (ºC)	weekday daytime	weekday overnight	weekend daylight	weekend overnight	standard deviation
25	0.9969	0.9976	0.9977	0.9982	0.0005
40	0.9657	0.9726	0.9747	0.9792	0.0056
60	0.8597	0.8832	0.8897	0.9067	0.0194
100	0.3197	0.3512	0.3263	0.3890	0.0314
150	0	0	0	0	0

Table C.7-2. Averaged measured TD MFR in different time periods

TD temperature(º	weekday daytime	weekday overnight	weekend daylight	weekend overnight	standard deviation

C)					
25	0.9278	0.8547	1.0191	1.2214	0.1587
40	0.7639	0.9346	0.8496	0.8479	0.0697
60	0.5719	0.7254	0.6085	0.6609	0.0667
100	0.3152	0.3649	0.2521	0.2570	0.0534
150	0.2485	0.3152	0.1674	0.1441	0.0783

In order to show how the variation of C_{OA} and d_p would influence this conclusion, I calculated the averaged C_{OA} and d_p in these four time periods (summarized in Table C.6) and using the C_{OA} and d_p in each time period together with the median tunnel POA volatility distribution to simulate the TD MFR from 25 – 150 ºC. The result is shown in the Table C.7-1. The last column of the Table C.7-1 shows the standard deviation of the MFR prediction under each TD temperature. It is an indication of the MFR variation caused by the changing C_{OA} and d_p and it is very small (around or less than 0.03) under all TD temperatures. Table C.7-2 summarized the average MFR in different time periods from the TD measurement, and the standard deviation is also shown in the last column. It is an indication of the MFR variation caused by C_{OA}, d_p and the volatility distribution. The standard deviations in Table C.7-1 are much smaller than standard deviations in Table C.7-2 under all TD temperatures. It means that the variation of C_{OA} and d_p plays a minor role on the comparison of TD MFR over different time periods. Therefore, I can conclude from Figure 5 that the POA volatility distribution measured in the tunnel does not have a strong temporal variation.

Table C.8 TD-GC-MS measured organic mass fraction from all bare-Q samples

Bare-Q filter collection time			log C*				
date	start time	end time	-2	-1	0	1	2
1/23/2014	12:00:00 PM	12:45:00 PM	0.11 (0.09 - 0.14)	0.08 (0.06 - 0.1)	0.11 (0.08 - 0.13)	0.14 (0.12 - 0.16)	0.21 (0.19 - 0.24)
1/23/2014	1:00:00 PM	1:45:00 PM	0.12 (0.09 - 0.14)	0.08 (0.06 - 0.1)	0.08 (0.07 - 0.1)	0.14 (0.12 - 0.16)	0.2 (0.17 - 0.22)
1/23/2014	2:00:00 PM	2:45:00 PM	0.08 (0.07 - 0.1)	0.07 (0.05 - 0.08)	0.09 (0.07 - 0.11)	0.17 (0.14 - 0.2)	0.23 (0.21 - 0.26)
1/23/2014	3:00:00 PM	3:45:00 PM	0.09 (0.07 - 0.11)	0.07 (0.05 - 0.08)	0.08 (0.06 - 0.1)	0.16 (0.14 - 0.19)	0.22 (0.2 - 0.25)
1/24/2014	2:15:00 PM	2:50:00 PM	0.05 (0.04 - 0.06)	0.06 (0.05 - 0.07)	0.09 (0.07 - 0.11)	0.19 (0.16 - 0.22)	0.26 (0.23 - 0.28)
1/24/2014	3:00:00 PM	3:45:00 PM	0.04 (0.03 - 0.05)	0.04 (0.04 - 0.05)	0.07 (0.06 - 0.08)	0.17 (0.14 - 0.2)	0.23 (0.2 - 0.26)
1/24/2014	4:00:00 PM	4:45:00 PM	0.04 (0.03 - 0.05)	0.05 (0.04 - 0.05)	0.08 (0.06 - 0.1)	0.17 (0.15 - 0.2)	0.25 (0.23 - 0.28)
1/24/2014	5:00:00 PM	5:45:00 PM	0.06 (0.04 - 0.07)	0.05 (0.04 - 0.06)	0.08 (0.07 - 0.1)	0.16 (0.13 - 0.19)	0.23 (0.2 - 0.26)
1/31/2014	5:06:00 PM	6:36:00 PM	0.03 (0.02 - 0.03)	0.04 (0.03 - 0.05)	0.08 (0.06 - 0.09)	0.16 (0.14 - 0.19)	0.27 (0.24 - 0.3)
2/2/2014	12:01:00 PM	1:31:00 PM	0.07 (0.06 - 0.09)	0.07 (0.06 - 0.09)	0.09 (0.07 - 0.1)	0.19 (0.16 - 0.22)	0.23 (0.21 - 0.26)
2/2/2014	4:00:00 PM	4:45:00 PM	0.14 (0.11 - 0.16)	0.07 (0.05 - 0.08)	0.08 (0.06 - 0.1)	0.18 (0.15 - 0.21)	0.17 (0.15 - 0.19)
2/2/2014	5:00:00 PM	5:45:00 PM	0.08 (0.07 - 0.1)	0.05 (0.04 - 0.06)	0.06 (0.04 - 0.07)	0.11 (0.09 - 0.13)	0.18 (0.16 - 0.2)
2/3/2014	12:00:00 PM	12:45:00 PM	0.03 (0.02 - 0.04)	0.09 (0.07 - 0.11)	0.1 (0.08 - 0.12)	0.15 (0.13 - 0.18)	0.23 (0.21 - 0.26)
2/3/2014	1:00:00 PM	1:45:00 PM	0.02 (0.02 - 0.03)	0.1 (0.08 - 0.12)	0.13 (0.11 - 0.16)	0.18 (0.15 - 0.21)	0.23 (0.2 - 0.25)
2/3/2014	4:00:00 PM	4:45:00 PM	0.02 (0.02 - 0.03)	0.1 (0.08 - 0.12)	0.13 (0.1 - 0.16)	0.18 (0.15 - 0.21)	0.23 (0.2 - 0.26)
2/3/2014	5:00:00 PM	5:45:00 PM	0.05 (0.04 - 0.06)	0.03 (0.02 - 0.03)	0.05 (0.04 - 0.06)	0.12 (0.1 - 0.14)	0.18 (0.16 - 0.2)
2/4/2014	12:06:00 PM	1:36:00 PM	0.04 (0.04 - 0.05)	0.05 (0.04 - 0.06)	0.09 (0.07 - 0.11)	0.19 (0.16 - 0.22)	0.27 (0.24 - 0.29)
2/4/2014	4:01:00 PM	5:31:00 PM	0.02 (0.02 - 0.02)	0.12 (0.1 - 0.14)	0.18 (0.14 - 0.22)	0.24 (0.2 - 0.28)	0.18 (0.16 - 0.2)

Table continue

Bare-Q filter collection time			log C*				Emission Factors	
date	start time	end time	3	4	5	6	EF_Q (mg/kg-fuel)	EF_OA (mg/kg-fuel)
1/23/2014	12:00:00 PM	12:45:00 PM	0.16 (0.14 - 0.19)	0.15 (0.13 - 0.17)	0.03 (0.02 - 0.03)	0.02 (0.01 - 0.02)	140.91	75.09
1/23/2014	1:00:00 PM	1:45:00 PM	0.14 (0.12 - 0.16)	0.18 (0.15 - 0.21)	0.04 (0.03 - 0.05)	0.02 (0.01 - 0.02)	102.98	54.62
1/23/2014	2:00:00 PM	2:45:00 PM	0.12 (0.1 - 0.14)	0.17 (0.14 - 0.19)	0.05 (0.04 - 0.06)	0.02 (0.01 - 0.02)	86.86	38.81
1/23/2014	3:00:00 PM	3:45:00 PM	0.14 (0.12 - 0.16)	0.17 (0.15 - 0.2)	0.04 (0.03 - 0.05)	0.02 (0.02 - 0.03)	70.83	29.11
1/24/2014	2:15:00 PM	2:50:00 PM	0.14 (0.11 - 0.16)	0.15 (0.13 - 0.17)	0.05 (0.04 - 0.06)	0.02 (0.01 - 0.02)	51.25	19.57
1/24/2014	3:00:00 PM	3:45:00 PM	0.15 (0.13 - 0.18)	0.2 (0.17 - 0.23)	0.06 (0.05 - 0.07)	0.03 (0.03 - 0.04)	72.53	32.43
1/24/2014	4:00:00 PM	4:45:00 PM	0.14 (0.12 - 0.17)	0.19 (0.16 - 0.22)	0.05 (0.04 - 0.06)	0.03 (0.02 - 0.04)	55.26	23.14
1/24/2014	5:00:00 PM	5:45:00 PM	0.13 (0.11 - 0.15)	0.2 (0.17 - 0.23)	0.07 (0.05 - 0.08)	0.03 (0.02 - 0.04)	73.80	29.62
1/31/2014	5:06:00 PM	6:36:00 PM	0.17 (0.14 - 0.2)	0.14 (0.12 - 0.16)	0.04 (0.03 - 0.05)	0.07 (0.05 - 0.09)	-	-
2/2/2014	12:01:00 PM	1:31:00 PM	0.17 (0.14 - 0.2)	0.08 (0.07 - 0.1)	0.04 (0.03 - 0.05)	0.05 (0.04 - 0.06)	44.80	19.74
2/2/2014	4:00:00 PM	4:45:00 PM	0.16 (0.13 - 0.18)	0.16 (0.13 - 0.18)	0.02 (0.02 - 0.03)	0.03 (0.02 - 0.04)	47.58	19.50
2/2/2014	5:00:00 PM	5:45:00 PM	0.34 (0.28 - 0.39)	0.13 (0.11 - 0.15)	0.02 (0.02 - 0.02)	0.03 (0.02 - 0.03)	66.05	21.18
2/3/2014	12:00:00 PM	12:45:00 PM	0.22 (0.18 - 0.26)	0.13 (0.11 - 0.15)	0.02 (0.02 - 0.03)	0.03 (0.02 - 0.03)	126.67	55.66
2/3/2014	1:00:00 PM	1:45:00 PM	0.14 (0.12 - 0.17)	0.15 (0.13 - 0.17)	0.03 (0.02 - 0.03)	0.03 (0.02 - 0.04)	99.02	46.64
2/3/2014	4:00:00 PM	4:45:00 PM	0.13 (0.11 - 0.15)	0.15 (0.13 - 0.18)	0.03 (0.02 - 0.03)	0.03 (0.02 - 0.04)	69.40	29.95
2/3/2014	5:00:00 PM	5:45:00 PM	0.21 (0.17 - 0.24)	0.29 (0.24 - 0.33)	0.04 (0.03 - 0.05)	0.03 (0.02 - 0.04)	75.91	30.54
2/4/2014	12:06:00 PM	1:36:00 PM	0.15 (0.13 - 0.18)	0.12 (0.11 - 0.14)	0.03 (0.02 - 0.04)	0.05 (0.03 - 0.06)	87.60	50.72
2/4/2014	4:01:00 PM	5:31:00 PM	0.14 (0.12 - 0.16)	0.09 (0.08 - 0.1)	0.02 (0.02 - 0.02)	0.02 (0.01 - 0.03)	80.70	50.52

C.17 Preliminary range of the POA volatility distribution for atmospheric predictions

Table C.9-1 Quartz filter organic collection efficiency of SVOC and IVOC based on Zhao et al.[230,231]

log C_i* @ 298 K	Gasoline median collection efficiency	Diesel median collection efficiency
0	0.444	1.000
1	0.202	0.613
2	0.230	0.355
3	0.228	0.057
4	0.156	0.015
5	0.078	0.006
6	0.019	0.006[#]

[#]: The measurement data showed that for log C* = 6 bin of diesel vehicles, no organics in this C* bin was collected onto the quartz filter and the collection efficiency should be equal to zero. In order to do the calculation here, I assume it has the same collection efficiency with the adjacent log C* = 5 bin.

Table C.9-2. POA volatility distribution assuming non-unity SVOC and IVOC collection efficiency

log C_i* @ 298 K	Median (interquartile range) of fi based on gasoline correction	Median (interquartile range) of fi based on diesel correction
-2	0.01 (0.01 - 0.01)	0 (0 - 0)
-1	0.01 (0.01 - 0.02)	0 (0 - 0)
0	0.03 (0.03 - 0.04)	0 (0 - 0)
1	0.14 (0.13 - 0.15)	0.01 (0.01 - 0.01)
2	0.17 (0.15 - 0.18)	0.02 (0.02 - 0.03)
3	0.11 (0.10 - 0.13)	0.10 (0.09 - 0.12)
4	0.18 (0.15 - 0.20)	0.41 (0.37 - 0.44)
5	0.08 (0.06 - 0.10)	0.23 (0.21 - 0.29)

6	0.25 (0.20 - 0.27)	0.19 (0.14 - 0.22)

As discussed in the main text, since quartz filters cannot capture all the gas phase organics, these volatility distributions presented in Figure 5.4 and Table C.3 only represent the POA captured by the quartz filter under ambient conditions. Here instead of assuming the SVOC and IVOC collection efficiency of quartz filter is 100%, I estimated the efficiency based on Zhao et al. [230,231] and provided a primary range of POA volatility distribution that could be applied to the total loading of organics (POA plus vapors) in the atmosphere.

In Table C.9-1 I estimated the quartz filter collection efficiency of SVOC (log C* = 0 to 2) and IVOC (log C* = 3 to 6) based on the measurement data from Zhao et al. [230,231] As discussed in the main text, Zhao et al. [230,231] expanded the POA volatility distribution of May et al. [113,114] to include those IVOCs that broke through the quartz filter. To estimate these IVOCs, they added two absorbent tubes behind the quartz filters and quantified those organics captured by absorbent tubes. For each C* bin, I calculated the median organic collection efficiency by using the median organic concentration measured from quartz filters divided by the median total organic concentration quantified by both absorbent tubes and quartz filters. Zhao et al. [230,231] reported the gasoline and diesel vehicles measurements separately and I also presented the quartz filter collection efficiency based on their gasoline and diesel measurements separately in column 2 and 3, respectively, in Table C.9-1. Zhao et al. [230,231] did not include this part of data in their published manuscript; I obtained the data from the personal communication with the author.

In Table C.9-2 I corrected the POA volatility distributions measured in the Fort Pitt Tunnel in this study based on the quartz filter collection efficiency of SVOC and IVOC presented in the Table C.9-1. The tunnel volatility distributions were corrected based on either the gasoline or the diesel vehicle measurements and are presented separately in column 2 and 3, respectively, in Table C.9-1. I think the gasoline case would be closer to the actual situation since the tunnel traffic

was dominated by gasoline vehicles. As discussed in the main text, since the gas-particle partitioning of IVOC is very sensitive to temperature and the tunnel quartz filter samples were collected at a lower temperature compared with the dynamometer studies conducted by Zhao et al. [230,231], the tunnel quartz filters may have a higher IVOC collection efficiency compared with the quartz filters collected in the dynamometer studies. Therefore, volatility distributions presented in Table C.9-2 may overestimate the f_i of IVOC bins. The actual POA volatility distribution in the atmosphere would be somewhere in the range defined by the volatility distribution presented in Table C.9-2 and in Table C.3, which assumes quartz filter collection efficiencies of SVOC and IVOC equal to unity. This range can be used as a preliminary range of the POA volatility distribution for atmospheric predictions.

C.18 Emission factors calculated based on the quartz filter samples

Table S8 is in a separated Microsoft Excel file. It listed the volatility distribution measured from each bare-Q filter and the propagated uncertainty of the organic mass fraction (f_i) under each C* bin for each bare-Q sample. I also present the emission factors of total organics (EF_Q) and particle phase organics (EF_OA) of each quartz filter sample in Table S8. The Emission Factor (EF) was calculated using the following equation:

$$EF = \frac{C_{OA}}{(\Delta CO_2 + \Delta CO)} \mathrm{MW_c} \cdot \mathrm{f_c} \quad (3)$$

Where the C_{OA} is the OA mass concentration. For EF_Q the C_{OA} was calculated using the OC concentration measured from bare-Q filters multiplied by an organic-mass-to-organic-carbon ratio of 1.2. For EF_OA the C_{OA} was calculated using the bare-Q OC minus the QBT OC and then multiplied by 1.2. ΔCO_2 and ΔCO are the averaged background corrected CO_2 and CO concentrations measured in the tunnel during the time of filter sampling. MW_c is the molecular weight of carbon, and f_c is is the weight fraction of carbon in the fuel. The fuel carbon fraction of gasoline and diesel are 0.85 and 0.87 [63], respectively.

I did not correct the OC concentration measured from bare-Q and QBT filters for ambient background. Therefore, the emission factors reported in the Table C.8 may overestimate the emission factors in the tunnel. But it could still show the trend of emission factors in different time periods.

Appendix D
Supporting information for
Volatile Organic Compound Emissions from Natural Gas Production Facilities Measured in the Denver-Julesburg Basin, the Uintah Basin, and the Marcellus Shale

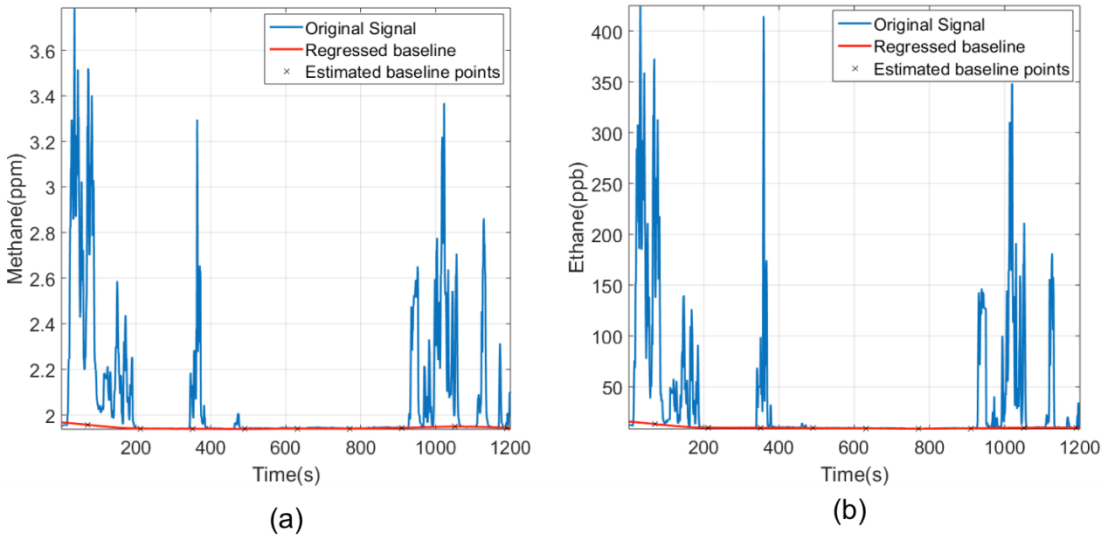

Figure D.1 Example of background correction of the methane and ethane measurements. Blue lines are the original measurement data, and red lines are the fitted ambient background concentrations.

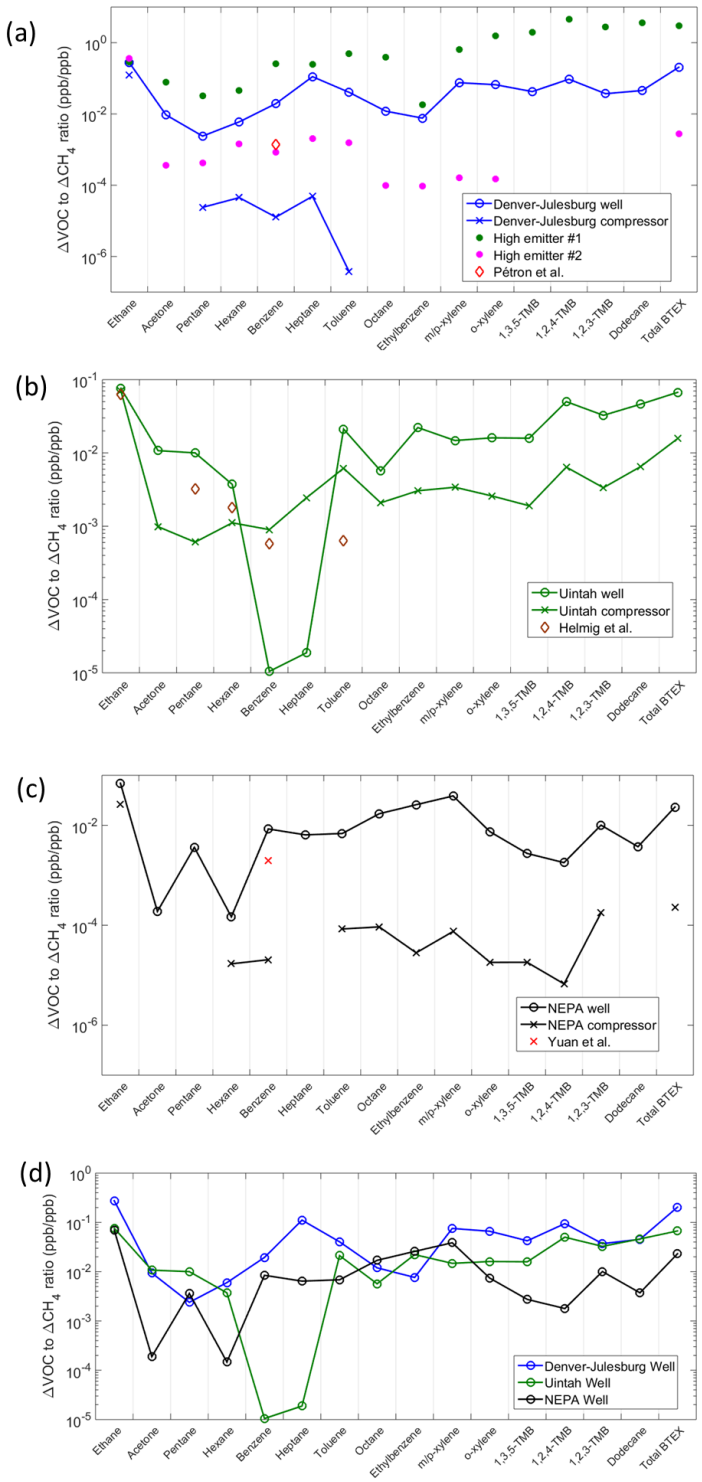

Figure D.2 Averaged background corrected VOC-to-CH_4 ratio measured at gas production facilities in (a) the Denver-Julesburg Basin, (b) the Uintah Basin, and (c) the NEPA. And (d) the comparison of the averaged VOC-to-CH_4 ratio measured at natural gas well pads in all three regions.

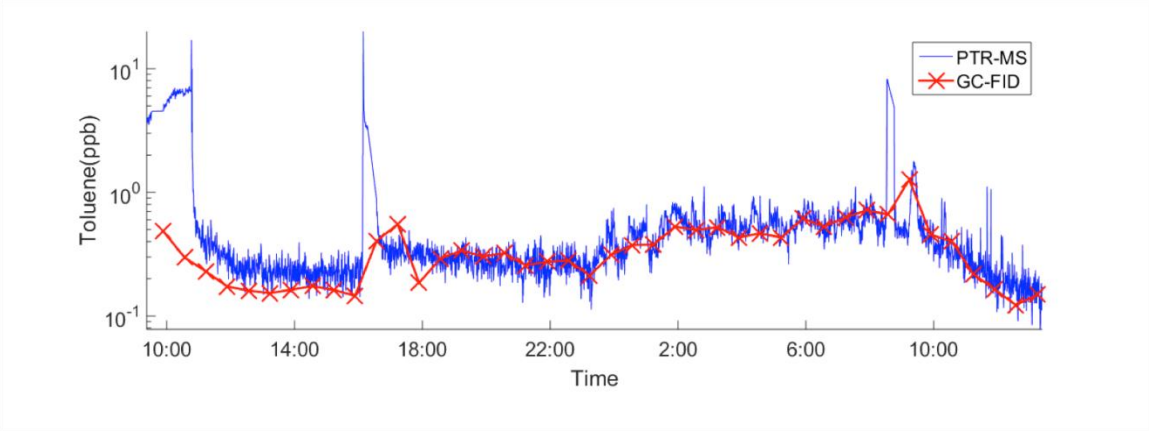

Figure D.3 Toluene concentrations concurrently measured by the PTR-MS (blue line) and the GC-FID (red line) downwind of one gas production wells in the Marcellus Shale. The measurement was from 10 am, 08/31/2016 to 12 pm, 09/01/2016.

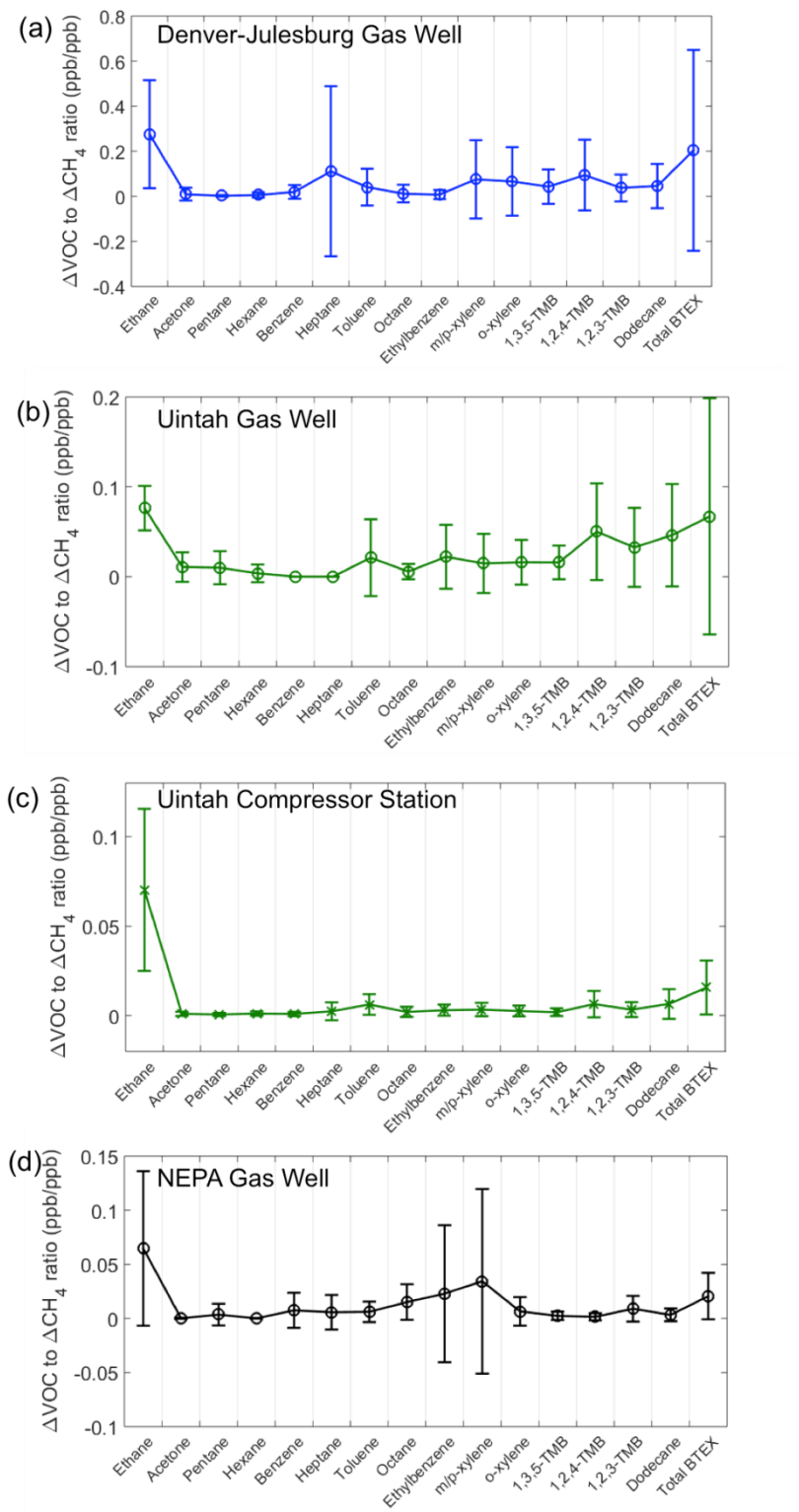

Figure D.4 Uncertainties of the background corrected VOC-to-CH_4 ratio measured at (a) gas wells in the Denver-Julesburg Basin, (b) gas wells in the Uintah Basin, (c) compressor stations in the Uintah Basin, and (d) gas wells in the NEPA. The symbols represent the mean value of all measurements, and the bars represent the standard deviation of all measurements.

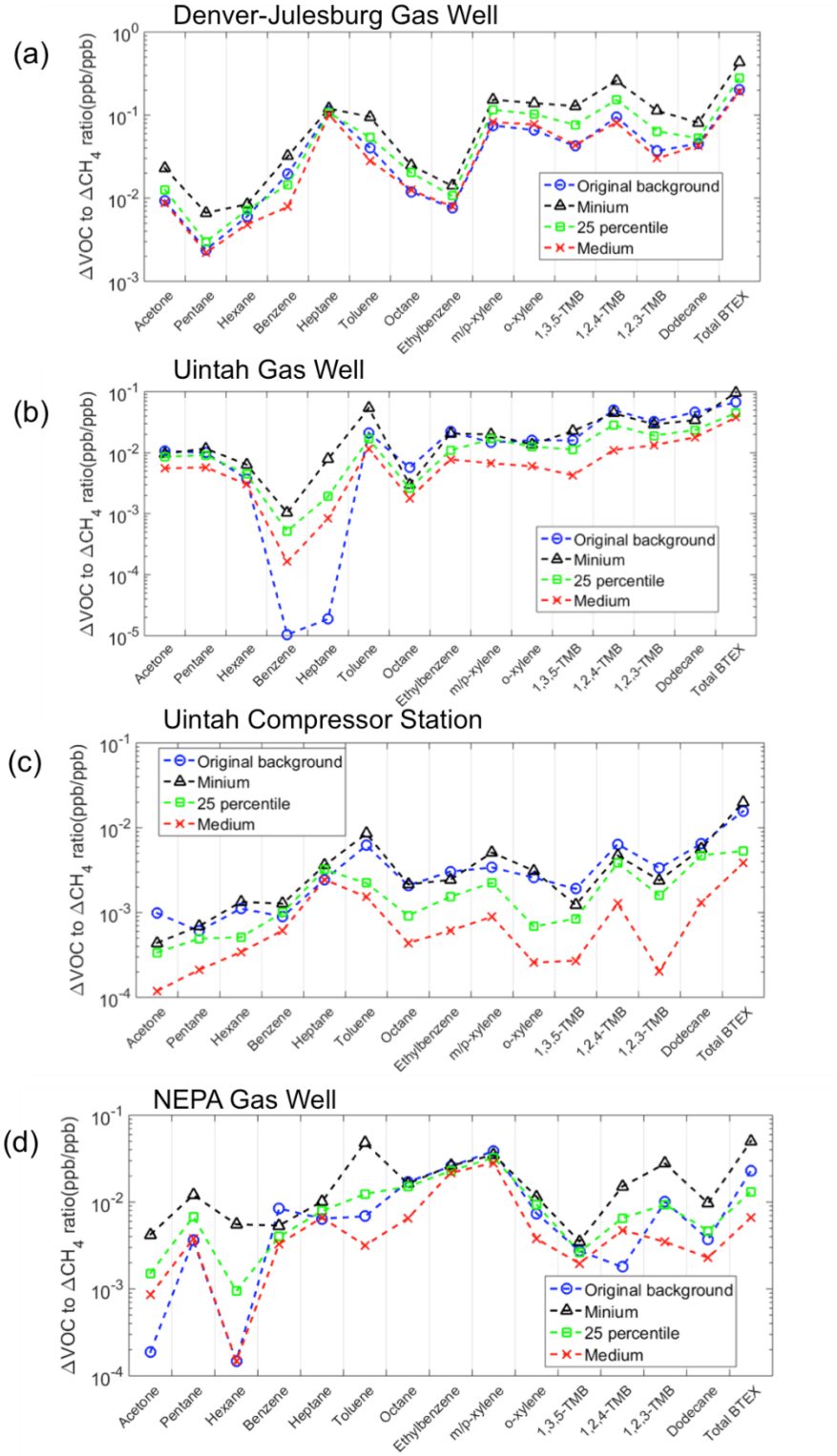

Figure D.5 The influence of the choice of the VOC regional background concentrations on the background corrected VOC-to-CH_4 ratio measured at (a) gas wells in the Denver-Julesburg Basin, (b) gas wells in the Uintah Basin, (c) compressor stations in the Uintah Basin, and (d) gas wells in the NEPA.

Table D.1 Correlation coefficients (R) between ΔVOC and ΔCH_4 measured in the Denver-Julesburg Basin, the Uintah Basin, and the NEPA

VOC species	Denver-Julesburg Well	Uintah Well	Uintah Compressor	NEPA Well
ethane	0.37	0.96	1.00	1.00
acetone	0.31	-0.24	0.90	-0.16
pentane	0.13	-0.20	0.95	-0.24
hexane	-0.12	0.11	0.95	0.57
benzene	0.04	0.82	0.97	-0.34
heptane	0.14	0.82	0.87	-0.19
toluene	-0.41	0.58	0.90	0.38
octane	-0.26	-0.05	0.83	-0.43
ethalbenzene	-0.18	0.20	-0.18	-0.12
m/p-xylene	-0.41	0.61	0.54	-0.31
o-xylene	-0.41	0.28	0.62	-0.52
1,3,5 - TMB	-0.11	-0.29	-0.53	0.03
1,2,4 - TMB	-0.44	-0.29	-0.57	-0.21
1,2,3 -TMB	-0.41	-0.28	-0.38	0.45
Dodecane	-0.12	-0.23	-0.60	0.56
BTEX	-0.41	0.53	0.91	0.10

Table D.2 Facility-level VOC emission rates measured in the Denver-Julesburg Basin, the Uintah Basin, and the NEPA

Unit: $\times 10^{-2}$ kg/h

Median value								
	Ethane	Acetone	Pentane	Hexane	Benzene	Heptane	Toluene	Octane
Denver-Julesburg well	46.89	0.18	0.35	0.56	10.62	12.24	0.78	0.02
Uintah well	15.04	2.34	0.59	0.16	0.00	0.00	2.46	1.39
Uintah compressor	93.50	2.93	2.43	4.80	0.38	0.00	44.11	13.17
NEPA well	24.65	0.00	0.00	0.01	3.00	0.00	4.52	21.56
25th percentile								
	Ethane	Acetone	Pentane	Hexane	Benzene	Heptane	Toluene	Octane
Denver-Julesburg well	4.26	0.01	0.00	0.00	0.38	0.30	0.09	0.00
Uintah well	6.34	0.17	0.15	0.00	0.00	0.00	0.45	0.79
Uintah compressor	64.65	1.11	0.56	1.29	0.00	0.00	10.58	2.43
NEPA well	11.88	0.00	0.00	0.00	1.47	0.00	0.26	1.59
75th percentile								
	Ethane	Acetone	Pentane	Hexane	Benzene	Heptane	Toluene	Octane
Denver-Julesburg well	513.09	4.02	7.81	21.38	36.20	86.47	54.24	26.66
Uintah well	31.79	6.65	7.68	0.32	0.00	0.00	8.27	11.15
Uintah compressor	405.21	7.76	4.47	12.16	6.13	34.69	65.00	28.50
NEPA well	39.93	0.00	0.29	0.22	6.79	2.45	12.83	48.82

Table continue

Unit: $\times 10^{-2}$ kg/h

Median value								
	Ethylbenzene	m/p-xylene	o-xylene	1,3,5-TMB	1,2,4-TMB	1,2,3-TMB	Dodecane	Total BTEX
Denver-Julesburg well	0.22	0.00	0.27	0.05	2.03	0.93	33.92	104.92
Uintah well	4.63	1.31	3.37	6.47	16.48	11.73	18.72	9.79
Uintah compressor	23.47	44.85	24.91	15.47	50.26	37.33	87.70	111.92
NEPA well	3.83	10.47	4.41	0.58	0.00	8.17	3.67	32.43
25th percentile								
	Ethylbenzene	m/p-xylene	o-xylene	1,3,5-TMB	1,2,4-TMB	1,2,3-TMB	Dodecane	Total BTEX
Denver-Julesburg well	0.00	0.00	0.00	0.00	0.00	0.00	0.00	0.49
Uintah well	1.25	0.00	1.40	0.26	5.36	2.31	5.13	7.47
Uintah compressor	5.95	3.20	5.14	4.04	13.94	5.11	29.95	3.95
NEPA well	0.71	2.20	0.00	0.06	0.00	0.50	0.27	7.13
75th percentile								
	Ethylbenzene	m/p-xylene	o-xylene	1,3,5-TMB	1,2,4-TMB	1,2,3-TMB	Dodecane	Total BTEX
Denver-Julesburg well	10.70	72.64	101.25	83.96	204.95	113.69	252.19	290.46
Uintah well	38.27	12.15	14.19	67.17	211.31	101.23	290.52	90.82
Uintah compressor	45.30	58.99	33.89	25.95	93.75	53.48	139.24	195.72
NEPA well	7.37	26.37	12.27	11.87	2.29	36.51	9.07	75.20

D.1 The VOC-to-CH_4 ratio measured at natural gas production facilities

The background corrected VOC-to-CH_4 ratios measured downwind of natural gas facilities are presented in Figure D.2. Only mean values of the measured VOC-to-CH_4 ratios are presented in Figure D.2, the standard deviations of the measured VOC-to-CH_4 ratios are presented in Figure D.4. The VOC-to-CH_4 ratios measured downwind of the gas wells and compressor stations in the Denver-Julesburg Basin is compared in Figure D.2 (a). As discussed in section 6.3.1, I excluded high emitters while calculating the mean VOC-to-CH_4 ratios of gas wells in order to make sure the results are not biased by high emitters. Only 2 samples were collected at one compressor station in the Denver-Julesburg Basin. Results show that the detected VOC species at the compressor station are about 2-3 order of magnitude lower than the gas wells, but since I only measured one compressor station, it may not represent the general trend for the entire region.

The VOC-to-CH_4 ratios measured at gas wells and compressor stations in the Uintah Basin are compared in Figure D.2 (b). The ethane-to- CH_4 ratios measured at gas wells and compressor stations are similar, but VOC species other than the benzene and heptane, the VOC-to-CH_4 ratios measured at gas wells are in general about 1 order of magnitude higher than the VOC-to-CH_4 ratios measured at compressor stations. The benzene-to-CH_4 ratio and the heptane-to-CH_4 ratio measured at gas wells are about two orders of magnitude lower than they measured at compressor stations. It is mainly because that for all nine gas well sites measured in the Uintah Basin, only one site has benzene and heptane concentrations higher than the regional background. The influence of the background on the estimation of VOC-to-CH_4 will be further discussed later.

In Figure D.2 (c) I compared the VOC-to-CH_4 ratios measured at gas wells and compressor stations in the NEPA. It should be noticed that only one sample was collected at one compressor station in the NEPA, therefore, the trend may not represent the general situation in the entire region. As shown in Figure D.2 (c), for all measured VOC species, the VOC-to-CH_4 ratios measured at gas wells are

about 1-2 order of magnitude higher than they measured at the compressor stations.

The averaged VOC-to-CH_4 ratios measured downwind of natural gas well pads in the Denver-Julesburg Basin, the Uintah Basin, and the NEPA are compared in Figure D.2 (d). In general, the VOC-to-CH_4 ratios measured in the Denver-Julesburg Basin are the highest among all three regions, while the VOC-to-CH_4 ratios measured in the NEPA are the lowest. The ethane-to-methane ratios measured at gas wells in the Uintah Basin and the NEPA are similar, while the ethane-to-methane ratio measured in the Denver-Julesburg Basin is about 4 times as the ethane-to-methane ratio measured in other two regions. The benzene-to-CH_4 ratio and the heptane-to-CH_4 ratio measured in the Uintah Basin are significantly lower than they measured in other gas production regions. The BTEX-to-CH_4 ratio measured at the gas wells in the Denver-Julesburg Basin is the highest, while it measured in the NEPA is the lowest among all three regions. The difference of the VOC-to-CH_4 ratios measured in all three gas production regions might be because that the VOC contents in the raw natural gas in these gas production fields are different, and/or the natural gas production facilities in these gas production fields have different characteristics on VOC emissions.

D.2 Influence of the background VOC concentrations on the VOC-to-CH_4 ratio

As shown in Figure 6.3, the VOC regional background concentrations are not always lower than all site downwind measurements. For some VOC species, the regional background concentrations are close to the median or even the 75^{th} percentile of all the site downwind measurements. The choice of background VOC concentrations may potentially change the calculated background corrected VOC-to-CH_4 ratio. In order to study the sensitivity of VOC-to-CH_4 ratio on the change of background VOC concentrations, for sites measured in each region, I used the original background concentration as well as the minimum value, the 25^{th} percentile, and the median value of all site downwind measurements as the

background VOC concentrations and recalculated the averaged VOC-to-CH_4 ratio. Results are shown in Figure D.5.

The variation of background VOC concentrations has a relatively limited influence (within 4 times) for all VOC-to-CH_4 ratios measured at gas well sites in the Denver-Julesburg Basin, as shown in Figure D.5(a).

For gas wells measured in the Uintah Basin (Figure D.5(b)), the variation of background VOC concentrations makes the benzene-to-CH_4 and heptane-to-CH_4 ratios varied in a range crossed 2-3 orders of magnitude. It is mainly because that the original background benzene and heptane concentrations measured in the Uintah Basin are larger than most of the gas well measurements. For all other species, the variation of VOC-to-CH_4 ratios are limited (within a factor of 5), and the VOC-to-CH_4 ratios calculated using the original background is very close to they calculated using the minimum site measurements as the background concentrations.

The background sensitivity of VOC-to-CH_4 ratios measured at the compressor stations in the Uintah Basin is presented in Figure D.5 (c). Since the VOC background concentrations are all lower than the site measurements, similar with the gas well measurements in the Uintah Basin, the VOC-to-CH_4 ratios calculated using the original background and minimum site measurements as background are very close for all VOC species.

The VOC-to-CH_4 ratios measured in the NEPA are in general more sensitive to the choice of background concentrations compared with sites measured in other regions (Figure D.5 (d)). The variations of the Acetone-to-CH_4 ratio and the Hexane-to-CH_4 ratio are over one order of magnitude.

To summarize, the VOC-to-CH_4 ratios of most VOC species we measured at the natural gas production sites are not sensitive to the change of background VOC concentrations, expect for those VOC species of which the measured background concentrations are higher than most of the site downwind measurements.